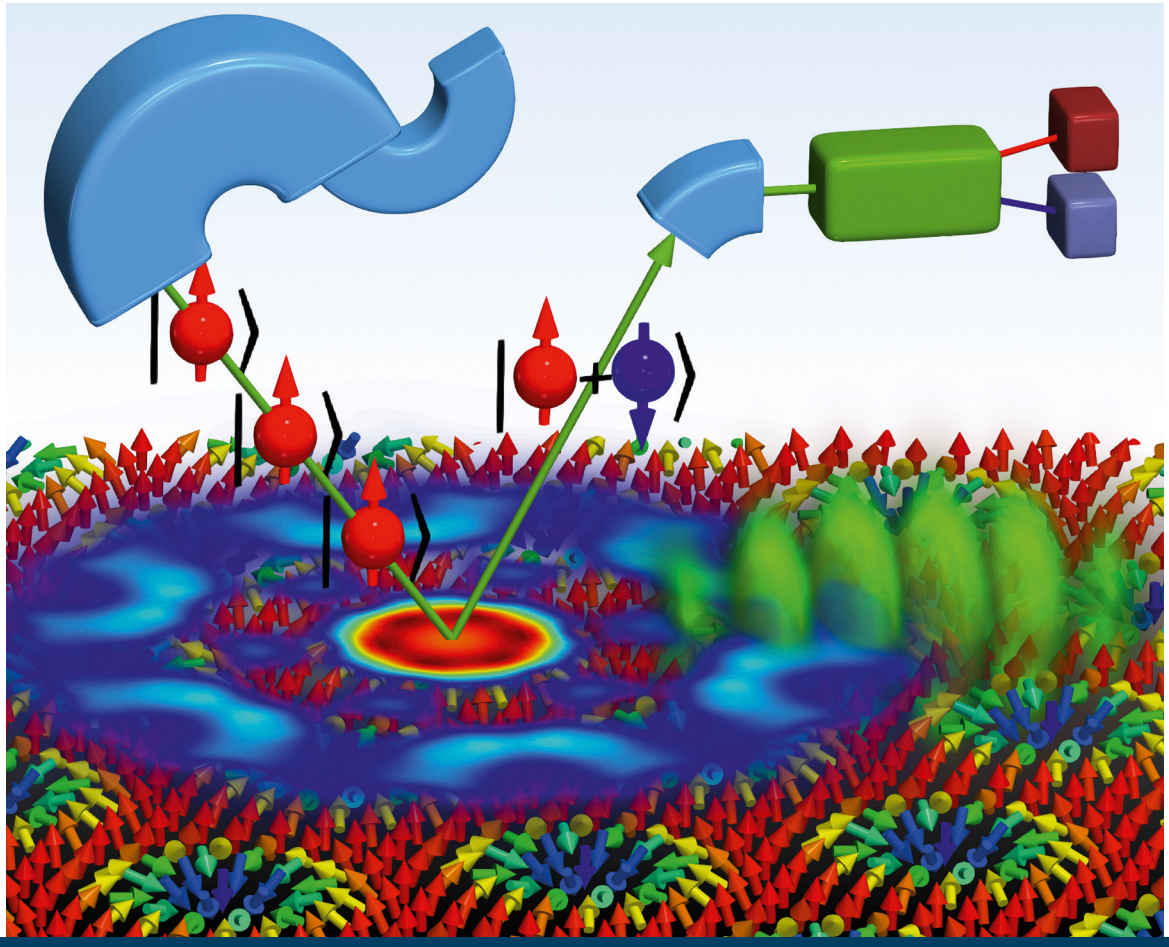

First-principles study of collective spin excitations in noncollinear magnets

Flaviano José dos Santos

Schlüsseltechnologien / Key Technologies
Band / Volume 212
ISBN 978-3-95806-459-1

Mitglied der Helmholtz-Gemeinschaft

JÜLICH
Forschungszentrum

Schriften des Forschungszentrums Jülich
Reihe Schlüsseltechnologien / Key Technologies Band / Volume 212

Forschungszentrum Jülich GmbH
Peter Grünberg Institut (PGI)
Quanten-Theorie der Materialien (PGI-1/IAS-1)

First-principles study of collective spin excitations in noncollinear magnets

Flaviano José dos Santos

Schriften des Forschungszentrums Jülich
Reihe Schlüsseltechnologien / Key Technologies Band / Volume 212

ISSN 1866-1807 ISBN 978-3-95806-459-1

Bibliografische Information der Deutschen Nationalbibliothek.
Die Deutsche Nationalbibliothek verzeichnet diese Publikation in der
Deutschen Nationalbibliografie; detaillierte Bibliografische Daten
sind im Internet über http://dnb.d-nb.de abrufbar.

Herausgeber und Vertrieb:	Forschungszentrum Jülich GmbH Zentralbibliothek, Verlag 52425 Jülich Tel.: +49 2461 61-5368 Fax: +49 2461 61-6103 zb-publikation@fz-juelich.de www.fz-juelich.de/zb
Umschlaggestaltung:	Grafische Medien, Forschungszentrum Jülich GmbH
Druck:	Grafische Medien, Forschungszentrum Jülich GmbH
Copyright:	Forschungszentrum Jülich 2020

Schriften des Forschungszentrums Jülich
Reihe Schlüsseltechnologien / Key Technologies, Band / Volume 212

D 82 (Diss. RWTH Aachen University, 2019)

ISSN 1866-1807
ISBN 978-3-95806-459-1

Vollständig frei verfügbar über das Publikationsportal des Forschungszentrums Jülich (JuSER)
unter www.fz-juelich.de/zb/openaccess.

Abstract

The pace of the current data revolution depends on the world's technological capability to store and process information. A great share of that is done by manipulating magnetic materials with astonishing speed and precision, which involves several dynamical processes. Among the latter are the collective spin excitations known as spin waves. Just like the strings of a guitar, spin waves are the natural "tunes" of a material's magnetization, and knowing their properties allows to predict, design and control technological devices.

In this thesis, we study the properties of spin waves in complex magnets focusing on systems of low-dimensionality. The manifestation of spin waves in collinear magnets, such as ferromagnets, has been extensively investigated. However, spin waves in noncollinear magnets are not fully understood yet. For instance, no experimental data is available concerning large-wavevector spin waves in thin films and surfaces. Nevertheless, novel noncollinear spin textures, such as the topologically nontrivial skyrmions, are at the heart of many recent proposals of information nanotechnologies for the future.

Therefore, we develop in this thesis an atomistic description of the spin waves in noncollinear magnets applicable to real materials. We achieve that by combining the density functional theory, as implemented within the Korringa-Kohn-Rostoker method, with the spin-wave adiabatic approximation. Effectively, we parametrize from first-principles a generalized quantum Heisenberg Hamiltonian accounting for relativistic effects of the spin-orbit coupling. Thus, besides calculating the magnetic exchange interaction, we also have access to the Dzyaloshinskii-Moriya interaction (DMI) and the magnetocrystalline anisotropy. To further relate our results with experimental works, we calculate the inelastic-electron-scattering spectrum using time-dependent perturbation theory. This led us to propose spin-resolved electron-energy-loss spectroscopy (SREELS) as an experimental tool to probe large-wavevector spin waves in noncollinear magnets.

We investigate ferromagnetic reconstructed cobalt thin films deposited on tungsten – Co/W(110). Our results are found to be in good agreement with recent high-resolution measurements with electron-energy-loss spectroscopy. Then, we study spin waves in a spin spiral and a skyrmion lattice to find that, counterintuitively, noncollinear magnets can host spin waves with zero spin angular momentum. Furthermore, we demonstrate that a full characterization of the spin waves in these systems requires spin-resolved spectroscopy such as SREELS.

We also explore antiferromagnetic materials and their complex spin textures, such as antiferromagnetic skyrmion lattices. From first-principles, we study two materials, a manganese monolayer on β–tungsten Mn/β–W and the Mn_5Si_3 compound. Using atomistic spin-dynamics simulations, we obtain an antiferromagnetic

spin-spiral ground state for the Mn/β–W. The Mn_5Si_3 has an antiferromagnetic collinear ground state just before the paramagnetic transition, where we investigate the hypothesis of the coexistence of collective spin excitations and diffusive spin fluctuations.

We predict the first material to host in-plane skyrmions (skyrmions living in an in-plane magnetization) stabilized by the DMI: 1 monolayer of reconstructed Co/W(110). Moreover, we demonstrate that its in-plane magnetization preserves the mirror symmetry of the crystal structure, which guarantees the coexistence of in-plane skyrmions and their antiparticles, the in-plane antiskyrmions, in the same material. Therefore, these in-plane skyrmions hold great potential for technological applications, especially because the dipole-dipole interaction, which limits the miniaturization of the usual skyrmions, acts to reduce the in-plane-skyrmion sizes. Finally, we also investigate the nonreciprocity of spin waves in noncollinear magnets induced by the DMI, which causes spin waves to acquire different properties while propagating in opposite directions. This allows us to propose experimental setups to extract the strength and direction of DMI in noncollinear magnets from inelastic scattering spectra, something which was so far not possible.

Zusammenfassung

Die Geschwindigkeit der gegenwärtigen digitalen Wandlung hängt von den weltweit verbreiteten technischen Leistung, Daten zu speichern und zu verarbeiten, ab. Ein großer Anteil ist auf die außerordentlich schnelle und präzise Manipulation von magnetischen Materialen zurückzuführen, welche viele dynamische Prozesse involviert. Letzteres beinhaltet die kollektive Spinanregung, welche auch als Spinwellen bekannt ist. Spinwellen sind, wie die Seiten einer Gitarre, die natürlichen Stimmen der Magnetisierung eines Materials. Das Kennen ihrer Eigenschaften erlaubt es technische Geräte vorherzusagen, zu entwerfen und zu kontrollieren.

Wir untersuchen die Merkmale von Spinwellen in komplexen Magneten mit Fokus auf niederdimensionale Systeme in dieser Arbeit. Die Ausprägung von Spinwellen in kollinearen Magneten, wie zum Beispiel in ferromagnetischen Materialien, wurde umfangreich erforscht. Dennoch sind Spinwellen in nicht kollinearen Magneten noch nicht vollständig verstanden. Zum Beispiel sind keine experimentelle Daten für Spinwellen mit großen Wellenvektoren in dünnen Schichten oder Oberflächen verfügbar. Dessen ungeachtet sind neuartige nicht kollineare Spinoberflächenstrukturen, wie die topologisch nicht trivialen Skyrmionen, das Herzstück der neuesten Vorschläge für die zukünftige Informationsverarbeitung im Bereich der Nanotechnologien.

Daher entwicklen wir in dieser Arbeit eine atomare Beschreibung der Spinwellen in nicht kollinearen Magneten, welche auf echte Materialen angewendet werden kann. Wir gelangen zu dieser Darstellung durch die Kombination der Dichtefunktional-Theorie, welche in der Korringa-Kohn-Rostoker Methode implementiert ist, mit der adiabatischen Spinwellennäherung. Wir parametrisieren aus den quantenmechanischen Grundprinzipien einen verallgemeinerten Heisenberg Hamiltonian, welcher für die relativistischen Effekte der Spin-Orbit-Koppelung Rechnung trägt. Daher haben wir, über die Berechnung der magnetischen Austauschwechselwirkung hinausgehend, Zugang zu der Dzyaloshinskki-Moriya Wechselwirkung (DMI) und der magnetokristallinen Anisotropie. Um unsere Ergebnisse weiter mit experimentellen Daten in Beziehung zu setzen, berechnen wir die inelastische Elektronenstreuung durch zeitabhängige Störungstheorie. Dies führt uns zu dem Vorschlag Spin-aufgelöste Elektronenenergieverlustspektroskopie (SREELS) als ein experimentelles Instrument zu verwenden, um Spinwellen mit großen Wellenvektoren in nicht kollinearen Magneten zu testen.

Wir untersuchen in Wolfram plazierte ferromagnetisch rekonstruierte feine Kobaltschichten – Co/W(110). Unsere Resultate zeigen, dass sie in guter Übereinstimmung mit den neuesten hochaufgelösten Messungen der Elektronenenergieverlustspektroskopie sind. Darauffolgend untersuchen wir Spinwellen in Spinspiralen und in einem Skyrmiongitter und stellen entgegen unserer Erwartungen fest, dass nicht kollineare Magnete Spinwellen ohne Spindrehimpuls aufnehmen können. Des Weiteren zeigen

wir, dass für eine vollständige Charakterisierung der Spinwellen in diesen Systemen Spin-aufgelöste Spektroskopie wie SREELS benötigt wird.

Wir erforschen ebenfalls antiferromagnetische Materialien und ihre komplexen Spinstrukturen wie antiferromagnetische Skyrmiongitter. Von Grund auf untersuchen wir zwei Materialien, eine Mangan Monoschicht auf β-Wolfram Mn/β–W und die Mn_5Si_3 Verbindung. Durch die Verwendung von atomarer Spindynamiksimulationen ergibt sich der antiferromagnetische Spin-Spiral-Grundzustand für Mn/ß-W. Mn_5Si_3 hat einen antiferromagnetisch kollinearen Grundzustand kurz vor dem paramagnetischen Übergang, wo wir die Hypothese der Koexistenz von kollektiven Spinanregungen und diffusen Spinfluktuationen erforschen.

Wir prognostizieren das erste Material, welches in Ebene Skyrmionen, Skyrmionen welche in einem in Ebene magnetisiertem Material leben, beinhaltet und durch DMI stabilisiert wird: Eine Einzelschicht aus rekonstruiertem Co/W(110). Weiterhin zeigen wir, dass die Magnetisierung in die Ebene die Spiegelsymmetrie der Kristallstruktur, welche die Koexistenz der in Ebene Skyrmionen und ihrer Antiteilchen, Antiskyrmionen in Ebene, im gleichen Material garantiert, erhält. Daher ergibt sich großes Potential für technische Anwendungen der in Ebene Skyrmionen, besonders auf Grund der Dipol-Dipol Wechselwirkung, welche die Miniaturisierung der gewöhnlichen Skyrmionen limitiert und reduzierend auf die in Ebene Skyrmionengröße wirkt.

Schlussendlich untersuchen wir die Nichtreziprozität von Spinwellen induziert durch DMI in nicht kollinearen Magneten, welche Spinwellen unterschiedliche Eigenschaften annehmen lässt während sie in gegensätzliche Richtungen propagieren. Dies erlaubt uns experimentelle Aufbauten vorzuschlagen, um die Stärke und Richtung von DMI in nicht kollinearen Magneten aus inelastischen Streuungsspektren zu extrahieren, was bis her noch nicht möglich gewesen ist.

Contents

Conventions and Abbreviations

	Notation	Mathematical object
$\mathbf{r}$, $\mathbf{R}$	bold letter	2 or 3-dim. vector
$\hat{\mathbf{r}}$	hat	normalized vector
r^α	superscript index	often labels a vector component
r_i	subscript index	lattice site, quantum number and other attributes
$\mathbf{A}$	bold capital letter	matrix (distinguished from vectors by context)
$\mathcal{H}$	calligraphic symbol	Hamiltonian

Abb.	Meaning
AFM	antiferromagnetic
ASA	atomic sphere approximation
BZ	Brillouin zone
DFT	density functional theory
DMI	Dzyaloshinskii-Moriya interaction
EELS	electron-energy-loss spectroscopy
FM	ferromagnetic
KKR	Korringa Kohn Rostoker
LDOS	local density of states
LLG	Landau Lifshitz Gilbert
LSDA	local spin density approximation
MCA	magnetocrystalline anisotropy
MEI	magnetic exchange interaction
ML	monolayer
SOC	spin-orbit coupling
SREELS	spin-resolved (EELS)

Chapter 1

Introduction

Our society is generating an unimaginable amount of data at ever-increasing rates. It is the era of *Big Data* and it is clear that we need to change our paradigms for data process and storage if we are to keep up with that demand. For the last two decades, the scientific community has been pushing to explore not only the charge but also the spin of the electrons in electronic devices, within the research field called *spintronics*. Despite the advances in the field, spintronics still relies on the motion of electrons, which often causes Ohmic losses. However, the spins of the electrons behold technological opportunities that go beyond charge and spin currents.

The electronic spins are responsible for most of the magnetism phenomenon in materials. In turn, every magnetic material behaves as an elastic medium: a perturbation of the local magnetization can propagate throughout the material analogously to the propagation of a wave in the sea. We call this phenomenon a spin wave, which are collective spin-excitations of magnetic materials. They were theoretically predicted by Bloch in 1930 and first measured almost three decades later by Brockhouse [1, 2].

Spin waves have a wide potential for technological applications. That is because they can propagate transporting energy, linear and angular momenta, and thus allowing information transmission through the material. Furthermore, because each spin can have a precessional motion while localized at a given crystal site, a spin wave propagates without transporting charge. Thus, we could think of a device that converts a voltage input into a spin wave for wave-based computing, which then generates an output that is converted back into a voltage. Such a device could have the advantages of parallel data processing on different wave frequencies, low power consumption, and allowing for neuromorphic and non-Boolean computing because we could also exploit the wave phase [3]. Spin waves have a wide range of wavelengths: from a few nanometers (and frequencies up to THz), where the magnetic exchange interaction dominates; to macroscopic wavelengths that are usually dominated by the magnetic dipole interaction. All these factors, together with the recent development of experimental techniques and the field of material sciences, attracted much attention to spin waves in the recent years [3–6]. The field of research that aims to develop means of using spin waves for information technologies is known as *magnonics*, and it is closely intertwined with spintronics.

Another current revolution in the field of magnetism concerns the exquisite spin textures (also called magnetic textures or magnetic configurations) related to chiral

interactions in noncentrosymmetric systems. These are noncollinear magnetic structures such as skyrmions, domain walls, magnetic bobbers and spin spirals [7–10], which arise from the delicate balance between intrinsic and extrinsic interactions, such as the magnetic exchange and Dzyaloshinskii-Moriya interactions, the magnetocrystalline anisotropy and external magnetic fields. While most studies focus on the static properties of these novel magnetic states, in this thesis, we focus on their dynamical properties due to the spin waves.

Besides the underlying magnetic interactions, spin waves are also sensitive to the magnetic textures. Therefore, understanding their properties in the various magnetic media is essential for future applications. A skyrmion, for example, is a localized noncollinear spin texture whose spins continuously winds from its parallel alignment with the background magnetization towards an antiparallel alignment at the center [7, 11, 12]. It is topologically distinct from the conventional magnetic textures, such as ferromagnetic and antiferromagnetic phases. It happens that spin waves of a topologically-nontrivial spin texture can inherit the topological properties of the medium. An example is the formation of topologically-protected edge states of a skyrmion lattice, which are immune to elastic backscattering [13, 14]. Thus, the study of unorthodox magnetic textures becomes relevant to the emergent field of *topotronics*, whose goal is to develop dissipationless electronics devices exploring the topological features of solid-state systems.

Due to their distinct topologies, it is not possible to transform a skyrmion into a ferromagnetic state without passing through a discontinuity of its topological properties, such as the topological charge. In the magnetization continuum limit, this discontinuity maps into an infinite barrier that guarantees the stability of skyrmions. In a real-world magnetic lattice, however, this energy barrier is finite, and while it assures robustness for the skyrmions, it is no longer sufficient to guarantee its stability. Instead, the occurrence and stability of skyrmions also depend on the specific magnetic properties of the system-material. Therefore, it becomes imperative in the latter context to accurately describe the magnetic properties of realistic materials, which requires cutting-edge first-principles simulations based on density functional theory (DFT).

The Dzyaloshinskii-Moriya interaction (DMI), responsible for the magnetic noncollinearity in the systems of our interest, can be best tailored by engineering the interface and surfaces between various materials. Often, we interface a magnetic material, such as Fe, Co, and Ni with heavy-element materials, such as W and Pt [15, 16]. This combination enhances spin-orbit coupling effects in the magnetic layers, which gives rise to a strong DMI. Therefore, multilayers, thin films, and surfaces are the perfect playground for our investigations. These structures have the further advantage of being inherently suitable for technological applications due to their reduced dimensionality.

The appeal of studying spin waves goes beyond their technological potential. They are also of fundamental interest in magnetism. In many cases, measuring the spin-wave properties of a system is the only way to determine its magnetic properties, such as the spatial dependence of the magnetic exchange interactions. The latter leads us to the next aspect of the present work, which is to advance the methodology of detecting and measuring spin waves.

An essential experimental technique to measure spin waves in magnetic thin

films is the electron-energy-loss spectroscopy (EELS) and its spin-polarized version (SPEELS) [17, 18]. While other techniques also have surface sensitivity, such as the Brillouin-light-scattering spectroscopy [19], only EELS can measure short-wavelength spin waves in thin films. However, up to now, EELS has only been used to investigate spin waves in ferromagnets. In such an experiment, an incoming electron can only excite spin waves in a ferromagnet if its spin is antiparallel to the spin of the magnetic sample. Thus, the spin of the electron can undergo a spin-flip process, which also transfers energy and linear momentum, decreasing the net magnetization of the sample by creating a spin-wave quantum, also known as a *magnon*. This picture changes, however, when the electrons are scattering from a noncollinear spin texture. Will the creation of a magnon require a spin-flip of the probing electron?

Thus, this thesis aims at contributing to three different aspects of the physics of spin waves and their applications: i) studying new spin textures; ii) providing a framework for material-specific investigation by parameterizing the magnetic models from first-principles calculations; iii) and connecting the theoretical results to experimental measurements. This thesis is organized as follows.

In Chapter 2, we give an introduction to magnetism, which shall help us to understand why some materials are magnetic while others are not. We introduce a generalize Heisenberg Hamiltonian that provides us with an adiabatic description of magnetic materials, which are regarded as composed of localized magnetic moments. In particular, we demonstrate that spin waves are the natural spin-excitation modes of magnetically ordered systems. We conclude by discussing how the spin-wave spectrum of a general noncollinear magnet can be systematically calculated within the adiabatic approximation. This equips us with a formalism suitable for a numerical implementation by writing the Hamiltonian in a matrix form, performing a Holstein-Primakoff transformation, and then a Bogoliubov diagonalization to obtain the spin-wave spectrum.

Chapter 3 is dedicated to discuss the *ab initio* methods used to obtain the Hamiltonian parameters in order to characterize the spin-wave properties of specific materials. Thus, we start providing an introduction to DFT and the Green function Korringa-Kohn-Rostoker (KKR) method [20]. Then, we discuss how the system's Green function connects to the parameters of the magnetic exchange and the Dzyaloshinskii-Moriya interactions by applying the infinitesimal rotation method [21, 22].

In Chapter 4, we develop a theory for the inelastic scattering of spin-$\frac{1}{2}$ particles from spin waves in noncollinear magnets. The scattering cross-section is proportional to the spin-spin correlation function, for which we derive a formula as a function of the spin-wave eigenvalues and eigenfunctions obtained in the adiabatic approximation described in Chapter 2.

Due to the recent high-resolution EELS experiments that measured for the first time up to three spin-wave modes [23–25], in Chapter 5, we study ferromagnetic ultrathin films with 3-8 monolayers of cobalt deposited on the tungsten (110) surface. The large lattice mismatch between cobalt and tungsten leads to the reconstruction of the cobalt film, which requires a large supercell to theoretically describe the resulting structure that consequently reduces the Brillouin zone (BZ). We discuss how one can unfold the spin-wave dispersion into the BZ of the unreconstructed

crystal structure, which enables a direct comparison between the theoretical and experimental results. Thus, because of the available experimental data, this study gives us a great opportunity to test our theoretical framework before we advance to investigate noncollinear magnets.

Within Chapter 6, we study our first noncollinear spin textures. Based on the scattering theory derived in Chapter 4, we propose the augmentation of the current (SP)EELS setups to include a spin filter of the scattered electrons. We called the resulting experiment, which provides us with the spin-resolved spin-wave spectra, a spin-resolved electron-energy-loss spectroscopy (SREELS) [26]. Then, we consider a model system consisting of a hexagonal-lattice monolayer with interactions between the nearest neighbors. We discuss the resulting SREELS spectra for three of the system's phases: a ferromagnetic phase, a spin spiral, and a skyrmion lattice. We dedicated the rest of the chapter to determine the main properties of the spin waves in these noncollinear magnets, showing how they can be detected through SREELS, and how they differ from the known textbook physics of ferromagnets. For example, we demonstrate that noncollinear spin textures can have spin-wave modes with opposite or even vanishing angular momenta, which is in strong contrast to spin waves of ferromagnets.

We dedicate Chapter 7 to investigate spin waves in noncollinear systems whose exchange interaction is predominately antiferromagnetic. Among others, we study antiferromagnetic spin spiral and antiferromagnetic skyrmion phases. We then study two particularly interesting materials: Mn/β–W and Mn_5Si_3 [27–29]. The results for the thermoelectric Mn_5Si_3 were compared with the experimental data provided by our collaborators, which contributed to elucidate an open question related to the spin-fluctuations of this material.

In Chapter 8, we focus on even thinner films, 1-3 monolayers, of Co/W(110), where the effects of the Dzyaloshinskii-Moriya interaction are expected to be more relevant. Thus, we employ the relativistic KKR method to determine the DMI properties of these films. The cobalt reconstruction breaks the C_{2v} symmetry of the W(110) substrate reducing the symmetry of the combined system into the C_s point group. As a result, we obtain nonvanishing out-of-plane components of the DMI. This property, together with the dominant in-plane magnetocrystalline anisotropy, makes 1Co/W(110) the first material predicted to host in-plane skyrmions, i.e., skyrmions that leaves in an in-plane magnetized system. This discovery has a profound impact on skyrmion research because it widens the scope of materials where skyrmions can be found by showing that in-plane magnetized material can host them too. While the dipole-dipole interaction prevents the formation of ultrasmall out-of-plane skyrmions [30], it helps to make in-plane skyrmions even smaller, which is desirable for technological devices. The in-plane magnetization of 1Co/W(110) preserves the mirror plane of the crystal structure. We demonstrate that this leads to skyrmion and antiskyrmion being energy degenerate, which guarantees their coexistence in this film. That is because these quasiparticles can be brought into each other via the symmetry operation given by the preserved mirror plane. Furthermore, the nanometric size of these skyrmionic structures, together with other conceptual advances, makes them of great interest in the field of spintronics, magnonics, and topotronics.

Chapter 9 concerns the phenomenon called nonreciprocity of spin waves, related

to the asymmetries of the spin-wave properties in the reciprocal space. It is caused by the Dzyaloshinskii-Moriya interaction and it was predicted theoretically to occur in ferromagnets, and it was subsequently observed with SPEELS in thin films of Fe on W(110) [31–33]. Measuring this nonreciprocity allows us to determine both the strength and the vectorial orientation of the DMI. In this last result chapter, therefore, we explore and solve the nontrivial problem of determining if spin waves in noncollinear magnets can also be nonreciprocal due to the DMI and under which condition this happens. Furthermore, we discuss the role of SREELS in unveiling these nonreciprocities. Finally, in Chapter 10, we conclude with our final remarks and perspectives for the present work.

After each chapter, the reader may find the appendices that concern the details and derivations of the results presented in the main text. While the comprehension of the discussion and results in the main text does not demand an examination of the appendices, the readers looking for a deeper insight will certainly benefit from the appendices' contents.

Chapter 2

Theory of spin waves

Spin waves are elementary collective spin excitations of magnetic materials. They cause the atomic spin moments to precess around their equilibrium axes in a coherent manner. The quantum of spin wave is called a magnon and its creation reduces the material's total angular momentum by $\hbar$. In this chapter, we present the foundations of the theoretical description of the spin-wave phenomenon in the adiabatic approximation. We start with an introduction to magnetism to understand the origin of the magnetic moments and the interactions they are often subjected to, such as the magnetic exchange and the Dzyaloshinskii-Moriya interactions. Next, we introduce a generalized Heisenberg model which provides us with a simple Hamiltonian to describe the magnetic properties, both static and dynamics of magnetic materials. Finally, we introduce the concept of spin waves within a semiclassical picture, which appears as natural precession modes of the interacting magnetic moments. Lastly, we show a quantum mechanical formalism for spin waves which allows us to systematically determine the energies and eigenmodes of any noncollinear magnet described by generalized Heisenberg Hamiltonian.

2.1 Introduction to magnetism

Magnetic materials are indispensable in our society. Their applications are countless going from data storage devices, passing through energy generation, up to medical therapies. But why are some materials magnetic while others are not? In fact, most materials we encounter in our daily lives seem to be nonmagnetic, i.e., they appear not to interact with a magnetic field or other magnets, such as wood, glass, plastics, etc. For a material to feature a finite magnetization, just like the decorative magnets on your fridge door, it has to fulfill a series of criteria. First, at the microscopic level, it has to be composed of atoms that possess finite magnetic moments, that is, atoms that are like tiny bar magnets themselves. Next, the atomic magnetic moments need to feature a long-range order such that they align along a preferential direction. The materials that fulfill these conditions are called ferromagnets.

However, many other magnetic materials present all sorts of orderings. Antiferromagnets, for example, have adjacent moments of the same magnitude anti-aligned to each other. There are even more complex structures, which have canted magnetic moments generating a noncollinear configuration, such as in spin spirals and skyrmion lattices. Spin spirals are formed when the magnetic moment orientation ro-

tates around a given axis with a well-defined rate when we move across the material. A skyrmion lattice, for example, can be obtained by superimposing multiple spin spirals, each with a different rotational axis. However, skyrmions can also appear isolated as local perturbations of a uniform magnetic background. We elaborate on these structures when discussing the ground states of magnetic systems in Sec. 2.2. Magnetic materials with no long-range ordering are called paramagnetic, and materials whose atoms have no permanent magnetic moments are called diamagnetic. For more detail, please refer to the standard texts on condensed matter physics such as Kittel [34] or Ashcroft and Mermin [35]. Many of the discussions in this chapter were also inspired by Refs. [36–39]. In the next section, we establish some important concepts in magnetism and discuss the origin of the atomic magnetic moments.

2.1.1 Magnetic moment and magnetization

The magnetic dipole moment $\mathbf{m}$ of an object is defined through the relation between the aligning torque $\boldsymbol{\tau}$ it experiences when subject to an external magnetic field $\mathbf{B}$:

$$\boldsymbol{\tau} = \mathbf{m} \times \mathbf{B} \quad . \tag{2.1}$$

Such torque is experienced, for example, by a current-carrying loop of wire when we apply a uniform magnetic field not aligned with the loop axis. For short, we refer to $\mathbf{m}$ as a magnetic moment.

In general, the magnetism in materials arises almost entirely from the magnetic moments due to electrons. The magnetic moments from the atomic nuclei are about 10^3 smaller than the electronic ones, therefore they are negligible for our study. We also neglect induced magnetic moments, which are generated as a response to external magnetic fields. We rather focus on permanent magnetic moments. There are two contributions to the total magnetic moment of an electron: the orbital and spin magnetic moments.

Orbital angular momentum

The orbital magnetic moment comes from the motion of the bound electrons in their stationary orbits and the current loops they cause within an ion [37]:

$$\mathbf{m}^{\mathrm{orb}} = \frac{1}{2} \int \mathbf{r} \times \mathbf{j} \, \mathrm{d}^3 r \quad , \tag{2.2}$$

considering that the ion rests in the origin. The magnetization current density can be expressed as:

$$\mathbf{j} = -e \sum_{j=1} \delta(\mathbf{r} - \mathbf{r}_j) \mathbf{v}_j \quad , \tag{2.3}$$

where $\mathbf{v}_j$ is the velocity of the ion j-th electron with electrical charge $-e$. As $\mathbf{j}$ is due to bound electrons, it must satisfy $\nabla \cdot \mathbf{j} = 0$, which ensures that its flux through any arbitrary volume is zero. Putting together the last two equations, we obtain:

$$\mathbf{m}^{\mathrm{orb}} = -\frac{e}{2} \sum_j \mathbf{r}_j \times \mathbf{v}_j = -\frac{1}{\hbar} \mu_{\mathrm{B}} \sum_j \mathbf{L}_j \quad , \tag{2.4}$$

where $\mathbf{L}_j = \mathbf{r}_j \times (m_e \mathbf{v}_j)$ is the angular momentum of the j-th electron, $\mu_\mathrm{B} = e\hbar/2m_e$ is the Bohr magneton, m_e is the electron mass, and $\hbar$ is the reduced Planck constant. The above expression relates the orbital magnetic moment of the electrons to their orbital angular momenta. As we can see, the magnetic moment and the angular momentum are always antiparallel to each other because the electron charge is negative. In the literature, however, often the minus sign is disregarded, which is the convention we follow for the whole of this thesis.

Spin angular momentum

The second contribution to the electronic magnetic moment comes from the spin angular momentum $\mathbf{S}$ of the electrons, and they are related by:

$$\mathbf{m}^{\mathrm{spin}} = \frac{1}{\hbar}\mu_\mathrm{B} g_e \mathbf{S} \quad . \tag{2.5}$$

The Lande's spin g-factor is given by

$$g_e = 2\left(1 + \frac{\alpha}{2\pi} + \mathcal{O}(\alpha^2)\right) \sim 2.0023 \quad , \tag{2.6}$$

where $\alpha = 1/137$ is the Sommerfeld's fine-structure constant. For most applications, we can assume $g_e = 2$ making the total magnetic moment, combining the orbital and spin contributions, to be given by

$$\mathbf{m} = \frac{\mu_B}{\hbar}(\mathbf{L} + 2\mathbf{S}) \quad . \tag{2.7}$$

Note that the magnetic moment $\mathbf{m}$ is not parallel/antiparallel to the total angular momentum $\mathbf{J} = \mathbf{L} + \mathbf{S}$.

Another common concept used in magnetism is that of the magnetization, which is defined as the volumetric density of magnetic moments and it can be written as:

$$\mathbf{M}(\mathbf{r}) = \frac{\mathrm{d}\mathbf{m}}{\mathrm{d}V} \quad . \tag{2.8}$$

In general, it varies from point to point inside of the material. Next, we want to understand two important aspects, the reason why some materials have atoms with permanent magnetic moments, and how do they order.

2.1.2 Magnetic moment origin

Isolated atom

We saw that a magnetic moment of an atom is associated with the orbital and spin momenta of its electrons. Let us now study how an *isolated* atom ends up with net orbital and spin momenta by considering a hydrogen atom. Because the elostractic potential of the hydrogen nucleus is spherically symmetric, the possible state for a single electron can be completely characterized by four quantum numbers, n, l, m_l, and m_s [38]:

1. n is the principal quantum number, which is associated with the number of radial nodes in the wavefunction;

2. l is the orbital-angular-momentum quantum number also called the azimuthal quantum number, and it is associated with the expectation value of orbital angular momentum: $\langle L^2 \rangle = \hbar^2 l(l+1)$, where $0 \leq l \leq n-1$;

3. m_l is the eigenvalue of the z-component of the orbital angular momentum in unit of $\hbar$, also known as the magnetic quantum number: $\langle L^z \rangle = \hbar m_l$, with $-l \leq m_l \leq l$;

4. And m_s is the spin quantum number, associated with the z–component of the spin angular momentum: $\langle S^z \rangle = \hbar m_s$, where $m_s = \pm 1/2$.

Note that we do not need to specify a quantum number associated with the total spin angular momentum, such as S^2, because it is always $1/2$.

States with the same principal quantum number n form a *shell*. In each shell, states with the same orbital angular momentum l form a *subshell*. By further specifying the magnetic quantum number m_l, we have an *orbital*. Each orbital has two channels since the spin quantum number m_s can assume two values. Each subshell is often labeled by a nX expression, where n is the principal quantum number and X denote $l = 0, 1, 2, 3$ by the letters s, p, d, f, respectively.

As we mentioned before, magnetic moments can have two origins, spin and orbital angular momenta. Since the addition of quantum angular momenta is no simple matter, especially when considering multiple electrons, we will consider the $L-S$ coupling scheme (also known as the Russel-Saunders coupling scheme). In this approximation, all the electron spins combine to form a single spin $\mathbf{S} = \sum_i \mathbf{S}_i$ and similarly, all the orbital angular momenta combine too $\mathbf{L} = \sum_i \mathbf{L}_i$. The total angular momentum of the atom can then simply be written as $\mathbf{J} = \mathbf{L} + \mathbf{S}$. This approach allows us to use the quantum numbers of the combined angular momenta L, M_L, S and M_S to label the states of the entire atom. Each of these numbers is simply the arithmetic sum of the correspondent values for each electron. Now, we also need to specify S, which can assume values different of $1/2$.

Next, we discuss how an isolated atom accommodates multiple electrons, and how we can determine its ground state [36, 38]. The energy of the orbitals depends only on n and l. In the ground state, an isolated atom will fill in first the orbitals with the lowest energies while respecting Pauli's exclusion principle, that is, no two electrons can share the same set of quantum numbers. Furthermore, the priority within each subshell is given by the Hund's rules: Electrons must occupy the orbitals that maximize S. This means that the orbitals of a subshell are each occupied with one electron, of parallel spins, before doubling the occupancy of each orbital. This first rule permits to minimize the Coulomb repulsing among electrons in the same subshell. For a given value of S, L is then maximized. This implies that the interaction among spins and among orbital momenta are both ferromagnetic, but the spin-spin interaction is stronger. The total angular momentum is given by $J = |L - S|$ if the subshell is less than half-full, or $J = L + S$ if it is more than half-full. When the subshell is half-full, $L = 0$, and so $J = S$. These differences in the total angular momentum are caused by a relativistic effect called spin-orbit coupling, which we will be discussed further in this chapter.

Localized magnetism

Hund's rules imply that no net angular momentum is expected from full subshells because for each electron with a given spin projection m_s there is another with $-m_s$; and similarly, there should be electrons with the opposite azimuthal quantum numbers. This is the case of the noble gases. Thus, it is easy to see that most elements of the periodic table will have a net angular momentum and, therefore, a magnetic moment when isolated.

That is also important to understand the origin of the permanent magnetic moment of some solids. It is especially the case for elements whose angular momentum comes from inner incomplete subshells whose electrons are less susceptible to be involved with bonding in a crystal. These elements can retain their magnetic moment when in a solid, which are then said to possess localized magnetism, once the electrons responsible for the magnetic moment are well localized in their respective crystal sites, such as in insulators.

Nevertheless, the observed magnetic moment in solids is often completely different from that in an isolated atom. This is especially true for the orbital angular momentum L, which is *quenched* because of the nonspherical electrostatic potential from surrounding atoms.

Itinerant magnetism - Hubbard model

In some metallic materials, the same electrons responsible for the electrical conduction give rise to magnetism [37]. Examples are $3d$ materials such as Fe, Co, and Ni. In this case, the Coulomb interaction produces a spin-dependent band shift when the system is below its critical temperature. In this way, one spin orientation becomes more favorable than the other, and the imbalance in the number of electrons in each spin channel yields a finite magnetization.

A simple model that describes this phenomenon is the Hubbard model [40], which is described by the Hamiltonian:

$$\mathcal{H} = \sum_{ij\sigma} t_{ij} c^{\dagger}_{i\sigma} c_{j\sigma} + \frac{1}{2} U \sum_{i\sigma} n_{i\sigma} n_{i\bar{\sigma}} \quad . \tag{2.9}$$

The operator $c^{\dagger}_{i\sigma}$ creates an electron with spin σ on the crystal site i, while $c_{j\sigma}$ destroys it on site j, and $n_{i\sigma} = c^{\dagger}_{i\sigma} c_{i\sigma}$ is the occupation number operator. $\bar{\sigma}$ represents the opposite spin projection of σ. The hopping integral t_{ij} contains the kinetic energy and the crystal potential, and it is associated with the probability of an electron to hop from site i to j. In this model, electrons are considered to interact among themselves only when on the same site, where they feel the screened effective Coulomb potential given by the parameter U. Therefore, it is a good approximation for metallic systems, where the Coulomb interaction is strongly screened.

The Hubbard model can be solved within the mean-field approximation using the Hartree-Fock decoupling of the four-operators terms of Eq. (2.9). Each of these terms is replaced by a combination of all possible operator pairs multiplied by the remaining operators' mean values. Thus, one obtains that the paramagnetic state is unstable when the system satisfies the Stoner criterion

$$U\rho(\mathrm{E_F}) \geq 1 \quad , \tag{2.10}$$

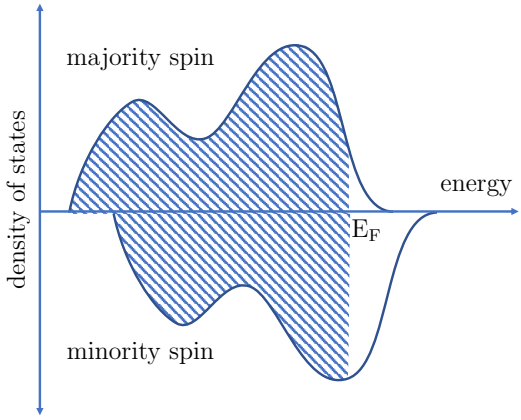

Figure 2.1: Density of states for the electrons in the majority and minority spin channels. The total number of electrons is given by the area between the curves and the horizontal axis integrated up to the Fermi level E_F. Due to the shift in the bands caused by the electron-electron interaction, the total number of electrons in the majority spin channel is larger than electrons in the minority one yielding a net magnetization.

where $\rho(E_F)$ is the density of states at the Fermi energy E_F. The system then orders magnetically and as a result, the density of states of the two spin channels are shifted apart in energy by

$$\Delta = Um \quad , \tag{2.11}$$

where the magnetization $m = n_\uparrow - n_\downarrow$, and $n_\sigma = \sum_i \langle n_{i\sigma} \rangle / N$. The imbalance of electrons due to the on-site exchange interaction that yields a net magnetization is illustrated in Fig. 2.1.

In some of the crystal sites, the density of electrons with spin up differs from that of electrons with spin down, which yields to a net local magnetic moment $\mathbf{m}_i$. One should have in mind, however, that these localized moments are generated by itinerant electrons that are not particularly localized in any atomic site. In this thesis, we consider the *adiabatic approximation* that regards the fast motion of the electrons as decoupled from the slower dynamics of the localized magnetic moments.

2.1.3 Zeeman energy

After understanding the origin of the magnetic moments, it is time to investigate how they interact with an applied magnetic field. For that, consider the quantum-mechanical Hamiltonian of a charged particle in an electromagnetic field, which is given by [38]

$$\mathcal{H} = \frac{1}{2m}\left(\frac{\hbar}{\mathrm{i}}\nabla - q\mathbf{A}\right)^2 + q\phi \quad . \tag{2.12}$$

We postulate that all the properties of the particle are described by the wavefunction $\psi(\mathbf{r}, t)$, which is a solution of the Schrödinger equation:

$$\mathrm{i}\hbar\frac{\mathrm{d}\psi}{\mathrm{d}t} = \mathcal{H}\psi \quad . \tag{2.13}$$

For a static electromagnetic field, this last equation describes how the wavefunction evolves with time while the Hamiltonian operator is time-independent within the Schrödinger picture. Thus, the wavefunction can be written as

$$\psi(\mathbf{r},t) = \psi(\mathbf{r})e^{-\mathrm{i}\mathcal{E}t/\hbar} \quad . \tag{2.14}$$

Replacing this expression in Eq. (2.13), we have that $\psi = \psi(\mathbf{r})$ must satisfy

$$-\frac{\hbar}{2m}\nabla^2\psi - \frac{\hbar}{\mathrm{i}}\frac{q}{2m}\Big(\nabla\cdot(\mathbf{A}\psi) + \mathbf{A}\cdot\nabla\psi\Big) + \Big(\frac{q^2}{2m}A^2 + q\phi\Big) = \mathcal{E}\psi \quad . \tag{2.15}$$

To evaluate the second term of the above equation, we will consider the following properties.

Using the Coulomb gauge, $\nabla\cdot\mathbf{A} = 0$, we have that

$$\nabla\cdot(\mathbf{A}\psi) = (\nabla\cdot\mathbf{A})\psi + \mathbf{A}\cdot\nabla\psi = \mathbf{A}\cdot\nabla\psi \quad . \tag{2.16}$$

Furthermore, for a uniform magnetic field, we have that:

$$\begin{aligned}\nabla\times(\mathbf{B}\times\mathbf{r}) =& \mathbf{B}\nabla\cdot\mathbf{r} - \mathbf{r}\nabla\cdot\mathbf{B} + (\mathbf{r}\cdot\nabla)\mathbf{B} - (\mathbf{B}\cdot\nabla)\mathbf{r}\\ =& (\nabla\cdot\mathbf{r})\mathbf{B} - (\mathbf{B}\cdot\nabla)\mathbf{r}\\ =& 3\mathbf{B} - \mathbf{B} = 2\mathbf{B}\\ =& 2\nabla\times\mathbf{A} \quad .\end{aligned} \tag{2.17}$$

From the last equation, we can choose to write

$$\mathbf{A} = \frac{1}{2}(\mathbf{B}\times\mathbf{r}) \quad , \tag{2.18}$$

which is known as the symmetric gauge. To derive the last two equations, we used the triple product expansion and the Maxwell's equation derived from Gauss' Law:

$$\nabla\cdot\mathbf{B} = 0 \quad , \tag{2.19}$$

which permit us to write $\mathbf{B} = \nabla\times\mathbf{A}$.

Thus, from the results in Eqs.(2.18) and (2.16), the second term of Eq. (2.15) becomes:

$$\begin{aligned}-\frac{\hbar}{\mathrm{i}}\frac{q}{m}\mathbf{A}\cdot\nabla\psi =& -\frac{\hbar}{\mathrm{i}}\frac{q}{2m}\big(\mathbf{B}\times\mathbf{r}\big)\cdot\nabla\psi\\ =& -\frac{q}{2m}\mathbf{B}\cdot\left(\mathbf{r}\times\left(\frac{\hbar}{\mathrm{i}}\nabla\right)\right)\psi\\ =& -\frac{q}{2m}\mathbf{B}\cdot\big(\mathbf{r}\times\mathbf{p}\big)\psi\\ =& -\frac{q}{2m}\mathbf{B}\cdot\mathbf{L}\psi\\ =& -\mathbf{m}\cdot\mathbf{B}\psi \quad ,\end{aligned} \tag{2.20}$$

where we used the scaler triple product identity $\mathbf{a}\cdot(\mathbf{b}\times\mathbf{c}) = (\mathbf{a}\times\mathbf{b})\cdot\mathbf{c}$, and the classical definition of angular momentum $\mathbf{L} = \mathbf{r}\times\mathbf{p}$. Disregarding the term proportional to A^2, which is usually negligible for small fields, we can define the

Zeeman energy that describes the interaction between a particle's magnetic moment and an external magnetic field:

$$\mathcal{H}_{\text{Zee}} = -\mathbf{m} \cdot \mathbf{B} \quad . \tag{2.21}$$

This equation implies that the energy is minimized when the dot product is maximum, i.e., when the magnetic moment $\mathbf{m}$ is parallel to the field. Even though we demonstrated the Zeeman interaction by considering a magnetic moment of orbital-angular-momentum origin, it also applies for the spin angular momentum.

A magnetic moment changes with a rate given by the torque it is subjected to:

$$\boldsymbol{\tau} = \frac{\mathrm{d}\mathbf{m}}{\mathrm{d}t} = \frac{\mu_B}{\hbar}\frac{\mathrm{d}\mathbf{L}}{\mathrm{d}t} \quad . \tag{2.22}$$

Furthermore, the time evolution of the angular momentum operator under the influence of a magnetic field is given by Schrödinger's equation of motion:

$$\begin{aligned} \frac{\mathrm{d}L^\alpha}{\mathrm{d}t} =& -\frac{\mathrm{i}}{\hbar}\left[L^\alpha, \mathcal{H}_{\text{Zee}}\right] \\ =& \frac{\mathrm{i}}{\hbar}\sum_\beta \left[L^\alpha, m^\beta B^\beta\right] \\ =& \frac{\mathrm{i}}{\hbar}\frac{\mu_B}{\hbar}\sum_\beta \left[L^\alpha, L^\beta\right] B^\beta \\ =& -\frac{\mu_B}{\hbar}\sum_{\beta\gamma} \varepsilon_{\alpha\beta\gamma} L^\gamma B^\beta \quad , \end{aligned} \tag{2.23}$$

where we used the angular momentum commutation relation

$$\left[L^\alpha, L^\beta\right] = \mathrm{i}\hbar \sum_\gamma \varepsilon_{\alpha\beta\gamma} L^\gamma \quad . \tag{2.24}$$

α, β, and γ are Cartesian-component indices, and $\varepsilon_{\alpha\beta\gamma}$ is the Levi-Civita symbol. In the last line of Eq. (2.23), we can identify the components of the cross product between the angular momentum and the magnetic field: $(\mathbf{L}\times\mathbf{B})^\alpha = \sum_{\beta\gamma} \varepsilon_{\alpha\beta\gamma} L^\beta B^\gamma$. As a result, we then obtain that

$$\boldsymbol{\tau} = \mathbf{m} \times \mathbf{B} \quad , \tag{2.25}$$

which recovers the phenomenological result in Eq. (2.1) that was our starting point for discussing magnetic moments.

2.1.4 Magnetic exchange interaction

The magnetic exchange interaction (MEI) is a coupling between spins of fundamental importance in magnetism. It is one of the main sources of long-range ordering in ferromagnets and antiferromagnets. The discussions in this section were inspired by Refs. [37, 38].

To understand the origin of the magnetic exchange interactions, let us consider a hydrogen molecule, constituted by two atoms, each with a proton and an electron.

The idea is to determine how the system energy is affected by the relative alignment of the electron spins. The energy is given by the expectation value of the Hamiltonian operator,

$$\langle E\rangle = \frac{\int \Phi^*(\mathbf{r}_1)\mathcal{H}\Phi(\mathbf{r}_2)\mathrm{d}^3r_1\mathrm{d}^3r_2}{\int \Phi^*(\mathbf{r}_1)\Phi(\mathbf{r}_2)\mathrm{d}^3r_1\mathrm{d}^3r_2} \quad , \tag{2.26}$$

where the Hamiltonian can be split into a unperturbed part and an interaction term:

$$\mathcal{H} = \sum_{i=1}^{2}\mathcal{H}_i + \mathcal{H}_I \quad . \tag{2.27}$$

The unperturbed, single-particle Hamiltonians of each electron are given by

$$\begin{aligned} \mathcal{H}_1 =& \frac{p_1^2}{2m} - \frac{q^2}{r_{1a}} \quad , \\ \mathcal{H}_2 =& \frac{p_2^2}{2m} - \frac{q^2}{r_{2b}} \quad , \end{aligned} \tag{2.28}$$

where p_i is the momentum of the i-th electron, and r_{ix} the distance between that electron and the x-proton. The interaction part is given by

$$\mathcal{H}_I = q^2\left(\frac{1}{r_{12}} + \frac{1}{R_{ab}} - \frac{1}{r_{1b}} - \frac{1}{r_{2a}}\right) \quad , \tag{2.29}$$

where the first two terms are due to the repulsive interaction between particles of the same charge, and the last two are due to the attraction between particles of opposite charges. We neglected the kinetic energy of the protons assuming that their positions are fixed, for they are much heavier than the electrons. Thus, the distance between protons a and b, R_{ab}, becomes a parameter. We are also neglecting the dipole-dipole interaction between the electron spins, as it is much weaker than the electrostatic interactions.

Symmetric and antisymmetric eigenfunctions

If the two atoms, a and b, are far apart in comparison to the atomic diameter, we can assume that a reasonable wavefunction Φ can be constructed from the ground-state orbitals of the isolated atoms given by:

$$\begin{aligned} \mathcal{H}_1\varphi_a(\mathbf{r}_1) =& E_0\varphi_a(\mathbf{r}_1) \\ \mathcal{H}_2\varphi_b(\mathbf{r}_2) =& E_0\varphi_b(\mathbf{r}_2) \quad . \end{aligned} \tag{2.30}$$

We could try

$$\Phi_I(\mathbf{r}_1,\mathbf{r}_2) = \varphi_a(\mathbf{r}_1)\varphi_b(\mathbf{r}_2) \quad , \tag{2.31}$$

or

$$\Phi_{II}(\mathbf{r}_1,\mathbf{r}_2) = \varphi_a(\mathbf{r}_2)\varphi_b(\mathbf{r}_1) \quad , \tag{2.32}$$

where $\mathbf{r}_{1(2)}$ corresponds to the position of the first (second) electron. Φ_I considers that the electron 1 is in the orbital of atom a, and electron 2 in atom b. In Φ_{II}, the picture is reversed. Because the electrons are indistinguishable, both trials seem

equally probable, leading us to consider their superposition instead. There are two possible combinations that lead to the correctly normalized probability:

$$\Phi^{\pm}(\mathbf{r}_1, \mathbf{r}_2) = \frac{1}{\sqrt{2}} \left(\varphi_a(\mathbf{r}_1)\varphi_b(\mathbf{r}_2) \pm \varphi_a(\mathbf{r}_2)\varphi_b(\mathbf{r}_1)\right) \quad . \tag{2.33}$$

Φ^+ is a symmetric function because when we exchange one electron for the other it remains unchanged. Doing this exchange in Φ^-, it acquires a minus sign, which makes it an antisymmetric function.

Pauli's exclusion principle

It also happens that electronic systems need to satisfy *Pauli's exclusion principle*, which states that no two fermions can occupy the same state simultaneously. This requirement is only satisfied by antisymmetric wavefunctions. This can be seen by assuming that both electrons occupy the same orbital by making $a = b$ in Eq. (2.33), which results in $\Phi^- = 0$. Nevertheless, we cannot disregard the symmetric function Φ^+ just yet, because Pauli's exclusion principle requires the total wavefunction to be antisymmetric and $\Phi^{\pm}$ corresponds only to the space part of it.

Since the Hamiltonian in Eq. (2.27) is spin independent, the total wavefunction Ψ must be an antisymmetric product of the space $|\Phi\rangle^{\pm}$ and spin $|S, m\rangle^{\pm}$ parts:

$$|\Psi\rangle = |\Phi\rangle^{\pm} |S, m\rangle^{\mp} \quad . \tag{2.34}$$

The plus (minus) sign indicates that the wavefunction is symmetry (antisymmetric). In a two-electron system, the total spin can have to values $S = 0$ or 1, thus, the spin part can be constructed as an antisymmetric singlet state

$$|0, 0\rangle^{-} = \frac{1}{\sqrt{2}} \left(|\uparrow\downarrow\rangle - |\downarrow\uparrow\rangle\right) \quad , \tag{2.35}$$

or a symmetric triplet state

$$\begin{aligned} |1, 1\rangle^{+} &= |\uparrow\uparrow\rangle \\ |1, 0\rangle^{+} &= \frac{1}{\sqrt{2}} \left(|\uparrow\downarrow\rangle + |\downarrow\uparrow\rangle\right) \\ |1, -1\rangle^{+} &= |\downarrow\downarrow\rangle \quad . \end{aligned} \tag{2.36}$$

Effective spin hamiltonian

We have then four antisymmetric solutions of Eq. (2.34):

$$\begin{aligned} |\Psi_1\rangle &= |\Phi\rangle^{+} |0, 0\rangle^{-} \\ |\Psi_2, m\rangle &= |\Phi\rangle^{-} |1, m\rangle^{+} \quad , \quad m = 0, \pm 1 \quad . \end{aligned} \tag{2.37}$$

As the Hamiltonian of Eq. (2.27) only acts on the space part $\mathcal{H} |\Phi\rangle^{\pm} = E^{\pm} |\Phi\rangle^{\pm}$, we have:

$$\begin{aligned} \mathcal{H} |\Psi_1\rangle &= E^{+} |\Psi_1\rangle \\ \mathcal{H} |\Psi_2, m\rangle &= E^{-} |\Psi_2, m\rangle \quad . \end{aligned} \tag{2.38}$$

This indicates that the spin-independent Hamiltonian $\mathcal{H}$ can be replaced by an effective Hamiltonian $\tilde{\mathcal{H}}$ that acts exclusively on the electron spins such that:

$$\begin{aligned} \tilde{\mathcal{H}} \left|0,0\right\rangle &= E^{+} \left|0,0\right\rangle \\ \tilde{\mathcal{H}} \left|1,m\right\rangle &= E^{-} \left|1,m\right\rangle \quad . \end{aligned} \tag{2.39}$$

To understand how such a Hamiltonian should look like, let us have $\mathbf{S}_i$ being the spin of the electron i. The expectation value of the spin operator square is given by

$$\mathbf{S}_i^2 = \hbar^2 S(S+1) = \hbar^2 \frac{3}{4} \quad , \tag{2.40}$$

and for the total spin, we have

$$\mathbf{S}^2 = (\mathbf{S}_1 + \mathbf{S}_2)^2 = \mathbf{S}_1^2 + \mathbf{S}_2^2 + 2\mathbf{S}_1 \cdot \mathbf{S}_2 = \frac{3}{2}\hbar^2 + 2\mathbf{S}_1 \cdot \mathbf{S}_2 \tag{2.41}$$

and in comparison with Eq. (2.40), we obtain

$$\frac{1}{\hbar^2}\mathbf{S}_1 \cdot \mathbf{S}_2 = \frac{1}{2}S(S+1) - \frac{3}{4} = \begin{cases} -\frac{3}{4} & \text{if} \quad S=0 \\ \frac{1}{4} & \text{if} \quad S=1 \end{cases} \quad . \tag{2.42}$$

From that, we can deduce that

$$\tilde{\mathcal{H}} = \frac{1}{4}\left(E^{+} + 3E^{-}\right) - (E^{+} - E^{-})\frac{1}{\hbar^2}\mathbf{S}_1 \cdot \mathbf{S}_2 \quad , \tag{2.43}$$

which has the same eigenvalues as $\mathcal{H}$. This new Hamiltonian describes the molecular Heisenberg model:

$$\mathcal{H} = J_0 - J_{12}\mathbf{S}_1 \cdot \mathbf{S}_2 \quad , \tag{2.44}$$

where the exchange coupling parameter is given by

$$J_{12} = \frac{1}{\hbar^2}\left(E^{+} - E^{-}\right) \quad . \tag{2.45}$$

This shows that if $E^{+} \neq E^{-}$, automatically a spontaneous magnetic order is favored. For $J_{12} > 0$, the spins couple ferromagnetically, tending to align parallel to each other. When the exchange parameter is negative, an antiferromagnetic alignment is favored, when the spins are aligned antiparallel.

Origin of the exchange coupling

To understand the origin of the energy difference between symmetric and antisymmetric space wavefunctions, which is proportional to the magnetic exchange parameter, let us further develop Eq. (2.26). The denominator is given by

$$\int (\Phi^{\pm}(\mathbf{r}_1, \mathbf{r}_2))^* \Phi^{\pm}(\mathbf{r}_1, \mathbf{r}_2) \mathrm{d}^3 r_1 \mathrm{d}^3 r_2 = 1 \pm \alpha^2 \quad , \tag{2.46}$$

where we assumed that the atomic orbitals are normalized $\int |\phi(\mathbf{r})| \mathrm{d}^3 r = 1$, and α is the overlap integral given by

$$\alpha = \int \phi_a^*(\mathbf{r}) \phi_b(\mathbf{r}) \mathrm{d}^3 r \quad . \tag{2.47}$$

Similarly, the numerator is found to be

$$\int (\Phi^{\pm}(\mathbf{r}_1,\mathbf{r}_2))^* \mathcal{H}(\mathbf{r}_1,\mathbf{r}_2)\Phi^{\pm}(\mathbf{r}_1,\mathbf{r}_2)\mathrm{d}^3r_1\mathrm{d}^3r_2 = 2E_0(1\pm\alpha^2) + V \pm U \quad , \tag{2.48}$$

where V is the *coulomb integral* and U the *exchange integral*, defined by

$$\begin{aligned} V &= \int \varphi_a^*(\mathbf{r}_1)\varphi_b^*(\mathbf{r}_2)\mathcal{H}_I(\mathbf{r}_1,\mathbf{r}_2)\varphi_a(\mathbf{r}_1)\varphi_b(\mathbf{r}_2)\mathrm{d}^3r_1\mathrm{d}^3r_2 \quad , \\ U &= \int \varphi_a^*(\mathbf{r}_2)\varphi_b^*(\mathbf{r}_1)\mathcal{H}_I(\mathbf{r}_1,\mathbf{r}_2)\varphi_a(\mathbf{r}_1)\varphi_b(\mathbf{r}_2)\mathrm{d}^3r_1\mathrm{d}^3r_2 \quad . \end{aligned} \tag{2.49}$$

U is called exchange integral because it corresponds to the transition probability of electrons switching positions, which becomes possible due to the interaction Hamiltonian. The energy of the symmetric and antisymmetric states are then

$$E^{\pm} = 2E_0 + \frac{V \pm U}{1 \pm \alpha^2} \quad , \tag{2.50}$$

and therefore, the difference is given by

$$E^+ - E^- = -2\frac{V\alpha^2 - U}{1-\alpha^4} = \hbar^2 J_{12} \quad . \tag{2.51}$$

The strength and sign of the exchange parameter depends on the balance between U, V and α. For the hydrogen molecule, J_{12} is negative meaning that the ground state corresponds to the antiparallel alignment of the electron spins.

We demonstrated that the interaction between electrons plus Pauli's exclusion principle leads to magnetic effects, even when the Hamiltonian is spin-independent, therefore unable to describe directly the interaction between two magnetic moments. Furthermore, the Heisenberg model can then be postulated as the generalization of the above developments for N interacting spins:

$$\mathcal{H} = -\frac{1}{2}\sum_{ij} J_{ij}\mathbf{S}_i \cdot \mathbf{S}_j \quad , \tag{2.52}$$

where we ignored the zero of Energy because we are mostly interested in the low excitations above the ground state. We could demonstrate that this Hamiltonian is valid for a pair of couple spins, however, there is no guarantee that for N-coupled spins the effective Hamiltonian keeps a similar form. In a real system, the interactions are often very complex such that the exchange interaction ceases to be well defined [38]. Nevertheless, it seems that the Heisenberg Hamiltonian as written above manage to capture and describe many observable magnetic phenomena in actual solids.

2.1.5 Spin-orbit coupling: MCA and DMI

The relativistic theory of the atom by Dirac leads to the spin-orbit coupling (SOC) correction to the energy. The SOC is in general small but it can be proportional to the square power of the atomic number, meaning that it becomes very important for heavy elements [36].

Instead, we can illustrate the origin of the spin-orbit coupling by considering the following [37]. In the rest frame of a charged nucleus, an electron moves through an electrostatic field, $\mathbf{E} = -\nabla\phi$ due to the nucleus. The electron in its rest frame "sees" a magnetic field $\mathbf{B}$, which in relativistic electrodynamics is given by

$$\bar{\mathbf{B}} = \gamma\left(\mathbf{B} - \frac{1}{c}\boldsymbol{\beta}\times\mathbf{E}\right) - \frac{\gamma^2}{\gamma+1}\boldsymbol{\beta}(\boldsymbol{\beta}\cdot\mathbf{B}) \quad , \tag{2.53}$$

where $\gamma = \left(1 - v^2/c^2\right)^{-1}$ is the Lorentz factor, c is the speed of light in vacuum, $\boldsymbol{\beta} = \mathbf{v}/c$, $\mathbf{E}$ and $\mathbf{B}$ are the fields in the rest frame of the nucleus ($\mathbf{B} = 0$), and bar fields are the ones in the electron rest frame. If $v \ll c$, $\gamma \approx 1$, then we have

$$\bar{\mathbf{B}} \approx -\frac{1}{c^2}\mathbf{v}\times\mathbf{E} \quad . \tag{2.54}$$

We could then postulate that the spin moment couples to this field, and so we should have an additional therm in the Hamiltonian:

$$\mathcal{H}_{\mathrm{SOC}} = 2\frac{\mu_B}{\hbar}\bar{\mathbf{B}}\cdot\mathbf{S} = \frac{e}{m_e c^2}(\mathbf{E}\times\mathbf{v})\cdot\mathbf{S} \quad . \tag{2.55}$$

In principle, any source of electric field can give rise to a coupling between the motion of the electron and its spin. However, because of the prefactor in the above equation, the effect is very small unless the field is very large. Such large fields can be experienced by electrons very near to the nucleus of an atom. Assuming that the electric field due nucleus is spherically symmetric:

$$\mathbf{E} = -\frac{\mathbf{r}}{r}\frac{\mathrm{d}\phi}{\mathrm{d}r} \quad , \tag{2.56}$$

where ϕ is the electric potential, and using that $\mathbf{L} = m_e\mathbf{r}\times\mathbf{v}$, we finally obtain

$$\mathcal{H}_{\mathrm{SOC}} = -\frac{e}{m_e^2 c^2}\left(\frac{1}{r}\frac{\mathrm{d}\phi}{\mathrm{d}r}\right)\mathbf{L}\cdot\mathbf{S} \quad . \tag{2.57}$$

This term couples the electron spin with its orbital motion due to the electric field of the nucleus. The above expression is too large by a factor of two from the one obtained through Dirac's theory.

Magnetocrystalline anisotropy

In an isolated isotropic atom, a change in the spin direction drags the orbital angular momentum along because of the spin-orbit coupling. In a crystal, however, the spatial isotropy is broken. This means that the system's energy depends on the alignment of the spherically asymmetric orbitals with the major axes of the crystal. Consequently, because of the SOC, the system's energy also will depend on the magnetic moment orientation. We name this phenomenon *magnetocrystalline anisotropy* (MCA).

If the system favors the alignment of the magnetic moment along a single particular direction, we say that it has a uniaxial anisotropy, and the spin Hamiltonian of this interaction can be written as

$$\mathcal{H}_K = -K\sum_i\left(\hat{\mathbf{k}}\cdot\mathbf{S}_i\right)^2 \quad , \tag{2.58}$$

where $\hat{\mathbf{k}}$ is a unity vector along the preferred direction, and K the anisotropy parameter that corresponds to the energy difference between the magnetic moments point along $\hat{K}$ or perpendicular to it. If $K > 0$, we say that the system has an easy-axis, for the energy is minimized when the magnetic moments are parallel to $\hat{K}$. It can happen, however, that K is negative, implying that the energy is minimal when the magnetic moments point anywhere perpendicular to $\hat{K}$. In this case, we say that the system has an easy-plane.

Depending on the crystal symmetry and electronic properties, some systems might be better modeled by two anisotropy axes, therefore they are called biaxial systems. There are even higher-order anisotropy effects, where the energy depends on the orientation of the spins relative to multiple axes, but that are not considered in this work.

Dzyaloshinskii-Moriya interaction

Besides giving rise to the magnetocrystalline anisotropy, spin-orbit coupling is also responsible for the Dzyaloshinskii-Moriya interaction (DMI) [41, 42]. It is a pair interaction that favors a perpendicular alignment between two spins. The DMI is represented by a vectorial coupling parameter that, besides containing the interaction strength, also determines a favored plane of rotation for the spin canting. The spin Hamiltonian of the DMI can be represented as

$$\mathcal{H}_{\mathrm{DMI}} = -\frac{1}{2}\sum_{ij} \mathbf{D}_{ij} \cdot \mathbf{S}_i \times \mathbf{S}_j \quad . \tag{2.59}$$

For this equation to make sense, the evaluation of the cross product should precede the inner product. The DMI only occurs in systems with broken inversion symmetry [42], a condition easily satisfied at surfaces and interfaces, but that can also happen in bulk materials. Heterostructures combining heavy metals with magnetic materials can induce strong and designable DMI.

The Dzyaloshinskii-Moriya interaction leads to multiple phenomena in magnetism. It can induce the formation of spin-spiral magnetic structures, skyrmions, and other noncollinear magnetic textures, which are the object of interest of this thesis. Also, the DMI leads to asymmetries in the spin-wave properties through the reciprocal space, which is known as the nonreciprocity of spin waves [31]. Chapter 9 is entirely dedicated to studying this phenomenon in noncollinear magnetic systems.

2.1.6 Generalized Heisenberg Hamiltonian

We can finally put all the magnetic interactions we discussed this far to obtain the following generalized Heisenberg Hamiltonian:

$$\mathcal{H} = -\frac{1}{2}\sum_{ij} J_{ij}\, \mathbf{S}_i \cdot \mathbf{S}_j - \frac{1}{2}\sum_{ij} \mathbf{D}_{ij} \cdot (\mathbf{S}_i \times \mathbf{S}_j) - \sum_i \mathbf{B} \cdot \mathbf{S}_i - \sum_\alpha K^\alpha \sum_i \left(S_i^\alpha\right)^2 \quad . \tag{2.60}$$

The first term corresponds to the magnetic exchange interaction, whose parameter J_{ij} couples the magnetic moments of sites i and j. Similarly, in the second term, $\mathbf{D}_{ij}$

represents the vector parameter of the Dzyaloshinskii-Moriya interaction. The third term is the Zeeman energy, due to a uniform external magnetic field. In comparison with Eq. (2.21), $\mathbf{B}$ was renormalized as $\mu_B/\hbar\mathbf{B} \rightarrow \mathbf{B}$ for simplicity. And finally, the last term corresponds to the uniaxial magnetocrystalline anisotropy with axes along $\alpha = x, y, z$. The Heisenberg model was conceptualized for magnetic insulators. However, it is also applicable to magnetic metals provided that they feature localized magnetic moments [37].

A very useful way to represent the above Hamiltonian is through its matrix representation:

$$\mathcal{H} = -\frac{1}{2}\sum_{ij} \mathbf{S}_i^\dagger \mathbf{J}_{ij} \mathbf{S}_j - \sum_i \mathbf{B}\cdot\mathbf{S}_i \quad , \tag{2.61}$$

where the exchange matrix $\mathbf{J}_{ij}$ contains all the intrinsic interactions of the system:

$$\mathbf{J}_{ij} = \begin{pmatrix} J_{ij}^x + 2K^x\delta_{ij} & D_{ij}^z & -D_{ij}^y \\ -D_{ij}^z & J_{ij}^y + 2K^y\delta_{ij} & D_{ij}^x \\ D_{ij}^y & -D_{ij}^x & J_{ij}^z + 2K^z\delta_{ij} \end{pmatrix} \quad . \tag{2.62}$$

The spin operators should be regarded as column vectors and their adjoint as row vectors:

$$\mathbf{S}_i = \begin{pmatrix} S_i^x \\ S_i^y \\ S_i^z \end{pmatrix} \quad , \quad \mathbf{S}_i^\dagger = \begin{pmatrix} S_i^x & S_i^y & S_i^z \end{pmatrix} \quad . \tag{2.63}$$

Therefore, $\mathbf{B} = \begin{pmatrix} B^x & B^y & B^z \end{pmatrix}$ should also be regarded as a row vector. The Hamiltonian representation in Eq. (2.61) is going to be particularly useful to calculate the spin-wave spectrum of noncollinear magnetic systems because it allows us to perform the various transformation in the Hamiltonian in a systematic manner.

2.2 Classical ground-state spin configurations

Previously, we discussed the origin of the magnetic moments and their interactions, such as the MEI and DMI. We focus now on the role of the different terms of the generalized Heisenberg Hamiltonian of Eq. (2.60) and their consequence to the classical ground-state spin configuration. We consider the limit of large spin quantum number S, such that we can replace each spin operator $\mathbf{S}_i$ in the Hamiltonian by classical vectors. Then, we search for the spin alignments with respect to each other, to the external fields, and to anisotropy axes, that are energetic mostly favorable. Sometimes, we find states that correspond to the minimum total energy, which corresponds to the ground state. However, there are states that correspond to local minima of the energy, which are called metastable states. We also consider that the magnitude of $\mathbf{S}_i$ is constant. The search for the ground state and meta-stable configurations is not a trivial matter. In general, we resort to numerical and/or analytical approached depending on the complexity of the set of interactions. Nevertheless, a metastable spin configuration of a system is the starting point to determine its spin-wave properties in the adiabatic approach.

2.2.1 Ferromagnetic and antiferromagnetic ground states

Let us consider a model system containing only a magnetic exchange interaction between nearest neighbors (n.n.), as described by

$$\mathcal{H} = -\frac{J}{2}\sum_{\langle ij\rangle}\mathbf{S}_i \cdot \mathbf{S}_j \quad . \tag{2.64}$$

If $J > 0$, the energy is minimized when the inner product is maximal, that is, when $\mathbf{S}_i$ and $\mathbf{S}_j$ are parallel. We then say that the system has a ferromagnetic ground state. For $J < 0$, however, the energy is minimized when the spins are antiparallel to each other if allowed by the lattice geometry, resulting in an antiferromagnetic ground state.

Note, the above Hamiltonian is completely isotropic, therefore it has nothing to say about the orientation of the spins with respect to a global reference frame. Thus, the MEI can give rise to long-range order, with spins parallel or antiparallel to each other, without determining the overall direction. In real materials, a preferential direction $\hat{\mathbf{k}}$ is often set by the magnetocrystalline anisotropy, which transforms the Hamiltonian into

$$\mathcal{H} = -\frac{J}{2}\sum_{\langle ij\rangle}\mathbf{S}_i \cdot \mathbf{S}_j - K\sum_i \left(\hat{\mathbf{k}} \cdot \mathbf{S}_i\right)^2 \quad . \tag{2.65}$$

Because the anisotropy term depend on the square of the projection of the spins along $\hat{\mathbf{k}}$, it does not distinguish between a ferromagnetic and an antiferromagnetic configuration.

In fact, the Mermin-Wagner theorem guarantees that the isotropic Heisenberg model does not present any long-range order at finite temperature in one and two dimensions [43]. Therefore, for surface and thin films, such as the ones that we study in this thesis, long-range order requires interactions that break the spin-rotational invariance, for instance, an external magnetic field or the magnetocrystalline anisotropy.

2.2.2 Cycloidal spin spirals - Analytical solution

Now, let us study the effects of the Dzyaloshinskii-Moriya interaction on the ground-state spin configurations. For that, consider a single layer of a hexagonal lattice of primitive vectors $\mathbf{a}_1 = a\hat{x}$ and $\mathbf{a}_2 = a(\hat{x}/2 + \sqrt{3}\hat{y}/2)$, where a is the lattice constant. Let us take into account only n.n. $J > 0$ and $\mathbf{D}_{ij} \propto \hat{z} \times \hat{r}_{ij}$ perpendicular to the bonds connecting sites. Spin spirals whose rotational axes are perpendicular to the plane that contains the spins are called cycloidal spin spirals. Assume that the classical ground state is a cycloidal spin spiral propagating with wavevector $\mathbf{Q} = Q\hat{\mathbf{y}}$ and rotation axis along x, i.e., with the spins rotating in the $y-z$ plane. Our job is to determine which Q corresponds to the lowest energy. With the help of Fig. 2.2, we rewrite the Hamiltonian as

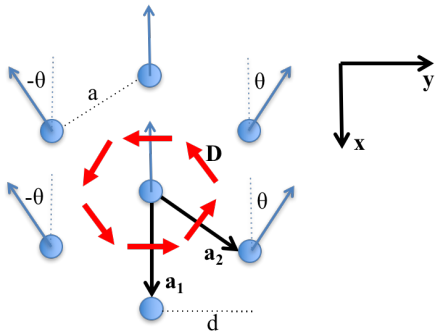

Figure 2.2: Sketch of a hexagonal lattice. The z-axis points out of the page. The spins tilt in the $y-z$ plane, but in the figure, we projected them onto the page plane.

$$\begin{aligned}\mathcal{H} &= -\frac{1}{2}\sum_{ij}\left[J_{ij}\mathbf{S}_i\cdot\mathbf{S}_j+\mathbf{D}_{ij}\cdot(\mathbf{S}_i\times\mathbf{S}_j)\right]\\ &= -\frac{1}{2}\sum_{ij}\left[J_{ij}S_iS_j\cos\theta_{ij}+D^x_{ij}S_iS_j\sin\theta_{ij}\right]\\ &= -\frac{1}{2}S^2\sum_{i}\left[J(2+4\cos\theta)+4D^x\sin\theta\right]\\ &= -S^2N\left[J(1+2\cos(dQ))+2D^x\sin(dQ)\right]\end{aligned} \tag{2.66}$$

where $\theta = Qd$ and $d = a\sqrt{3}/2$.

To find the minimal energy, we need to find the zeros of the derivative of this equation in respect to Q:

$$\frac{\mathrm{d}\mathcal{H}}{\mathrm{d}Q} = 2dS^2N\left[J\sin(dQ)-D\cos(dQ)\right]=0 \quad , \tag{2.67}$$

and therefore

$$\begin{aligned} J\sin(dQ)-D^x\cos(dQ) &= 0\\ \frac{J}{\sqrt{J^2+D^{x2}}}\sin(dQ)-\frac{D^{x2}}{\sqrt{J^2+D^{x2}}}\cos(dQ) &= 0\\ \cos\alpha\sin(dQ)-\sin\alpha\cos(dQ) &= 0\\ \sin(dQ-\alpha) &= 0 \quad ,\end{aligned} \tag{2.68}$$

where we defined

$$\cos\alpha = J/\sqrt{J^2+D^{x2}} \quad \text{and} \quad \sin\alpha = D^x/\sqrt{J^2+D^{x2}} \quad . \tag{2.69}$$

This gives that

$$\alpha = \arctan(D^x/J) \quad . \tag{2.70}$$

To satisfy Eq. (2.68), the argument of the sine function must equal $n\pi$ with $n = 0, \pm1, \pm2, ...$, which yields

$$Q = \frac{n\pi+\alpha}{d} \quad . \tag{2.71}$$

The only two inequivalent solutions are for $n = 0, 1$. For all other n, a translation by a reciprocal lattice vector brings the solution back to one of these two cases. If one of the solutions is a point of minimal energy the other one has to be of maximal energy. To check this, we have to take the second derivative of the Hamiltonian:

$$\frac{\mathrm{d}^2\mathcal{H}}{\mathrm{d}Q^2} = 2d^2S^2N\left\{J\cos(dQ) + D^x\sin(dQ)\right\} \quad , \tag{2.72}$$

which for the two cases reads (dropping the pre-factor that doesn't matter for the sign analysis):

$$\begin{aligned} n = 0 \qquad & \frac{\mathrm{d}^2\mathcal{H}}{\mathrm{d}Q^2} = J\cos\alpha + D^x\sin\alpha \quad , \\ n = 1 \qquad & \frac{\mathrm{d}^2\mathcal{H}}{\mathrm{d}Q^2} = J\cos(\pi+\alpha) + D^x\sin(\pi+\alpha) = -(J\cos\alpha + D^x\sin\alpha) \quad . \end{aligned} \tag{2.73}$$

This already proves that the two solutions have opposite concavity, therefore one must be a minimum energy point and the other a maximum point. By using Eq. (2.69), we have:

$$\begin{aligned} n = 0 \qquad & \frac{\mathrm{d}^2\mathcal{H}}{\mathrm{d}Q^2} = +\frac{J^2 + D^{x2}}{\sqrt{J^2 + D^{x2}}} > 0 \quad , \\ n = 1 \qquad & \frac{\mathrm{d}^2\mathcal{H}}{\mathrm{d}Q^2} = -\frac{J^2 + D^{x2}}{\sqrt{J^2 + D^{x2}}} < 0 \quad , \end{aligned} \tag{2.74}$$

which shows that

$$Q = \alpha/d \tag{2.75}$$

is the cycloidal spin spiral of the lowest energy. In the particular case where $J = 1$ and $D = 2/\sqrt{3}$, such that $D^x = 1$, we obtain that $Q = \pi/4d$, which corresponds to a spin-spiral wavelength $\lambda = 8d$. One should have in mind that we have no guarantee to have found the ground state because, in the beginning, we restricted our search among a particular set of spin spirals. However, it is easy to show that this spin spiral is lower in energy than the ferromagnetic order.

2.2.3 Skyrmion lattice - Atomistic spin dynamics simulation

We now consider the same model used in the previous section: a hexagonal monolayer with n.n. MEI and DMI. This time, let us apply a magnetic field $\mathbf{B} = B\hat{\mathbf{z}}$ perpendicular to the crystal plane. The Hamiltonian reads

$$\mathcal{H} = -\frac{1}{2}\sum_{ij}\left[J_{ij}\mathbf{S}_i\cdot\mathbf{S}_j + \mathbf{D}_{ij}\cdot\mathbf{S}_i\times\mathbf{S}_j\right] - B\sum_i (S_i^z)^2 \quad . \tag{2.76}$$

Differently from our search for spin spirals, this time we do not assume a specific form for the spin configuration. Often, we have no idea what the ground state looks like. Instead, we use a spin relaxation method based on the Landau–Lifshitz–Gilbert (LLG) [44–46] equation of motion:

$$\frac{\partial\mathbf{S}_i}{\partial t} = -\frac{\gamma}{(1+\lambda^2)}\left[\mathbf{S}_i\times\mathbf{B}_i^{\mathrm{eff}} + \lambda\mathbf{S}_i\times(\mathbf{S}_i\times\mathbf{B}_i^{\mathrm{eff}})\right] \quad , \tag{2.77}$$

where γ is the gyromagnetic ratio, $\mathbf{B}_i^{\text{eff}}$ is the effective field on site i, and the effective field is given by

$$\mathbf{B}_i^{\text{eff}} = -\frac{\partial \mathcal{H}}{\partial \mathbf{S}_i} \quad . \tag{2.78}$$

The first term in the right-hand side of the LLG equation is called the driving field, which means that an effective field perpendicular to the spins sets them into precession. The second term is a phenomenological damping term, which accounts for the energy transfer from the spins to the heat bath, and it is parametrized by λ. This *atomistic spin dynamics* method consists of starting from a guess spin configuration, e.g., a random configuration, then use the LLG equation to evolve the spin in time until an equilibrium configuration is reached. Throughout this thesis, we study spin textures and obtain the ground state and metastable phase of the systems in investigation using the *Spirit* code [47], which is an open-source multifunctional platform for atomistic spin dynamics simulations.

Let us make n.n. $J = 1$, $D = 1$ and $B = 0$ and choose a simulation box of dimensions $64\mathbf{a}_1 \times 64\mathbf{a}_2$, with periodic boundary condition. Starting the spin dynamics simulation from a random configuration, very often we obtain a spin spiral, as described in the previous section. Eventually, other metastable states are obtained, but one can verify that they have higher energy in comparison to the spin spiral.

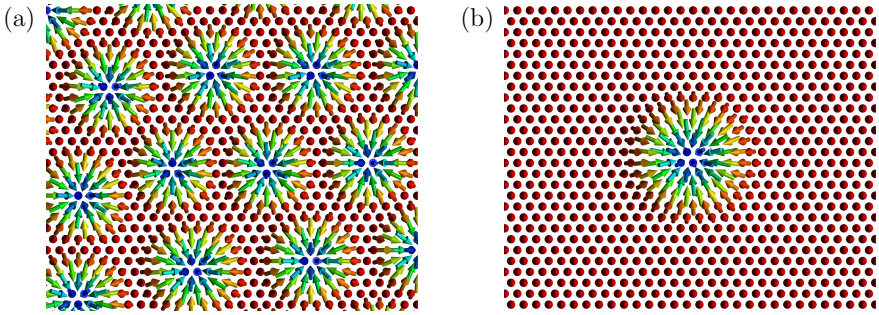

Figure 2.3: (a) Skyrmion lattice. An external magnetic field turns the spin-spiral ground state into a skyrmion lattice. (b) An isolated skyrmion is also stable. The spin configurations were obtained using atomistic spin dynamics simulation with the *Spirit* code. The Hamiltonian parameter were set to $J = 1$, $D^x = 1$, and $B = 1.5\,J$.

Finally, taking $B = 1.5J$, we find that a skyrmion lattice becomes the ground-state configuration, as shown in Fig. 2.3 (a). As an external magnetic field is required, we say that this skyrmionic phase is stabilized by the field. We can also stabilize an isolated skyrmion, by initializing the system in a ferromagnetic phase then nucleating the skyrmion by reversing the magnetization of a small circular area. As a result, the system relaxes into the skyrmion shown in Fig. 2.3 (b).

2.3 Introduction to spin waves

In the previous sections, we introduced the Heisenberg Hamiltonian and the magnetic interactions it describes. Furthermore, we demonstrated analytical and numerical techniques to obtain a system's classical ground state. This classical spin

configuration is our starting point to understand the spin-wave dynamics in the adiabatic approximation.

Let us start studying the spin dynamics of a crystal with localized magnetic moments in the limit of large spin quantum number S, where the spin operators can be regarded as classical vectors. We consider the following Hamiltonian with only the magnet magnetic exchange interaction:

$$\mathcal{H} = -\frac{1}{2}\sum_{ij} J_{ij}\mathbf{S}_i \cdot \mathbf{S}_j \quad . \tag{2.79}$$

We can write a classical equation of motion for each spin. An exerted torque in $\mathbf{S}$ due to an effective field causes it to precess, and the motion is governed by Landau-Lifshitz equation:

$$\hbar\frac{\mathrm{d}\mathbf{S}_i}{\mathrm{d}t} = -\mathbf{S}_i \times \mathbf{B}_i^{\text{eff}} \quad , \tag{2.80}$$

and the effective field is given by

$$\mathbf{B}_i^{\text{eff}} = -\frac{\mathrm{d}\mathcal{H}}{\mathrm{d}\mathbf{S}_i} = \sum_j J_{ij}\mathbf{S}_j \quad . \tag{2.81}$$

This means that all other spins coupled to $\mathbf{S}_i$ through the exchange interaction contribute to the effective field that it experiences.

Substituting Eq.(2.81) into (2.80), we obtain

$$\frac{\mathrm{d}\mathbf{S}}{\mathrm{d}t} = -\sum_j J_{ij}\big((S_i^y S_j^z - S_i^z S_j^y)\hat{\mathbf{x}} + (S_i^z S_j^x - S_i^x S_j^z)\hat{\mathbf{y}} + (S_i^y S_j^x - S_i^x S_j^y)\hat{\mathbf{z}}\big) \quad . \tag{2.82}$$

Now, suppose that we have a ferromagnetic ground state with magnetization along z and that the motion of the spin consists of a precession of small amplitude around the equilibrium direction. This implies that $S^z \approx S$ and that we can disregard higher-order terms of S^x and S^y. Thus, we obtain

$$\frac{\mathrm{d}\mathbf{S}_i}{\mathrm{d}t} = -S\sum_j J_{ij}\big((S_i^y - S_j^y)\hat{\mathbf{x}} + (S_j^x - S_i^x)\hat{\mathbf{y}}\big) \quad . \tag{2.83}$$

Note that in Eq. (2.83), the dynamics of the x–components of the spins depends on the dynamics of the y–components, and vice-versa. We can decouple the equations for the spin components through the following transformation

$$S^{\pm} = S^x \pm \mathrm{i}S^y \quad . \tag{2.84}$$

$S^{\pm}$ are known as circular components of $\mathbf{S}$. As a result, we obtain

$$\begin{aligned} -\mathrm{i}\frac{\mathrm{d}S_i^+}{\mathrm{d}t} &= S\sum_j J_{ij}(S_i^+ - S_j^+) \\ \mathrm{i}\frac{\mathrm{d}S_i^-}{\mathrm{d}t} &= S\sum_j J_{ij}(S_i^- - S_j^-) \quad . \end{aligned} \tag{2.85}$$

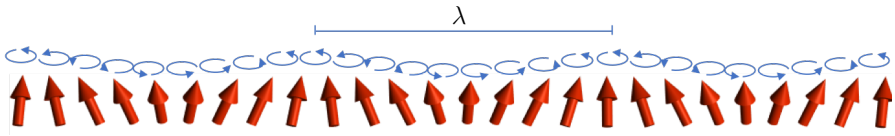

Figure 2.4: Schematic spin dynamics of a spin wave. All spins precess with the same frequency around their equilibrium axes. The phase shift is determined by spin-wave wavevector $\mathbf{k}$. The wavelength $\lambda = 2\pi/k$.

Now, the equations of motion can be solved independently. Exploiting the translational symmetry of the system, we can Fourier transform the above equations to obtain

$$\mp \mathrm{i} \frac{\mathrm{d}S^{\pm}_{\mathbf{k}}(t)}{\mathrm{d}t} = S(J_0 - J_{\mathbf{k}}) S^{\pm}_{\mathbf{k}}(t) \quad , \tag{2.86}$$

where $J_{\mathbf{k}} = \sum_i e^{\mathrm{i}\mathbf{k}\cdot\mathbf{r}_{ij}} J_{ij}$. The solutions of the above equation are of the type $S^{\pm}_{\mathbf{k}}(t) = S^{\pm}_{\mathbf{k}} e^{-\mathrm{i}\omega^{\pm}_{\mathbf{k}} t}$, we then obtain the following eigenvalue equations:

$$\mp \omega^{\pm}_{\mathbf{k}} S^{\pm}_{\mathbf{k}} = S(J_0 - J_{\mathbf{k}}) S^{\pm}_{\mathbf{k}} \quad , \tag{2.87}$$

where the eigenvalues are

$$\omega^{\pm}_{\mathbf{k}} = \mp S(J_0 - J_{\mathbf{k}}) \quad . \tag{2.88}$$

These eigenvalues correspond to the energies of the system's eigenmodes. The dynamics of the spins for one of such an eigenmode with wavevector $\mathbf{k}$ is represented in Fig. 2.4. Each spin is in precessing around the magnetization direction with a frequency given by ω_k. The phase shift of the precessional motion from site i to site j is given by $\mathbf{k} \cdot \mathbf{r}_{ij}$. Thus, this natural collective precessional eigenmode is called a *spin wave*, which propagates in a ferromagnet with wavelength $\lambda = 2\pi/k$.

2.3.1 Quantum theory of spin waves

In the previous sections, we saw that spin waves surge as eigenstates of the classical Heisenberg Hamiltonian. Now, we want to regard the spins as quantum operators again. Let us then consider the following Hamiltonian:

$$\mathcal{H} = -\frac{1}{2} \sum_{ij} J_{ij} \mathbf{S}_i \cdot \mathbf{S}_j - \sum_i B^z S^z_i \quad , \tag{2.89}$$

with $J_{ij} > 0$. In sec. 2.2.1, we saw that a ferromagnetic phase is the classical ground state of such a model. Here, we are also considering a small field along z to break the infinite degeneracy due to the invariance of the EMI under a global rotation. Thus, all spins point up along z. This ferromagnetic state is also the exact ground state of the quantum Hamiltonian, which we can represent as

$$|0\rangle = \prod_{i=1}^{N} |S\rangle_i \quad . \tag{2.90}$$

This means that each spin is in an eigenstate of S^z_i with eigenvalue S:

$$S^z_i \, |S\rangle_i = S \, |S\rangle_i \quad . \tag{2.91}$$

It is also defined by:

$$\mathcal{H}\left|0\right\rangle = E_0\left|0\right\rangle \quad , \tag{2.92}$$

where E_0 is the ground state energy. $\left|0\right\rangle$ is the state that corresponds to the maximum magnetization $S^z_{\text{tot}} = NS$. For simplicity, in this section, we use the convention that $\hbar = 1$.

Spin circular components

Now, our task is to find the excited states of the Hamiltonian of Eq. (2.89). For that, let us use the circular components of $\mathbf{S}$ operator, as introduced in Eq. (2.84). Because the Cartesian components of the spin operator obey the commutation relation given, using Einstein summation convention, by $\left[S_i^\alpha, S_j^\beta\right] = \mathrm{i}\epsilon_{\alpha\beta\gamma}\delta_{ij}S_i^\gamma$, the circular components must obey:

$$\left[S_i^+, S_j^-\right] = \delta_{ij}2S_i^z \quad \text{and} \quad \left[S_i^\pm, S_j^z\right] = \mp\delta_{ij}S_i^\pm \quad . \tag{2.93}$$

S^- and S^+ are also known as lowering and raising operators, respectively, because they act to create a local deviation of 1 in the eigenvalue of the S^z operator:

$$\begin{aligned} S_i^-\left|S,m\right\rangle_i &= \sqrt{(S-m+1)(S+m)}\left|S,m-1\right\rangle_i \quad , \\ S_i^+\left|S,m\right\rangle_i &= \sqrt{(S-m)(S+m+1)}\left|S,m+1\right\rangle_i \quad , \\ S_i^z\left|S,m\right\rangle_i &= m\left|S,m\right\rangle_i \quad . \end{aligned} \tag{2.94}$$

Here, we have changed the notation to have S and m corresponding to the eigenvalues of S^2 and S^z, respectively.

Holstein-Primakoff transformation

Let us introduce the local spin-deviation operator defined as:

$$\hat{n} = S - S^z \quad , \tag{2.95}$$

whose eigenvalues are

$$n = S - m \quad . \tag{2.96}$$

A decrease in m, i.e., lowering the spin projection, increases the local spin deviation n. Note that the eigenvalues of n is bounded: $0 \leq n \leq 2S$. For a fixed S, we can label the $\left|S,m\right\rangle$ states in terms of n. Thus, the action of S^- can be written as:

$$\begin{aligned} S^-\left|n\right\rangle &= \sqrt{(2S-n)(1+n)}\left|n+1\right\rangle \\ &= \sqrt{2S}\sqrt{1-\frac{n}{2S}}\sqrt{1+n}\left|n+1\right\rangle \quad . \end{aligned} \tag{2.97}$$

The last equation reminds us of how the harmonic-oscillator creation operator acts:

$$a^\dagger\left|n\right\rangle = \sqrt{n+1}\left|n+1\right\rangle \quad , \tag{2.98}$$

where n is the number of energy quanta in the state $|n\rangle$. Thus, we can relate the circular components of the spin operator to the harmonic-oscillator creation and annihilation operators:

$$\begin{aligned} S_i^- &= \sqrt{2S} a_i^\dagger \hat{f}_i \quad , \\ S_i^+ &= \sqrt{2S} \hat{f}_i a_i \quad , \\ S_i^z &= S - \hat{n}_i \quad , \end{aligned} \tag{2.99}$$

where $\hat{n}_i = a_i^\dagger a_i$. This is the so called Holstein-Primakoff transformation [48–50]. $\hat{f}_i$ is a nonlinear operator defined by:

$$\hat{f}_i = \sqrt{1 - \frac{\hat{n}_i}{2S}} \quad , \tag{2.100}$$

which is only well defined if $n_i \leq 2S$ implying that Eq. (2.99) is not truly compatible with the harmonic oscillator that has a unbounded spectrum of $\hat{n}$.

Nevertheless, we expect that at low temperatures very few spin deviations occur, such that the statistical average of $\hat{n}$ is small and

$$\frac{\hat{n}}{2S} \ll 1 \quad . \tag{2.101}$$

In this case, we can assume $\hat{f} = 1$, which linearizes Eq. (2.99). Also, the creation and annihilation operators obey boson commutation relations:

$$\left[a_i, a_j^\dagger\right] = \delta_{ij} \quad , \quad \left[a_i^\dagger, a_j^\dagger\right] = 0 \quad , \quad [a_i, a_j] = 0 \quad , \tag{2.102}$$

which follow directly from the commutation relations of the spin operators.

Magnons: the spin-wave quanta

In the ferromagnetic ground state, each local spin is in a state $|S\rangle_i$ of maximum spin projection along z, that is, $m = S$. Thus, the creation and annihilation operators act in such a state as follows:

$$\begin{aligned} a_i^\dagger |S\rangle_i &= |S-1\rangle_i \quad , \\ a_i |S\rangle &= 0 \quad . \end{aligned} \tag{2.103}$$

Within the adiabatic approximation, we can construct N linearly independent states by acting with creation operator on the ground state:

$$|i\rangle = a_i^\dagger |0\rangle = |S-1\rangle_i \prod_{j \neq i}^{N} |S\rangle_j \quad . \tag{2.104}$$

Each one of those states has a localized reduction of the expectation value of S_i^z in a different site i. For that, $|i\rangle$ is known as a one-deviation state and has a total magnetization of $(N-1)S$. One can verify that none of the one-deviation states is an eigenfunction of the Hamiltonian.

However, if the spins are in a Bravais lattice such that the Hamiltonian has translational symmetry, we can Fourier transform the one-deviation state such as to obtain:

$$|\mathbf{k}\rangle = \frac{1}{\sqrt{N}} \sum_i e^{i\mathbf{k}\cdot\mathbf{r}_i} |i\rangle \quad . \tag{2.105}$$

Each state characterized by the wavevector $\mathbf{k}$ is a superposition of all the one-deviation states, each with a different phase given by $\mathbf{k}\cdot\mathbf{r}_n$ and, because of that, it resembles classical spin waves. We can also see the above equation as:

$$|\mathbf{k}\rangle = a^\dagger_{\mathbf{k}} |0\rangle \quad , \quad \text{where} \quad a^\dagger_{\mathbf{k}} = \frac{1}{\sqrt{N}} \sum_i e^{i\mathbf{k}\cdot\mathbf{r}_i} a^\dagger_i \quad . \tag{2.106}$$

Because $|\mathbf{k}\rangle$ has total magnetization of $NS-1$, we say that $a^\dagger_{\mathbf{k}}$ creates a state with one quantum of spin wave, which is called a magnon, with wavevector $\mathbf{k}$ and spin angular momentum of -1. This angular momentum is not localized, but spread out evenly throughout the entire system, as can be inferred by the expectation value of the local spin deviation:

$$\langle \mathbf{k}| \hat{n}_i |\mathbf{k}\rangle = \frac{1}{N} \quad . \tag{2.107}$$

Likewise, $a_{\mathbf{k}}$ can destroy a magnon with the corresponding wavevector:

$$a_{\mathbf{k}} |\mathbf{k}\rangle = |0\rangle \quad , \quad \text{where} \quad a_{\mathbf{k}} = \frac{1}{\sqrt{N}} \sum_i e^{-i\mathbf{k}\cdot\mathbf{r}_i} a_i \quad . \tag{2.108}$$

$a^\dagger_{\mathbf{k}}$ and $a_{\mathbf{k}}$ are called creation and annihilation magnon operators, respectively. They leave invariant the boson commutation relations:

$$\left[a_{\mathbf{k}}, a^\dagger_{\mathbf{k}'}\right] = \delta_{\mathbf{k}\mathbf{k}'} \quad , \quad [a_{\mathbf{k}}, a_{\mathbf{k}'}] = 0 \quad , \quad \left[a^\dagger_{\mathbf{k}}, a^\dagger_{\mathbf{k}'}\right] = 0 \quad . \tag{2.109}$$

Most importantly, $|\mathbf{k}\rangle$ is also an eigenstate of the Hamiltonian, as we will show next.

Spin-wave spectrum

To evaluate the action of the Hamiltonian on $|\mathbf{k}\rangle$, let us first rewrite it in terms of the magnon operators. Starting from the spin circular components of Eq.(2.84), we can relate the Hamiltonian to the creation and annihilation operators through the Holstein-Primakoff transformation of Eq. (2.99), assuming the low-temperature regime and keeping only terms up to the quadratic order:

$$\begin{aligned}
\mathcal{H} &= -\frac{1}{2} \sum_{ij} J_{ij} (S^x_i S^x_j + S^y_i S^y_j + S^z_i S^z_j) - \sum_i B^z S^z_i \\
&= -\frac{1}{2} \sum_{ij} J_{ij} \left(S(a_i a^\dagger_j + a^\dagger_i a_j) + (S - a_i a^\dagger_i)(S - a_j a^\dagger_j) \right) - \sum_i B^z (S - a^\dagger_i a_i) \\
&= -\frac{1}{2} \sum_{ij} J_{ij} S \left(a_i a^\dagger_j + a^\dagger_i a_j - a^\dagger_i a_i - a^\dagger_j a_j + S \right) - \sum_i B^z (S - a^\dagger_i a_i) \quad .
\end{aligned} \tag{2.110}$$

Next, we can use the boson commutation relations to relate all the terms that depend on the creation and annihilation operators:

$$\begin{aligned}\mathcal{H} &= -\frac{1}{2}\sum_{ij}\left(J_{ij}S\left(a_i a_j^\dagger + a_i^\dagger a_j + S\right) - J_0 S\left(a_i^\dagger a_j + a_i^\dagger a_j\right)\delta_{ij}\right) - \sum_i B^z(S - a_i^\dagger a_i) \\ &= -\frac{1}{2}\sum_{ij}\left(J_{ij}S\left(\delta_{ij} + 2a_i^\dagger a_j + S\right) - J_0 2S a_i^\dagger a_j \delta_{ij}\right) - NSB^z + \sum_{ij} B^z a_i^\dagger a_j \delta_{ij} \\ &= \sum_{ij}\Big((J_0 S + B^z)\delta_{ij} - J_{ij}S\Big)a_i^\dagger a_j - \frac{1}{2}NS^2 J_0 - NSB^z \quad ,\end{aligned} \tag{2.111}$$

where $J_0 = \sum_i J_{ij}$. Above, the constant term, which does not depend on the operators, can be identified as the energy of the ground state:

$$E_0 = -\frac{1}{2}NS^2 J_0 - NSB^z \quad . \tag{2.112}$$

We proceed by expressing the operators in terms of their Fourier counterparts, given by the inverse Fourier transformations of Eqs. (2.106) and (2.108). After some derivation, we obtain:

$$\begin{aligned}\mathcal{H} &= \sum_{ij}\Big((J_0 S + B^z)\delta_{ij} - J_{ij}S\Big)\frac{1}{N}\sum_{\mathbf{k}\mathbf{k}'} e^{-\mathrm{i}\mathbf{k}\cdot\mathbf{r}_i} e^{\mathrm{i}\mathbf{k}'\cdot\mathbf{r}_j} a_{\mathbf{k}}^\dagger a_{\mathbf{k}'} + E_0 \\ &= \sum_{\mathbf{k}\mathbf{k}'}\sum_{ij}\Big((J_0 S + B^z)\delta_{ij} - J_{ij}S\Big)e^{\mathrm{i}\mathbf{k}'\cdot\mathbf{r}_{ij}}\frac{1}{N}e^{-\mathrm{i}(\mathbf{k}-\mathbf{k}')\cdot\mathbf{r}_i} a_{\mathbf{k}}^\dagger a_{\mathbf{k}'} + E_0 \\ &= \sum_{\mathbf{k}\mathbf{k}'}\Big(J_0 S + B^z - J_{\mathbf{k}'}S\Big)\delta(\mathbf{k}-\mathbf{k}')a_{\mathbf{k}}^\dagger a_{\mathbf{k}'} + E_0 \\ &= \sum_{\mathbf{k}}\epsilon_{\mathbf{k}} a_{\mathbf{k}}^\dagger a_{\mathbf{k}} + E_0 \quad ,\end{aligned} \tag{2.113}$$

where the energy of the spin wave with wavevector $\mathbf{k}$ is

$$\epsilon_{\mathbf{k}} = S(J_0 - J_{\mathbf{k}}) + B^z \quad , \tag{2.114}$$

and the Fourier transformation of the MEI parameter is given by:

$$J_{\mathbf{k}} = \sum_j J_{ij} e^{\mathrm{i}\mathbf{k}\cdot\mathbf{r}_{ij}} \quad , \quad \mathbf{r}_{ij} = \mathbf{r}_j - \mathbf{r}_i \quad . \tag{2.115}$$

During the derivation of Eq. (2.113), we used the following properties: $J_{ii} = 0$, because the MEI does not couple a spin to itself; $J_{ij} = J_{ji}$, which implies that the MEI is symmetric; Eq. (2.115), naturally, assumes translational symmetry of the lattice; and

$$\delta(\mathbf{k}-\mathbf{k}') = \frac{1}{N}\sum_i e^{-\mathrm{i}(\mathbf{k}-\mathbf{k}')\cdot\mathbf{r}_i} \quad . \tag{2.116}$$

Note that if $J_{ij} > 0$, then $\epsilon_{\mathbf{k}} \geq 0$ implying that the energies of the spin waves are always equal or higher than that of the ground state. Therefore, every spin wave

corresponds to an excitation. For $\mathbf{k} = 0$ and $B^z \to 0$, we have that $\epsilon_{\mathbf{k}} \to 0$, which means that this spin wave has the same energy as the ground state. In other words, it does not cost energy to excite such a state. This state that corresponds to all spins precessing in phase is predicted by the Goldstone's theorem and, therefore, is called Goldstone's mode.

Also, all the eigenfunction forms a basis that diagonalizes the Hamiltonian:

$$\langle \mathbf{k}' | \, \mathcal{H} \, | \mathbf{k} \rangle = (E_0 + \epsilon_{\mathbf{k}}) \delta_{\mathbf{k}'\mathbf{k}}. \tag{2.117}$$

In this sense, determining the energies and eigenfunction of the spin waves is equivalent to the diagonalization of the linearized Holstein-Primakoff Hamiltonian.

By keeping only up to the quadratic order of the creation and annihilation operators, we have simplified the Heisenberg model Hamiltonian, whose set of eigenstates consists of one-magnon states. Thus, this approach is called the *harmonic approaximation* or the *linear spin-wave approaximation* of the Heisenberg model. It is exact for a single magnon but might represent a good approximation if the number of magnons is small, which is the case for the low-temperature regime.

2.4 Spin waves in noncollinear magnets

In the previous section, we presented a quantum mechanical description of spin waves in ferromagnets. We saw that a quantum of spin waves can be created through the action of a boson creation operator in the ground state. As a result, we obtain a state with a total angular moment reduced by 1. Now, we determine the spin-wave properties of systems whose ground state is a noncollinear spin configuration. We do so by using the same concepts used previously to calculate the spectrum and eigenfunctions of spin waves of a ferromagnet. The difference relies on: the need to represent each spin in its local reference frame, where we can properly define the Holstein-Primakoff transformation; and the need to carefully and numerically diagonalize the Hamiltonian, which evokes a Bogoliubov transformation to ensure that the obtained eigenstates remain bosons. Furthermore, with the matrix representation of the Hamiltonian, given in Eq. 2.61, one is able to systematize the process in such a way that is very suitable for numerical implementation.

2.4.1 Local reference frame and Holstein-Primakoff transformation

Once again, towards computing the spin-wave spectrum of a noncollinear magnet, we must determine its classical ground state. The direction of each spin in this state determines the z–axis of a new and local reference frame for that spin. Operators in the local reference frame are indicated by a prime. Thus, this transformation can be written as

$$\mathbf{S}_i = \mathbf{O}_i \mathbf{S}'_i \quad , \tag{2.118}$$

where the rotation matrix is given by

$$\mathbf{O}_i = \mathbf{O}_z(\phi_i)\mathbf{O}_y(\theta_i) = \begin{pmatrix} \cos\phi_i & -\sin\phi_i & 0 \\ \sin\phi_i & \cos\phi_i & 0 \\ 0 & 0 & 1 \end{pmatrix} \begin{pmatrix} \cos\theta_i & 0 & \sin\theta_i \\ 0 & 1 & 0 \\ -\sin\theta_i & 0 & \cos\theta_i \end{pmatrix} \quad . \tag{2.119}$$

ϕ_i is the polar and θ_i is the azimuthal angle of $\mathbf{S}_i$ in the global reference frame. Now, with each spin pointing along z (in its reference frame), we can perform a Holstein-Primakoff transformation as given by Eq. (2.99), which will replace the spin operator by creation and annihilation operators:

$$\mathbf{S}'_i = \mathbf{M}_i \mathbf{a}_i \quad , \tag{2.120}$$

where

$$\mathbf{M}_i = \sqrt{\frac{S_i}{2}} \begin{pmatrix} 1 & 1 & 0 \\ -i & i & 0 \\ 0 & 0 & \sqrt{\frac{2}{S_i}} \end{pmatrix} \quad \text{and} \quad \mathbf{a}_i = \begin{pmatrix} a_i \\ a_i^\dagger \\ S_i - a_i^\dagger a_i \end{pmatrix} \quad . \tag{2.121}$$

After these two processes, the transformed Hamiltonian can now be written as:

$$\mathcal{H} = -\frac{1}{2} \sum_{ij} \mathbf{a}_i^\dagger \tilde{\mathbf{J}}_{ij} \mathbf{a}_j - \sum_i \tilde{\mathbf{B}}_i \cdot \mathbf{a}_i \quad , \tag{2.122}$$

where

$$\tilde{\mathbf{J}}_{ij} = \mathbf{M}_i^\dagger \mathbf{O}_i^T \mathbf{J}_{ij} \mathbf{O}_j \mathbf{M}_j = \left(\begin{array}{cc|c} \tilde{J}_{ij}^{++} & \tilde{J}_{ij}^{+-} & \tilde{J}_{ij}^{+z} \\ \tilde{J}_{ij}^{-+} & \tilde{J}_{ij}^{--} & \tilde{J}_{ij}^{-z} \\ \hline \tilde{J}_{ij}^{z+} & \tilde{J}_{ij}^{z-} & \tilde{J}_{ij}^{zz} \end{array} \right) = \begin{pmatrix} \mathbf{A}_{ij}^{2\times 2} & \mathbf{B}_{ij}^{2\times 1} \\ \mathbf{B}_{ij}^{1\times 2} & \tilde{J}_{ij}^{zz} \end{pmatrix} \tag{2.123}$$

and

$$\tilde{\mathbf{B}}_i = \mathbf{B}_i \mathbf{O}_i \mathbf{M}_i = \begin{pmatrix} \tilde{B}_i^- & \tilde{B}_i^+ & \tilde{B}_i^z \end{pmatrix} \quad . \tag{2.124}$$

Next, we can group terms of different order of the creation/annihilation operators keeping only up to the quadratic order:

$$\mathcal{H} = \mathcal{H}_0 + \mathcal{H}_1 + \mathcal{H}_2 \quad , \tag{2.125}$$

where

$$\mathcal{H}_2 = -\frac{1}{2} \sum_{ij} \mathbf{a}_i^\dagger \mathbf{H}_{ij} \mathbf{a}_j \quad \text{and} \quad \mathcal{H}_0 = -\frac{1}{2} \tilde{J}_{\mathbf{0}}^{zz} \Big(\sum_i S_i + N \Big) - \sum_i \tilde{B}_i^z \Big(S_i + \frac{1}{2} \Big) \quad , \tag{2.126}$$

with

$$\begin{aligned} \mathbf{H}_{ij} = \mathbf{A}_{ij}^{2\times 2} - \big(\tilde{B}_i^z + \tilde{J}_{\mathbf{0}}^{zz} \big) \mathbf{I}^{2\times 2} \delta_{ij} = \begin{pmatrix} H_{ij}^{++} & H_{ij}^{+-} \\ H_{ij}^{-+} & H_{ij}^{--} \end{pmatrix} \quad , \\ \tilde{J}_{\mathbf{0}}^{zz} = \sum_j \tilde{J}_{ij}^{zz} S_j \quad \text{and now} \quad \mathbf{a}_i = \begin{pmatrix} a_i \\ a_i^\dagger \end{pmatrix} . \end{aligned} \tag{2.127}$$

The zero-order term $\mathcal{H}_0$ is a constant and correspond to the energy of the classical ground state. The first-order $\mathcal{H}_1$ vanishes if the correct classical ground state has been considered. The second-order $\mathcal{H}_2$ describes the excited states and, therefore, we will focus on it now.

Considering that the system has periodicity given by the translation vectors $\mathbf{r}$, we can perform the following Fourier transformation:

$$\mathbf{a_k} = \frac{1}{\sqrt{N}} \sum_i e^{-i\mathbf{k}\cdot\mathbf{r}_i} \mathbf{a}_i \quad , \quad \text{where} \quad \mathbf{a_k} = \begin{pmatrix} a_\mathbf{k} \\ a^\dagger_{-\mathbf{k}} \end{pmatrix} \quad . \tag{2.128}$$

Our Hamiltonian features now this very simple form:

$$\mathcal{H}_2 = -\frac{1}{2} \sum_\mathbf{k} \mathbf{a}^\dagger_\mathbf{k} \mathbf{H_k} \mathbf{a_k} \quad , \tag{2.129}$$

whose matrix $\mathcal{H}_\mathbf{k}$ is, in general, not diagonal. In fact, it is only diagonal for ferromagnets with one atom in the unit cell.

2.4.2 Diagonalization and Bogoliubov transformation

To find the spin-wave excitations, we consider the quantum mechanical equation of motion of the creation and annihilation operators [51, 52]:

$$i\frac{d\mathbf{a}_i}{dt} = [\mathbf{a}_i, \mathcal{H}_2] \quad . \tag{2.130}$$

By evaluating the commutator in the previous equation, we obtain:

$$i\frac{d\mathbf{a}_i}{dt} = \sum_j \mathbf{D}_{ij} \mathbf{a}_j \quad , \tag{2.131}$$

where the dynamical matrix is given by

$$\mathbf{D}_{ij} = -\frac{1}{2} \begin{pmatrix} (H^{++}_{ij} + H^{--}_{ji}) & (H^{+-}_{ij} + H^{+-}_{ji}) \\ -(H^{-+}_{ij} + H^{-+}_{ji}) & -(H^{++}_{ji} + H^{--}_{ij}) \end{pmatrix} \quad . \tag{2.132}$$

Because $\mathcal{H}_2$ is Hermitian, the following relations hold:

$$H^{++}_{ij} = H^{--}_{ji} \quad , \quad H^{++}_{ij} = (H^{--}_{ij})^* \quad , \quad H^{+-}_{ij} = H^{+-}_{ji} \quad , \quad H^{+-}_{ij} = (H^{-+}_{ij})^* \quad . \tag{2.133}$$

Therefore, the dynamical matrix in Eq. (2.132) can be simplified to

$$\mathbf{D}_{ij} = \begin{pmatrix} -H^{++}_{ij} & -H^{+-}_{ij} \\ H^{-+}_{ij} & H^{--}_{ij} \end{pmatrix} = \mathbf{g}\mathbf{H}_{ij} \quad , \tag{2.134}$$

where

$$\mathbf{g} = \begin{pmatrix} -1 & 0 \\ 0 & 1 \end{pmatrix} \quad . \tag{2.135}$$

Please note that $\mathbf{gg} = \mathbf{1}$. Considering the Fourier transformation of Eq. (2.128) and assuming stationary solutions of these operators $\mathbf{a_k}$, such that they depend on time only via a global phase, as in

$$\mathbf{a_k}(t) = e^{-i\omega_\mathbf{k} t} \mathbf{a_k} \quad , \tag{2.136}$$

we obtain for Eq. (2.131) the following eigenvalue equation:

$$\mathbf{D_k a_k} = \omega_{\mathbf{k}} \mathbf{a_k} \quad . \tag{2.137}$$

For the general problem, we diagonalize $\mathbf{D_k}$ numerically, but for a simple set of interactions, it can also be solved analytically. The eigenvalues of $\mathbf{D_k}$ equals the one of the Hamiltonian $\mathbf{H_k}$, but they come in pairs with opposite signs. On the following, we are going to show how diagonalizing $\mathbf{D_k}$ provides the eigenvalues and eigenfunctions of $\mathbf{H_k}$. For simplicity, we are going to drop the $\mathbf{k}$ index. $\mathbf{D}$ is not Hermitian, therefore we need to define left and right eigensolutions as follows:

$$\mathbf{D}\mathcal{R}_r = \omega_r \mathcal{R}_r \quad , \quad \mathcal{L}_r \mathbf{D} = \omega_r \mathcal{L}_r \quad , \tag{2.138}$$

where $\mathcal{R}_r$ is a column eigenvector, $\mathcal{L}_r$ is a row eigenvector and r is the eigenvalue index. In matrix form, this can be written as

$$\mathbf{D}\boldsymbol{\mathcal{R}} = \boldsymbol{\mathcal{R}}\boldsymbol{\Omega} \quad , \quad \boldsymbol{\mathcal{L}}\mathbf{D} = \boldsymbol{\Omega}\boldsymbol{\mathcal{L}} \quad , \tag{2.139}$$

where $\boldsymbol{\mathcal{L}}$ and $\boldsymbol{\mathcal{R}}$ contain all left and right eigenvectors of $\mathbf{D}$ as rows and columns, respectively. $\boldsymbol{\Omega}$ is a diagonal matrix containing the eigenvalues of $\mathbf{D}$. In this way, we have that

$$\boldsymbol{\mathcal{L}}\mathbf{D}\boldsymbol{\mathcal{R}} = \boldsymbol{\mathcal{L}}\boldsymbol{\mathcal{R}}\boldsymbol{\Omega} \quad . \tag{2.140}$$

Because we want $\boldsymbol{\mathcal{R}}$ to represent boson operators, it must satisfy the proper commutation relations that can be expressed as [51, 53]:

$$\boldsymbol{\mathcal{R}}^\dagger \mathbf{g} \boldsymbol{\mathcal{R}} = \mathbf{g} \quad , \quad \boldsymbol{\mathcal{R}} \mathbf{g} \boldsymbol{\mathcal{R}}^\dagger = \mathbf{g} \quad . \tag{2.141}$$

Based on Eq. (2.141), we can show that knowing the right eigenvectors we can construct the left ones via:

$$\boldsymbol{\mathcal{L}} = \mathbf{g}\boldsymbol{\mathcal{R}}^\dagger \mathbf{g} \quad . \tag{2.142}$$

Here follows the proof:

$$\begin{aligned}
\mathbf{D}\boldsymbol{\mathcal{R}} &= \boldsymbol{\mathcal{R}}\boldsymbol{\Omega} \\
\mathbf{g}\mathbf{g}\mathbf{D}\boldsymbol{\mathcal{R}} &= \boldsymbol{\mathcal{R}}\boldsymbol{\Omega} \\
\boldsymbol{\mathcal{R}}\mathbf{g}\boldsymbol{\mathcal{R}}^\dagger\mathbf{g}\mathbf{D}\boldsymbol{\mathcal{R}} &= \boldsymbol{\mathcal{R}}\boldsymbol{\Omega} \\
\mathbf{g}\boldsymbol{\mathcal{R}}^\dagger\mathbf{g}\mathbf{D}\boldsymbol{\mathcal{R}} &= \boldsymbol{\Omega} \\
\boldsymbol{\mathcal{L}}\mathbf{D}\boldsymbol{\mathcal{R}} &= \boldsymbol{\Omega} \\
\boldsymbol{\mathcal{L}}\mathbf{D}\boldsymbol{\mathcal{R}}\boldsymbol{\mathcal{L}} &= \boldsymbol{\Omega}\boldsymbol{\mathcal{L}} \\
\boldsymbol{\mathcal{L}}\mathbf{D} &= \boldsymbol{\Omega}\boldsymbol{\mathcal{L}} \quad ,
\end{aligned} \tag{2.143}$$

where we have used the implication of this construction that $\boldsymbol{\mathcal{L}}\boldsymbol{\mathcal{R}} = \boldsymbol{\mathcal{R}}\boldsymbol{\mathcal{L}} = \mathbf{1}$.

Starting from Eq. (2.140), we have:

$$\begin{aligned}
\boldsymbol{\mathcal{L}}\mathbf{D}\boldsymbol{\mathcal{R}} &= \boldsymbol{\Omega} \\
\mathbf{g}\boldsymbol{\mathcal{R}}^\dagger\mathbf{g}\mathbf{D}\boldsymbol{\mathcal{R}} &= \boldsymbol{\Omega} \\
\boldsymbol{\mathcal{R}}^\dagger\mathbf{H}\boldsymbol{\mathcal{R}} &= \mathbf{g}\boldsymbol{\Omega} = \boldsymbol{\Lambda} \\
\mathbf{H} &= \boldsymbol{\mathcal{L}}^\dagger\boldsymbol{\Lambda}\boldsymbol{\mathcal{L}} \quad ,
\end{aligned} \tag{2.144}$$

where $\mathbf{\Lambda} = \mathbf{g\Omega}$ is diagonal and positive. This equation reveals that $\boldsymbol{\mathcal{R}}$ generates a transformation into a basis where the Hamiltonian is diagonal:

$$\mathcal{H}_2 = -\frac{1}{2}\sum_{\mathbf{k}} \mathbf{a}_{\mathbf{k}}^{\dagger}\mathbf{H}_{\mathbf{k}}\mathbf{a}_{\mathbf{k}} = -\frac{1}{2}\sum_{\mathbf{k}} \mathbf{a}_{\mathbf{k}}^{\dagger}\boldsymbol{\mathcal{L}}_{\mathbf{k}}^{\dagger}\mathbf{\Lambda}_{\mathbf{k}}\boldsymbol{\mathcal{L}}_{\mathbf{k}}\mathbf{a}_{\mathbf{k}} = -\frac{1}{2}\sum_{\mathbf{k}} \mathbf{b}_{\mathbf{k}}^{\dagger}\mathbf{\Lambda}_{\mathbf{k}}\mathbf{b}_{\mathbf{k}} \quad , \tag{2.145}$$

$$\mathcal{H}_2 = -\frac{1}{2}\sum_{\mathbf{k}} \mathbf{b}_{\mathbf{k}}^{\dagger}\mathbf{\Lambda}_{\mathbf{k}}\mathbf{b}_{\mathbf{k}} = -\frac{1}{2}\sum_{\mathbf{k}} \mathbf{b}_{\mathbf{k}}^{\dagger}\boldsymbol{\mathcal{R}}_{\mathbf{k}}^{\dagger}\mathbf{H}_{\mathbf{k}}\boldsymbol{\mathcal{R}}_{\mathbf{k}}\mathbf{b}_{\mathbf{k}} = -\frac{1}{2}\sum_{\mathbf{k}} \mathbf{a}_{\mathbf{k}}^{\dagger}\mathbf{H}_{\mathbf{k}}\mathbf{a}_{\mathbf{k}} \quad , \tag{2.146}$$

where

$$\mathbf{b}_{\mathbf{k}} = \boldsymbol{\mathcal{L}}_{\mathbf{k}}\mathbf{a}_{\mathbf{k}} \quad , \quad \mathbf{b}_{\mathbf{k}}^{\dagger} = \mathbf{a}_{\mathbf{k}}^{\dagger}\boldsymbol{\mathcal{L}}_{\mathbf{k}}^{\dagger} \quad , \tag{2.147}$$

$$\mathbf{a}_{\mathbf{k}} = \boldsymbol{\mathcal{R}}_{\mathbf{k}}\mathbf{b}_{\mathbf{k}} \quad , \quad \mathbf{a}_{\mathbf{k}}^{\dagger} = \mathbf{b}_{\mathbf{k}}^{\dagger}\boldsymbol{\mathcal{R}}_{\mathbf{k}}^{\dagger} \quad . \tag{2.148}$$

$\mathbf{b}_{\mathbf{k}}$ and $\mathbf{b}_{\mathbf{k}}^{\dagger}$ are a new set of bosons, the magnon annihilation and creation operators, respectively. This transformation is known as the Bogoliubov transformation, especially famous in the field of superconductivity.

2.4.3 Spin-wave dispersion of: a ferromagnet, a spin-spiral and a skyrmion lattice

Now, we would like to show the dispersion-relation obtained with the formalism of the previous sections for a ferromagnet, a spin spiral, and a skyrmion lattice. The dispersion-relation consists of the eigenvalues of the Hamiltonian as a function of the wavevector $\mathbf{k}$. We calculated all these three cases with the same Bravais lattice of primitive vectors $\mathbf{a}_1 = a\hat{\mathbf{x}}$ and $\mathbf{a}_2 = a(\frac{1}{2}\hat{\mathbf{x}} + \frac{\sqrt{3}}{2}\hat{\mathbf{y}})$, with $a = 8$; and with same unit cell containing 64 atoms. The ground-state spin configurations inputted were the ones obtained as described in Sec. 2.2. The parameters used were: ferromagnet $\{J = 1\}$; spin spiral $\{J = 1,\ D = 2J/\sqrt{3}\}$; and skyrmion lattice $\{J = 1,\ D = J,\ K = 0.25J,\ B = 0.36J\}$.

Fig. 2.5 (a) shows the dispersion curves for the ferromagnetic case. Many bands appear because the Goldstone mode of the ferromagnet gets folded due to the reduction of the Brillouin zone when considering many atoms in the unit cell. We discuss the unfolding of such a spectrum in Chapter 5. Fig. 2.5 (b-c) presents the dispersion curves for the spin spiral and the skyrmion lattice. We can observe that the dispersion curves of the skyrmion lattice feature many gaps and some dispersionless bands. The dispersion relations were calculated through the reciprocal space path shown on the bottom-right corner of Fig. 2.5. More details on the spin-wave properties of these systems are discussed in Chapter 6, together with their inelastic scattering spectra.

Spin-wave dynamics

We can use the following equations to describe the spin precession of every site in the local reference frame:

$$\begin{aligned} S'^{x,r}_i(\mathbf{k}) &= A_i^{x,r}\cos(\omega_r t + \mathbf{r}_i\cdot\mathbf{k} + \phi_i^{x,r}) \quad , \\ S'^{y,r}_i(\mathbf{k}) &= A_i^{x,r}\sin(\omega_r t + \mathbf{r}_i\cdot\mathbf{k} + \phi_i^{y,r}) \quad , \\ S'^{z,r}_i(\mathbf{k}) &= 1 \quad , \end{aligned} \tag{2.149}$$

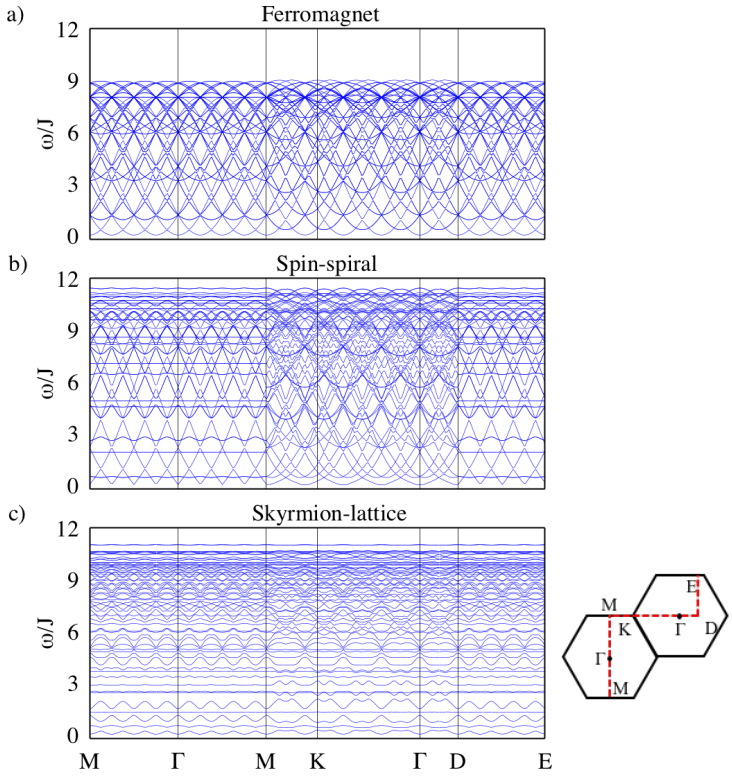

Figure 2.5: Spin-wave dispersion for (a) a ferromagnetic phase, (b) a spin spiral, and (c) a skyrmion lattice as obtained with the schemed described in this section. We considered the same unit cell with 64 atoms for all the three systems. For the ferromagnet and the spin spiral, that is not the minimum unit cell, which yields the folding of the spin-wave dispersion curves.

where the phases and amplitudes were obtained from the calculated right-eigenvectors via:

$$\mathcal{R}_i^{+,r} = A_i^{x,r} e^{i\phi_i^{x,r}} \quad \text{and} \quad \mathcal{R}_i^{-,r} = A_i^{y,r} e^{i\phi_i^{y,r}} \quad . \tag{2.150}$$

Here, i labels the atomic sites, r is the mode index and $\mathbf{k}$ the wavevector of the spin-wave. $\mathcal{R}_i^r$ are the right-eigenvector elements. Then, the precessing spin was brought into the global reference frame via:

$$\mathbf{S}_i^r = \mathbf{O}_i \mathbf{S}_i'^r \quad . \tag{2.151}$$

2.5 Angular momentum of spin waves in noncollinear magnets

In this section, we want to compute the angular momentum of a given spin-wave mode. This quantity will be fundamental to understand the inelastic-electron-

scattering spectra studied in Chapters 6, 7, and 9. First, we calculate the total magnetization of a system for a given spin-wave mode. We then compare it to the magnetization of the ground state. The magnetization difference is then attributed to the angular momentum of the spin-wave mode. The total magnetization of a spin-wave state of wavevector $\mathbf{q}$ and mode index s is a vector quantity given by the expectation value of the total spin operator:

$$\langle \mathbf{S}^{tot}_{\mathbf{q}s} \rangle = \sum_{i\mu} \langle \mathbf{q}s | \mathbf{S}_{i\mu} | \mathbf{q}s \rangle = \sum_{\mu} \mathbf{O}_{\mu} \mathbf{M}_{\mu} \sum_{i} \langle \tilde{0} | b_{\mathbf{q}s} \mathbf{a}_{i\mu} b^{\dagger}_{\mathbf{q}s} | \tilde{0} \rangle \quad , \tag{2.152}$$

where the sums run over all unit cells i and all basis sites μ. In our notation, the vector of creation and annihilation operators is

$$\mathbf{a}_{i\mu} = \begin{pmatrix} a_{i\mu} \\ a^{\dagger}_{i\mu} \\ S_{\mu} - a^{\dagger}_{i\mu} a_{i\mu} \end{pmatrix} \quad . \tag{2.153}$$

Next, we need to write a and $a^{\dagger}$ in the reciprocal space and in terms of b and $b^{\dagger}$. The Fourier transformation is given by

$$\begin{aligned} a^{\dagger}_{i\mu} =& \frac{1}{\sqrt{N}} \sum_{\mathbf{k}} e^{-\mathrm{i}\mathbf{k}\cdot\mathbf{R}_i} a^{\dagger}_{\mathbf{k}\mu} \quad , \\ a_{i\mu} =& \frac{1}{\sqrt{N}} \sum_{\mathbf{k}'} e^{\mathrm{i}\mathbf{k}'\cdot\mathbf{R}_i} a_{\mathbf{k}'\mu} \quad , \\ a^{\dagger}_{i\mu} a_{i\mu} =& \frac{1}{N} \sum_{\mathbf{k}'\mathbf{k}} e^{\mathrm{i}(\mathbf{k}'-\mathbf{k})\cdot\mathbf{R}_i} a^{\dagger}_{\mathbf{k}\mu} a_{\mathbf{k}'\mu} \quad , \end{aligned} \tag{2.154}$$

and the Bogoliubov transformation is as follows:

$$a^{\dagger}_{\mathbf{k}\mu} = \sum_{\alpha,r} \mathcal{R}^{+\alpha}_{\mu r}(\mathbf{k}) b^{\alpha}_{\mathbf{k}r} \quad , \qquad a_{\mathbf{k}'\mu} = \sum_{\beta,r'} \mathcal{R}^{-\beta}_{\mu r'}(\mathbf{k}') b^{\beta}_{\mathbf{k}'r'} \quad . \tag{2.155}$$

Here, we can already conclude that the first two components of $\langle \tilde{0} | b_{\mathbf{q}} \mathbf{a}_i b^{\dagger}_{\mathbf{q}} | \tilde{0} \rangle$ will be zero because it evolves the expectation value of an odd number of one of the new boson operators on the ground state. Focusing on the third component, we have:

$$a^{\dagger}_{i\mu} a_{i\mu} = \frac{1}{N} \sum_{\mathbf{k}'\mathbf{k}} e^{\mathrm{i}(\mathbf{k}'-\mathbf{k})\cdot\mathbf{R}_i} \sum_{\alpha\beta,r'r} \mathcal{R}^{+\alpha}_{\mu r}(\mathbf{k}) \mathcal{R}^{-\beta}_{\mu r'}(\mathbf{k}') b^{\alpha}_{\mathbf{k}r} b^{\beta}_{\mathbf{k}'r'}. \tag{2.156}$$

We will see that the terms where $\alpha = \beta$ will give a zero expectation values, because they result on an even number of b or $b^{\dagger}$ operators. Now we can evaluate the local

expectation value:

$$\begin{aligned}\langle\tilde{0}|b_{\mathbf{q}s}a^z_{i\mu}b^\dagger_{\mathbf{q}s}|\tilde{0}\rangle =&S_\mu - \langle\tilde{0}|b_{\mathbf{q}s}a^\dagger_{i\mu}a_{i\mu}b^\dagger_{\mathbf{q}s}|\tilde{0}\rangle\\ =&S_\mu - \frac{1}{N}\sum_{\mathbf{k}'\mathbf{k}} e^{\mathrm{i}(\mathbf{k}'-\mathbf{k})\cdot\mathbf{R}_i}\sum_{\alpha\beta,r'r}\mathcal{R}^{+\alpha}_{\mu r}(\mathbf{k})\mathcal{R}^{-\beta}_{\mu r'}(\mathbf{k}')\,\langle\tilde{0}|b_{\mathbf{q}s}b^\alpha_{\mathbf{k}r}b^\beta_{\mathbf{k}'r'}b^\dagger_{\mathbf{q}s}|\tilde{0}\rangle\\ =&S_\mu - \frac{1}{N}\sum_{\mathbf{k}'\mathbf{k}} e^{\mathrm{i}(\mathbf{k}'-\mathbf{k})\cdot\mathbf{R}_i}\times\\ &\sum_{r'r}(\mathcal{R}^{++}_{\mu r}(\mathbf{k})\mathcal{R}^{--}_{\mu r'}(\mathbf{k}')+\mathcal{R}^{+-}_{\mu r}(\mathbf{k})\mathcal{R}^{-+}_{\mu r'}(\mathbf{k}'))\delta(\mathbf{q}-\mathbf{k})\delta(\mathbf{q}-\mathbf{k}')\delta_{sr}\delta_{sr'}\\ =&S_\mu - \frac{1}{N}\big(\mathcal{R}^{++}_{\mu s}(\mathbf{q})\mathcal{R}^{--}_{\mu s}(\mathbf{q})+\mathcal{R}^{+-}_{\mu s}(\mathbf{q})\mathcal{R}^{-+}_{\mu s}(\mathbf{q})\big)\quad .\end{aligned} \tag{2.157}$$

In the above equation, only terms for $\alpha \neq \beta$ survived, otherwise an odd number of b or $b^\dagger$ would be obtained, which assures the vanishing of the expectation values. As all states of the kind $|\mathbf{q}s\rangle$ form an orthonormal basis, it follows that the expectation value is only nonzero for $\mathbf{q} = \mathbf{k} = \mathbf{k}'$, and $s = r = r'$. Finally, the total expectation value is

$$\begin{aligned}\langle\mathbf{S}^{tot}_{\mathbf{q}\mathbf{s}}\rangle =&\sum_\mu \mathbf{O}_\mu\mathbf{M}_\mu\sum_i\langle\tilde{0}|b_{\mathbf{q}\mathbf{s}}\mathbf{a}_{i\mu}b^\dagger_{\mathbf{q}\mathbf{s}}|\tilde{0}\rangle\\ =&\sum_\mu \mathbf{O}_\mu\sqrt{\frac{S_\mu}{2}}\begin{pmatrix}1 & 1 & 0\\ -\mathrm{i} & \mathrm{i} & 0\\ 0 & 0 & \sqrt{\frac{2}{S_\mu}}\end{pmatrix}\sum_i\begin{pmatrix}0\\ 0\\ \langle\tilde{0}|b_{\mathbf{q}s}a^z_{i\mu}b^\dagger_{\mathbf{q}s}|\tilde{0}\rangle\end{pmatrix}\\ =&\sum_\mu \mathbf{O}_\mu\begin{pmatrix}0\\ 0\\ NS_\mu-\big(\mathcal{R}^{++}_{\mu s}(\mathbf{q})\mathcal{R}^{--}_{\mu s}(\mathbf{q})+\mathcal{R}^{+-}_{\mu s}(\mathbf{q})\mathcal{R}^{-+}_{\mu s}(\mathbf{q})\big)\end{pmatrix}\quad .\end{aligned} \tag{2.158}$$

Good. But, what about the expectation value in the ground state? Let us first calculate the local expectation value:

$$\begin{aligned}\langle\tilde{0}|a^z_{i\mu}|\tilde{0}\rangle =&S_\mu - \langle\tilde{0}|a^\dagger_{i\mu}a_{i\mu}|\tilde{0}\rangle\\ =&S_\mu - \frac{1}{N}\sum_{\mathbf{k}'\mathbf{k}} e^{\mathrm{i}(\mathbf{k}'-\mathbf{k})\cdot\mathbf{R}_i}\sum_{\alpha\beta,r'r}\mathcal{R}^{+\alpha}_{\mu r}(\mathbf{k})\mathcal{R}^{-\beta}_{\mu r'}(\mathbf{k}')\,\langle\tilde{0}|b^\alpha_{\mathbf{k}r}b^\beta_{\mathbf{k}'r'}|\tilde{0}\rangle\\ =&S_\mu - \frac{1}{N}\sum_{\mathbf{k}'\mathbf{k}} e^{\mathrm{i}(\mathbf{k}'-\mathbf{k})\cdot\mathbf{R}_i}\sum_{r'r}\mathcal{R}^{+-}_{\mu r}(\mathbf{k})\mathcal{R}^{-+}_{\mu r'}(\mathbf{k}')\delta(\mathbf{k}-\mathbf{k}')\delta_{r'r}\\ =&S_\mu - \frac{1}{N}\sum_{\mathbf{k}r}\mathcal{R}^{+-}_{\mu r}(\mathbf{k})\mathcal{R}^{-+}_{\mu r}(\mathbf{k})\quad ,\end{aligned} \tag{2.159}$$

then, the total expectation value is given by:

$$\begin{aligned}\langle\mathbf{S}^{tot}_0\rangle =&\sum_\mu \mathbf{O}_\mu\mathbf{M}_\mu\sum_i\langle\tilde{0}|\mathbf{a}_{i\mu}|\tilde{0}\rangle\\ =&\sum_\mu \mathbf{O}_\mu\begin{pmatrix}0\\ 0\\ NS_\mu-\sum_{\mathbf{k}r}\mathcal{R}^{+-}_{\mu r}(\mathbf{k})\mathcal{R}^{-+}_{\mu r}(\mathbf{k})\end{pmatrix}\quad .\end{aligned} \tag{2.160}$$

We can define the angular moment of the spin wave as the difference between the expectation value of $\mathbf{S}^{tot}_{\mathbf{q}s}$ in the spin-wave state and the ground state one:

$$\langle \mathbf{S}^{tot}_{\mathbf{q}s} \rangle - \langle \mathbf{S}^{tot}_{0} \rangle = \sum_{\mu} \mathbf{O}_{\mu} \begin{pmatrix} 0 \\ 0 \\ \mathcal{F}_{\mu s}(\mathbf{q}) \end{pmatrix} \quad , \tag{2.161}$$

where for simplicity, we defined

$$\mathcal{F}_{\mu s}(\mathbf{q}) = \sum_{\mathbf{k}r} \mathcal{R}^{+-}_{\mu r}(\mathbf{k}) \mathcal{R}^{-+}_{\mu r}(\mathbf{k}) - \left[\mathcal{R}^{++}_{\mu s}(\mathbf{q}) \mathcal{R}^{--}_{\mu s}(\mathbf{q}) + \mathcal{R}^{+-}_{\mu s}(\mathbf{q}) \mathcal{R}^{-+}_{\mu s}(\mathbf{q}) \right] \quad . \tag{2.162}$$

Note that the first term of this quantity is constant but requires an integration through the entire Brillouin zone, which is related to the amplitude of the zero-point spin fluctuations of the ground state.

2.6 Summary

In this chapter, we gave a short introduction to magnetism. We saw that the magnetic exchange interaction has a purely electrostatic and quantum mechanical origin, where Pauli's principle played an important role. Furthermore, we discussed that spin-orbit coupling is responsible for the Dzyaloshinskii-Moriya interaction and magnetocrystalline anisotropy. Bringing these interactions together, we introduced the generalized Heisenberg Hamiltonian, which is an effective spin Hamiltonian that allows us to study the magnetic properties of a material in a very efficient way.

We went further on understanding the role of each of the above-mentioned interactions for the classical ground state. For example, we saw that the MEI is responsible for the ferromagnetic and antiferromagnetic phases. Meanwhile, noncollinearity could be brought in via the DMI, which can favor spin spiral and, in competition with an external magnetic field, skyrmion formations.

We introduced the concept of spin waves. Then, we derived the spin-wave dispersion in the adiabatic approximation for noncollinear magnets by determining the eigenstates and eigenvalues of the quantum Heisenberg Hamiltonian. To achieve this goal, we considered a matrix representation of the Hamiltonian, where we could transform the spins to their local frame in a simple manner. Then, we performed the Holstein-Primakoff transformation, replacing the spins with creation and annihilation operators. Finally, we studied how to diagonalize the resulting Hamiltonian preserving the boson character of the eigenfunctions via the Bogoliubov transformation.

There are other methods to calculate the spin-wave spectrum of a material. For example, by calculating the transversal dynamical magnetic susceptibility [54–56], one can access a material's magnetic excitation spectrum, which includes spin waves. Often, this magnetic response function is obtained in linear response theory, and it can provide information about the life-time of the spin excitations. However, such a method is much more computationally demanding and involving in comparison with the adiabatic approximation that will be used throughout this thesis.

In the next chapter, we discuss how to calculate the parameters of the interaction, such as the MEI J_{ij} or the DMI $\mathbf{D}_{ij}$, from *first-principles* calculations. For

that, we will discuss how to map the electronic structure obtained via density functional theory as implemented within the Korringa-Kohn-Rostoker method to the generalized Heisenberg Hamiltonian.

Chapter 3

First-principles parametrization of the Heisenberg Hamiltonian

In Chapter 2, we introduced a generalized Heisenberg Hamiltonian. It lets us determine the spin-wave properties in the adiabatic approximation for materials whose magnetic moments are seen as localized in the atomic sites. To predict the properties of a specific material, we need the system-specific parameters of the Hamiltonian associated with all the pertinent interactions. A way to obtain these parameters is by fitting the model predictions to the experimental data if any is available. Yet, this might not be a trivial task given the possibility of too many degrees of freedom being involved or insufficient experimental data. Alternatively, we resort to *ab initio* simulations, that allow us to determine the model parameters from a fundamental quantum-mechanical description of the electronic structure of a crystal. As a result, we end up with a parametrized Heisenberg Hamiltonian that allows us to make realistic predicts for the material.

This chapter starts with an introduction to the quantum-mechanical many-body problem for electrons in a crystal. Next, we discuss the *density functional theory* (DFT) [57, 58], which tackles the many-body problem by focusing on the charge density of the electronic system instead of its wavefunction. Among the many possible DFT frameworks, we introduce the Korringa-Kohn-Rostoker method (KKR) [59–62], based on Green functions and multiple-scattering theory. Once a system's Green function is known, we can calculate its magnetic exchange and Dzyaloshinskii-Moriya interactions through the infinitesimal-rotations method [21, 31, 63].

3.1 Introduction

Everything we experience in our daily life results from the quantum mechanical manifestation of nature (except for gravity!). In this sense, classical physics is a set of approximative models, which reproduce the results of quantum mechanics in the appropriate limits. We can use classical mechanics to engineer a building, e.g., the Burj Khalifa with its height of 0.8 km, by just knowing that concrete and steel have, respectively, good resistance against compression and tension. However, as soon as we ask ourselves why these materials have these particular properties, you are exposed to the peculiarities of quantum mechanics.

In conclusion, whatever is the faced problem, a few layers in-depth, it is fun-

damentally quantum mechanical. Consider, for example, the problem of producing and storing clean energy, which is one of our main contemporary challenges. Solving it demands new technologies, which in turn requires new materials exploiting novel condensed-matter phenomena. Therefore, soon enough we are in need of a quantum description of the materials because their constituents, atoms and molecules, obey the laws of quantum mechanics.

The good news is, it seems that we have already a pretty good idea of the quantum mechanics laws, that is, the equations that govern the interactions between atomic and subatomic particles. Furthermore, the predictions that we have made through it are of incredible accuracy. On the downside, we cannot solve these equations exactly for any practical problem in condensed matter physics! In this section, some of the discussions are inspired by Ref. [64].

3.1.1 Schrödinger equation and wavefunction

We want to describe a condensed matter system composed of nuclei and electrons. By now, let us assume that the nuclei are static. In quantum mechanics, all the information that can be inquired about such a physical system with N interacting electrons is provided by its many-body wavefunction $\psi(\mathbf{r}_1, \mathbf{r}_2, ..., \mathbf{r}_N, t)$ (we disregarded the spins in this notation). In turn, this wavefunction is the antisymmetric solution of the time-dependent Schrödinger equation, which is given by:

$$\mathrm{i}\frac{\partial}{\partial t}\psi(\mathbf{r}_1, \mathbf{r}_2, ..., \mathbf{r}_N, t) = \mathcal{H}\psi(\mathbf{r}_1, \mathbf{r}_2, ..., \mathbf{r}_N, t) \quad . \tag{3.1}$$

In this chapter, we use the atomic Rydberg units, where $\hbar = 2m_e = e^2/2 = 1$, where m_e is the rest mass of the electron and e its charge. Neglecting relativist corrections, the Hamiltonian that appears in the Schrödinger equation is composed by three contributions:

$$\mathcal{H} = -\sum_{i=1}^{N} \nabla_i^2 + \sum_{i<j} \frac{2}{|\mathbf{r}_i - \mathbf{r}_j|} - \sum_{i}^{N}\sum_{j}^{M} \frac{2Z_j}{|\mathbf{r}_i - \mathbf{R}_j|} \quad , \tag{3.2}$$

where M is the number of nuclei of the system. The first term corresponds to the total kinetic energy of the electrons. It is a noninteracting term since the kinetic energy of an electron does not explicitly depend on the other electrons. The second term is the Coulomb potential of the interaction between all the electrons among themselves, and therefore, it is a many-body term. Likewise, the last term is also a many-body contribution that describes the interaction between the electrons and the electrically charged nuclei of the atoms.

Solving analytically the Schrödinger equation for a system with more than a few electrons is impossible. And the fact that the wavefunction is a function of the position of all particles involved is an insurmountable impediment for a direct computational attempt. To clarify that, consider that we want to calculate the wavefunction of an iron atom with its 26 electrons. Let us try to discretized the space, within a box containing the Fe atom, in a grid of $10 \times 10 \times 10$ points. That makes 10^3 possible positions for each electron. Furthermore, the wavefunction should inform the probability of finding an electron in a given position for each possible configuration of the remaining electrons. That accounts for 10^{78} possible configurations,

and for each of them, we need to evaluate the wavefunction. Even before thinking about how to solve the Schrödinger equation of such a problem, let us consider to store this function: If we could use a hydrogen atom to store a complex number, the required physical memory would have the mass of the observable universe! [65]

3.1.2 Born-Oppenheimer approximation

In fact, nuclei of atoms do move and their vibrations are directed related to the temperature of the material. Nevertheless, nuclei are much more massive than electrons, therefore, their dynamics are much slower. Thus, one might consider that during the dynamics of the nuclei, the electrons follow and adapt to every new configuration almost instantaneously. On the other hand, in the electron dynamics perspective, the nuclei are fixed, hence their positions become no more than parameters. This is the *Born-Oppenheimer approximation* [66] (adiabatic approximation), that decouples the motion of nuclei and electron, and effectively reduces the electron-nucleus interactions in Eq. (3.2) into a noninteracting term. Thus, the electrostatic potential from the nucleus can be regarded as an external potential just like other externally applied fields. The Hamiltonian can then be written as

$$\mathcal{H} = \mathcal{T} + \mathcal{W} + \mathcal{V}_{\text{ext}} \quad , \tag{3.3}$$

where $\mathcal{T}$ is the kinetic energy, $\mathcal{W}$ the electron-electron interaction, and $\mathcal{V}_{\text{ext}}$ is the external potential which includes the nuclear electrostatic potential.

This is the first simplification towards an effective description of a system of interacting particles, for it leaves *only* the electron-electron interaction responsible for all the difficulties.

3.2 Density functional theory - DFT

Until the 50s, we believed that determining the quantum mechanical behavior of a system requires to solve the Schrödinger equation to obtain the system's wavefunction. A game-changer came with the work of Hohenberg and Kohn that demonstrated that we could actually determine all observables of a given system as a functional of the charge density, which could be obtained via an energy minimization process.

3.2.1 Hohenberg and Kohn theorem

In 1960, Hohenberg and Kohn [57] demonstrated the theorem that states the following:

Theorem 1 *Consider the Hamiltonian of Eq. 3.3 with an arbitrary external potential, if the ground-state is nondegenerate, there is a one-to-one mapping between the external potential up to a constant, the ground-state wavefunction, and the ground-state electron density:*

$$\mathcal{V}_{\text{ext}}(\mathbf{r}) \Longleftrightarrow \psi_{\text{gs}}(\mathbf{r}_1, \mathbf{r}_2, \ldots, \mathbf{r}_N) \Longleftrightarrow n_{\text{gs}}(\mathbf{r}) \quad . \tag{3.4}$$

In the above equation, ψ_{gs} is the ground-state wavefunction and $n_{\text{gs}}(\mathbf{r})$ the ground-state density:

$$n_{\text{gs}}(\mathbf{r}) = \sum_{i=1}^{N} \int \mathrm{d}^3 r_1 \cdots \int \mathrm{r}^3 r_N \psi^*_{\text{gs}}(\mathbf{r}_1, \ldots, \mathbf{r}_N) \delta(\mathbf{r} - \mathbf{r}_i) \psi_{\text{gs}}(\mathbf{r}_1, \ldots, \mathbf{r}_N) \quad . \tag{3.5}$$

The uniqueness of the ground-state density allows us to represent not only the Hamiltonian but any other observable as a functional of the density, which gives the name *density functional theory*. Nevertheless, we still need to be able to find that density. Hohenberg and Kohn went further and also showed that [57]:

Theorem 2 *The ground-state density $n_{\text{gs}}(\mathbf{r})$ minimizes the total energy functional $E[n] = \langle \mathcal{H} \rangle$:*

$$\min\big[E[n]\big] = E[n_{\text{gs}}] \quad . \tag{3.6}$$

This means that we can obtain the density through the variational principle. For example, we could start with a guess for the density, then making small variations in search of the energy functional minimum while preserving the number of electrons $N = \int \mathrm{d}^3 n(\mathbf{r})$. The problem is that we do not know the functional $E[n]$. If it were known and sufficiently simple, determining the ground-state energy would be a simple minimization exercise of a functional of the three-dimensional density function. Therefore, a major part of solving the many-body problem consists of determining good approximations of the energy functional.

For magnetic materials, the energy is written as a functional of the charge density and of the spin density, which for collinear magnetic materials can be written as:

$$m_{\text{gs}}(\mathbf{r}) = n^{\uparrow}_{\text{gs}}(\mathbf{r}) - n^{\downarrow}_{\text{gs}}(\mathbf{r}) \quad , \tag{3.7}$$

where $n^{\alpha}_{\text{gs}}(\mathbf{r})$ is the spin-dependent density. Hence, the energy, that can now be written as $E[n_{\text{gs}}, m_{\text{gs}}]$, should be minimized with respect to the charge and spin densities.

3.2.2 Kohn and Sham equation

Kohn and Sham proposed to construct a fictitious system of noninteracting particles that has the same ground-state density as the many-body system of interest [58]. The solutions of the noninteracting problem could be found by solving the Kohn-Sham equation:

$$\Big(-\nabla^2 + \mathcal{V}_{\text{eff}}[n_{\text{gs}}] \Big) \phi_i(\mathbf{r}) = \epsilon_i \phi_i(\mathbf{r}) \quad , \tag{3.8}$$

which has the form of a single-particle Schrödinger equation, and ϕ_i are known as Kohn-Sham orbitals. ϵ_i are the orbital eigenvalues, which individually have no meaning unless the system is of noninteracting electrons. The mapping between the many-body and the noninteracting problems is obtained through the effective potential $\mathcal{V}_{\text{eff}}$, which is a *unknown* functional of the ground-state density. Note that the density can be computed from the Kohn-Sham orbitals simply via

$$n(\mathbf{r}) = \sum_{i=1}^{\text{occ.}} |\phi_i(\mathbf{r})|^2 \quad . \tag{3.9}$$

However, these orbitals are solutions of Eq. (3.8), which depends on the density. Therefore, the Kohn-Sham equation is solved self-consistently. This process consists of starting from a plausible guess for the density, solve the Kohn-Sham equation to compute the orbitals from which a new density is obtained to be used in the next recursive step. The circle is repeated until the input density equals to the output one within the required precision.

We attempt to construct the unknown effective potential in the following way:

$$\mathcal{V}_{\text{eff}}(\mathbf{r}) = \mathcal{V}_{\text{ext}}(\mathbf{r}) + \mathcal{V}_{\text{H}}(\mathbf{r}) + \mathcal{V}_{\text{xc}}(\mathbf{r}) \quad , \tag{3.10}$$

where $\mathcal{V}_{\text{ext}}$ is the external potential including the nuclear electrostatic potentials; $\mathcal{V}_{\text{H}}$ is the Hartree potential given by

$$\mathcal{V}_{\text{H}}(\mathbf{r}) = \int \frac{2n(\mathbf{r}')}{|\mathbf{r} - \mathbf{r}'|} \mathrm{d}^3 r' \quad , \tag{3.11}$$

which represents a noninteracting mean-field electrostatic contribution from the electrons in the system; and $\mathcal{V}_{\text{xc}}$ is the *exchange-correlation* potential, which is defined by Eq. (3.10). That is, the exchange-correlation potential is given by the difference between the true and unknown potential and the Hartree-approximation potential $(\mathcal{V}_{\text{ext}}(\mathbf{r}) + \mathcal{V}_{\text{H}}(\mathbf{r}))$, therefore it accounts for the many-body effects, such as the exchange coupling due to Pauli's exclusion principle and electronic correlations. Our hope is that the two first terms of Eq. (3.10) are the most relevant and that $\mathcal{V}_{\text{xc}}$, which is unknown, accounts for a small contribution.

Thus, the energy functional of the Kohn-Sham system, which needs to be minimized, can be written as

$$E[n] = T_{\text{s}}[n] + E_{\text{H}}[n] + E_{\text{xc}}[n] + E_{\text{ext}}[n] \quad . \tag{3.12}$$

The first term is the noninteracting kinetic energy of the occupied Kohn-Sham orbitals:

$$T_{\text{s}}[n] = -\sum_{i=1}^{\text{occ.}} \int \phi_i^*(\mathbf{r}) \nabla^2 \phi_i(\mathbf{r}) \mathrm{d}^3 r \quad . \tag{3.13}$$

The second corresponds to the Hartree energy, which can be written as

$$E_{\text{H}}[n] = \iint \frac{n(\mathbf{r}) n(\mathbf{r}')}{|\mathbf{r} - \mathbf{r}'|} \mathrm{d}^3 r \mathrm{d}^3 r' \quad . \tag{3.14}$$

The third term E_{xc} is the exchange-correlation energy, which remains unknown, and it is connected to $\mathcal{V}_{\text{xc}}$ by

$$\mathcal{V}_{\text{xc}}[n_{\text{gs}}](\mathbf{r}) = \left. \frac{\delta E_{\text{xc}}[n]}{\delta n(\mathbf{r})} \right|_{n(\mathbf{r}) = n_{\text{gs}}(\mathbf{r})} \quad . \tag{3.15}$$

Next, we discuss a simple, yet very useful, approximation for the exchange-correlation energy.

3.2.3 Local density approximation - LDA

One of the biggest challenges for any DFT approach is to properly approximate the exchange-correlation energy such that we can reproduce the properties of the desired system. Another important fact to be taken into account is the computational cost of a given approach. One of the first and simplest methods is called the local density approximation (LDA) [58], where the exchange-correlation energy is given by:

$$E_{\mathrm{xc}}^{\mathrm{LDA}}[n] = \int e_{\mathrm{xc}}^{\mathrm{hom}}\big(n(\mathbf{r})\big)\mathrm{d}^3r \quad , \tag{3.16}$$

where $e_{\mathrm{xc}}^{\mathrm{hom}}[n(\mathbf{r})]$ is the exchange-correlation energy of the homogeneous electron gas, which is a local function of the density and can be calculated accurately with a combination of analytical result and quantum Monte Carlo simulation [67].

The LDA is then a reasonable approach for a system whose density varies slowly throughout the space. In this thesis, we use an extension of this approximation, which accounts for different spin channels called the *local spin density approximation* (LSDA) [67]:

$$E_{\mathrm{xc}}^{\mathrm{LSDA}}[n,m] = \int e_{\mathrm{xc}}^{\mathrm{hom}}\big(n(\mathbf{r}),m(\mathbf{r})\big)\mathrm{d}^3r \quad , \tag{3.17}$$

where $m = |\mathbf{m}|$ with the spin density is given in terms of the Kohn-Sham orbitals by

$$\mathbf{m}(\mathbf{r}) = \sum_i \phi_i^\dagger(\mathbf{r})\boldsymbol{\sigma}\phi_i(\mathbf{r}) \quad . \tag{3.18}$$

Here, $\boldsymbol{\sigma} = (\sigma^x, \sigma^y, \sigma^z)$ is a vector of Pauli matrices. There are many other approximations for the exchange-correlation energy, such as the generalized gradient approximation (GGA), which involves not only the local density by also its local gradient.

3.3 Korringa-Kohn-Rostoker method - KKR

We extend our discussion to the Korringa-Kohn-Rostoker (KKR) method, which was formulated by Korringa [59] in 1947 and later by Kohn and Rostoker [60] in 1954. It is a multiple-scattering theory that consists of dividing the problem of calculating the electronic structure of a solid into two parts: solving a single-site scattering problem for each atom in isolation; then incorporating the structural information of the solid by solving a multiple-scattering problem.

This approach becomes particularly powerful when formulated in terms of Green functions [61, 68]. For example, it allows us to treat systems without translational invariance such as single impurities and clusters in real space. This is possible because we can compute the Green functions of different parts of the systems in isolation and obtain the Green function of the total system via the Dyson equation. This section follows some of the discussions contained in Refs. [20, 64, 69–71].

3.3.1 Green-function basics

Consider a system described by a time-independent Hamiltonian $\mathcal{H}_0$ subject to a perturbation given by a potential $\mathcal{V}$. Let us suppose that the eigenfunctions of $\mathcal{H}_0$

are known:

$$\mathcal{H}_0 \left|\psi_0\right\rangle = \epsilon_0 \left|\psi_0\right\rangle \quad , \tag{3.19}$$

and that we seek for the eigenfunctions $|\psi\rangle$ of the perturbed system given by $\mathcal{H} = \mathcal{H}_0 + \mathcal{V}$, which are solutions of the Schrödinger equation:

$$\begin{aligned} (\mathcal{H}_0 + \mathcal{V}) \left|\psi\right\rangle =& \epsilon \left|\psi\right\rangle \\ (\epsilon - \mathcal{H}_0) \left|\psi\right\rangle =& \mathcal{V} \left|\psi\right\rangle \quad . \end{aligned} \tag{3.20}$$

$\mathcal{V}|\psi\rangle$ can be identified as the inhomogeneous part of this differential equation in comparison to Eq. (3.19). The Green function of the unperturbed system is defined as the operator that satisfies:

$$(z\mathbb{1} - \mathcal{H}_0)\mathcal{G}_0(z) = \mathbb{1} \quad , \tag{3.21}$$

where z is a complex number and $\mathbb{1}$ is the identity operator.

Similarly, the Green function of the whole (perturbed) system described by $\mathcal{H} = \mathcal{H}_0 + \mathcal{V}$ is given by

$$\mathcal{G}(z) = (z\mathbb{1} - \mathcal{H})^{-1} \quad . \tag{3.22}$$

If the complete set of eigenfunctions of this Hamiltonian is $\{|\psi_n\rangle\}$, we can write a *spectral representation* of the Green function, which is given by:

$$\mathcal{G}(z) = \sum_n \frac{\left|\psi_n\right\rangle \left\langle\psi_n\right|}{z - \epsilon_n} \quad . \tag{3.23}$$

The Green function has different limits in the real axis depending on from each side of the complex plane we are approaching:

$$\begin{aligned} \mathcal{G}^+(\epsilon) &= \lim_{|\eta|\to 0} \mathcal{G}(\epsilon + \mathrm{i}|\eta|) \quad , \\ \mathcal{G}^-(\epsilon) &= \lim_{|\eta|\to 0} \mathcal{G}(\epsilon - \mathrm{i}|\eta|) \quad . \end{aligned} \tag{3.24}$$

$\mathcal{G}^+$ is called advanced and $\mathcal{G}^-$ retarded Green functions, and they are the adjoint conjugate of each other.

The Lippmann-Schwinger equation allows us to obtain the solution of the perturbed system in terms of the perturbation potential $\mathcal{V}$, and the unperturbed solution $|\psi_0\rangle$:

$$\left|\psi\right\rangle = \left|\psi_0\right\rangle + \mathcal{G}_0(\epsilon)\mathcal{V}\left|\psi\right\rangle \quad . \tag{3.25}$$

However, the desired solution $|\psi\rangle$ appears in both side of the equation. We can iteratively insert the above equation into itself to produce a Born series:

$$\begin{aligned} \left|\psi\right\rangle =& \left|\psi_0\right\rangle + \mathcal{G}_0(\epsilon)\mathcal{V}\left|\psi_0\right\rangle + \mathcal{G}_0(\epsilon)\mathcal{V}\mathcal{G}_0(\epsilon)\mathcal{V}\left|\psi_0\right\rangle + \mathcal{G}_0(\epsilon)\mathcal{V}\mathcal{G}_0(\epsilon)\mathcal{V}\mathcal{G}_0(\epsilon)\mathcal{V}\left|\psi_0\right\rangle + \dots \\ =& \left|\psi_0\right\rangle + \mathcal{G}_0(\epsilon)\mathcal{T}\left|\psi_0\right\rangle \quad , \end{aligned} \tag{3.26}$$

where we defined the *transition matrix* (t–matrix) as

$$\mathcal{T}(z) = \mathcal{V} + \mathcal{V}\mathcal{G}_0(z)\mathcal{V} + \mathcal{V}\mathcal{G}_0(z)\mathcal{V}\mathcal{G}_0(z)\mathcal{V} + \dots \quad . \tag{3.27}$$

The Born series do not always converge. Nevertheless, one could still obtain the t–matrix through a direct inversion.

In fact, we do not need to calculate a system's eigenfunction to obtain the expected value of a given observable, this can be calculated directly from the Green function, via

$$\langle \mathcal{A} \rangle = \mp \frac{1}{\pi} \mathrm{Im} \int_{-\infty}^{+\infty} f(\epsilon) \mathrm{Tr}[\mathcal{A} G^{\pm}(\epsilon)] \mathrm{d}\epsilon \quad , \tag{3.28}$$

where $f(\epsilon)$ is the Fermi-Dirac distribution function [72]. The density of states can be obtained simply by taking the trace of the Green function:

$$n(\epsilon) = \mp \frac{1}{\pi} \mathrm{Im}\, \mathrm{Tr}\, \mathcal{G}^{\pm}(\epsilon) \quad . \tag{3.29}$$

Thus, it is also important to know how to obtain the Green functions of the perturbed system, such that we can obtain its properties without the need for computing its eigenfunctions, which allows the implementation of efficient methods that scale linearly with the number of atoms [73, 74]. This can be obtained via the *Dyson equation*:

$$\mathcal{G}(z) = \mathcal{G}_0(z) + \mathcal{G}_0(z)\mathcal{V}\mathcal{G}(z) = \mathcal{G}_0(z)(\mathbb{1} - \mathcal{G}_0(z)\mathcal{V})^{-1} \quad . \tag{3.30}$$

The matrix inversion required in this equation is sometimes an insurmountable problem, e.g., when the matrix is nonsparse and of very high order. Inserting the last equation into itself iteratively, we obtain

$$\mathcal{G}(z) = \mathcal{G}_0(z) + \mathcal{G}_0(z)\mathcal{T}\mathcal{G}_0(z) \quad , \tag{3.31}$$

where the t–matrix $\mathcal{T}$ could be calculated via Eq. (3.27) without a direct inversion. When the perturbation potential $\mathcal{V}$ is small, such that the series in Eq. (3.27) converges well, the accuracy of the calculation can be controlled by choosing where to truncate the series.

3.3.2 Atomic sphere approximation - ASA

In the Green function formalism of the KKR method, we divide the space that contains the material through a Voronoi decomposition. In this process, we usually pick the center of each atom as seeds for the decomposition. Then, we identify the region of space whose points are closer to a particular seed. Each region is called a Voronoi cell. Often, we have to divide the vacuum regions near to the material in a similar manner by choosing vacuum atomic sites.

Centered in each Voronoi seed, we construct a Wigner–Seitz cell: a sphere with the same volume as the Voronoi cell. By construction, the Wigner-Seitz spheres overlap. For the sake of simplicity, we do not consider spin-orbit coupling for now, nor noncollinear magnetic structures, such that the Green function is diagonal in the spin space requiring only a single label $\sigma = \uparrow, \downarrow$ to characterize the spin. The Kohn-Sham potential in a given position of space $\mathbf{r}$ is then given by the sum over all Wigner-Seitz cells:

$$V^{\sigma}(\mathbf{r}) = \sum_{i=1}^{N} v_i^{\sigma}(\mathbf{r}_i) \quad , \tag{3.32}$$

where $\mathbf{r}_i = \mathbf{r} - \mathbf{R}_i$ and $\mathbf{R}_i$ is the location of the i–th Wigner-Seitz-cell center. In the atomic sphere approximation (ASA), we consider that all the charge is contained within the Wigner-Seitz sphere and that its electrostatic potential is spherically symmetric:

$$v_i^\sigma(\mathbf{r}) = \begin{cases} v_i^\sigma(r) & : \quad r < r_{\mathrm{WS}} \\ 0 & : \quad r > r_{\mathrm{WS}} \end{cases} \quad , \tag{3.33}$$

where r_{WS} is the radius of the correspondent Wigner-Seitz sphere.

Our goal now is to obtain the Green function for each spin channel, which should satisfy

$$\big(E - H^\sigma(\mathbf{r})\big) G^\sigma(\mathbf{r}, \mathbf{r}', E) = \delta(\mathbf{r} - \mathbf{r}') \quad , \tag{3.34}$$

where $H^\sigma(\mathbf{r}) = -\nabla^2 + V^\sigma(\mathbf{r})$. For that, we divide the problem into two steps. First, we solve a single-site problem for each Wigner-Seitz cell. Then, we solve a structural problem connecting the single-site solutions. Throughout the following subsections, we drop the spin index σ.

3.3.3 Single-site problem

We want to calculate the Green function of an isolated atom. We start by considering a free electron system, that is, when $v(\mathbf{r}) = 0$, which we will use as a reference system because we can obtain an analytical solution for it. The free-electron Green function $g(\mathbf{r}, \mathbf{r}', E)$ is simply given by:

$$g(\mathbf{r}, \mathbf{r}', E) = -\frac{1}{4\pi} \frac{e^{\mathrm{i}k|\mathbf{r}-\mathbf{r}'|}}{|\mathbf{r} - \mathbf{r}'|} \quad , \tag{3.35}$$

where $e^{\mathrm{i}k|\mathbf{r}-\mathbf{r}'|}$ represents an outgoing spherical wave, which is an eigenfunction of the free-electron problem with $k = \sqrt{E}$. As the potential is zero, this system is spherically symmetric. Even when it is nonzero, within the atomic sphere approximation, the potential inside of each Wigner-Seitz cell is considered spherically symmetric. This invites us to expand the Eq. (3.35) in terms of the spherical functions:

$$g(\mathbf{r}, \mathbf{r}', E) = \sum_L Y_L(\hat{\mathbf{r}}) g_l(r, r', E) Y_L(\hat{\mathbf{r}}') \quad , \tag{3.36}$$

where $\hat{\mathbf{r}} = \hat{\mathbf{r}}/r$ is a unit vector in the direction of $\mathbf{r}$, and $Y_L(\hat{\mathbf{r}})$ is the real spherical harmonics of the combined index $L = (l, m)$ of angular momentum l and magnetic quantum number m. The coefficients are given by

$$g_l(r, r', E) = -\mathrm{i}k j_l(kr_<) h_l(kr_>) \quad , \tag{3.37}$$

where $r_< = \min(r, r')$ and $r_> = \max(r, r')$. $j_l(x)$ is the spherical Bessel function and $h_l(x) = j_l(x) + \mathrm{i}n_l(x)$ is the spherical Hankel function of the first kind, which is a linear combination of a Bessel function with a Neumann function $n_l(x)$. All of these functions, $j_l(x)$, $n_l(x)$ and $h_l(x)$ are solutions of the free-particle radial Schrödinger equation:

$$\left(-\frac{1}{r} \frac{\partial^2}{\partial r^2} r + \frac{l(l+1)}{r^2} \right) R_l(r, E) = E R_l(r, E) \quad , \tag{3.38}$$

which is obtained by assuming a decomposition of the wavefunction into a radial and an angular solutions: $\psi(\mathbf{r}, E) = R_l(r, E)Y_L(\hat{\mathbf{r}})$. Equation (3.37) diverges at the origin because the Hankel function diverges for $x \to 0$, while the Bessel function remains finite.

Spherical potential of finite range

For a general spherical potential $v_i(r)$ nonvanishing inside of the i–th Wigner-Seitz cell, we cannot find an analytical expression for the Green function. However, we can construct the solution by considering the free-electron system as an unperturbed system and the potential $v(r)$ as the perturbation. The single-site Green function $\mathring{G}$ then reads

$$\mathring{G}(\mathbf{r}, \mathbf{r}', E) = \sum_L Y_L(\hat{\mathbf{r}})\mathring{G}_l(r, r', E)Y_L(\hat{\mathbf{r}}') \quad , \tag{3.39}$$

where the expansion coefficients are given in terms of the solution of the perturbed problem:

$$\mathring{G}_l(r, r', E) = -\mathrm{i}kR_l(r_<, E)H_l(r_>, E) \quad . \tag{3.40}$$

Note that these coefficients only depend on l, instead of l and l'. That is because the spherical potential conserves angular momentum, therefore, no transition between states of different angular momentum is allowed. The wavefunctions of the perturbed system can be obtained in terms of the unperturbed (free-electron) Green function and wavefunctions through the Lippmann-Schwinger equation in its integral form:

$$\begin{aligned} R_l(r, E) =& j_l(kr) + \int_0^{r_{\mathrm{MT}}} r'^2 g_l(r, r', E)v(r')R_l(r', E)\mathrm{d}r' \quad , \\ H_l(r, E) =& h_l(kr) + \int_0^{r_{\mathrm{MT}}} r'^2 g_l(r, r', E)v(r')H_l(r', E)\mathrm{d}r' \quad . \end{aligned} \tag{3.41}$$

For $r > r_{\mathrm{WS}}$, these functions read

$$\begin{aligned} R_l(r, E) =& j_l(kr) - \mathrm{i}kt_l(E)h_l(r', E) \quad , \\ H_l(r, E) =& h_l(kr) \quad , \end{aligned} \tag{3.42}$$

where the t-matrix for the single-site problem is given by

$$t_l(E) = \int_0^{r_{\mathrm{MT}}} r'^2 j_l(kr')v(r')R_l(r', E)\mathrm{d}r' \quad . \tag{3.43}$$

3.3.4 Structural problem

Recalling, we have divided the space into Wigner-Seitz cells. A general position of the space is given by $\mathbf{x} = \mathbf{r} + \mathbf{R}_i$, where $\mathbf{R}_i$ is the location of the i–th cell center and $\mathbf{r}$ is contained in its Wigner-Seitz sphere. An addition theorem for the Hankel functions reads: [20]

$$h_L(\mathbf{r}' + \mathbf{R}_{ij}, E) = \sum_{L'} g^{\mathrm{str}}_{iL,jL'}(E)J_{L'}(\mathbf{r}', E) \quad , \tag{3.44}$$

where $\mathbf{R}_{ij} = \mathbf{R}_j - \mathbf{R}_i$, and we used the abbreviations:

$$\begin{aligned} J_L(\mathbf{r}, E) =& j_l(kr)Y_L(\hat{\mathbf{r}}) \quad , \\ H_L(\mathbf{r}, E) =& h_l(kr)Y_L(\hat{\mathbf{r}}) \quad . \end{aligned} \tag{3.45}$$

The coefficients of the expansion in Eq. 3.44 are the *structural Green functions* given by

$$g^{\mathrm{str}}_{iL,jL'}(E) = -(1-\delta_{ij})4\pi \mathrm{i}\sqrt{E}\sum_{L''} \mathrm{i}^{l-l'+L''} C_{LL'L''} H_{L''}(-\mathbf{R}_{ij}, E) \quad . \tag{3.46}$$

The summation in the above equation is finite because the Gaunt coefficients

$$C_{LL'L''} = \int Y_L(\hat{\mathbf{r}}) Y_{L'}(\hat{\mathbf{r}}) Y_{L''}(\hat{\mathbf{r}}) \mathrm{d}\Omega \tag{3.47}$$

vanish for $l'' > l + l'$. Thus, the free-electron Green function can now be written as [61]

$$\begin{aligned} g(\mathbf{x}, \mathbf{x}', E) =& g_{ij}(\mathbf{r}, \mathbf{r}', E) \\ =& -\frac{1}{4\pi} \frac{e^{\mathrm{i}k|(\mathbf{r}+\mathbf{R}_i)-(\mathbf{r}'+\mathbf{R}_j)|}}{|(\mathbf{r}+\mathbf{R}_i)-(\mathbf{r}'+\mathbf{R}_j)|} \\ =& -\mathrm{i}k \sum_L J_L(\mathbf{r}_<, E) H_L(\mathbf{r}_>, E)\delta_{ij} + \sum_{LL'} J_L(\mathbf{r}, E) g^{\mathrm{str}}_{iL,jL'}(E) J_{L'}(\mathbf{r}', E) \quad . \end{aligned} \tag{3.48}$$

Structural Green function with spherical potential

Note that the Green function in Eq. (3.48) has the following general form:

$$g_{ij}(\mathbf{x}, \mathbf{x}', E) = \mathring{g}_{ii}(\mathbf{x}, \mathbf{x}', E)\delta_{ij} + g^{\mathrm{str}}_{ij}(\mathbf{x}, \mathbf{x}', E) \quad . \tag{3.49}$$

The first term in the right-hand side is a single-site contribution and the second term is a nonlocal contribution that corresponds to the structural part. Again using the free-electron problem as the unperturbed system, we can construct the Green function for the system with the spherical Kohn-Sham potential: $G_{ij}(\mathbf{x}, \mathbf{x}', E) = \mathring{G}_{ii}(\mathbf{x}, \mathbf{x}', E)\delta_{ij} + G^{\mathrm{str}}_{ij}(\mathbf{x}, \mathbf{x}', E)$, where the single-site term is given by Eq. (3.39) and

$$G^{\mathrm{str}}_{ij}(\mathbf{x}, \mathbf{x}', E) = \sum_{LL'} Y_L(\hat{\mathbf{r}}) R_{iL}(r, E) G^{\mathrm{str}}_{iL,jL'}(E) R_{jL'}(r, E) Y_{L'}(\hat{\mathbf{r}}) \quad . \tag{3.50}$$

The regular and irregular solutions are given by Eq. (3.41), and the coefficients that contain the information about the multiple scattering process are given by:

$$G^{\mathrm{str}}_{iL,jL'}(E) = g^{\mathrm{str}}_{iL,jL'}(E) + \sum_{kL''} g^{\mathrm{str}}_{iL,kL''}(E) t_{l''}(E) G^{\mathrm{str}}_{kL'',jL'}(E) \quad , \tag{3.51}$$

where $t_l(E)$ is the single-site t–matrix of Eq. (3.43). In practice, we exploit via Fourier transformation the translational periodicity to solve the above equation in reciprocal space:

$$G_{L,L'}(\mathbf{k}, E) = g^{\mathrm{str}}_{L,L'}(\mathbf{k}, E) + \sum_{L''} g^{\mathrm{str}}_{L,L''}(\mathbf{k}, E) t_{l''}(E) G^{\mathrm{str}}_{L'',L'}(\mathbf{k}, E) \quad . \tag{3.52}$$

For layered systems, instead of using directly a free-electron system as the reference to construct the full Green function, one can use a constant muffin-tin repulsive potential as the reference system. This yields sparse the matrix that needs to be inverted to obtain the t–matrix. Hence, this process can be made to scale linearly with the number of atoms [73].

Energy integration

Within the Green function KKR method, to reduce the computational costs, we perform energy integrations such as in Eq. (3.28) by dividing the integration interval into two parts:

$$\int_{-\infty}^{E_\mathrm{F}} \mathrm{d}E = \sum_{\text{core states}} + \int_{E_\mathrm{B}}^{E_\mathrm{F}} \mathrm{d}E \quad . \tag{3.53}$$

This requires to identify an energy E_B that is higher than the energies of the core states but lower than those of the valence states. Furthermore, we explore the analytical continuity properties of the Green function. Thus, we perform the integration through an energy contour integration in the complex plane instead of sticking to the real axis [72]. This helps to improve the accuracy of the calculation because the Green function is smoother away from the real axis.

3.3.5 Full potential

We can go beyond the atomic sphere approximation, where the Kohn-Sham potential of each site is regarded as spherically symmetric and confined to the muffin-tin sphere. In the full-potential treatment [69, 70], we divide the space through the Voronoi construction. Now, we also introduce a step-function for each site i, such that

$$\Theta_i(\mathbf{x}) = \begin{cases} 1 & \text{for } \mathbf{x} \text{ in the Voronoi cell } i \ , \\ 0 & \text{otherwise} \quad , \end{cases} \tag{3.54}$$

which we refer to as shape-function, that allows us to write a continuous description of the crystal potential

$$V_i(\mathbf{x}) = V(\mathbf{x} + \mathbf{R}_i)\Theta_i(\mathbf{x}) \quad . \tag{3.55}$$

The shape-function can also be expressed in terms of spherical harmonics:

$$\Theta_i(\mathbf{x}) = \sum_L \Theta_{iL}(x) Y_L(\mathbf{x}) \quad . \tag{3.56}$$

The expansion of the Green function in the full-potential case follows procedures similar to those discussed before. We also subdivide the on-site problem into spherical and nonspherical parts. Furthermore, we can treat the nonspherical contribution as a perturbation because it is usually small compared to the spherical part. Thus, we first obtain the solutions for the spherical potential, then we calculate the whole on-site Green function through the Lippmann-Schwinger equation, for example.

3.3.6 Spin-orbit coupling

As discussed in Sec. 2.1.5, a very important relativist effect in magnetism is the coupling between the spin and orbital angular momenta of the electrons, which in the nonrelativistic limit, $v \ll c$, can be described by the following Hamiltonian:

$$\mathcal{H}_{\mathrm{SOC}} = V_{\mathrm{SOC}} = \frac{1}{M(r)^2 c^2}\left(\frac{1}{r}\frac{\mathrm{d}V(r)}{\mathrm{d}r}\right)\mathbf{L}\cdot\mathbf{S} \quad , \tag{3.57}$$

where c is the speed of light in vacuum. $V(r)$ refer to the Kohn-Sham potential, as it depends on the derivate of the potential, one expect it to be stronger the closer the electrons are to the nuclei. The second consequence is that the SOC scales with the nuclei charges, hence, it becomes more prominent for heavy elements. The relativistic mass $M(r)$ is given by

$$M(r) = \frac{1}{2} + \frac{E - V(r)}{2c^2} \quad . \tag{3.58}$$

We consider the SOC as an addition to the Hamiltonian, therefore, the total potential that goes into the Schrödinger equation can be decomposed as

$$V^{tot} = \begin{pmatrix} V^{\uparrow\uparrow} & 0 \\ 0 & V^{\downarrow\downarrow} \end{pmatrix} + \begin{pmatrix} V^{\uparrow\uparrow}_{\mathrm{SOC}} & V^{\uparrow\downarrow}_{\mathrm{SOC}} \\ V^{\downarrow\uparrow}_{\mathrm{SOC}} & V^{\downarrow\downarrow}_{\mathrm{SOC}} \end{pmatrix} \quad . \tag{3.59}$$

This means that SOC couples the two spin channels, and, in contrast to what we have been doing so far, we need to explicitly take the spin into account.

To determine SOC potential, we need to calculate the prefactor in Eq. (3.57), which involves a derivative of the potential. To improve the derivative accuracy, we can split the potential into a contribution from the nucleus charge Z, which has an analytical form $-2Z/r$, and the electronic contribution:

$$\frac{\partial V(r)}{\partial r} = \frac{2Z}{r^2} + \frac{\partial V^e(r)}{\partial r} \quad . \tag{3.60}$$

The electrons contribution to the potential, which consists of the Hartree and exchange-correlation terms, is differentiated numerically.

Because the single-site solutions are expanded in real spherical harmonics, it is also convenient to expand $\mathbf{L}\cdot\mathbf{S}$ on the same basis. The SOC potential can be written as

$$V^{2\times2}_{\mathrm{SOC}} = -\frac{1}{M(r)^2 c^2}\left(\frac{1}{r}\frac{\mathrm{d}V(r)}{\mathrm{d}r}\right)\begin{pmatrix} L^z & L^- \\ L^+ & -L^z \end{pmatrix} \quad , \tag{3.61}$$

where $L^{\pm}$ are the ladder operators $L^{\pm} = L^x \pm \mathrm{i}L^y$, which can be easily decomposed in terms of complex spherical harmonics $\mathcal{Y}_{lm}$ because we know how the operators act on them:

$$L^z\,|\mathcal{Y}_{lm}\rangle = m\,|\mathcal{Y}_{lm}\rangle \quad , \quad L^{\pm}\,|\mathcal{Y}_{lm}\rangle = \sqrt{l(l+1) - m(m\pm1)}\,|\mathcal{Y}_{lm}\rangle \quad . \tag{3.62}$$

Finally, one needs to transform the complex spherical harmonics into real ones. Once, we have the SOC potential, it can be treated as a perturbation potential from which the total Green function is obtained by solving the Dyson and Lippmann-Schwinger equations as explained previously. More details can be found in Ref. [70, 75].

3.3.7 KKR self-consistent cycle

To conclude this introduction to the Green function KKR method, let us have a look at the steps required for a practical implementation of the Green function KKR method [69]:

1. We start by determining the Voronoi cells centered around the atoms. For surface calculations, the vacuum regions in touch with the material are also split into Voronoi cells just if they were atomic layers.

2. An initial potential V^{ini} is chosen. For bulk calculations, often we use potential previously computed for isolated atoms. For a thin film, the converged potential for a corresponding bulk material could be used.

3. Solving the single-site problem for each cell, to obtain R_l and t_l using Eqs. (3.41) and (3.43).

4. Setting up the reference system $g^{\text{str}}_{L,L'}$ through Eq. (3.46).

5. Solving the Dyson equation in Eq. (3.52) and integrating over the k–space to obtain the real-space Green function and therefore the on-site elements $G_{ii}(E)$, which are required to compute the charge density.

6. Performing the energy contour integration to obtain the charge density.

7. Determining the new potential V^{out} by solving the Poisson's equation and computing the exchange-correlation potential V_{xc}.

8. Comparing the initial and final potential. If they differ more than a set tolerance, mix V^{ini} and V^{out} then do all the steps again from item 3.

3.4 Parametrization of the Heisenberg model

The generalized Heisenberg Hamiltonian, introduced in Sec. 2.1.6, provides a seemingly simplified description of the magnetism for materials with localized magnetic moments:

$$\mathcal{H} = -\frac{1}{2}\sum_{ij} J_{ij}\,\mathbf{S}_i \cdot \mathbf{S}_j - \frac{1}{2}\sum_{ij} \mathbf{D}_{ij} \cdot (\mathbf{S}_i \times \mathbf{S}_j) - \sum_i \mathbf{B} \cdot \mathbf{S}_i - \sum_\alpha K^\alpha \sum_i (S_i^\alpha)^2 \quad . \tag{3.63}$$

The four terms are: the magnetic exchange interaction (MEI) with parameter J_{ij}; the Dzyaloshinskii-Moriya interaction (DMI) with vector parameter $\mathbf{D}_{ij}$; the Zeeman coupling to an external magnetic field $\mathbf{B}$; and the uniaxial magnetocrystalline anisotropies (MCA) whose parameters are K^α.

The simplest term is the Zeeman energy, that couples an external magnetic field to the spin moments. It requires the determination of the net magnetic moment in each site. Also, as this magnetic moment can be composed of orbital and spin angular momentum, the proper g-factor would have to be determined. In this thesis, however, we only consider magnetic moment from the spins and so, $g = 2$.

In the rest of this section, we aim at obtaining MEI and DMI parameters from the Green function KKR method, which we described in the previous sections, as well as the magnetocrystalline anisotropy. The Hamiltonian is treated as classical.

3.4.1 Infinitesimal-rotations method for the MEI and DMI

Let us start with the magnetic exchange interaction. Taking only the MEI into consideration, the Hamiltonian reads

$$\mathcal{H}_{\mathrm{MEI}} = -\frac{1}{2}\sum_{ij} J_{ij}\,\mathbf{S}_i \cdot \mathbf{S}_j \quad , \tag{3.64}$$

where the spins are classical vectors and for simplification, we take $S_i = 1$. In the following, we discuss two methods to calculate the magnetic exchange parameter J_{ij}.

Energy difference between states with local spin flips

The first method is based on computing the total energy difference when one or more spins are flipped locally. Consider that the system is described by the Hamiltonian in Eq. (3.64) and that it has a ferromagnetic ground state. In that state, the system has total energy given by

$$E_{\mathrm{GS}} = E_{\mathrm{FM}} + C \quad , \tag{3.65}$$

where $E_{\mathrm{FM}} = -\frac{1}{2}\sum_{ij} J_{ij}$ is the energy due to the magnetic interactions and C accounts for all the nonmagnetic contribution to the energy. If we flip the spin in site i, the total energy changes to

$$E_i = E_{\mathrm{GS}} + 2\left(\frac{1}{2}\sum_j J_{ij} + \frac{1}{2}\sum_j J_{ji}\right) = E_{\mathrm{GS}} + 2J_i \quad , \tag{3.66}$$

where we used that the symmetry properties of the MEI, $J_{ij} = J_{ji}$, and we also defined $J_i = \sum_j J_{ij}$. Similarly, we construct another state by flipping two spins, one in site i and another in site j, whose total energy reads

$$E_{ij} = E_{\mathrm{GS}} + 2J_i + 2J_j - 4J_{ij} \quad . \tag{3.67}$$

Isolating J_{ij}, we obtain that the MEI coupling between sites i and j is given by:

$$J_{ij} = \frac{1}{4}\big(-E_{\mathrm{GS}} + E_i + E_j - E_{ij}\big) \quad . \tag{3.68}$$

To evaluate the expression in Eq. (3.68), one needs to compute the total energy of four configurations: the ground state; the state with the i–th spin flipped; the one with the j–th spin flipped; and the state with both, the i–th and j-th spins simultaneously flipped. This method can also be used for magnetic ground states other than the ferromagnetic, and it is mostly suitable for confined systems, such as magnetic molecules. For periodic systems, such as crystals, it would require an *ab initio* scheme where one can flip a single spin in real space, which is most of the

time a nontrivial task. If the interactions are very short-ranged, however, one can overcome this drawback by using supercells.

The current method requires determining the total energy of the system accurately because the energy variation due to the flip of one or two spins might be small in comparison with the total energy of the ground state. Also, this approach assumes that the magnetic exchange parameter does not change from one magnetic configuration to the other. This assumption is not very severe for magnetic insulators, where the exchange parameter seems mostly constant for various magnetic configurations [21, 76]. However, if this assumption is not satisfied, we must find other means through which we can compute the J_{ij} parameters.

Infinitesimal-rotations method

The expansion of the energy up to second-order on the small deviations of the spins have the form of the Heisenberg Hamiltonian. Thus, strictly speaking, the Hamiltonian in Eq. (3.64) is valid to describe the system's dynamics that only involve small deviations from its ground state. Therefore, the parametrization of the model ideally should satisfy these restrictions too. In this context, Liechtenstein *et al.* [21] proposed computing J_{ij} from the total energy difference caused by *infinitesimal rotations* of the spin moments from their ground-state orientations. This would, therefore, respect the validity regime of the model Hamiltonian. Nevertheless, this approach would still suffer from the problem of needing the determination of the total energy with high accuracy.

The issue was solved using Andersen's *magnetic force theorem* [77, 78], which approximates the change in the total energy by the corresponding change of the one-particle energies:

$$\delta E = \int_{-\infty}^{E_\mathrm{F}} (E - E_\mathrm{F}) \delta n(E) \, \mathrm{d}E = - \int_{-\infty}^{E_\mathrm{F}} \delta N(E) \, \mathrm{d}E \quad , \tag{3.69}$$

where $n(E) = \frac{\mathrm{d}N}{\mathrm{d}E}$ is the density of states, and $N(E)$ is the number of electronic states with energy smaller or equal to E. Next, the one-particle energy variation is associated with the system's t-matrix via Lloyd's formula [79]:

$$N(E) = N_0(E) + \frac{1}{\pi} \mathrm{Im Tr} \ln \mathbf{T}(E) \quad , \tag{3.70}$$

where the scattering path operator $\mathbf{T}$ whose inverse is given by

$$(\mathbf{T}^{-1})^{ij}_{L\sigma,L'\sigma'} = t^{-1}_{iL\sigma\sigma'} \delta_{ij} \delta_{LL'} \delta_{LL'} - G^{ij}_{LL'} \delta_{\sigma\sigma'} \quad , \tag{3.71}$$

and t is the single-site t-matrix and G is the Green function. In the final result, one connects directly the MEI parameters to the nonrelativistic KKR Green functions:

$$J_{ij} = \frac{1}{4\pi} \int^{E_\mathrm{F}} \mathrm{Im Tr}_L \Big[\Delta^i(E) G^{ij}_\uparrow \Delta^j(E) G^{ji}_\downarrow(E) \Big] \mathrm{d}E \quad , \tag{3.72}$$

where $\Delta^i = t^i_\uparrow - t^i_\downarrow$ is the difference between the spin up and down channels of the t-matrix on site i. The expression in Eq. (3.72) is known as the Liechtenstein-Katsnelson-Antropov-Gubanov formula or, for short, the LKAG formula.

Relativistic effects

As discussed in Sec. 2.1.5, relativistic effects are important for a system without inversion symmetry, such as in layered systems and interfaces. In the relativistic framework, the Hamiltonian in Eq. (3.64) is no longer valid since the invariance under a global rotation of the spins is lost. Thus, Udvardi *et al.* [22] proposed an extension of the work by Liechtenstein *et al.* [21] by mapping the energy change due to the infinitesimal rotations to a fully relativistic KKR method.

The first-principles results are then mapped on a classical spin Hamiltonian [63]:

$$\mathcal{H} = -\frac{1}{2}\sum_{ij} \mathbf{S}_i^{\mathrm{T}} \mathcal{J}_{ij} \mathbf{S}_j - \sum_i K(\mathbf{S}_i) \quad , \tag{3.73}$$

where $\mathcal{J}_{ij}$ is a 3×3 inter-site interaction matrix and $\mathbf{S}_i$ is regarded as a column unit vector. The second term corresponds to the on-site magnetic anisotropy. The interaction matrix can be decomposed as

$$\mathcal{J}_{ij} = J_{ij}\mathbb{1} + \mathcal{J}_{ij}^{\mathrm{S}} + \mathcal{J}_{ij}^{\mathrm{A}} \quad , \tag{3.74}$$

where $\mathbb{1}$ is the identity matrix, the isotropic MEI is given by

$$J_{ij} = \frac{1}{3}\mathrm{Tr}\mathcal{J}_{ij} \quad , \tag{3.75}$$

and the symmetric and antisymmetric parts of $\mathcal{J}_{ij}$ are defined by

$$\begin{aligned} \mathcal{J}_{ij}^{\mathrm{A}} =& \frac{1}{2}\big(\mathcal{J}_{ij} - \mathcal{J}_{ij}^{\mathrm{T}}\big) \quad , \\ \mathcal{J}_{ij}^{\mathrm{S}} =& \frac{1}{2}\big(\mathcal{J}_{ij} + \mathcal{J}_{ij}^{\mathrm{T}}\big) - J_{ij}\mathbb{1} \quad , \end{aligned} \tag{3.76}$$

where $\mathcal{J}_{ij}^{\mathrm{T}}$ is the transpose of $\mathcal{J}_{ij}$.

The antisymmetric contribution to the interaction matrix corresponds to the Dzyaloshinskii-Moriya interaction, which can be shown to map onto

$$\mathcal{H}_{\mathrm{DMI}} = -\frac{1}{2}\sum_{ij} \mathbf{D}_{ij} \cdot \mathbf{S}_i \times \mathbf{S}_j \quad , \tag{3.77}$$

where the DMI vector components are given by

$$D_{ij}^x = \frac{1}{2}\big(\mathcal{J}_{ij}^{yz} - \mathcal{J}_{ij}^{zy}\big) \quad , \quad D_{ij}^y = \frac{1}{2}\big(\mathcal{J}_{ij}^{xz} - \mathcal{J}_{ij}^{zx}\big) \quad , \quad D_{ij}^z = \frac{1}{2}\big(\mathcal{J}_{ij}^{xy} - \mathcal{J}_{ij}^{yx}\big) \quad . \tag{3.78}$$

Finally, the symmetric traceless contribution $\mathcal{J}_{ij}^{\mathrm{S}}$ corresponds to an anisotropic exchange interaction. In particular, the on-site term $\mathbf{S}_i^{\mathrm{T}} \mathcal{J}_{ii} \mathbf{S}_i$ contains only the symmetric contribution, which can be added as a second-order contribution to the magnetic anisotropy $K(\mathbf{S}_i)$ [22]. It turns out that $\mathcal{J}_{ij}^{\mathrm{S}}$ is generally small, and therefore, we do not consider its effect in the present work.

In practice, to access all the elements of the interaction matrix, one needs to perform the calculation with the magnetization aligned along three orthogonal directions, e.g. x, y and z.

Magnetocrystalline anisotropy - MCA

For each magnetization-rotated direction, x, y, and z, we compute the total energy of the system, which then gives us their energy differences:

$$\begin{aligned} E^{xy} &= E^{y} - E^{x} \quad , \\ E^{yz} &= E^{z} - E^{y} \quad , \\ E^{zx} &= E^{x} - E^{z} \quad . \end{aligned} \tag{3.79}$$

These energy difference are used to parametrize the MCA axes. Imagine that the system has a single MCA axis along z, then

$$K^{z} = E^{zx} = -E^{yz} \quad . \tag{3.80}$$

and $E^{xy} = 0$. In case of two axes, let say along x and y, we have

$$\begin{aligned} K^{x} &= -E^{zx} \quad , \\ K^{y} &= E^{yz} \quad . \end{aligned} \tag{3.81}$$

The signs were chosen such that a positive value of K corresponds to an easy-axis, and a negative value to an easy-plane. At using this method to compute the MCA parameters, one should have in mind that these energy differences are very small in comparison to the total energy, which makes it a numerical challenge.

3.5 Conclusions

In this chapter, we introduced the density functional theory to describe quantum mechanically the electronic and magnetic properties of materials. In particular, we discussed the Korringa-Kohn-Rostoker method [61], which is based on a multiple-scattering theory to evaluate the physical properties of materials in terms of their Green functions. Finally, we discussed how this *ab initio* method allows us to parametrize the Heisenberg Hamiltonian through the infinitesimal-rotations method introduced by Liechtenstein *et al.* [21], and extended by Udvardi *et al.* [22] to account for relativist effects. Within this approach, we can obtain the parameters for the magnetic exchange interaction, Dzyaloshinskii-Moriya interaction, and the magnetocrystalline anisotropy. Together, these tools give us the potential of describing and predicting material and system-specific properties, including their spin waves. The first-principles parametrization scheme described in this chapter will be used to study, thin films of Co/W(110) in Chapters 5 and 8, and a thin film of Mn/β-W and bulk Mn_5Si_3 in Chapter 7.

Chapter 4

Inelastic-scattering theory

We saw in Chapter 2 that, in the adiabatic approximation, spin waves are the excited states of a spin system described the Heisenberg Hamiltonian. The energies of these excitations define the system's intrinsic spin-excitation spectrum. When experimentally probing the spin waves of a material, one should have in mind that the observed data results not only from the intrinsic spin-wave properties but also from the nature and properties of the probe. In this chapter, we connect the adiabatic spin-wave spectrum of a noncollinear magnet to the inelastic-scattering spectrum of probing particles, such as electrons and neutrons. We derive an expression for the particle's inelastic-scattering rate, which is a quantity that can be measured experimentally. The theoretical framework is described in the first section, where we calculate the transition rate using the time-dependent perturbation theory. In the second section, we apply this theory for noncollinear magnets utilizing the spin-wave eigenvalues and eigenfunctions obtained as described in Chapter 2. This chapter is also based on Ref. [26] written by the author of this dissertation.

4.1 Scattering theory

Scattering experiments have been essential to physics, e.g., they have led us to the discovery of the atoms and their constituents. These experiments can be performed using the scattering of light and other projectiles, such as neutrons and electrons, determining crystal, electronic and magnetic properties of materials, and in particular, their excitations [80–83]. Probing spin waves with light is restricted to the very-short-wavevector regime, such as in Brillouin-light-scattering spectroscopy [84]. Electrons and neutrons, however, are suitable to probe spin waves throughout large areas of the reciprocal space. Spin waves of large wavevectors are dominated by magnetic exchange mechanisms, which are this thesis's subject of interest. While neutrons are employed to study bulk materials, electrons are the candidate of choice for surface and thin films because of their large scattering cross-section and small penetration length [17, 18].

4.1.1 General framework

A complete theory of particle diffraction from a magnetic material is highly involved, in particular for electrons whose electric charge yields a strong interaction with the

sample [85, 86]. As our interest is in the inelastic signal of magnetic origin, we simplify the problem by treating the material as composed of localized spins in the ground state, which interact locally with the particle's spin-$\frac{1}{2}$ via an exchange coupling. For disregarding the electric-charge effects, for example, we can treat neutrons and electrons on an equal footing. Nevertheless, in the rest of this chapter, we use electrons as our prototypical particle.

We split the Hamiltonian of the problem into the following parts:

$$\begin{aligned}\mathcal{H}_{\mathrm{e}} =& \frac{\mathbf{p}^2}{2m_{\mathrm{e}}} \quad , \\ \mathcal{H}_{\mathrm{m}} =& -\frac{1}{2}\sum_{mn}\sum_{\alpha\beta} S_m^\alpha J_{mn}^{\alpha\beta} S_n^\beta - \sum_n \sum_\alpha B_n^\alpha S_n^\alpha \quad , \\ \mathcal{H}_{\mathrm{em}} =& \sum_n \sum_\alpha U_n\, \delta(\mathbf{r}-\mathbf{R}_n)\, \sigma^\alpha S_n^\alpha \quad .\end{aligned} \tag{4.1}$$

The electron beam is described by the free-electron Hamiltonian $\mathcal{H}_{\mathrm{e}}$, with $\mathbf{p}$ the linear momentum operator and m_{e} the electron mass. The magnetic lattice is described by the generalized Heisenberg Hamiltonian $\mathcal{H}_{\mathrm{m}}$, as introduced in Eq. (2.61), with S_n^α being the α-component of the atomic spin operator for site n, $J_{mn}^{\alpha\beta}$ the elements of the tensor describing the pairwise interactions between sites m and n, and B_n^α the α-component of the magnetic field acting on site n. The coupling between the atomic spins and the spin of the probing electrons is described by $\mathcal{H}_{\mathrm{em}}$, with U_n the interaction strength, $\mathbf{r}$ the position operator for the electrons, $\mathbf{R}_n$ the position vector for site n, and σ^α the Pauli matrix for the α-component of the electron spin.

Next, we assume that the probing electrons and the magnetic sample are decoupled for times $t < 0$. Then, we can specify the initial state of the electron beam as consisting of a plane-wave with well-defined energy E_i, wavevector $\mathbf{k}_i$, and spin s_i:

$$\langle \mathbf{r}|\mathbf{k}_i s_i\rangle = e^{\mathrm{i}\mathbf{k}_i\cdot\mathbf{r}}\,|s_i\rangle \quad , \qquad E_i = \frac{\mathbf{k}_i^2}{2m} \quad , \qquad |s_i\rangle\langle s_i| = \frac{1}{2}\left(\sigma^0 + \mathbf{n}_i\cdot\boldsymbol{\sigma}\right) \quad . \tag{4.2}$$

Henceforth $\hbar = 1$. The spinor $|s_i\rangle$ defines the spin polarization of the electron to be along the direction $\mathbf{n}_i$. The eigenstates of the spin Hamiltonian are assumed to be known:

$$\mathcal{H}_{\mathrm{m}}\,|\lambda\rangle = E_\lambda\,|\lambda\rangle \quad , \qquad E_0 \leq E_\lambda \quad . \tag{4.3}$$

Before the interaction with the electron beam, the magnetic sample is in its ground state $|0\rangle$, with energy E_0. The state of the combined system at $t = 0$ is then the tensor product of the two initial states:

$$|i\rangle \equiv |\mathbf{k}_i s_i 0\rangle = |\mathbf{k}_i s_i\rangle \otimes |0\rangle \quad . \tag{4.4}$$

This state evolves in time under the action of the complete Hamiltonian $\mathcal{H} = \mathcal{H}_{\mathrm{e}} + \mathcal{H}_{\mathrm{m}} + \mathcal{H}_{\mathrm{em}}$, according to the Schrödinger equation,

$$\mathrm{i}\frac{\mathrm{d}}{\mathrm{d}t}\,|\Psi(t)\rangle = \mathcal{H}\,|\Psi(t)\rangle \quad . \tag{4.5}$$

By isolating the interaction term, the total Hamiltonian can be split as $\mathcal{H} = \mathcal{H}_0 + \mathcal{H}_{\mathrm{em}}$, with $\mathcal{H}_0 = \mathcal{H}_{\mathrm{e}} + \mathcal{H}_{\mathrm{m}}$. We can then introduce the time evolution operator,

which connects the system's state at a later time t to the initial state $|i\rangle = |\Psi(0)\rangle$, in the following form:

$$|\Psi(t)\rangle = e^{-\mathrm{i}\mathcal{H}_0 t}\,\mathcal{U}(t)\,|i\rangle \quad , \tag{4.6}$$

where

$$\mathcal{U}(t) = 1 - \mathrm{i}\int_0^t \mathrm{d}t_1\;\mathcal{H}_{\rm em}(t_1)\,\mathcal{U}(t_1) \quad , \quad \text{and} \quad \mathcal{H}_{\rm em}(t) = e^{\mathrm{i}\mathcal{H}_0 t}\,\mathcal{H}_{\rm em}\,e^{-\mathrm{i}\mathcal{H}_0 t} \quad . \tag{4.7}$$

This integral equation follows directly from the Schrödinger equation. Note that $\mathcal{U}(t)$ appears on both sides of the integral equation. Replacing it into itself iteratively, we find

$$\begin{aligned}\mathcal{U}(t) =& 1 - \mathrm{i}\int_0^t \mathrm{d}t_1\;\mathcal{H}_{\rm em}(t_1) + (-\mathrm{i})^2\int_0^t \mathrm{d}t_1\int_0^{t_1}\mathrm{d}t_2\;\mathcal{H}_{\rm em}(t_1)\,\mathcal{H}_{\rm em}(t_2) + \ldots \\ =& 1 + \mathcal{U}_1(t) + \mathcal{U}_2(t) + \ldots\end{aligned} \tag{4.8}$$

This expansion corresponds to performing time-dependent perturbation theory in $\mathcal{H}_{\rm em}$.

4.1.2 Transition probability

The probability of finding the system at a later time in some final state $|f\rangle = |\mathbf{k}_f s_f \lambda\rangle$, up to second order in $\mathcal{H}_{\rm em}$, is given by

$$\begin{aligned}P(i\to f,t) &= \big|\langle f|\Psi(t)\rangle\big|^2 \\ &= \langle i|\,\mathcal{U}^\dagger(t)|f\rangle\langle f|\,\mathcal{U}(t)|i\rangle \\ &\approx P_0(i\to f,t) + P_1(i\to f,t) + P_2(i\to f,t) \quad ,\end{aligned} \tag{4.9}$$

where $P_n(i\to f,t)$ is the transition-probability contribution of n-th order:

$$\begin{aligned}P_0(i\to f,t) =& \big|\langle f|i\rangle\big|^2 \quad , \\ P_1(i\to f,t) =& \langle i|f\rangle\langle f|\,\mathcal{U}_1(t)|i\rangle + \langle i|\,\mathcal{U}_1^\dagger(t)|f\rangle\langle f|i\rangle \quad , \\ P_2(i\to f,t) =& \langle i|\,\mathcal{U}_1^\dagger(t)|f\rangle\langle f|\,\mathcal{U}_1(t)|i\rangle + \langle i|f\rangle\langle f|\,\mathcal{U}_2(t)|i\rangle + \langle i|\,\mathcal{U}_2^\dagger(t)|f\rangle\langle f|i\rangle \quad .\end{aligned} \tag{4.10}$$

The above probabilities must satisfy conservation of probability law

$$\sum_f P(i\to f,t) = 1 \quad . \tag{4.11}$$

For example, if $\sum_f P_0(i\to f,t) = 1$ then $\sum_f P_n(i\to f,t) = 0$ for $n > 0$. The transition amplitudes in Eq. (4.10) are

$$\langle f|\,\mathcal{U}_1(t)|i\rangle = -\mathrm{i}\int_0^t \mathrm{d}t_1\,\langle f|e^{\mathrm{i}\mathcal{H}_0 t_1}\,\mathcal{H}_{\rm em}\,e^{-\mathrm{i}\mathcal{H}_0 t_1}|i\rangle = \frac{1-e^{\mathrm{i}E_{fi}t}}{E_{fi}}\,\langle f|\mathcal{H}_{\rm em}|i\rangle \quad , \tag{4.12}$$

$$\begin{aligned}\langle f|\,\mathcal{U}_2(t)|i\rangle &= -\sum_v\int_0^t \mathrm{d}t_1\int_0^{t_1}\mathrm{d}t_2\,\langle f|e^{\mathrm{i}\mathcal{H}_0 t_1}\,\mathcal{H}_{\rm em}|v\rangle\langle v|e^{-\mathrm{i}\mathcal{H}_0(t_1-t_2)}\,\mathcal{H}_{\rm em}\,e^{-\mathrm{i}\mathcal{H}_0 t_2}|i\rangle \\ &= \sum_v\left(\frac{e^{\mathrm{i}E_{fi}t}-1}{E_{fi}\,E_{vi}} - \frac{e^{\mathrm{i}E_{fv}t}-1}{E_{fv}\,E_{vi}}\right)\langle f|\mathcal{H}_{\rm em}|v\rangle\langle v|\mathcal{H}_{\rm em}|i\rangle \quad ,\end{aligned} \tag{4.13}$$

where $E_{ab} = E_a - E_b$. A complete set of (virtual) states was introduced for the second-order amplitude.

4.1.3 Scattering rate

A scattering experiment measures the flux of particles per energy and per solid angle that is coming out of the sample. This outgoing flux normalized by the incoming flux is called the *differential scattering cross section*, which is proportional to the *scattering rate* given by the time derivative of the transition probability:

$$\frac{\mathrm{d}\sigma}{\mathrm{d}\omega\,\mathrm{d}\Omega} \propto \Gamma(i\to f,t) = \frac{\mathrm{d}P(i\to f,t)}{\mathrm{d}t} \quad , \tag{4.14}$$

where ω represents the energy transfered by the probing electron, see Chapter 13: *Inelastic Scattering from Phonons* of Ref. [87]. Let us now analyze the scattering rate attributed to each contribution of the transition probability given by Eq. (4.9). The transition probability of zeroth-order is only nonvanishing if the final state has a finite overlap with the initial state. As $|f\rangle = |\mathbf{k}_f s_f \lambda\rangle$, this requires $\mathbf{k}_f = \mathbf{k}_i$ and $\lambda = 0$. Therefore, it corresponds to an elastic scattering: $E_{fi} = 0$. The spinors give, see Eq. (4.2),

$$P_0(i\to f,t) = |\langle s_f|s_i\rangle|^2 = \frac{1}{4}\,\mathrm{Tr}\,(\sigma^0 + \mathbf{n}_i\cdot\boldsymbol{\sigma})\,(\sigma^0 + \mathbf{n}_f\cdot\boldsymbol{\sigma}) = \frac{1}{2}\,(1+\mathbf{n}_i\cdot\mathbf{n}_f) \quad . \tag{4.15}$$

This means that measuring the spin component of the outgoing electron with a spin detector which is not aligned with the polarization of the incident electron beam then leads to a cosine dependence on the angle between them. Nevertheless, this transition-probability contribution is time-independent yielding to a zero transition rate.

The first-order contribution to the transition probability is

$$P_1(i\to f,t) = \frac{1-e^{\mathrm{i}E_{fi}t}}{E_{fi}}\,\langle i|f\rangle\langle f|\mathcal{H}_{\mathrm{em}}|i\rangle + \frac{1-e^{-\mathrm{i}E_{fi}t}}{E_{fi}}\,\langle i|\mathcal{H}_{\mathrm{em}}|f\rangle\langle f|i\rangle \quad , \tag{4.16}$$

and it also corresponds to an elastic process because, again, $\langle f|i\rangle$ must be finite, so $E_{fi}\to 0$. The respective scattering rate is given by

$$\begin{aligned}\Gamma_1(i\to f,t) &= \frac{\mathrm{d}P_1}{\mathrm{d}t}(i\to f,t)\\ &= -\mathrm{i}\left(\langle s_i|s_f\rangle\langle \mathbf{k}_i s_f 0|\mathcal{H}_{\mathrm{em}}|\mathbf{k}_i s_i 0\rangle - \langle \mathbf{k}_i s_i 0|\mathcal{H}_{\mathrm{em}}|\mathbf{k}_i s_f 0\rangle\langle s_f|s_i\rangle\right)\\ &= \sum_n U_n\,\langle 0|\mathbf{S}_n|0\rangle\cdot(\mathbf{n}_i\times\mathbf{n}_f) \quad .\end{aligned} \tag{4.17}$$

Its detection requires a crossed setup: the polarization of the outgoing electron must be measured along a direction perpendicular to the polarization of the incident beam, yielding information about the component of the magnetization of the sample perpendicular to those two axes.

The second-order contribution is the most interesting one, as it describes inelastic scattering, therefore, giving us access to the excited states (spin waves) of the system. As seen in Eq. (4.10), it has two contributions. The first contribution to the transition probability is

$$P_{2,1}(i\to f,t) = \langle i|\,\mathcal{U}_1^\dagger(t)|f\rangle\langle f|\,\mathcal{U}_1(t)|i\rangle = 2\,\frac{1-\cos(E_{fi}t)}{(E_{fi})^2}\,|\langle f|\mathcal{H}_{\mathrm{em}}|i\rangle|^2 \quad , \tag{4.18}$$

with the scattering rate

$$\Gamma_{2,1}(i\to f,t) = 2\,\frac{\sin(E_{fi}t)}{E_{fi}}\,|\langle f|\mathcal{H}_{\rm em}|i\rangle|^2 \underset{t\to\infty}{=} 2\pi\,\delta(E_{fi})\,|\langle f|\mathcal{H}_{\rm em}|i\rangle|^2 \quad . \tag{4.19}$$

This is the familiar Fermi's Golden Rule. The delta function imposes energy conservation:

$$0 = E_{fi} = \left(E_\lambda + \frac{\mathbf{k}_f^2}{2m}\right) - \left(E_0 + \frac{\mathbf{k}_i^2}{2m}\right) = E_\lambda - E_0 - \omega \quad , \tag{4.20}$$

with $\omega = \left(\frac{\mathbf{k}_f^2}{2m} - \frac{\mathbf{k}_i^2}{2m}\right) = E_\lambda - E_0$ the energy transferred from the electron beam to the magnetic sample. Likewise, we can define $\mathbf{q} = \mathbf{k}_i - \mathbf{k}_f$ as the momentum transferred to the magnetic sample.

The second part in the second-order contribution to the transition probability is given by

$$\begin{aligned} P_{2,2}(i\to f,t) = &\sum_v \left(\frac{e^{{\rm i}E_{fi}t}-1}{E_{fi}\,E_{vi}} - \frac{e^{{\rm i}E_{fv}t}-1}{E_{fv}\,E_{vi}}\right)\langle i|f\rangle\langle f|\mathcal{H}_{\rm em}|v\rangle\langle v|\mathcal{H}_{\rm em}|i\rangle \\ &+ \sum_v \left(\frac{e^{-{\rm i}E_{fi}t}-1}{E_{fi}\,E_{vi}} - \frac{e^{-{\rm i}E_{fv}t}-1}{E_{fv}\,E_{vi}}\right)\langle i|\mathcal{H}_{\rm em}|v\rangle\langle v|\mathcal{H}_{\rm em}|f\rangle\langle f|i\rangle \quad . \end{aligned} \tag{4.21}$$

Due to the presence of the overlap $\langle f|i\rangle$, it contributes only to $\omega = 0$ and $\mathbf{q} = \mathbf{0}$. As we are interested in inelastic scattering, we will not analyze this term further.

4.1.4 Inelastic scattering rate

From the analysis in the previous section, we can define the *inelastic* scattering rate as expected from Fermi's Golden Rule:

$$\Gamma_{if}(\mathbf{q},\omega) = 2\pi \sum_{\lambda\neq 0} \delta(E_\lambda - E_0 - \omega)\;|\langle \mathbf{k}_f s_f \lambda|\mathcal{H}_{\rm em}|\mathbf{k}_i s_i 0\rangle|^2 \quad , \tag{4.22}$$

with ω and $\mathbf{q}$ the energy and momentum transferred from the electron beam to the magnetic sample.

We assume that the ground state of the magnetic sample is commensurate with the atomic lattice. Then we can separate the position vector of every magnetic atom as $\mathbf{R}_{n\nu} = \mathbf{R}_n + \mathbf{R}_\nu$, letting $\mathbf{R}_n$ label the origin of the n-th magnetic unit cell, and $\mathbf{R}_\nu$ the basis vector inside the magnetic unit cell. The coupling Hamiltonian is assumed to have the translational symmetry of the magnetic unit cell, so

$$\mathcal{H}_{\rm em} = \sum_{n\nu} U_\nu\,\delta(\mathbf{r} - \mathbf{R}_{n\nu})\,\boldsymbol{\sigma}\cdot\mathbf{S}_{n\nu} \quad . \tag{4.23}$$

If the magnetic atoms are chemically distinct, their coupling strength might be atom-dependent, hence U_ν. The matrix elements are then

$$\langle \mathbf{k}_f s_f \lambda|\mathcal{H}_{\rm em}|\mathbf{k}_i s_i 0\rangle = \sum_\beta \langle s_f|\sigma^\beta|s_i\rangle \sum_\nu U_\nu\, e^{{\rm i}\mathbf{q}\cdot\mathbf{R}_\nu}\,\langle\lambda|\sum_n e^{{\rm i}\mathbf{q}\cdot\mathbf{R}_n} S^\beta_{n\nu}|0\rangle \tag{4.24}$$

$$= \sqrt{N_l}\sum_\beta \langle s_f|\sigma^\beta|s_i\rangle \sum_\nu U_\nu\, e^{{\rm i}\mathbf{q}\cdot\mathbf{R}_\nu}\,\langle\lambda|S^\beta_\nu(\mathbf{q})|0\rangle \quad , \tag{4.25}$$

$$\langle \mathbf{k}_i s_i 0|\mathcal{H}_{\rm em}|\mathbf{k}_f s_f \lambda\rangle = \sum_\alpha \langle s_i|\sigma^\alpha|s_f\rangle \sum_\mu U_\mu\, e^{-\mathrm{i}\mathbf{q}\cdot\mathbf{R}_\mu}\, \langle 0|\sum_n e^{-\mathrm{i}\mathbf{q}\cdot\mathbf{R}_m} S^\alpha_{m\nu}|\lambda\rangle \tag{4.26}$$

$$= \sqrt{N_l} \sum_\alpha \langle s_i|\sigma^\alpha|s_f\rangle \sum_\mu U_\mu\, e^{-\mathrm{i}\mathbf{q}\cdot\mathbf{R}_\mu}\, \langle 0|S^\alpha_\mu(-\mathbf{q})|\lambda\rangle \quad . \tag{4.27}$$

N_l is the number of unit cells under Born-von Karman periodic boundary conditions.

Spin-spin correlation tensor

Putting together the last results, the inelastic scattering rate of Eq. (4.22) can be expressed as

$$\Gamma_{if}(\mathbf{q},\omega) = 2\pi\, N_l\, N_b \sum_{\alpha\beta} \langle s_i|\sigma^\alpha|s_f\rangle\langle s_f|\sigma^\beta|s_i\rangle\, \frac{1}{N_b} \sum_{\mu\nu} U_\mu U_\nu\, e^{\mathrm{i}\mathbf{q}\cdot\mathbf{R}_{\mu\nu}} \mathcal{N}^{\alpha\beta}_{\mu\nu}(\mathbf{q},\omega) \quad , \tag{4.28}$$

with $\mathbf{R}_{\mu\nu} = \mathbf{R}_\nu - \mathbf{R}_\mu$, and N_b is the number of basis atoms in each unit cell, so $N_l N_b$ is the total number of magnetic atoms. And the *spin-spin correlation tensor* was defined as

$$\mathcal{N}^{\alpha\beta}_{\mu\nu}(\mathbf{q},\omega) = \sum_{\lambda\neq 0} \delta(E_\lambda - E_0 - \omega)\, \langle 0|S^\alpha_\mu(-\mathbf{q})|\lambda\rangle\langle\lambda|S^\beta_\nu(\mathbf{q})|0\rangle \quad , \tag{4.29}$$

which has the periodicity of the magnetic lattice, with $\alpha, \beta = x, y, z$ the components of the spin operators, and describes the intrinsic spin excitations of the magnetic sample.

The scattering rate combines the information about the intrinsic spin excitations, contained in $\mathcal{N}^{\alpha\beta}_{\mu\nu}(\mathbf{q},\omega)$, with the information about the spin polarization of the incoming and detected electrons (Pauli matrices) and the wave nature of the electrons, leading to interference between different contributions (the Fourier phase factor).

Polarization tensor

We can find an explicit expression for the dependence of the scattering rate on the electron spin polarization:

$$\begin{aligned} \mathcal{P}^{\alpha\beta}_{if} &= \langle s_i|\sigma^\alpha|s_f\rangle\langle s_f|\sigma^\beta|s_i\rangle \\ &= \frac{1}{4}\,\mathrm{Tr}\left(\sigma^0 + \mathbf{n}_i\cdot\boldsymbol{\sigma}\right)\sigma^\alpha\left(\sigma^0 + \mathbf{n}_f\cdot\boldsymbol{\sigma}\right)\sigma^\beta \\ &= \frac{1}{2}\left(\left(1 - \sum_\gamma n_i^\gamma\, n_f^\gamma\right)\delta_{\alpha\beta} + n_i^\alpha\, n_f^\beta + n_i^\beta\, n_f^\alpha + \mathrm{i}\sum_\gamma \varepsilon_{\alpha\beta\gamma}\left(n_i^\gamma - n_f^\gamma\right)\right) \quad , \end{aligned} \tag{4.30}$$

Here $\delta_{\alpha\beta}$ is the usual Kronecker delta, and $\epsilon_{\alpha\beta\gamma}$ the Levi-Civita symbol. To illustrate, consider the spin polarization of the incoming electrons to be $+z$ or $-z$, and the spin polarization of the outgoing electrons also to be measured along $+z$ or $-z$. We have, therefore, four possible spin channels. To each channel, we associate a polarization tensor $\mathcal{P}^{\alpha\beta}$ that selects the spin components of the magnetic sample that can be

measured:

$$\begin{array}{c|ccc} \mathcal{P}^{++} & x & y & z \\ \hline x & 0 & 0 & 0 \\ y & 0 & 0 & 0 \\ z & 0 & 0 & 1 \end{array} , \quad \begin{array}{c|ccc} \mathcal{P}^{--} & x & y & z \\ \hline x & 0 & 0 & 0 \\ y & 0 & 0 & 0 \\ z & 0 & 0 & 1 \end{array} , \quad \begin{array}{c|ccc} \mathcal{P}^{+-} & x & y & z \\ \hline x & 1 & +\mathrm{i} & 0 \\ y & -\mathrm{i} & 1 & 0 \\ z & 0 & 0 & 0 \end{array} , \quad \begin{array}{c|ccc} \mathcal{P}^{-+} & x & y & z \\ \hline x & 1 & -\mathrm{i} & 0 \\ y & +\mathrm{i} & 1 & 0 \\ z & 0 & 0 & 0 \end{array} . \tag{4.31}$$

We see that $\mathcal{P}^{++}$ and $\mathcal{P}^{--}$ are the same, and connect with $\mathcal{N}^{zz}_{\mu\nu}(\mathbf{q},\omega)$. $\mathcal{P}^{+-}$ connects with $\mathcal{N}^{-+}_{\mu\nu}(\mathbf{q},\omega)$, and $\mathcal{P}^{-+}$ connects with $\mathcal{N}^{+-}_{\mu\nu}(\mathbf{q},\omega)$.

For a ferromagnetic sample with a ground state of total spin along $+z$, only $\mathcal{N}^{+-}_{\mu\nu}(\mathbf{q},\omega)$ is finite. $\mathcal{P}^{-+}$ means that the spin polarization of the incoming electron beam is $-z$, antiparallel to the total spin of the sample. As the outgoing electron is detected with $+z$ spin polarization, the ferromagnetic sample lost $\hbar$ of angular momentum, corresponding to the lowering of the spin associated with the creation of a spin wave. If $\mathcal{N}^{-+}_{\mu\nu}(\mathbf{q},\omega)$ were finite, then the sample would gain $\hbar$ of angular momentum. More intriguingly, a finite $\mathcal{N}^{zz}_{\mu\nu}(\mathbf{q},\omega)$ describes spin excitations with no net exchange of angular momentum between the electron beam and the magnetic sample. More on that will be discussed in Chapter 6.

4.2 Spin-spin correlation tensor for noncollinear magnets

We saw in Chapter 2 that the spin-wave spectrum (dispersion) of noncollinear magnets can be rather dense (see Fig. 2.5). This is especially due to the large unit cell associated with the magnetic structure. To understand what out of the intrinsic spectrum can be actually excited and detected via inelastic electron scattering, we need to calculate the scattering rate, given by Eq. (4.28).

Let us start by defining an excited state $|\lambda\rangle = |\mathbf{k}, r\rangle$ of wavevector $\mathbf{k}$ and mode index r as created by the action of a new boson operator on the ground state $|\tilde{0}\rangle$:

$$b_r^\dagger(\mathbf{k})\,|\tilde{0}\rangle = |\mathbf{k}, r\rangle \quad , \quad b_r(\mathbf{k})\,|\tilde{0}\rangle = 0 \quad \text{and} \quad \langle \mathbf{k}r|\tilde{0}\rangle = 0 \quad , \tag{4.32}$$

such that $|\mathbf{k}, r\rangle$ is an eigenstate of the Hamiltonian:

$$\mathcal{H}_2\,|\mathbf{k}, r\rangle = \epsilon_r(\mathbf{k})\,|\mathbf{k}, r\rangle \quad . \tag{4.33}$$

$\mathcal{H}_2$ is the linearized Hamiltonian given by Eq. (2.126). The relation between the new and the old boson operators is given by the Bogoliubov transformation in Eq. 2.147, which can be rewritten as:

$$a_\mu^\alpha(\mathbf{k}) = \sum_{\beta,r} \mathcal{R}^{\alpha\beta}_{\mu r}(\mathbf{k}) b_r^\beta(\mathbf{k}) \quad , \tag{4.34}$$

where $\alpha, \beta = \pm$ to represents the creation or annihilation operators ($a^+ = a^\dagger$ and $a^- = a$). μ and ν are site indexes within a unit cell. For more details, see Sec. 2.4.2.

To calculate the scattering rate, we need to evaluate the spin-spin correlation tensor:

$$\mathcal{N}^{\alpha\beta}_{\mu\nu}(\mathbf{q},\omega) = \sum_{\mathbf{k}r} \delta\left(E_0 + \omega - E_r(\mathbf{k})\right) \langle\tilde{0}|S^\alpha_\mu(-\mathbf{q})|\mathbf{k}r\rangle \langle \mathbf{k}r|S^\beta_\nu(\mathbf{q})|\tilde{0}\rangle \quad , \tag{4.35}$$

where

$$S_\nu^\beta(\mathbf{q}) = \frac{1}{\sqrt{N_l}} \sum_n e^{i\mathbf{q}\cdot\mathbf{R}_n} S_{n\nu}^\beta \quad . \tag{4.36}$$

We can rewrite the spin operator as:

$$\begin{aligned} S_{n\nu}^\beta =& O_\nu^{\beta+} S'^{+}_{n\nu} + O_\nu^{\beta-} S'^{-}_{n\nu} + O_\nu^{\beta z} S'^{z}_{n\nu} \\ =& O_\nu^{\beta+} \sqrt{2S_\nu} a_{n\nu} + O_\nu^{\beta-} \sqrt{2S_\nu} a^\dagger_{n\nu} + O_\nu^{\beta z}(S_{n\nu} - a^\dagger_{n\nu} a_{n\nu}) \quad , \end{aligned} \tag{4.37}$$

where S'^{α} is the spin operator in the local reference frame related to the global representation via the rotation matrix $O_\nu^{\alpha\beta}$. We obtain that the left matrix element in Eq. (4.35) reads

$$\begin{aligned} \langle \tilde{0}|S_\mu^\alpha(-\mathbf{q})|\mathbf{k}, r\rangle = \frac{1}{\sqrt{N_l}} \sum_n e^{-i\mathbf{q}\cdot\mathbf{R}_n} \times \\ \left(O_\mu^{\alpha+} \sqrt{2S_\mu}\, \langle \tilde{0}|a_{n\mu}|\mathbf{k}, r\rangle + O_\mu^{\alpha-} \sqrt{2S_\mu}\, \langle \tilde{0}|a^\dagger_{n\mu}|\mathbf{k}, r\rangle + O_\mu^{\alpha z}\, \langle \tilde{0}|a^\dagger_{n\mu} a_{n\mu}|\mathbf{k}, r\rangle \right) \quad . \end{aligned} \tag{4.38}$$

Using Eqs. (4.32), (4.34), and the boson commutation relations, the right-hand-side terms of the previous equation are then given by

$$\begin{aligned} \langle \tilde{0}|a_{n\mu}|\mathbf{k}, r\rangle =& \frac{1}{\sqrt{N_l}} e^{i\mathbf{k}\cdot\mathbf{R}_n} \mathcal{R}_{\mu r}^{--} \quad , \\ \langle \tilde{0}|a^\dagger_{n\mu}|\mathbf{k}, r\rangle =& \frac{1}{\sqrt{N_l}} e^{i\mathbf{k}\cdot\mathbf{R}_n} \mathcal{R}_{\mu r}^{+-} \quad , \\ \langle \tilde{0}|a^\dagger_{n\mu} a_{n\mu}|\mathbf{k}, r\rangle =& 0 \quad . \end{aligned} \tag{4.39}$$

Then, Eq. (4.38) becomes:

$$\langle \tilde{0}|S_\mu^\alpha(\mathbf{q})|\mathbf{k}, r\rangle = \sqrt{2S_\mu}\delta(-\mathbf{q}+\mathbf{k}) \left(O_\mu^{\alpha+} \mathcal{R}_{\mu r}^{--}(\mathbf{k}) + O_\mu^{\alpha-} \mathcal{R}_{\mu r}^{+-}(\mathbf{k}) \right) \quad , \tag{4.40}$$

where we used that

$$\delta(\mathbf{q}) = \frac{1}{N_l} \sum_n e^{i\mathbf{q}\cdot\mathbf{R}_n} \quad , \tag{4.41}$$

as demonstrated in Apx. 4.A. In a similar way, we obtain the right matrix element of Eq. (4.35):

$$\langle \mathbf{k}, r|S_\nu^\beta(\mathbf{q})|\tilde{0}\rangle = \sqrt{2S_\nu}\delta(\mathbf{q}-\mathbf{k}) \left(O_\nu^{\beta+} \mathcal{R}_{\nu r}^{-+}(\mathbf{k}) + O_\nu^{\beta-} \mathcal{R}_{\nu r}^{++}(\mathbf{k}) \right) \quad . \tag{4.42}$$

Plugging Eqs. (4.40) and (4.42) back into Eq. (4.35), we finally obtain an expression for the spin-spin correlation tensor in terms of the eigenstates and eigenenergies of the noncollinear spin Hamiltonian:

$$\begin{aligned} \mathcal{N}_{\mu\nu}^{\alpha\beta}(\mathbf{q}, \omega) = 2\sqrt{S_\mu S_\nu} \sum_r \delta\big(E_0 + \omega - E_r(\mathbf{q})\big) \times \\ \left[O_\mu^{\alpha+}(\mathcal{R}_{\mu r}^{++}(\mathbf{q}))^* + O_\mu^{\alpha-}(\mathcal{R}_{\mu r}^{-+}(\mathbf{q}))^* \right] \left[O_\nu^{\beta+} \mathcal{R}_{\nu r}^{-+}(\mathbf{q}) + O_\nu^{\beta-} \mathcal{R}_{\nu r}^{++}(\mathbf{q}) \right] \quad . \end{aligned} \tag{4.43}$$

Also, we need to be able to represent the rotation matrix from the xyz representation into the $+-z$. This is given by the transformation

$$\mathbf{O}^+ = \mathbf{M}'\mathbf{O}\mathbf{M}'^{-1} \quad , \tag{4.44}$$

where

$$\mathbf{M}' = \begin{pmatrix} 1 & i & 0 \\ 1 & -i & 0 \\ 0 & 0 & 1 \end{pmatrix} \quad . \tag{4.45}$$

4.3 Summary

In this chapter, we derived in second-order perturbation theory the inelastic-scattering rate for spin-$\frac{1}{2}$ particle, such as electrons and neutrons, from spin waves in noncollinear magnets. We saw that this rate involves the spin-spin correlation tensor and the polarization tensor. The spin-spin correlation tensor was calculated within the spin-wave adiabatic approximation, which was described in Chapter 2, and it contains information about the intrinsic spin-excitations of the system. Meanwhile, the polarization tensor controls the connection between the spins of the incoming and outgoing particles with the different elements of the spin-spin correlation tensor. In Chapter 6, we will apply the present theory for the three different magnetic phases of a model system, whose intrinsic spin-wave spectra were calculated in Chapter 2: a ferromagnetic, a spin spiral, and a skyrmion-lattice phase. There, we will also discuss a proposal for an experimental setup designed to give access to different components of the spin-spin correlation tensor in magnetic thin films.

Appendix

4.A Summation of exponentials over lattice points

Consider the following lattice summation that appears very often in condensed matter physics of crystal:

$$\sum_{l=1}^{N} e^{\mathrm{i}qR_l} \quad , \tag{4.46}$$

where $R_l = al$, and a is the lattice constant. We want to evaluate this sum.

Now, let us consider the following geometric progression:

$$\begin{aligned} S_N = \sum_{l=1}^{N} a_1 p^{(l-1)} =& a_1\big(1 + p + p^2 + ... + p^{(n-1)}\big) \quad \text{, therefore} \\ pS_N =& a_1(p + p^2 + \ldots + p^N) \quad . \end{aligned} \tag{4.47}$$

In the above equation, subtracting the first line from the second, we obtain

$$\begin{aligned} S_N - pS_N =& a_1 - a_1 p^N \\ S_N(1-p) =& a_1(1-p^N) \\ S_N =& a_1 \frac{1-p^N}{1-p} \quad . \end{aligned} \tag{4.48}$$

Our original sum can be written in terms of this geometric progression:

$$\sum_{l=1}^{N} e^{\mathrm{i}qR_l} = \sum_{l=1}^{N} e^{\mathrm{i}qa} e^{\mathrm{i}qa(l-1)} = \sum_{l=1}^{N} e^{\mathrm{i}qa} (e^{\mathrm{i}qa})^{(l-1)} \quad , \tag{4.49}$$

then $a_1 = e^{\mathrm{i}qa}$ and $p = e^{\mathrm{i}qa}$, therefore, Eq. (4.48) gives:

$$\sum_{l=1}^{N} e^{\mathrm{i}qR_l} = e^{\mathrm{i}qa} \frac{1 - e^{\mathrm{i}qaN}}{1 - e^{\mathrm{i}qa}} \quad . \tag{4.50}$$

Let us consider Born-von Karman boundary condition, which imposes that a given multiple of the wavelength associated with q, $\lambda = 2\pi/q$, has to be of the size of the box, $L = aN$, where N is the total number of unit cells and a the lattice constant. This restricts $\mathbf{q}$ in the following way:

$$\begin{aligned} n\lambda =& L = aN \\ n\frac{2\pi}{q} =& aN \\ q =& \frac{2\pi}{a}\frac{n}{N} \quad , \end{aligned} \tag{4.51}$$

where $n = 0, 1, \ldots, +\infty$. With such a restriction, the summation through equation (4.50) has a very predictable outcome:

$$\sum_{l=1}^{N} e^{\mathrm{i}qR_l} = e^{\mathrm{i}qa}\frac{1 - e^{\mathrm{i}\frac{2\pi}{a}\frac{n}{N}aN}}{1 - e^{\mathrm{i}qa}} = e^{\mathrm{i}qa}\frac{1 - e^{\mathrm{i}2\pi n}}{1 - e^{\mathrm{i}qa}} = 0 \quad , \tag{4.52}$$

provided that $e^{\mathrm{i}qa} \neq 1$. When $e^{\mathrm{i}qa} = 1$, that is, $q = 2\pi n/a$ (for $n = -\infty, \ldots, -1, 0, 1, \ldots, +\infty$), we can evaluate from the original version of the sum:

$$\sum_{l=1}^{N} e^{\mathrm{i}qR_l} = \sum_{l=1}^{N} e^{\mathrm{i}2\pi nla/a} = \sum_{l=1}^{N} e^{\mathrm{i}2\pi nl} = \sum_{l=1}^{N} 1 = N \quad . \tag{4.53}$$

Therefore, our solution reads:

$$\sum_{l=0}^{N-1} e^{\mathrm{i}qR_l} = N \sum_{n=-+\infty}^{n=+\infty} \delta_{q,2\pi n/a} \quad . \tag{4.54}$$

Another interesting fact is that the imaginary part of the lattice sum, a sum of sine functions, is always zero:

$$\sum_{l} e^{\mathrm{i}qR_l} = \sum_{l} \cos(qR_i) + \mathrm{i}\sum_{l} \sin(qR_l) = \sum_{l} \cos(qR_l) = N \sum_{n=-+\infty}^{n=+\infty} \delta_{q,2\pi n/a} \quad . \tag{4.55}$$

This fact is illustrated in Fig. 4.A.1, where unitarian circles in the complex plane were drawn for $N = 3, 4, 5$, and 6, as examples. The sum over l is restricted to the points indicated by the arrows. Each point has a counterpart whose sine has the additive opposite value. The exception is for $qR_l = 2\pi n$, which has no counterpart but whose sine is also zero.

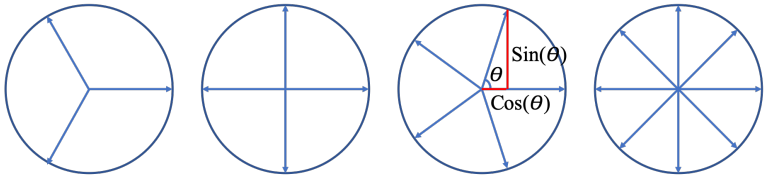

Figure 4.A.1: Unitarian circle in the complex plane. The circles were split into intervals of $2\pi/N$ for $N = 3, 4, 5$, and 6. The sum of the sine of the point angles gives always zero.

In the continuous limit of a three-dimension space, the sum yields:

$$\sum_{\mathbf{R}} e^{\mathrm{i}\mathbf{q}\cdot\mathbf{R}} = (2\pi)^3 \frac{N}{V} \sum_{\mathbf{K}} \delta(\mathbf{q} - \mathbf{K}) \quad , \tag{4.56}$$

where $\mathbf{K}$ are the reciprocal space vectors. See appendix A.4 of Ref. [87] for more details.

Chapter 5

Surface-reconstructed Co ultrathin films on W(110)

In this chapter, we study collinear ferromagnets as an introduction to the problem of computing the spin-wave spectrum and connecting it to the experimental data by parameterizing a spin Hamiltonian from *ab initio* calculations. For that, we investigate surface-reconstructed ultrathin films of cobalt deposited on tungsten (110) surface, where for the first time more than one spin-wave mode was resolved by electron-energy-loss spectroscopy (EELS) [24]. The surface reconstruction of these Co/W(110) films makes the problem rather nontrivial, for it requires first-principles calculations with large supercells. Furthermore, the consequent reduction of the Brillouin zone demands the unfolding of the spin-wave spectrum if one is to compare the theoretical results with the experimental data. We show that this unfolding can be achieved within the scattering theory developed in Chapter 4 by properly choosing the phase for the scattering response of the different layers. We also analyze the strength and oscillation of the intralayer and interlayer magnetic interactions and investigate the resulting spin-wave dispersions as a function of the thickness of the Co films. In particular, we highlight and explain the strong impact of the electronic-state hybridization at the Co–W interface on the magnetic exchange interactions and the spin-wave dispersions. We compare our results to the recent measurements based on EELS of Ref. [24]. Good overall agreement with experimental data can be obtained by considering the possible overestimation of the intra-atomic exchange splitting, stemming from the local-spin-density approximation, and adopting an appropriate correction. This chapter is also based on Ref. [88] by the author of the present thesis.

5.1 Introduction

Until very recently, only one spin-wave mode of multiple-layer magnetic films was experimentally observed with EELS [18]. This was in stark contrast with the theoretical expectation of one mode per layer of a uniform ferromagnetic thin film, based on a simple Heisenberg model. A more sophisticated theoretical description, taking into account the spin-wave suppression due to Landau damping (decay into Stoner excitations), also predicted that more modes should be observed [89]. This has been recently borne out experimentally, due to a large improvement in the en-

ergy resolution of the EELS spectrometers (now $\sim$ 2 meV), making it possible for the first time to resolve up to three spin-wave modes [24, 25, 90]. Faced with such a wealth of experimental results, it becomes essential to perform detailed theoretical investigations, in order to ascertain the quality of the current methods and our understanding of the underlying physics.

Therefore, in this chapter, we study theoretically the spin-wave properties of thin films of cobalt deposited on tungsten (110), following the work of Michel *et al.* [24], which revisits the initial investigation of Vollmer *et al.* [18]. These systems are peculiar since a realistic simulation of its electronic properties requires us to consider the surface reconstruction of Co thin films, leading to dramatic computational costs because of the large supercells with several inequivalent atoms. We study the electronic and magnetic properties of these films using density functional theory within the Green-function Korringa-Kohn-Rostoker (KKR) method described in Chapter 3. The magnetic exchange interactions are obtained using the infinitesimal-rotation method also discussed in Chapter 3. We computed spin-wave dispersions in the adiabatic approximation as introduced in Chapter 2, which has limitations stemming from the neglect of the interaction between the collective spin-wave modes and the continuum of Stoner excitations. The latter leads to Landau damping [91, 92], which can heavily damp the spin-wave modes, and it may also renormalize the spin-wave energies. However, it has been argued theoretically and demonstrated by explicit calculations [89, 93, 94] that the Heisenberg model description is reasonable for low spin-wave energies and not too large wavevectors, which is precisely the range relevant to (SP)EELS and the one in which we are interested.

Although it is responsible for the magnetocrystalline anisotropy (MCA) and the Dzyaloshinskii-Moriya interaction (DMI), in this chapter, we left out spin-orbit coupling from the calculations. The MCA determines the ferromagnetic easy axis and leads to the zero wavevector gap in the spin-wave dispersion, while the DMI favors the formation of noncollinear magnetic structures. In Ref. [24], the MCA gap is unresolvable and no DMI-induced asymmetries in the spin-wave dispersions were measured, which must be due to the strong ferromagnetic exchange interactions. In view of the considerable complexity of the problem already without relativistic effects, we chose to leave this aspect for an investigation in Chapter 8, where we study even thinner films of Co/W(110), such as the single monolayer Co film for which the impact of the DMI cannot be disregarded.

The chapter is organized as follows. First, we explain the unfolding scheme of the spin-wave spectrum in inhomogeneous ferromagnets in Sec. 5.2, which is necessary to connect the theoretical results with the experimental data. Then, the ground-state properties obtained from first-principles calculations are analyzed in Sec. 5.3, including the magnetic exchange interactions. The latter is then used in Sec. 5.4 to compute the adiabatic spin-wave dispersions. Finally, our conclusions are gathered in Sec. 5.5.

5.2 Spin waves in an inhomogeneous ferromagnet

Co thin films deposited on W(110) are inhomogeneous ferromagnets. Besides the vertical inhomogeneity due to the layered structure, there is also lateral inhomogeneity, due to a surface reconstruction. Thus, the intrinsic spin-wave spectrum

is complex and, therefore, not necessarily simply related to the experimental measurements. One must consider how the experimental apparatus interacts with the magnetic system. As we explained in the introduction, newly developed high energy resolution EELS is one of the motivations for this chapter. A complete description of an EELS experiment requires a detailed multiple scattering analysis of the probing electrons, taking into account all inelastic effects. Here, we restrict ourselves to the description provided in Chapter 4 aiming at a simplified connection between theory and experiment.

Let us consider the spins of the Co atoms as classical vectors of constant length $\mathbf{S}_{i\mu} = (M_{i\mu}/2)\hat{\mathbf{S}}_{i\mu}$, where $\hat{\mathbf{S}}_{i\mu}$ are unit vectors in the direction of the atom's magnetic moments that have magnitude $M_{i\mu}$. Thus, the classical Heisenberg Hamiltonian for an inhomogeneous ferromagnet, containing only the magnetic exchange interaction, can be written as

$$\mathcal{H} = -\frac{1}{2}\sum_{i\mu}\sum_{j\nu} J_{i\mu,j\nu}\,\mathbf{S}_{i\mu}\cdot\mathbf{S}_{j\nu} \quad . \tag{5.1}$$

Here i, j label unit cells forming a Bravais lattice, while μ, ν run over the N_b basis atoms. The position of a particular magnetic moment is given by $\mathbf{R}_{i\mu} = \mathbf{R}_i + \mathbf{R}_\mu$. The magnetic exchange interactions are symmetric, $J_{j\nu,i\mu} = J_{i\mu,j\nu}$, and depend only on the distance between unit cells, $J_{i\mu,j\nu} = J_{\mu\nu}(\mathbf{R}_{ij})$ with $\mathbf{R}_{ij} = \mathbf{R}_j - \mathbf{R}_i$.

The adiabatic spin-wave eigenvalues and eigenvectors, considering an atom basis with more than one atom, are given by the following eigenvalue equation:

$$\mp\omega S^{\pm}_{\mu}(\mathbf{q}) = S^{\pm}_{\mu}(\mathbf{q})\sum_{\nu} S_\nu J_{\mu\nu}(0) - S_\mu \sum_{\nu} S^{\pm}_{\nu}(\mathbf{q}) J_{\mu\nu}(\mathbf{q}) \quad , \tag{5.2}$$

where $J_{\mu\nu}(\mathbf{q}) = \sum_j e^{\mathrm{i}\mathbf{k}\cdot\mathbf{R}_{ij}} J_{i\mu,j\nu}$, $S^{\pm}_{\mu} = S^{x}_{\mu} \pm \mathrm{i}S^{y}_{\mu}$, and $S_\mu = M_\mu/2$. We leave the derivation of the above equation for the Apx. 5.A. As discussed in Sec. 4.1.4, for ferromagnets whose spins point along $+z$, only the $\mathcal{N}^{+-}(\mathbf{q},\omega)$ component of the spin-spin correlation tensor is nonvanishing, which is given by:

$$\mathcal{N}^{+-}_{\mu\nu}(\mathbf{q},\omega) = 2\sqrt{S_\mu S_\nu}\sum_{r}^{N_b} \delta\big(\omega - \omega_r(\mathbf{q})\big) S^{-}_{r\mu}(\mathbf{q}) S^{-}_{r\nu}(\mathbf{q}) \quad , \tag{5.3}$$

where r label each of the N_b spin-wave modes. The above quantity is in the heart of the unfolding scheme we will discuss next. The practical use of Eq. (5.3) requires a numerical representation of the delta function, for which we employ the Lorentzian function $\delta(\omega) \simeq (\eta/\pi)/(\omega^2 + \eta^2)$, introducing the broadening parameter η.

5.2.1 Unfolding of the spin-wave spectrum

As discussed in Chapter 4, the differential scattering cross section in Eq. (4.14) between an initial probe state (with energy E_i, momentum $\mathbf{k}_i$ and spin s_i) and final probe states (with E_f, $\mathbf{k}_f$ and s_f), which are collected in a solid angle window $\mathrm{d}\Omega$, is proportional to the scattering rate:

$$\frac{\mathrm{d}\sigma}{\mathrm{d}\omega\,\mathrm{d}\Omega} \propto \Gamma_{if}(\boldsymbol{q},\omega) \quad , \tag{5.4}$$

with the energy and momentum transfer defined as

$$E_i - E_f = \omega \quad , \quad \mathbf{k}_i - \mathbf{k}_f = \mathbf{q} + \mathbf{G} \quad , \tag{5.5}$$

where $\omega > 0$ corresponds to energy absorption and vice-versa. Momentum is conserved up to a reciprocal lattice vector $\mathbf{G}$, except for nonperiodic directions (for films only in-plane momentum is fixed by Bragg scattering). It is the spectrum defined by the scattering rate that can be compared to the experimental data.

For *inelastic scattering* involving spin waves (relatively low energy compared to that of the probing electron beam), the scattering rate is proportional to the spin-spin correlation tensor given by Eq. (4.29). Furthermore, with the application to layered systems in mind, we can split the basis index into two, $\mathbf{R}_\mu \to \mathbf{R}_{l\mu} = \mathbf{R}_l + \mathbf{b}_\mu$, with $\mathbf{R}_l$ the origin for layer l, and $\mathbf{b}_\mu$ the location of a basis atom with respect to the origin of layer l. Thus, we obtain that the scattering rate is proportional to

$$\Gamma_{if}(\mathbf{q},\omega) \propto \sum_{l'l} A_{l'l} \sum_{\mu\nu} e^{\mathbf{i}\mathbf{q}\cdot\mathbf{b}_{\mu\nu}} \mathcal{N}^{+-}_{l'\mu,l\nu}(\mathbf{q},\omega) \quad . \tag{5.6}$$

with the vector $\mathbf{b}_{\mu\nu} = \mathbf{b}_\nu - \mathbf{b}_\mu$. In the above equation, we explicitly separated the sum over layers. In a scattering experiment, due to the wave nature of the probing beam, the response of every atom arrives at the detector with different phases. The resulting interference is destructive for most modes arising from atoms which are crystallographically nearly equivalent (for example in the same layer); the waves that interfere constructively lead to the experimentally detected signal. Such phase differences are encoded in the Fourier factor of Eq. (5.6), and they define the *unfolding* of the computed spin-wave bands.

The factor $A_{l'l}$ describes the phase of the different-layer responses, and it has assumed many forms in the literature. Taroni *et al.* [95] consider $A_{l'l} = e^{\mathbf{i}\mathbf{q}\cdot\mathbf{R}_{l'l}}$, with $\mathbf{R}_{l'l} = \mathbf{R}_l - \mathbf{R}_{l'}$, and they show that this choice leads to the suppression of the optical spin-wave modes in $\Gamma_{if}(\mathbf{q},\omega)$. With this particular choice, the probed system is excited uniformly which leads to the acoustic mode only. Using arguments from scattering theory, Rajeswari *et al.* [96] proposed $A_{l'l} = e^{-(z_{l'}+z_l)/\lambda_\mathrm{d}}\, e^{\mathbf{i}\mathbf{q}\cdot\mathbf{R}_{l'l}}$, where z_l is the distance between layer l and the surface of the film, and λ_d is the finite penetration depth of the electron beam. This explains the experimental detection of optical modes in the EELS experiment.

Here, we are solely interested in the spin-wave dispersion, rather than their spectral line shapes and intensities, as they cannot be accessed within the spin-wave adiabatic approximation since no electron-hole excitations or any other source of damping is included. Therefore, we introduce $A_{l'l} = \delta_{l'l}$, which gives equal weight to the contributions of each layer to the intensity of a given spin-wave mode, and it yields the layer-resolved density of spin-wave excitations. This is an appropriate choice to trace out the dispersion of each spin-wave branch throughout the entire Brillouin zone without a parameter-dependent intensity function. We emphasize that none of the choices mentioned above for $A_{l'l}$ affects the spin-waves energy dispersion, but only the intensities of the bands. The unfolding procedure is illustrated in Fig. 5.2.1 for the trivial case of a trilayer with uniform nearest-neighbor magnetic interaction, described in two ways: with a basis of one atom per layer and with a basis of ten atoms per layer. The spin-wave dispersions computed from Eq. (5.2) then comprise 3 and 30 branches, respectively, as can be seen in the figure. Applying

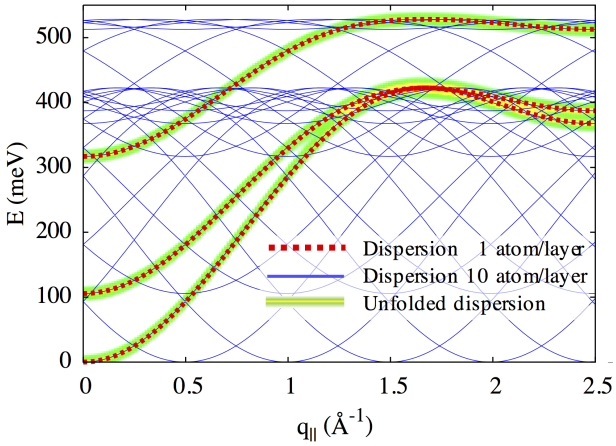

Figure 5.2.1: Illustrating the unfolding scheme. The spin-wave dispersion of a uniform trilayer is calculated using Eq. (5.2) with 1 atom per layer (red dashed lines) or 10 atoms per layer (blue solid lines). We considered nearest-neighbour intralayer and interlayer magnetic interactions $J = 9\,\text{meV}$, a moment of $1\,\mu_\text{B}$ for all atoms, and the lattice constant $a_\text{Co} = 2.51\,\text{Å}$. The unfolding (green-yellow color map) is obtained via Eq. (5.6), with our choice of $A_{l'l} = \delta_{l'l}$.

Eq. (5.6) to the case of the 30 bands shows that we recover the dispersion of the case with 3 bands, due to the indistinguishability of the 10 atoms in each layer. The uniform intensity of the bands throughout the Brillouin zone is a direct consequence of our choice of $A_{l'l}$.

5.3 Ground state properties

The atomic structure for Co/W(110) discussed in the next section was validated with Quantum Espresso [97], using the Projector Augmented Wave method with a kinetic energy cutoff of 50 Ry, in the Γ-point approximation. The magnetic moments and the magnetic exchange interactions are obtained with the Green-function KKR method in the Local Spin Density Approximation (LSDA), and the atomic sphere approximation (ASA) with full charge density (angular momentum cutoff $\ell_\text{max} = 3$), which were introduced in Chapter 3. We consider a slab geometry with open boundary conditions along the stacking direction, including two vacuum regions, each 6 Å thick. The energy integration is performed in the upper complex energy plane, [72] with 30 points in a rectangular path and 5 Matsubara frequencies, for a temperature $T = 500\,\text{K}$. The two-dimensional (2D) Brillouin zone integration was performed with a mesh of 30×30 and 5×20 k-points, for free-standing and supported films, respectively. The magnetic exchange interactions are obtained from the infinitesimal rotations of the magnetic moments as expressed in the Liechtenstein-Katsnelson-Antropov-Gubanov (LKAG) formula [21]. For these calculations, the number of Matsubara frequencies was increased to 10, with $T = 100\,\text{K}$, and the k-mesh was refined to 100×100 and 20×80, for free-standing and supported films, respectively.

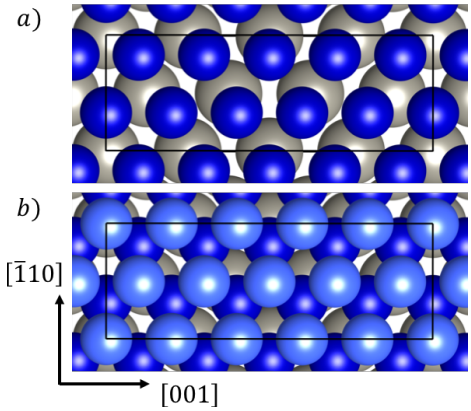

Figure 5.3.1: (a) Top view of a Co ML on W(110), in the 4×1 reconstruction. The dark blue spheres represent Co atoms, while the gray ones are W atoms. The crystallographic directions for bulk W are also indicated. Five Co atoms are covering four W atoms in the [001] direction. (b) 2ML Co on W(110) in hcp stacking. The Co layer at the interface is shown with dark blue spheres, while light blue spheres depicting the second Co layer.

5.3.1 Atomic structure

We consider two kinds of systems: free-standing Co films comprising 3–8 monolayers (ML), with the bulk Co hcp structure, and Co films deposited on the W(110) surface with the same coverage range, but following a reconstructed hcp structure found experimentally [98–102]. The free-standing Co films are used to identify which characteristics of the spin-wave dispersion arise from the reduced dimensionality and which can be attributed to the W(110) substrate.

hcp cobalt grows pseudomorphically on W(110), up to a coverage of 0.7 ML. Beyond that, a reconstruction of the cobalt structure takes place due to the large lattice mismatch ($a_{\mathrm{Co}} = 2.51\,\text{Å}$, $a_{\mathrm{W}} = 3.16\,\text{Å}$). The mismatch between the W(110) and the Co(0001) lattices is of 26% in the W[001] direction and 3% in the $[1\bar{1}0]$, and it is relieved by a 4×1 reconstruction, where five Co atoms cover four W atoms in the W[001] direction. This corresponds to a stretching of the bulk Co(0001) lattice by 1% along the W[001] and 3% along the W$[1\bar{1}0]$. The resulting supercell contains 10 atoms in each Co layer and 8 in each W layer. Possible in-plane modulations of the Co atomic positions and vertical relaxations have been considered in Ref. [100] and in our calculations. They were found to have only a minor impact on the magnetic exchange interactions, so we adopted a simplified structural model. Every Co atom in a given layer is at the same height, and sits on a slightly distorted hexagonal lattice, as shown in Fig. 5.3.1 (a); Fig. 5.3.1 (b) illustrates the hcp stacking of 2 ML Co on W(110). The vertical interlayer distance was fixed at the bulk values similarly to the free standing Co films, $d_{\mathrm{Co\text{–}Co}} = 2.03\,\text{Å}$ and $d_{\mathrm{W\text{–}W}} = 2.23\,\text{Å}$, while at the interface $d_{\mathrm{Co\text{–}W}} = 2.13\,\text{Å}$. The W(110) substrate is modeled using six W layers. In total, we have between 132 atoms (3Co ML) and 182 atoms (8Co ML) in our computational unit cell.

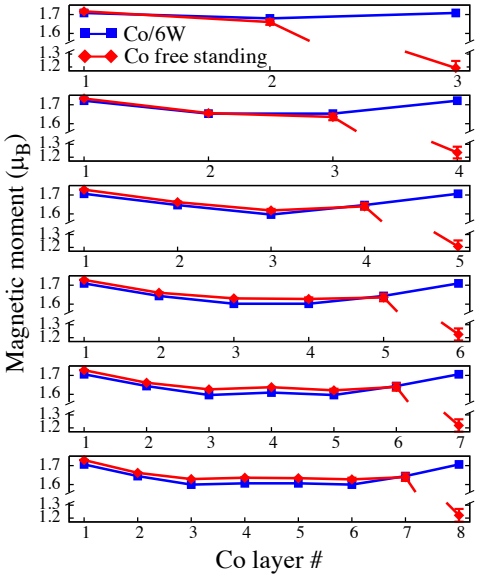

Figure 5.3.2: Layer-resolved spin magnetic moments for free-standing and supported Co films. For the supported films with n layers, Co layer 1 is the surface layer and Co n is at the W(110) interface. The magnetic moments for the supported films are averaged over the ten Co atoms in each layer, with the error bar indicating the spread.

5.3.2 Magnetic moments and electronic structure

We begin the investigation of the impact of the interface with W(110) on the magnetic properties of Co thin films by analyzing some ground-state properties. Fig. 5.3.2 compares the layer-resolved spin magnetic moments of free-standing Co films with the layer-averaged values for Co/W(110) films. The magnetic moments for the supported Co films are very close to those of free-standing films of the same thickness, except for the Co layer at the interface with W(110). There the magnetic moments are 30% smaller, and there is some variability among the ten Co atoms comprising that layer, as indicated by the error bar in Fig. 5.3.2. The interfacial W(110) layer acquires an average spin magnetic moment of $0.076\,\mu_B$, which is antiparallel to the Co magnetic moments and insensitive to the thickness of the Co film.

The explanation for the strong reduction of the magnetic moment of Co at the interface is found in the hybridization of the Co d-states with the W d-states, as seen in the layer-resolved density of states (LDOS), Fig. 5.3.3. Contrasting with the LDOS for bulk-like layers, there is an increase of spectral weight near the Fermi energy, which is responsible for the reduction of the spin magnetic moment of the Co interface layer. A comparison with the electronic structure of free-standing films of the same thickness reveals that the LDOS for the other Co layers is only weakly disturbed by the presence of the W(110) interface; this also explains why the spin magnetic moments are very similar for both kinds of systems, except for the interface layer.

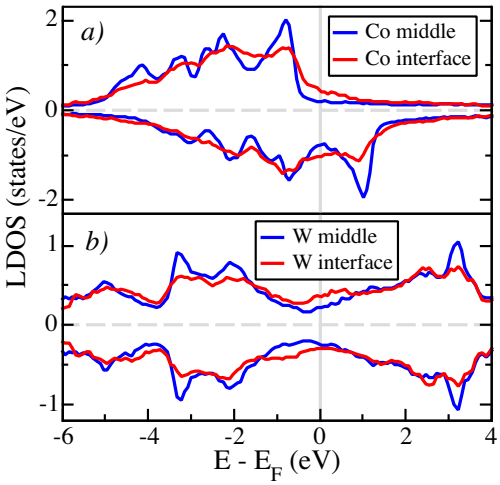

Figure 5.3.3: LDOS for the 8Co/W(110) slab. The energy zero marks the Fermi energy. Positive values correspond to the majority spin LDOS and negative ones to the minority spin LDOS. (a) Comparison of the average LDOS for the Co layers at the interface and in the middle of the Co film (bulk-like). (b) Comparison of the average LDOS for the W layers at the interface and in the middle of the W film (bulk-like). The smearing of bulk-like peaks and transfer of spectral weight to near the Fermi energy signal the strong Co–W hybridization at the interface. These changes lead to reduced magnetic moments for the Co layer at the interface, and also impact the magnetic exchange interactions.

5.3.3 Magnetic exchange interactions

First, we consider the nearest-neighbor interaction, see Fig. 5.3.4, where both the intralayer and the interlayer couplings are shown. Significant changes are only apparent for the Co layer at the W(110) interface, for which we find reduced intralayer and interlayer couplings, comparing with the free-standing films.

The magnetic exchange interactions are fairly long-ranged, and they reflect the symmetry of the electronic states that give rise to them. Fig. 5.3.5 shows some representative cases: the intralayer magnetic exchange interaction between the first Co atom in a given layer and all the others in the same layer, up to a cutoff of 30 Å. In this figure, the value of J is multiplied by d^2 (d being the distance between atoms) to compensate for the decay with distance. The sign changes, which oscillates with the distance, lead to the alternation between ferromagnetic and antiferromagnetic interactions.

For thicker films, the Co layers away from the W(110) interface reproduce the behavior of the freestanding Co films. The presence of the interface modifies the long-range behavior of the magnetic interactions for the two Co layers next to it (see the panels on the right-hand side of Fig. 5.3.5). This is in contrast with the change in the spin magnetic moments and nearest-neighbor magnetic exchange interactions, which are only significantly impacted by the Co layer in contact with W(110). The symmetry of the pattern for slowly decaying interactions is also modified next to the

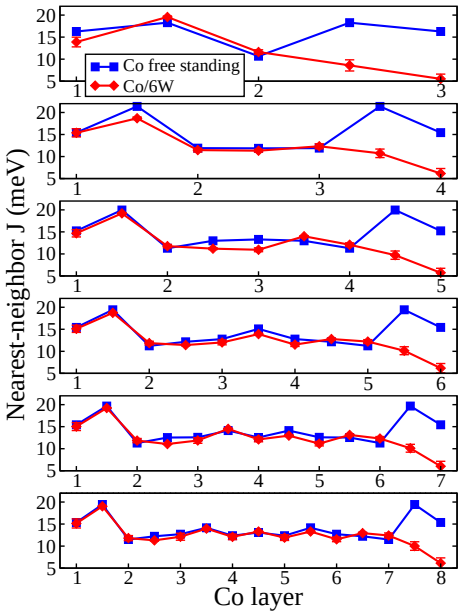

Figure 5.3.4: Nearest-neighbour magnetic exchange parameter J among Co atoms, for free-standing and supported Co films of different thickness. For Co/W(110), the interface layers are on the right-hand side. The intralayer parameter for layer n is labeled by the same integer, while the coupling between layers n and $n+1$ is labeled by $n+1/2$. For the supported films, the average J is shown, with the spread given as an error bar. Due to the Co–W hybridization, the coupling strength decreases for the Co layer at the interface.

interface, being reduced from hexagonal to twofold for the Co layer at the W(110) interface.

5.3.4 Focusing origin

In Fig. 5.3.5), the anisotropic spatial dependence of the J_{ij}'s and their slower decay along the six nearest-neighbor directions arises from the hexagonal shape of the Co d-bands in the Brillouin zone, near the Fermi energy, which we aim to demonstrate next. First, we consider the shape of the layer-resolved Fermi surface contours for the free-standing Co 8ML slab. The results are shown in Fig. 5.3.6 for the first four layers (the other four are equivalent due to the mirror symmetry of the free-standing film), together with the respective intralayer maps of the magnetic interactions. The Fermi surface of the majority-spin channel features circular contours in the center of the Brillouin zone and hexagon-like ones away from the center. These hexagon-like bands have flat regions, which enhances the group velocity of the occupied electronic states, mediating an enhanced magnetic interaction for pairs of atoms aligned with their group velocity.

To corroborate our interpretation, we make use of a simple tight-binding model with a single orbital per atom forming a 1ML hexagonal lattice. The Hamiltonian

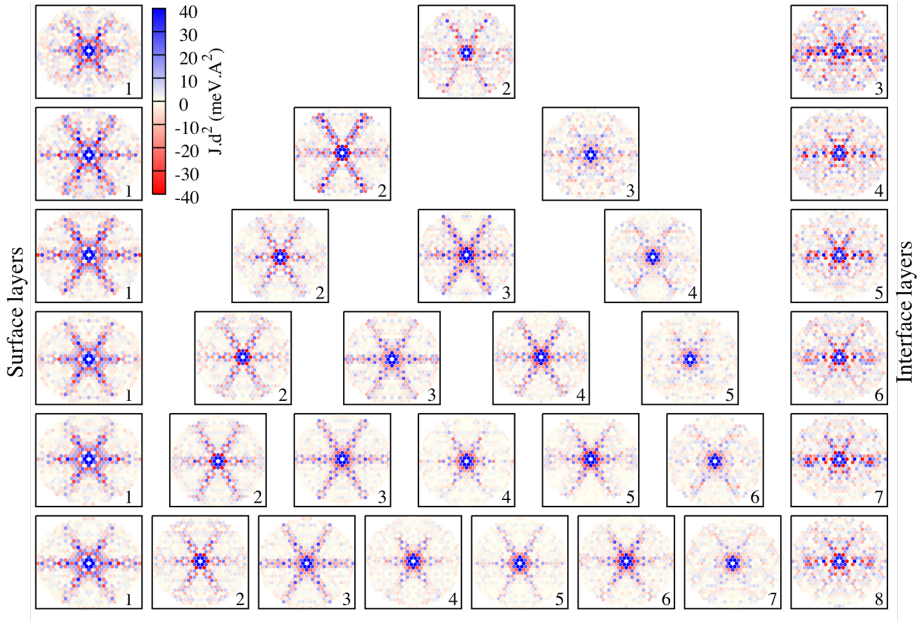

Figure 5.3.5: Maps of the intralayer magnetic exchange interactions in real space, for 3-8ML Co on W(110). Each map shows the magnetic exchange interaction, J_{ij}, between the first Co atom in a given layer, i, and all other Co atoms in the same layer, j, up to a cutoff radius of 30 Å. The J_{ij} are multiplied by d^2, where d is the distance between the i and j atoms. The panels on the right-hand side correspond to those of Co layers in the vicinity of W.

reads

$$\mathcal{H} = t \sum_{\langle ij \rangle \sigma} a^{\dagger}_{i\sigma} a_{j\sigma} + U \sum_{i} (n_{i\uparrow} - n_{i\downarrow}) \quad , \tag{5.7}$$

where t is the hopping parameter that connects nearest-neighbour atoms, and U creates the spin splitting of the two bands. The operator $a_{i\sigma}$ ($a^{\dagger}_{i\sigma}$) annihilates (creates) an electron with spin σ on site i, and $n_{i\sigma} = a^{\dagger}_{i\sigma} a_{i\sigma}$ is the number operator. Using the translational symmetry of the system, the Hamiltonian can be transformed into

$$\mathcal{H} = \sum_{\mathbf{k}\sigma} H_{\mathbf{k}\sigma} = \sum_{\mathbf{k}\sigma} (t_{\mathbf{k}} + U_{\sigma})\, a^{\dagger}_{\mathbf{k}\sigma} a_{\mathbf{k}\sigma} \tag{5.8}$$

where $U_{\sigma} = +U, -U$ for $\sigma = \uparrow, \downarrow$, respectively. And

$$t_{\mathbf{k}} = t \sum_{\langle i,j \rangle} e^{i\mathbf{k}\cdot\mathbf{R}_{ij}} \quad \text{and} \quad a_{\mathbf{k}} = \frac{1}{\sqrt{N}} \sum_{j} e^{i\mathbf{k}\cdot\mathbf{R}_{j}} a_j \quad . \tag{5.9}$$

From this model one can easily calculate the magnetic exchange coupling via the LKAG formula [21] that provides the connection between the electronic structure and the magnetic exchange interactions, as discussed in Chapter 3:

$$J_{ij} = \frac{U^2}{\pi} \int^{E_F} \mathrm{Im}\,\mathrm{Tr}[G_{ij\uparrow}(E) G_{ij\downarrow}(E)]\, \mathrm{d}E \quad , \tag{5.10}$$

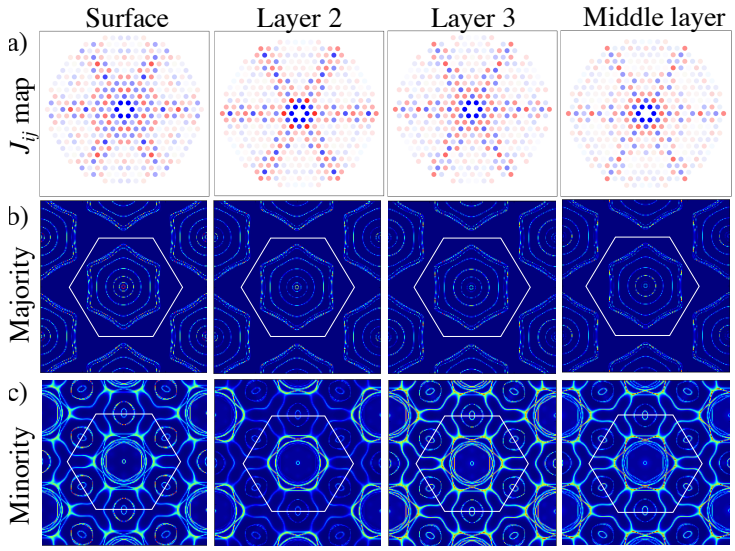

Figure 5.3.6: Panel (a) shows the intralayer J_{ij} maps for the first layers of a 8ML Co free-standing slab. Panels (b) and (c) present the correspondent layer-resolved Fermi surface contours for the majority and minority spin channels, respectively. The J_{ij} are multiplied by d^2, where d is the distance between the i and j atoms.

where the real space Green-function is given as

$$G_{ij\sigma}(E) = \frac{1}{\Omega_{BZ}} \int e^{-i\mathbf{k}\cdot\mathbf{R}_{ij}} G_{\mathbf{k}\sigma}(E)\, \mathrm{d}\mathbf{k} \quad , \tag{5.11}$$

and

$$G_{\mathbf{k}\sigma}(E) = \frac{1}{E - E_0 - H_{\mathbf{k}\sigma} + \mathrm{i}\eta} \quad , \tag{5.12}$$

where E_0 corresponds to the center of mass of the band and $\eta \to 0$.

The DOS of this model is shown in Fig. 5.3.7. Fig. 5.3.8 displays the Fermi surface contours for Fermi energies marked in Fig. 5.3.7. In the left column (panels (a), (c) and (e)), the Fermi energy is set near the bottom of the two bands, where the energy band dispersion is almost isotropic, see panels (c) and (e). In the right column (panels (b), (d) and (f)), the Fermi energy is chosen to match the Van Hove singularity of the majority spin band, arising from the hexagonal shape of the energy dispersion. The real-space map of the magnetic exchange interactions for both cases is shown in panels (a) and (b). Panel (a) shows a very isotropic map, mainly marked by the periodic radial oscillation associated with Fridel oscillation. Panel (b) shows the impact of the hexagonal shape of the energy bands near the Fermi energy, featuring a sixfold-symmetric focusing pattern. We thus have illustrated our proposition that the anisotropy of the magnetic exchange interactions in real space is a direct consequence of the anisotropy of the electronic energy bands in reciprocal space that mediate the interactions (see similar effects obtained with adatoms in Refs. [103–106]).

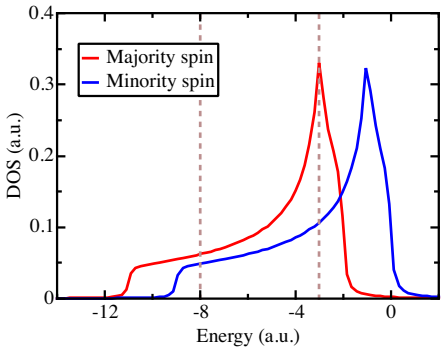

Figure 5.3.7: Total density of states of the two-band model given in Eq. (5.7). The dashed lines mark a Fermi energy near the bottom of the two bands (left), and another at the Van Hove singularity (right). The correspondent Fermi surface is almost isotropic in the first case, and very anisotropic in the other; see Fig. 5.3.8. $t = -1$, $U = 1$, $E_0 = -4$, and $\eta = 0.1$ a.u.

5.4 Spin-wave dispersions

Having characterized the ground-state magnetic properties of the Co films, we can finally understand the properties of the spin-wave dispersions.

5.4.1 Free-standing versus supported films

The spin-wave dispersions for the free-standing and supported Co thin films are calculated within the adiabatic approach described in Sec. 5.2, initially for a thickness of 8ML, as shown in Fig. 5.4.1. The blue lines are the results for the free-standing film, while the gray lines stand for the supported film. The large number of spin-wave bands in the supported film is due to the lateral inhomogeneity arising from the surface reconstruction, and *a priori* it is unclear how a comparison with the free-standing case can be made. This is answered by the unfolding procedure summarized in Eq. (5.6), the result being shown as the background color map. One can then focus on the unfolded dispersion of the supported film when comparing to the free-standing calculation.

There are two main points of interest when comparing the free-standing and supported calculations. First, we consider the spin-wave energies at $q_{\|} = 0$. For example, the second spin-wave branch (first optical mode) for the 3ML free-standing film is slightly higher in energy than for the 3ML W-supported film, while for the 4 and 5ML thicknesses the ordering is reversed. However, these energy differences decrease for thicker slabs (which is also true for other modes). These energy gaps between the different modes at $q_{\|} = 0$ are mainly determined by the interlayer exchange coupling, which is modified only near the Co/W interface. For thicker films, the contribution from the interface becomes less important, and both free-standing and supported films should become similar. Also, the higher-energy modes are more strongly affected by the substrate. Returning to the 8Co/W film of Fig. 5.4.1, we observe that the first four modes are very close to the corresponding free-standing

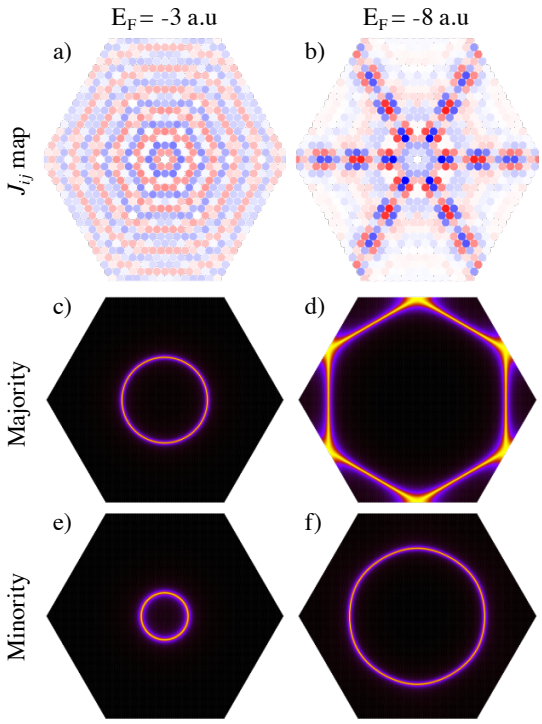

Figure 5.3.8: J_{ij} maps for two different Fermi energies (a) $E_F = -8$ a.u. and (b) $E_F = -3$ a.u. Panels (c) and (e) are the majority and minority Fermi surface contours for $E_F = -3$ a.u., respectively, and panels (d) and (f) are the majority and minority Fermi surface contours for $E_F = -8$ a.u. The J_{ij} are multiplied by d^2, where d is the distance between the i and j atoms. $t = -1$, $U = 1$, $E_0 = -4$, and $\eta = 0.1$ a.u.

ones in the small-q region, while the higher modes still differ.

The second point of interest is the stiffness of the spin-wave branches, which indicates how strongly the spin-wave energy increases with the wavevector. We find that, for all modes and all thicknesses, the stiffness is larger for the free-standing films than for the supported ones. Therefore, the substrate softens the spin-waves. This is more pronounced for the first mode (also known as the acoustic mode), where the result of the two calculations spread apart for wavevectors larger than about $0.3\,\text{Å}^{-1}$ to $0.4\,\text{Å}^{-1}$, as can be seen in Fig. 5.4.1.

In the small wavevector regime, the spin-wave dispersions are quadratic,

$$E_n(q_\parallel) \approx E_n(0) + D_n q_\parallel^2 \quad , \tag{5.13}$$

where D_n is the stiffness constant of the n-th mode. A full comparison between the stiffnesses of different modes in different thicknesses for both free-standing and supported films is shown in Fig. 5.4.2. In addition, Fig. 5.4.2 also shows the experimental stiffnesses extracted from the dispersion published in Ref. [24]. We defer the comparison between theory and experiment to the next section, where the experimental data is also plotted in Fig. 5.4.4. The quadratic fit to Eq. (5.13) was applied

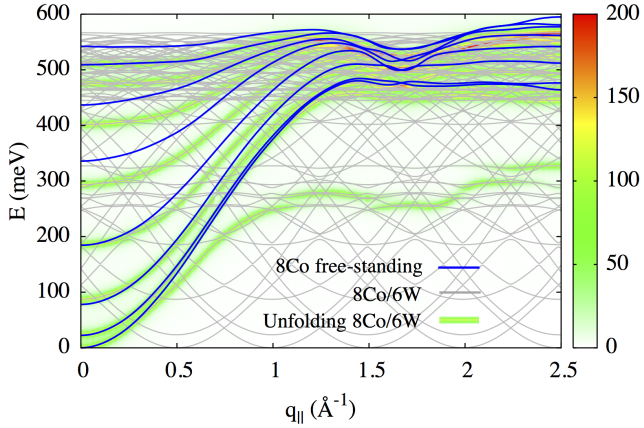

Figure 5.4.1: Spin-wave dispersion for the free-standing and W-supported 8ML Co film (blue and gray lines, respectively). The color map corresponds to the unfolded dispersion for the supported films, Eq. (5.6), with a Lorentzian broadening of width 4 meV. The intensity of the color map is in arbitrary units.

to the dispersion curves in the range $q_{\parallel} \in [0.0, 0.3]\,\text{Å}^{-1}$. As pointed out before, one can observe that systematically the free-standing films have higher stiffness, with the differences to the supported films being larger for higher modes and thinner films.

To unravel the impact of the substrate on the spin-wave dispersions, we discuss a simplified magnetic interaction model, using only nearest-neighbor couplings. We have learned in Sec. 5.3 that the tungsten substrate mainly decreases the following: (a) the intralayer coupling of the Co interface layer (Fig. 5.3.4); (b) the interlayer coupling between the Co interface layer and the adjacent Co layer (Fig. 5.3.4); and (c) the magnetic moment of the Co interface layer (Fig. 5.3.2). To establish the qualitative impact of each of these factors on the spin-wave dispersions, we parametrized a nearest-neighbor model for an 8ML film with the data of Figs. 5.3.2 and 5.3.4, which pertain to the free-standing case. The resulting dispersions are shown with black-dashed lines in all panels of Fig. 5.4.3, and they will serve as a reference.

In Fig. 5.4.3 (a), we decreased by 60% the intralayer exchange coupling of the last Co layer (ratio taken from Fig. 5.3.4). Comparing with the reference model (black-dashed), the main differences are the strong reduction of the acoustic mode stiffness and the lowering of its energy throughout the Brillouin zone. Fig. 5.4.3 (b) shows the impact of decreasing by 50% only the interlayer coupling between the last Co layer and the adjacent one. Almost all spin-wave branches are modified, and their energy lowered, but the overall bandwidth is mostly preserved. The acoustic mode is lowered only next to the border of the Brillouin zone (the crossing point of the higher branches). Fig. 5.4.3 (c) reveals that reducing only the magnetic moment of the last Co layer by 30% (Fig. 5.3.2) leads to a very small deviation from the

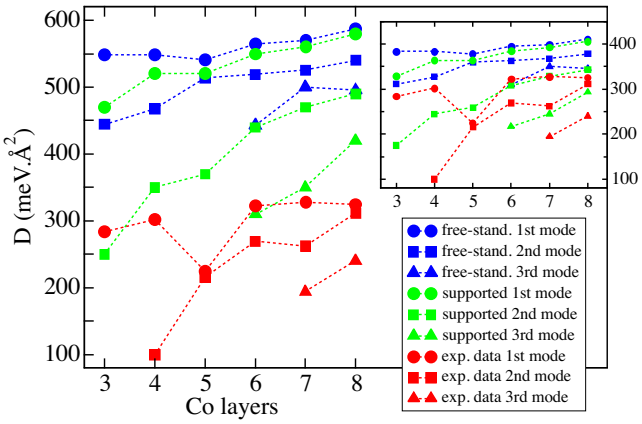

Figure 5.4.2: Stiffness constants obtained from fitting the spin-wave branches of Fig. 5.4.4 to Eq. (5.13). Blue refers to the free-standing calculations while green stands for the supported case. Red indicates the stiffness of the experimental data[24]. For all fits, only points with $q_{\parallel} < 0.3\,\text{Å}^{-1}$ were considered. Circles correspond to the first (acoustic) mode, squares to the second mode, and triangles to the third one. The inset presents the same data as above with free-standing and supported results rescaled down by 30%, as will be discussed in Sec. 5.4.2. The supported films capture the experimental trends better than the free-standing ones.

reference model, except for the highest branch, which gets pushed higher in energy. Lastly, Fig. 5.4.3 (d) shows the result of combining all three modifications. Most of the characteristics of the full calculations of Fig. 5.4.1 are present: changes in $E_n(0)$, the reduction of the stiffness of the modes, and the lowering of the acoustic mode.

5.4.2 Theoretical vs experimental dispersion

We saw that the theoretical stiffnesses are systematically higher than the experimental ones [24]. Fig. 5.4.2 shows that the stiffnesses of the acoustic mode range from 450 to 600 meV Å^2 for both free-standing and supported calculations, while the experimental ones range from 200 to 300 meV Å^2. One possible reason for the discrepancy is the sensitivity of the fit to the available experimental data. On the one hand, the number of experimental data points in this range is rather small, and the spin-wave energies cannot be experimentally determined for $q_{\parallel} \to 0$ due to limitations of the EELS technique [24]. On the other hand, including experimental data at higher $q_{\parallel}$ also increases the uncertainty in the fitting procedure, due to the difficulty in extracting the spin-wave energies from broad experimental peaks [24].

It is also known that DFT in the LSDA overestimates the exchange splitting of metallic ferromagnets, such as Co and Ni, and consequently their magnetic moments and magnetic exchange coupling. In the work of Müller *et al.* [107], it is reported that LSDA calculation for bulk fcc cobalt leads to an exchange splitting 30% higher at Γ'_{25} (even 55% at Γ_{12}) with respect to the experimental value. The same work points to a way for an improved description of the electronic structure, based on many-

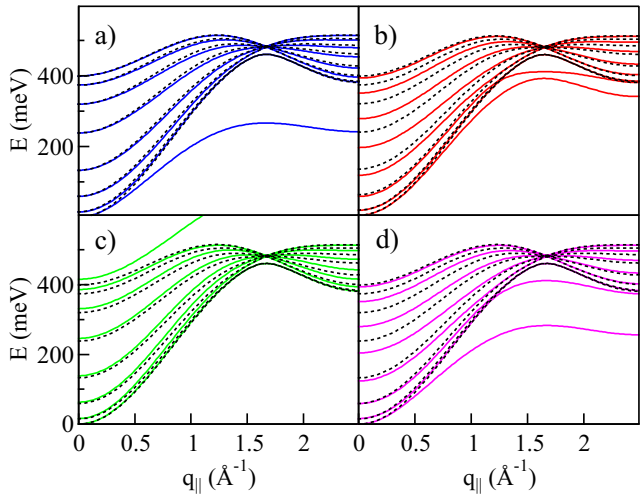

Figure 5.4.3: Dispersion curves for a nearest-neighbor Heisenberg model of an 8ML Co film, based on the parameters given in Figs. 5.3.2 and 5.3.4 for the free-standing films. The black-dashed lines in all panels represent the result obtained with unmodified parameters, while the solid lines show the dispersion upon the following changes: (a) The intralayer coupling of the last Co layer is reduced by 60%. (b) The interlayer coupling between the interface Co layer and its adjacent layer is reduced by 50%. (c) The magnetic moment of the interface Co layer is reduced by 30%. (d) The effect of combining all the changes in the parameters.

body perturbation theory. However, such methods are already computationally very demanding for bulk systems containing just a few atoms in the unit cell, which makes them unfeasible for the structurally complex thin films we considered.

Reference [107] also pointed out that an alternative is to rescale the exchange splitting self-consistently in the LSDA calculation, $B_{\mathrm{xc}} \to \alpha\, B_{\mathrm{xc}}$, which then renormalizes the magnetic parameters of the Heisenberg model computed from first-principles. Unfortunately, the magnitude of the rescaling is unknown *a priori*. The magnetic interactions are affected in a nonlinear way by α, as we verified in our calculations. We note that an empirical reduction of $J(\mathbf{q})$ by 15% was already explored in Ref. [108], to bring theoretical and experimental results for fcc Co/Cu(001) into an agreement. For free-standing hcp cobalt films, we observed that reducing the exchange splitting up to 20% ($\alpha = 0.8$) has an overall effect of rescaling the exchange interactions, but by a different factor, $J(\mathbf{q}) \to \beta\, J(\mathbf{q})$. For an 8ML free-standing Co film, a reduction of the magnetic interactions by 30% ($\beta = 0.7$) is approximately obtained from a rescaling of the exchange splitting in the 10-20% range ($\alpha \in [0.8, 0.9]$).

Figure 5.4.4 shows the theoretical results with the 30% reduction of J, together with the experimental data of Ref. [24]. We obtain very good agreement with the experimental results, in particular for the supported films. A single rescaling parameter is enough to describe well both the energies of the standing modes ($q_{\parallel} = 0$) and the stiffnesses, for all film thicknesses and modes (only small deviations remain

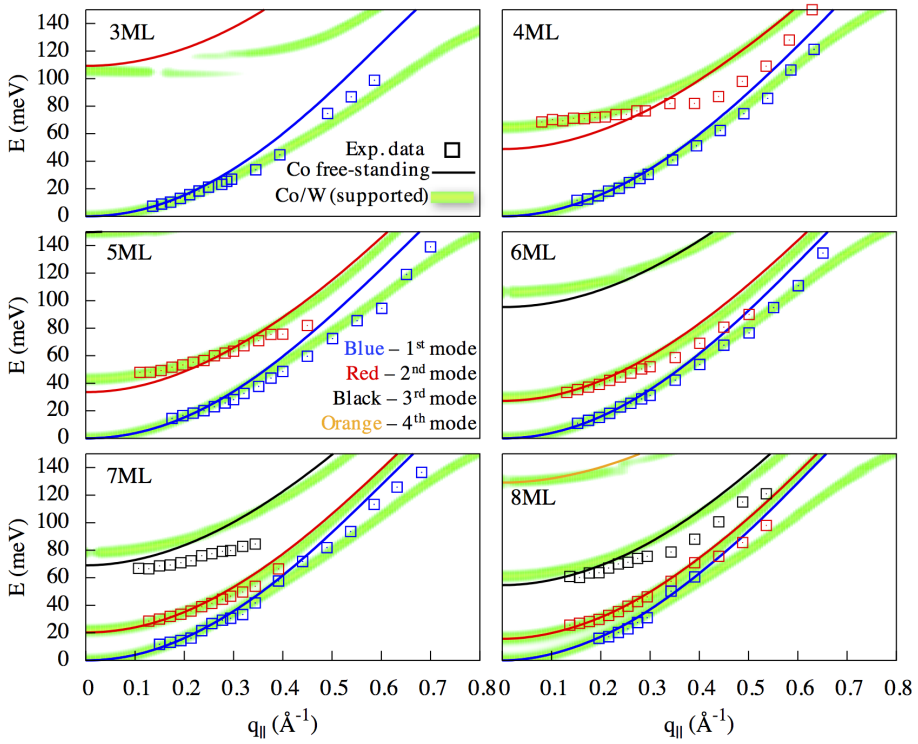

Figure 5.4.4: Comparison of calculated (lines) and experimentally measured spin-wave dispersions (squares, from Ref. [24]) for several thicknesses. The thin lines are the spin-wave branches obtained for the free-standing films, while the thick green-yellow lines (actually a color map) correspond to the unfolded dispersion for the W-supported films, Eq. (5.6). In the unfolding scheme, a Lorentzian broadening of width 4 meV was considered. The magnetic exchange coupling has been uniformly rescaled down by 30%.

for the third mode of 7 and 8ML films). The inset in Fig. 5.4.2, comparing the experimental stiffnesses with the rescaled theoretical ones, highlights that our results for the supported films capture much better the trends in the experimental data. Such a simultaneous match can not be achieved with the free-standing films, even by changing β arbitrarily. For example, if we adjust β to obtain good agreement for the optical mode energies at $q_{\parallel} = 0$ of the 4-5ML films, then the computed dispersions become much stiffer than the experimental ones; the optical mode energies at $q_{\parallel} = 0$ for 6-8ML films that were already matching well would then go off. As explained in the previous sections, the Co-W hybridization at the interface endows the supported film dispersions with the right features, $q_{\parallel} = 0$ energies and stiffnesses, reproducing the characteristics of the experimental data. For reference, a direct comparison of the theoretical results without rescaling with the experimental measurements can be found in Appendix 5.B.

5.5 Conclusions

The agreement between theoretical calculations and experimental measurements, shown in Fig. 5.4.4, required a rescaling of the magnetic interactions strength, attributed to the expected overestimation of the spin splitting in the first-principles calculations. We have explored other possibilities for the discrepancy between theory and experiment. One might wonder if the failure lies with the adiabatic approach for the calculation of the spin-wave excitations. Ref. [94] performed calculations for a Fe ML on W(110), comparing the results of the adiabatic approach to those including the coupling to the Stoner continuum, and found no substantial differences. However, this can be system-dependent. Recently, another possible explanation was put forward: finite-temperature softening of the spin-wave dispersion, as seen by calculating the dynamical structure factor for Fe overlayers on Ir(001) [109]. The idea is that temperature leads to a finite canting angle of the neighboring magnetic moments, which can reduce the strength of the magnetic exchange interactions [110]. However, the temperature can only play a role if the Curie temperature is close to the experimental temperature, which does not seem to be the case for Co/W(110), judging from the strength of the magnetic interactions. In short, the blame seems to lay on the LSDA approximation, and a computationally efficient first-principles correction to the spin splitting remains to be found.

We demonstrate in this chapter that the interface matters in determining the dispersion of the spin-waves of the entire magnetic thin film. Our first-principles calculations provided an extensive theoretical characterization of the impact of the tungsten substrate on the spin-waves of the cobalt ultrathin films. We found that only the Co layer directly at the interface with W is strongly affected, leading to a reduced spin moment, and weakened intralayer and interlayer magnetic exchange interactions. The qualitative differences between the spin-wave dispersions of free-standing and W-supported films are well explained by a simple nearest-neighbor Heisenberg model, which takes into account the changes in the magnetic properties of the Co layer at the interface. Taking into account the likely overestimated spin splitting of Co in the first-principles calculations, we found that good agreement with available EELS measurements could be reached for a realistic reduction of the strength of the magnetic exchange interactions.

Having validated our method with the rather complex material treated in this chapter, we are in a position of computing inelastic-scattering spectrum for non-collinear magnets, which we will do in the next chapter.

Appendix

5.A Spin-wave eigenvalues and eigenvectors of inhomogeneous ferromagnets

In this section, we want to write down the spin equation of motion that determines the spin waves in inhomogeneous ferromagnets with more than one atom in the unit cell. Only the magnetic exchange interaction is considered, as described by the Hamiltonian in Eq. (5.1). A given spin in the system rests at position $\mathbf{R}_{i\mu} = \mathbf{R}_i + \mathbf{R}_\mu$, where $\mathbf{R}_i$ points to the origin of unit cell i and $\mathbf{R}_\mu$ points, within the unit cell, the position of the basis atom μ. Thus, the effective field that applies a torque in $\mathbf{S}_{i\mu}$, and given by Eq. (2.80), is generalized to

$$\mathbf{B}_{i\mu}^{\text{eff}} = \sum_{j\nu} J_{i\mu,j\nu} \mathbf{S}_{j\nu} \quad . \tag{5.14}$$

The equation of motion in Eq. (2.80) then becomes:

$$\begin{aligned} \frac{\mathrm{d}\mathbf{S}_{i\mu}}{\mathrm{d}t} = &- \sum_{j\nu} \left[J_{i\mu,j\nu} \left(S_{i\mu}^y S_\nu - S_\mu S_{j\nu}^y \right) \right] \hat{\mathbf{x}} \\ &- \sum_{j\nu} \left[J_{i\mu,j\nu} \left(S_\mu S_{j\nu}^x - S_{i\mu}^x S_\nu \right) \right] \hat{\mathbf{y}} \quad , \end{aligned} \tag{5.15}$$

where we considered the spin motion to consist of small precession around the z–axis implying in $S_{i\mu}^x, S_{i\mu}^y \ll 1$, and $S_{i\mu}^z \approx S_\mu$. To decouple the equation of motion for each of the components of the spin, we introduce the circular components of the spins as given by Eq. (2.84), such that we obtain:

$$\begin{aligned} \mathrm{i}\frac{\mathrm{d}S_{i\mu}^+ + S_{i\mu}^-}{\mathrm{d}t} &= \sum_{j\nu} \left[J_{ij} \left(S_\nu(-S_{i\mu}^+ + S_{i\mu}^-) + S_\mu(S_{j\nu}^+ - S_{j\nu}^-) \right) \right] \\ \mathrm{i}\frac{\mathrm{d}S_{i\mu}^+ - S_{i\mu}^-}{\mathrm{d}t} &= \sum_{j\nu} \left[J_{ij} \left(S_\nu(-S_{i\mu}^+ - S_{i\mu}^-) + S_\mu(S_{j\nu}^+ + S_{j\nu}^-) \right) \right] \quad . \end{aligned} \tag{5.16}$$

From these two equations, we can get other two by summing or subtracting them, obtaining decoupled equations for the spin circular components:

$$\begin{aligned} -\mathrm{i}\frac{\mathrm{d}S_i^+}{\mathrm{d}t} &= S \sum_{j\nu} \left[J_{i\mu,j\nu} \left(S_\nu S_{i\mu}^+ - S_\mu S_{j\nu}^+ \right) \right] \\ \mathrm{i}\frac{\mathrm{d}S_i^-}{\mathrm{d}t} &= S \sum_{j\nu} \left[J_{i\mu,j\nu} \left(S_\nu S_{i\mu}^- - S_\mu S_{j\nu}^- \right) \right] \quad . \end{aligned} \tag{5.17}$$

We can exploit the system's translational symmetry via the lattice Fourier transform:

$$S^{\pm}_{\mathbf{k}\mu} = \frac{1}{\sqrt{N}} \sum_i e^{-\mathrm{i}\mathbf{k}\cdot\mathbf{R}_i} S^{\pm}_{i\mu} \quad , \quad S^{\pm}_{i\mu} = \frac{1}{\sqrt{N}} \sum_{\mathbf{k}} e^{\mathrm{i}\mathbf{k}\cdot\mathbf{R}_i} S^{\pm}_{\mathbf{k}\mu} \quad . \tag{5.18}$$

Then, by left multiplying Eq. (5.17) by $\frac{1}{\sqrt{N}} \sum_i e^{-\mathrm{i}\mathbf{k}\cdot\mathbf{R}_i}$, one gets

$$\begin{aligned} -\mathrm{i}\frac{\mathrm{d}S^{+}_{\mu}(\mathbf{k},t)}{\mathrm{d}t} =& S^{+}_{\mu}(\mathbf{k},t) \sum_{\nu} J_{\mu\nu}(0) S_{\nu} - S_{\mu} \sum_{\nu} J_{\mu\nu}(\mathbf{k}) S^{+}_{\nu}(\mathbf{k},t) \\ \mathrm{i}\frac{\mathrm{d}S^{-}_{\mu}(\mathbf{k},t)}{\mathrm{d}t} =& S^{-}_{\mu}(\mathbf{k},t) \sum_{\nu} J_{\mu\nu}(0) S_{\nu} - S_{\mu} \sum_{\nu} J_{\mu\nu}(\mathbf{k}) S^{-}_{\nu}(\mathbf{k},t) \quad , \end{aligned} \tag{5.19}$$

where the Fourier transformed exchange interaction matrix was defined as

$$J_{\mu\nu}(\mathbf{k}) = \sum_i e^{\mathrm{i}\mathbf{k}\cdot\mathbf{R}_{ij}} J_{i\mu,j\nu} \quad . \tag{5.20}$$

Finally, by taking the temporal dependence in the form $S^{\pm}_{\mu}(\mathbf{k},t) = S^{\pm}_{\mu}(\mathbf{k}) e^{-\mathrm{i}\omega^{\pm}_{\mathbf{k}} t}$, where $S^{\pm}_{\mu}(\mathbf{k})$ is now only a time-independent complex amplitude, we obtain

$$\mp\omega^{\pm} S^{\pm}_{\mu}(\mathbf{k}) = \sum_{\nu} S^{\pm}_{\mu}(\mathbf{k}) J_{\mu\nu}(0) S_{\nu} - \sum_{\nu} S_{\mu} J_{\mu\nu}(\mathbf{k}) S^{\pm}_{\nu}(\mathbf{k}) \quad . \tag{5.21}$$

After a few manipulations:

$$\begin{aligned} \mp\omega^{\pm} S^{\pm}_{\mu}(\mathbf{k}) =& \sum_{\nu} S_{\nu} \sum_{\xi} \delta_{\xi\mu} J_{\xi\nu}(0) S^{\pm}_{\xi}(\mathbf{k}) - S_{\mu} \sum_{\nu} J_{\mu\nu}(\mathbf{k}) S^{\pm}_{\nu}(\mathbf{k}) \\ \mp\omega^{\pm} S^{\pm}_{\mu}(\mathbf{k}) =& \sum_{\xi} S_{\xi} \sum_{\nu} \delta_{\nu\mu} J_{\nu\xi}(0) S^{\pm}_{\nu}(\mathbf{k}) - S_{\mu} \sum_{\nu} J_{\mu\nu}(\mathbf{k}) S^{\pm}_{\nu}(\mathbf{k}) \\ \mp\omega^{\pm} S^{\pm}_{\mu}(\mathbf{k}) =& \sum_{\nu} \left(\sum_{\xi} S_{\xi} \delta_{\nu\mu} J_{\nu\xi}(0) - S_{\mu} J_{\mu\nu}(\mathbf{k}) \right) S^{\pm}_{\nu}(\mathbf{k}) \quad , \end{aligned} \tag{5.22}$$

we can rewrite Eq. (5.21) as

$$\mp\omega^{\pm}_{r} S^{\pm}_{r\mu}(\mathbf{k}) = \sum_{\nu} \tilde{J}_{\mu\nu} S^{\pm}_{r\mu}(\mathbf{k}) \quad , \tag{5.23}$$

whose the eigenvalues $\mp\omega^{\pm}_{r}$ associated with the spin-wave mode r is obtained by diagonalizing the matrix

$$\tilde{J}_{\mu\nu} = \delta_{\nu\mu} \sum_{\xi} S_{\xi} J_{\nu\xi}(0) - S_{\mu} J_{\mu\nu}(\mathbf{k}) \quad . \tag{5.24}$$

In general, this matrix is not hermitian, therefore, an appropriated diagonalization is to be performed following the steps discussed in Sec 2.4.2.

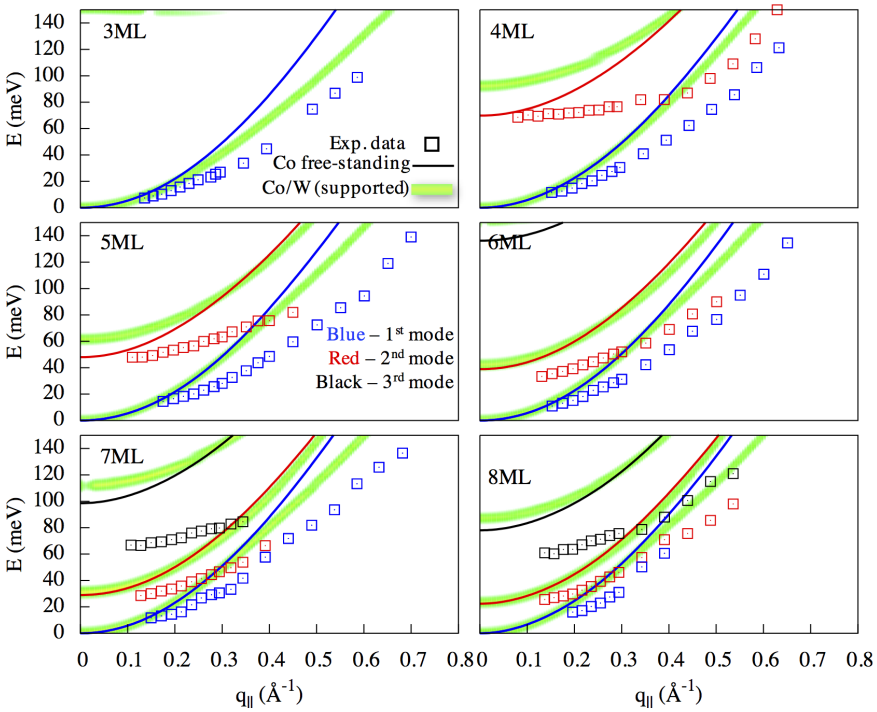

Figure 5.B.1: Comparison of calculated (lines) and experimentally measured spin-wave dispersions (squares, from Ref. [24]) for several thicknesses. The thin lines are the spin-wave branches obtained for the free-standing films, while the thick green-yellow lines (actually a color map) correspond to the unfolded dispersion for the W-supported films, Eq. (5.6). In the unfolding scheme, a Lorentzian broadening of width 4 meV was considered.

5.B Direct theory-experiment comparsion

In Fig. 5.4.4 we have shown that a comparison between the theoretical results with the exchange coupling reduced by 30% and the experimental data of Ref. [24], led to very good agreement, especially for the calculation of cobalt deposited on tungsten. Here, we also present a direct comparison using unscaled parameters obtained by first-principles; see Fig. 5.B.1. The spin-wave stiffnesses and $q_{\parallel} = 0$ energies are overestimated in the theoretical results, which led us to explore possible explanations for this disagreement, as described in the main text.

Chapter 6

Spin-resolved electron-energy-loss spectroscopy (SREELS)

After having studied ferromagnetic systems in the previous chapter, we now turn our focus onto noncollinear magnetic textures. We are interested in how inelastic electron scattering, being suitable for investigations of surfaces and thin films, can detect the collective spin-excitation spectra of noncollinear magnets, and what kind of information we can acquire through it. We take as an example a hexagonal lattice of spins in three of its magnetic phases: a spin spiral, a topologically-nontrivial skyrmion lattice, and the ferromagnetic phase serving as a reference. To reveal the particularities of spin waves in such noncollinear samples, we propose the usage of spin-resolved electron-energy-loss spectroscopy augmented with a spin analyzer, which would allow to experimentally access different elements of the spin-spin correlation tensor introduced in Chapter 4. With the spin analyzer detecting the polarization of the scattered electrons, four spin-dependent scattering channels are defined, permitting to filter and select specific spin-wave modes. Then, we demonstrate that counterintuitively and in contrast to the ferromagnetic case, even non-spin-flip scattering processes can generate spin waves in noncollinear substrates. The obtained dispersion and lifetime of the excitation modes permit us to fingerprint the magnetic nature of the material. This chapter is also based on Ref. [26] written by the author of this dissertation.

6.1 Introduction and motivation

Recently and as mentioned in Chapter 1, exquisite magnetic states related to chiral interactions in noncentrosymmetric systems have been discovered and intensively investigated. They are noncollinear magnetic structures such as skyrmions and antiskyrmions, magnetic bobbers and spin spirals, which are at the heart of many proposals for future information nanotechnology [7–10, 111]. These states arise from the delicate balance of internal and external interactions, such as the magnetic exchange, Dzyaloshinskii-Moriya and magnetic fields, which can trigger topologically nontrivial properties [12, 112–114]. Most important for applications is the formation of these complex spin textures in ultrathin films, given that they can be tailored by the structure and composition of heterogeneous multilayers [15, 114, 115]. Concurrently, spin waves have been explored for their potential application in spintronic

and magnonic devices [4, 5, 116–118]. However, the behavior of spin waves in these noncollinear systems is only now beginning to be understood [13, 119–127].

Do spin waves inherent special properties due to the topology of the magnetic structure that may lead to revolutionary applications? To start answering this question, we need to understand the manifestation of spin waves in these novel magnetic phases: how they may be excited, controlled and detected. Noncollinear magnetic structures intrinsically feature many spin-wave bands (or modes) due to the breaking of translational and rotational symmetries, as we showed in Chapter 2. However, only a few of them can be excited or detected by a given experimental setup. Thus, a discussion of spin-wave excitations must go together with the exciting/probing technique. On the one hand, inelastic neutron-scattering and microwave resonance have been used to investigate collective spin-excitations in bulk chiral helimagnets and two-dimensional skyrmion lattice [120, 121, 123, 126]. While the first lacks surface sensitivity, the second is restricted to excitations near the Γ–point, as mentioned in Chapter 4. On the other hand, inelastic electron scattering has been applied with great success to study spin waves in ultrathin films [17, 18, 24, 25, 88, 128–132], due to the large scattering cross section of the electrons. However, to the best of our knowledge, it has only been employed for ferromagnets. The same is true from the theoretical side [85, 133].

Currently, inelastic electron scattering to study spin waves is performed in two setups, the electron-energy-loss spectroscopy (EELS) and the spin-polarized electron-energy-loss spectroscopy (SPEELS). While the first allows for great energy resolution, the second is necessary to fully characterize spin waves in ferromagnets, including their angular momenta [18, 24, 25]. To investigate these spin excitations in noncollinear magnets, we need to go beyond.

6.2 Experimental proposal

We propose an experimental setup based on SPEELS [17, 18], but adding a spin-filter to the scattered electrons, which we will call spin-resolved electron-energy-loss spectroscopy (SREELS), see Fig. 6.2.1. It consists of preparing a spin-polarized monochromatic electron beam, which then scatters from the first few layers of the sample surface. Scattered electrons may exchange energy, angular and linear momentum due to the creation or annihilation of spin waves. By the conservation laws of these quantities, measuring their exchanges informs upon spin-wave states of the magnetic system. An incoming beam with up or down spin polarization generates outgoing electrons in a quantum superposition of up and down states, due to atomic spin moments not aligned with the beam polarization axis. Then, by filtering the spin of the outgoing electrons, two non-spin-flip scattering channels, up-up and down-down, and two spin-flip ones, up-down and down-up, are defined. The meaning of these channels will be discussed later with specific examples.

We consider an incoming (outgoing) beam with energy E_i (E_f), wavevector $\mathbf{k}_\mathrm{i}$ ($\mathbf{k}_\mathrm{f}$), and spin projection s_i (s_f), which interacts with a sample held at zero temperature, i.e., in its ground state. These variables define the energy absorbed by the sample $\omega = E_\mathrm{i} - E_\mathrm{f}$, and the linear and angular momentum transferred, $\mathbf{q} = \mathbf{k}_\mathrm{i} - \mathbf{k}_\mathrm{f}$ and $m = s_\mathrm{i} - s_\mathrm{f}$, respectively. There are thus three distinct angular momentum scattering channels, $m = 0, \pm 1$, according to the four possible combinations of s_i

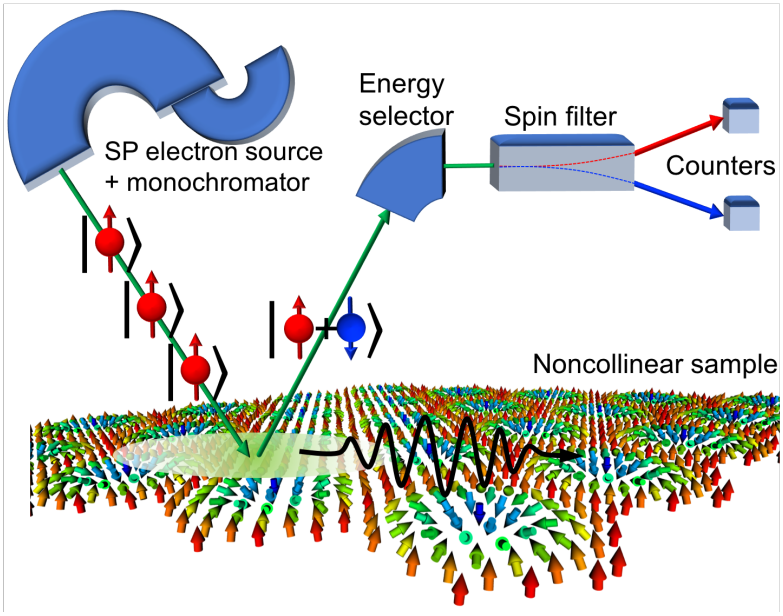

Figure 6.2.1: Schematic picture of spin-resolved electron-energy-loss spectroscopy (SREELS). A monochromatic spin-polarized (SP) electron beam is aimed at the surface of a noncollinear magnetic sample. The magnetic noncollinearity leads to a mixed spin state of the outgoing electrons. These are then collected for spectroscopical analysis, having both their energy and spin characterized.

and s_f.

As discussed in Chapter 4, we assume that the electrons couple with the atomic spins via a local exchange interaction $\boldsymbol{\sigma} \cdot \mathbf{S}_\mu$, where μ labels the basis atom in the unit cell, $\boldsymbol{\sigma}$ is the Pauli vector describing the electron spin, and $\mathbf{S}_\mu$ is the vector operator describing the atomic spin. Starting from the Schrödinger equation for the coupled system of electron beam and magnetic sample, time-dependent perturbation theory leads to Fermi's Golden Rule for the transition rate between initial and final electron states, as given by Eq. (4.28), reads:

$$\Gamma_{if}(\mathbf{q},\omega) \propto \sum_{\alpha\beta} \sigma^{\alpha}_{s_i s_f} \sigma^{\beta}_{s_f s_i} \sum_{\mu\nu} e^{\mathrm{i}\mathbf{q}\cdot\mathbf{R}_{\mu\nu}} \mathcal{N}^{\alpha\beta}_{\mu\nu}(\mathbf{q},\omega) \quad . \tag{6.1}$$

Here $\alpha, \beta = +, -, z$, $\sigma^{\pm} = (\sigma^x \pm \mathrm{i}\sigma^y)/2$, and $\sigma^{\alpha}_{s_i s_f} = \langle s_i | \sigma^{\alpha} | s_f \rangle$ with z being the spin quantization axis of the beam polarization. The wave nature of the electron beam leads to the Fourier factor connecting the basis atoms in the unit cell ($\mathbf{R}_{\mu\nu} = \mathbf{R}_\nu - \mathbf{R}_\mu$), and is responsible for the unfolding of the spin-wave modes, as discussed in Chapter 5. The information about the spin excitations of the sample is contained in the spin-spin correlation tensor, given by Eq. (4.43):

$$\begin{aligned} \mathcal{N}^{\alpha\beta}_{\mu\nu}(\mathbf{q},\omega) = 2\sqrt{S_\mu S_\nu} \sum_r \delta\big(E_0 + \omega - E_r(\mathbf{q})\big) \times \\ \left[O^{\alpha+}_{\mu}(\mathcal{R}^{++}_{\mu r}(\mathbf{q}))^* + O^{\alpha-}_{\mu}(\mathcal{R}^{-+}_{\mu r}(\mathbf{q}))^*\right] \left[O^{\beta+}_{\nu}\mathcal{R}^{-+}_{\nu r}(\mathbf{q}) + O^{\beta-}_{\nu}\mathcal{R}^{++}_{\nu r}(\mathbf{q})\right] \quad , \end{aligned} \tag{6.2}$$

where O_μ is the rotation matrix that maps the local reference frame of the μ–th spin into the global frame. $\mathcal{R}_r(\mathbf{q})$ and $E_r(\mathbf{q})$ represent the eigenvector and eigenvalue associated with the r–th spin-wave mode as obtained via the Bogoliubov transformation in Sec. 2.4.2. It is the possibility of accessing different elements of the $\mathcal{N}_{\mu\nu}^{\alpha\beta}(\mathbf{q},\omega)$ tensor in distinct SREELS spin channels that provides unique information about the spin-excitations of complex noncollinear magnets, as will be demonstrated in the following.

6.3 SREELS of different magnetic phases

We illustrate the significance of the general result discussed above with a hexagonal monolayer model as depicted in Fig. 6.3.1 (a), which is described by the following Hamiltonian:

$$\mathcal{H} = -\frac{1}{2}\sum_{\langle i,j\rangle}\left(J\,\mathbf{S}_i\cdot\mathbf{S}_j + D\,\hat{\mathbf{n}}_{ij}\cdot(\mathbf{S}_i\times\mathbf{S}_j)\right) - B\sum_i S_i^z - K\sum_i (S_i^z)^2 \quad , \tag{6.3}$$

which was previously discussed in Sec. 2.1.6. The sums run over all lattice sites i and over all nearest-neighbor pairs $\langle i,j\rangle$ with its lattice constant taken as the unit of length ($a = 1$). J is a positive constant for an isotropic magnetic exchange interaction favoring, therefore, a ferromagnetic alignment between spins. D is the coupling parameter of the Dzyaloshinskii-Moriya interaction, which favors canting of the spins. Its direction is $\hat{\mathbf{n}}_{ij} = \hat{\mathbf{z}}\times\hat{\mathbf{R}}_{ij}$, orthogonal to both the bond direction and the normal to the monolayer plane, as shown in Fig. 6.3.1 (a). Such DMI configuration favors the formation of cycloidal spin spirals. B is the external magnetic field and K is the uniaxial anisotropy. The atomic spin is set to $S = 1$ and J is taken as the unit of energy, defining the remaining model parameters as $D = J$, $B = 0.36\,J$ and $K = 0.25\,J$. We then construct $\mathcal{N}_{\mu\nu}^{\alpha\beta}(\mathbf{q},\omega)$ by calculating the spin waves states of this model within the adiabatic approach, as explained in Sec. 2.4. We now apply our formalism to three different magnetic states.

6.3.1 Ferromagnet

With $D = 0$, the ground state of the spin model is ferromagnetic and its total spin is maximal, see Fig. 6.3.1 (b). With the polarization of the beam parallel to the spin of the sample, we find only one active inelastic scattering channel, the down-up, shown in Fig. 6.3.1 (d). The spectrum was calculated through the reciprocal space path depicted in Fig. 6.3.1 (c), where we observe a single and continuous spin-wave branch. This spectrum corresponds to the creation of collective excitations with angular momenta of -1. That is, spin waves in ferromagnetic systems have spin angular momenta opposite to the spins of the ground state. And that is why we find no signal from spin waves in any of the other SREELS spin channels, as discussed in Sec. 4.1.4. This is the picture familiar from (SP)EELS experiments [17, 18, 23]. In Fig. 6.3.1 (d), we observe the energy minimum at the Γ–point, where the energy gap is caused by the external magnetic field and the magnetic anisotropy.

For the ferromagnetic state, we only need one magnetic site per unit cell. Had we chosen an atom basis with more atoms, such as the one we used for Fig. 2.5 (a), we

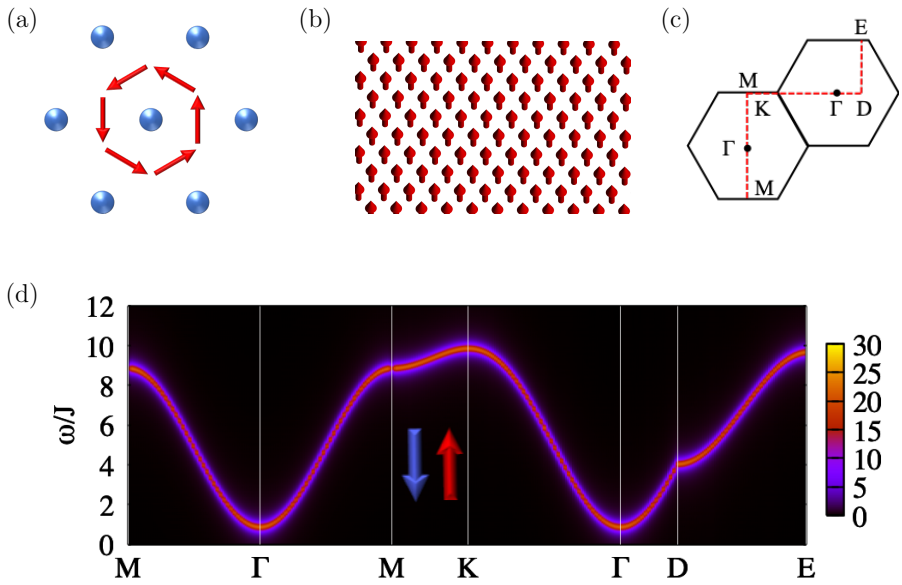

Figure 6.3.1: (a) The hexagonal lattice spin model. We consider only nearest-neighbor interactions. The red arrows represent the DMI vectors that can lead to spin spirals and skyrmion lattices. (b) In the absence of the DMI, the ground state is a ferromagnetic phase. (c) The reciprocal-space path through which we calculated the SREELS spectra. (d) SREELS down-up scattering channel for the ferromagnetic phase, the only one nonvanishing for this spin configuration when the polarization of the probing electrons is parallel to the spins of the magnetic system.

would have gotten many spin-wave modes. Calculating the inelastic scattering spectrum does the work of unfolding the spin-wave dispersion as discussed in Chapter 5, which recovers the picture of one atom per unit cell.

6.3.2 Spin spiral

Keeping now only J and D in the spin model, the ground state becomes a spin-spiral. We considered a cycloidal spin spiral of wavevector $\mathbf{Q} = Q\,\hat{\mathbf{y}}$. Its energy is minimized by $Q = \alpha/d$, where $\alpha = \arctan(\sqrt{3}D/2J)$ and $d = a\sqrt{3}/2$ is the distance between rows of parallel spins, as was demonstrated in Sec. 2.2.2. For convenience, we set $D = 2J/\sqrt{3}$ leading to a spin-spiral wavelength $\lambda = 8d$, as in Fig. 6.3.2 (a). This magnetic state has zero net magnetization.

Figure 6.3.2 (c-d) shows the spin-resolved inelastic electron scattering spectra calculated from Eq. (6.1) on the path of Fig. 6.3.2 (b). We considered the electron beam polarization along z — up and down are defined with respect to this axis. The spin-conserving channels ($m = 0$) always present the same response, because they measure scattering processes that have zero net angular momentum and, therefore, are insensitive to the spin of the probing electrons. Here, the spin-flip channels are equivalent because of the symmetry of the magnetic structure with respect to z.

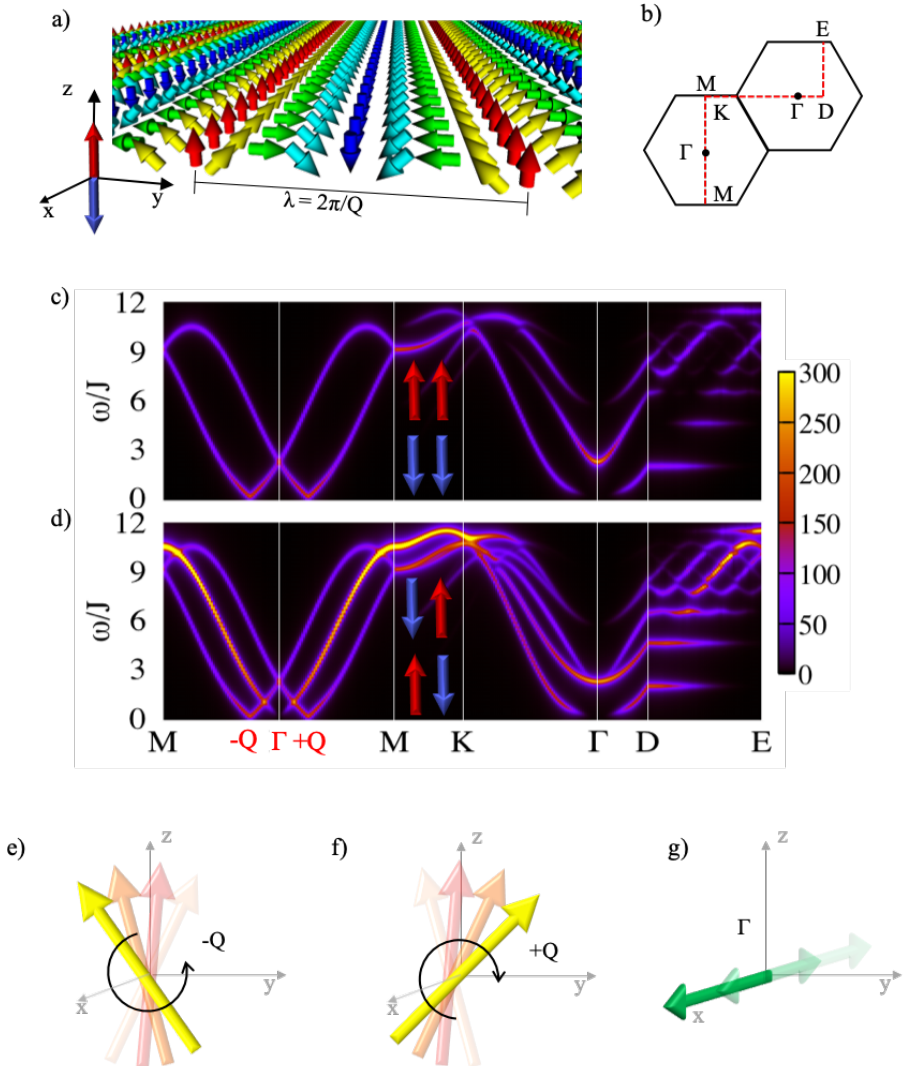

Figure 6.3.2: Spin-waves for a spin-spiral structure, beam polarization along z. (a) Spin-spiral ground state and crystallographic axes. The red and blue arrows correspond to the two considered spin polarizations of the electron beam. (b) Path in reciprocal space being considered for the calculations of the SREELS spectra. These are shown in (c) for the spin-conserving channels, and in (d) for the spin-flip channels. The arrow pairs indicate the initial and final electron spin polarization for each channel. (e-g) Sketch of the low-frequency motion of the net atomic spin for the three spin-wave modes with minima in $-Q$, $+Q$ and Γ, respectively.

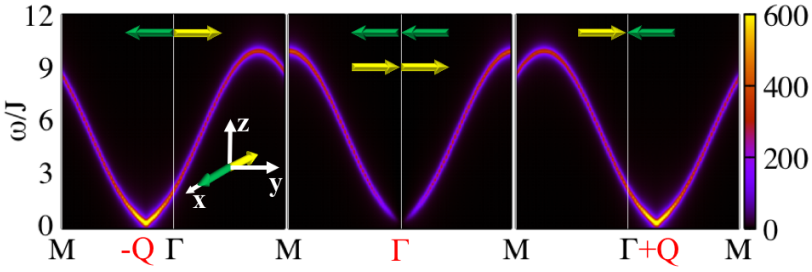

Figure 6.3.3: SREELS spectra for spin-waves in a spin-spiral as in Fig. 6.3.2. Here, the beam polarization is along x, which is aligned with the precession axis of the spin-waves. Thus, each scattering channel probes a single spin-wave mode.

Three modes are clearly observed in the spin-flip channels, Fig. 6.3.2 (d), as sharp and well-defined dispersing features through the M–Γ–M path. They have energy minima in −Q, Γ and +Q, which we will use to label them. These modes are the three universal helimagnon modes [120], in contrast to the single Goldstone mode in ferromagnets, such as the one shown in Fig. 6.3.1 (d). For low frequency, the −Q and +Q are excitations that yield a net atomic spin rotating counter-clockwise and clockwise, respectively, in the $z - y$ plane, see Fig. 6.3.2 (e-f). For the Γ–mode, however, the total atomic spin does not rotate but oscillates linearly along with the x–axis, as in Fig. 6.3.2 (g). Note the highly anisotropic dispersion-relation around the Γ–point. It is linear or quadratic for spin-waves propagating parallel or transversal to $\mathbf{Q}$, respectively, as seen in Fig. 6.3.2 (d), paths M–Γ–M and K–Γ–D [119, 134]. Furthermore, Fig. 6.3.2 (c-d, path D-E) shows the formation of one-dimensional spin-waves, as indicated by the dispersionless bands [120, 135].

The dynamics of the spin-wave modes depicted in Fig. 6.3.2 (e-g) indicates the x–axis as the natural quantization axis. It defines left and right spin projections. An incident electron with up or down polarization corresponds to a superposition of left and right spinors with respect to the x–axis. The −Q (+Q) mode can be excited by an electron with left (right) polarization, which then undergoes a spin-flip and goes out with right (left) polarization. Therefore, −Q and +Q are seen by the spin detector as a superposition of the up and down polarizations, and this makes them be detected in all channels. Due to quantum interference, the Γ–mode disappears from the non-spin-flip channels, and it is intensified in the spin-flip ones, see Fig. 6.3.2 (c-d). Now, if we rotate the polarization of the electron beam to be aligned with the x–axis, each mode will appear in a distinct scattering channel, as demonstrated in Fig. 6.3.3. Also, overall the intensities are higher now with the polarization axis along the spin-wave precession axis. In practice, controlling the polarization direction of the beam and of the spin detector, which indeed are independent, allows SREELS to select or render undetected certain spin-wave modes.

6.3.3 Skyrmion lattice

An increasing external magnetic field is responsible for deforming the spin-spiral phase into a conical state, then into the skyrmion lattice [123]. We concentrate on the skyrmion lattice shown in Fig. 6.3.4 (a), which was obtained via numerical

energy minimization using an atomistic-spin-dynamics simulation. The polarization of the electron beam is again along z. Fig. 6.3.4 (c-e) shows the SREELS spectra on the path displayed in Fig. 6.3.4 (b). Fig. 6.3.4 (c) demonstrates that the spin-wave spectrum of a skyrmion lattice inherits the two-mode structure found for the spin spiral (see Fig. 6.3.2 (c), although both branches are now much broader. Contrary to the usual spin-wave broadening due to coupling to phonons or electrons [89, 136, 137], here it originates in the noncollinearity of the magnetization. Note that the down-up spectrum in Fig. 6.3.4 (d) has overall a higher intensity than the up-down one in Fig. 6.3.4 (e), due to the upward total atomic spin of the system. Still in Fig. 6.3.4 (d), around Γ we observe that the gapless feature has a quadratic dispersion, while the one with a minimum at $\omega/J \sim 3$ disperses linearly.

Fig. 6.3.4 (f-h) depicts the time evolution of the spin-wave modes responsible for the high-intensity spots at the Γ–point in the various channels. The color maps represent the z–component of the local atomic spins, and the arrows illustrate the total atomic spin. The hotspot in the non-spin-flip channels, Fig. 6.3.4 (c), is due to a breathing mode, where the skyrmion core shrinks and enlarges periodically. It has zero net angular momentum, as seen by the dynamics of the total atomic spin in Fig. 6.3.4 (f). Two rotational modes identified in the down-up channel near $\omega/J \sim 3$ and at zero are clockwise, and the dynamics of their total atomic spin indicates that they possess downward angular moments, Fig. 6.3.4 (g). A counter-clockwise rotational mode is responsible for the faint hotspot in the up-down channel, Fig. 6.3.4 (h), therefore, with upward angular momentum. This explains their appearance in their respective scattering channels.

6.4 Conclusions and discussion

In this chapter, we showed that inelastic electron scattering can reveal various spin-wave phenomena in noncollinear magnets throughout the reciprocal space. We demonstrated that it can measure anisotropies in the dispersion relation, such as the linear and quadratic behavior along different propagation directions, and the localization of spin waves along certain directions that yields to desired spin-wave channeling for spintronics [119, 120, 134, 135]. Furthermore, we showed that manipulating the polarization of the electron beam allows us to select and filter the spin-wave modes, which in practice permits us to improve the energy resolution of the dispersion curves by detecting a particular spin-wave mode without the interference of nearby modes.

The realization of the SREELS may be applied to fingerprint magnetic phases from their unique signatures on the spin-wave spectra. It could, for example, help to distinguish between a skyrmion tube and a magnetic bobber lattice in thin films [10]. These two phases may have similar magnetic profiles at the very surface, but they differ deeper inside the film, which impacts on their spin-wave properties.

Recent developments have allowed full spin characterization of flying electrons by surface skew-scattering [138]. This could be used as a spin-filter in SREELS, but it might also require a high-intensity electron beam, to compensate for the low efficiency of the spin detection. A more efficient and intuitive way could be a Stern-Gerlach apparatus for electrons. However, the feasibility of such an experiment has been discussed since the earliest years of quantum mechanics. The difficulties

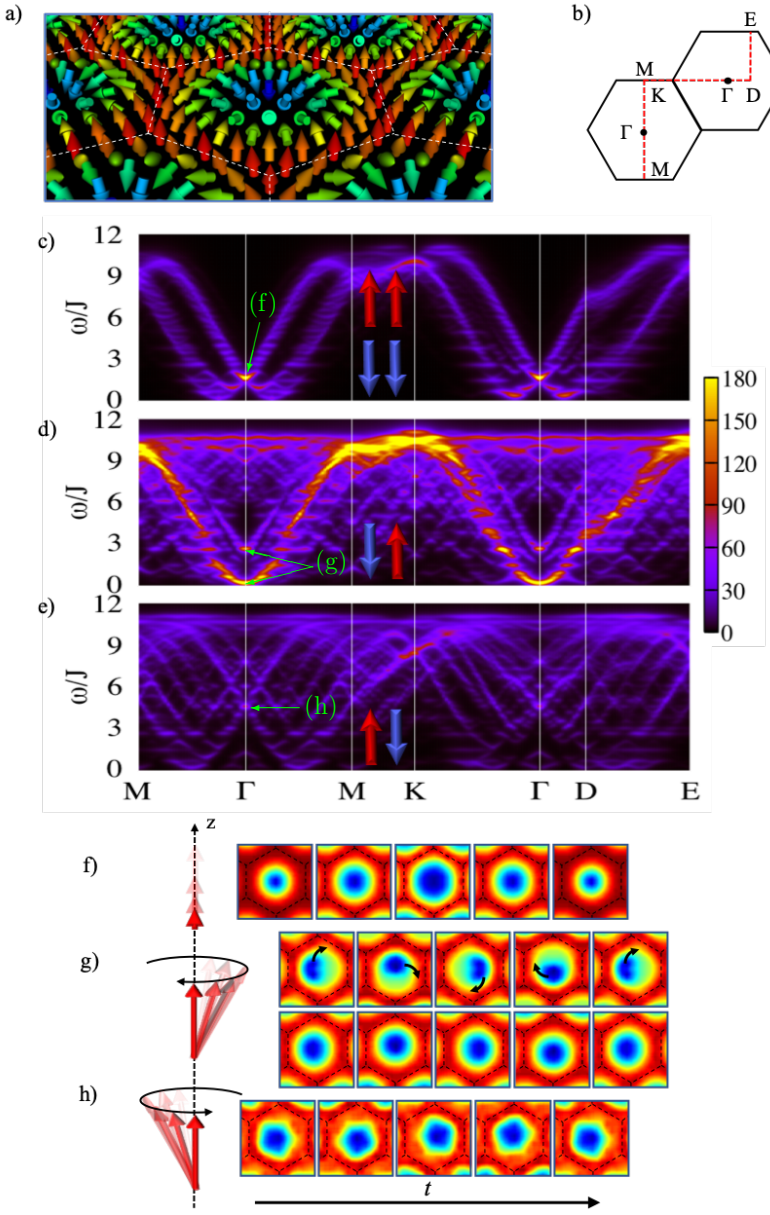

Figure 6.3.4: Spin-waves in a skyrmion lattice. (a) Shows the ground state spin structure of the system. The colors represent the z-component of the spins. (b) Depicts the path on which all four SREELS spectra were calculated, (c-e). (f–h) snapshots of the z–component of the local atomic spins over time (as color maps), depicting the spin-wave motion at the hotspots (indicated by the green arrows) of the spectra. Same color scale as in (a). (f) corresponds to a breathing mode that is measured in the non-spin-flip channels. (g) and (h) are clockwise and counter-clockwise rotational modes observed in the down-up and up-down channels, respectively.

are associated with the Lorentz forces acting on the electrons and fundamental quantum limitations, blurring the magnetic effects on the classical trajectory of the electrons [139–141]. Nevertheless, further theoretical developments have shown that quantum effects are essential but they do not overwhelm the spin-related effects on the electron's trajectory, leaving open the possibility of creating an electron-polarizing beam splitter [142–144]. Therefore, we hope that our work will encourage investigations on such a spin-splitter by providing an important application.

Despite the enrichment that the spin analysis brings to the discussion, spin waves in noncollinear systems can be measured with the existing (SP)EELS setups. Their spectra would consist of combinations of the different scattering channels that we have described for SREELS. However, one loses the ability to understand and determine the nontrivial angular momenta of spin waves in noncollinear magnets. Furthermore, as discussed in Chapter 4, the theoretical framework developed for SREELS could also be extended to other experimental techniques, such as spin-polarized inelastic neutron scattering.

In this chapter, we have discussed the fundamental properties of spin waves in noncollinear using a simple model system. For the next chapters, we continue this investigation and apply our theoretical approach for realistic materials, for which the Hamiltonian parameters are obtained from first-principles calculations. In particular, in the next chapter, we investigate systems whose magnetic exchange interaction is dominantly antiferromagnetic.

Chapter 7

Antiferromagnetic noncollinear spin textures

Up to here, we studied the behavior of spin waves in ferromagnets, as in the case of reconstructed thin films of Co/W(110), and in two noticeable noncollinear spin textures, namely a spin spiral and a skyrmion lattice. These systems shared a common feature, their predominant ferromagnetic exchange coupling. Therefore, the canting induced by the Dzyaloshinskii-Moriya interaction (DMI) could be seen locally as a small deviation from the ferromagnetic state.

Antiferromagnetic materials are internally magnetic, but with spins antialigned to their neighbors causing the net magnetization to be zero. This makes the magnetism in these materials "invisible", but at the same time extremely valuable for spintronics [145, 146]. For example, high-density random access memories that are more stable against magnetic field perturbations have been proposed based on antiferromagnetic materials [147]. Therefore, in this chapter, we explore the main characteristics of collective spin excitations in noncollinear magnetic samples with strong antiferromagnetic predominance.

The chapter is divided into four parts: The first part addresses in a model basis unidimensional spin spirals arising in antiferromagnets due to the DMI, and the breaking of reciprocal symmetry of the spin-wave dispersion when the system is subject to an external magnetic field. Then, the second section deals with the physics of spin waves in antiferromagnetic bidimensional systems, including skyrmionic spin structures. The third part is an *ab initio* study of a monolayer of manganese deposited on β–tungsten (Mn/β–W), which is a promising antiferromagnetic system for spintronics. And finally, the fourth part concerns the *ab initio* investigation of bulk Mn_5Si_3. Here, we compared our results to experimental inelastic-neutron-scattering data shining some light onto an open question related to the nature of the excitations responsible for the inelastic spectrum of this material [29].

7.1 Antiferromagnetism in a spin chain

To set the stage, let us start by studying an antiferromagnetic unidimensional spin chain. We consider a spin chain with only negative nearest-neighbor magnetic exchange coupling J. An easy-axis magnetocrystalline anisotropy K along z is also introduced to set a preferred alignment direction. The system is then described by

the generalized Heisenberg Hamiltonian described in Section 2.1.6 that reads

$$\mathcal{H} = -\frac{1}{2}\sum_{\langle ij\rangle} J\mathbf{S}_i \cdot \mathbf{S}_j - \frac{1}{2}\sum_{\langle ij\rangle} D\hat{\mathbf{n}}_{ij} \cdot \left(\mathbf{S}_i \times \mathbf{S}_j\right) - K\sum_i \left(S_i^z\right)^2 - B\sum_i S_i^z \quad , \quad (7.1)$$

which also includes the Dzyaloshinskii-Moriya interaction of strength D and direction $\hat{\mathbf{n}}_{ij}$, and an external uniform magnetic field B along z. The brackets indicate a sum over the nearest-neighbor pairs.

Throughout this chapter, we calculate the inelastic-scattering spectra of the various spin systems. They are calculated as explained in Chapters 4 and 6 based on the description of spin waves in noncollinear magnets given in Chapter 2. For simplicity, each inelastic-scattering spectrum shown in this chapter is composed of the sum of all the spin scattering channels. The ground-state or metastable spin configurations were obtained through atomistic-spin-dynamics simulations based on the Landau–Lifshitz–Gilbert equation of motion, as discussed in Sec. 2.2.3 and implemented in the *Spirit* code [47].

7.1.1 The effect of the DMI and the magnetic field in the spin waves of collinear antiferromagnets

When B and D are zero, i.e., considering only the magnetic exchange interaction (MEI) and the magnetocrystalline anisotropy, the ground state of the system corresponds to a collinear alignment of the spins parallel to the anisotropy easy-axis z. The nearest-neighbor spins are antialigned to each other, as shown in Fig. 7.1.1 (a). The inelastic-scattering spectrum shows a single branch even though one could expect two because of the two sublattices (one for up and the other for down spins), which increases the number of internal degrees of freedom, see Fig. 7.1.1 (b). This system has two rotational spin-wave modes with opposite sense of precession, labeled $+Q$ and $-Q$, which are degenerate. They have energy minima at Γ and at the Brillouin zone border X, but the scattering intensity vanishes towards the former one. The energy gap is due to the magnetic anisotropy.

If the Dzyaloshinskii-Moriya vector is collinear with the magnetic moments, the energy degeneracy of the spin-wave branches is broken, and they shift in opposite directions in the reciprocal space, see Fig. 7.1.2 (a). This happens because the relative canting between spins when precessing for a given wavevector k other than X can be energetically favored by the DMI. This phenomenon is similar in nature to the Rashba effect, where electrons acquire a finite group velocity at zero wavevector due to the spin-orbit coupling [32]. Because of that, we call it a spin-wave Rashba effect. The shift is proportional to the DMI strength [31]. Yet, $+Q$ and $-Q$ are reciprocally symmetric with respect to the X–point. This means that spin waves propagate just as easy in both spin-chain directions, but with opposite chirality. Finally, turning on the external magnetic field, we observe a break of the reciprocity, causing the $-Q$ mode to have higher energies, while the $+Q$ goes lower, as observed in Fig. 7.1.2 (b). The magnetic field favors now a particular rotational sense, the one corresponding to the Larmor precession.

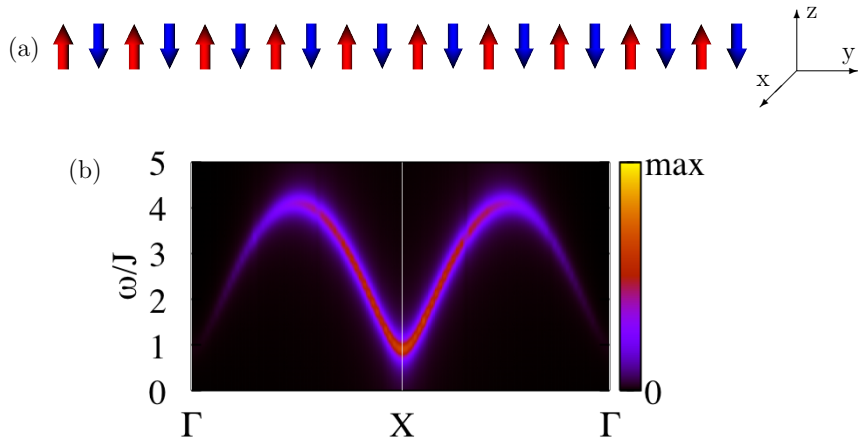

Figure 7.1.1: Antiferromagnetic spin chain. a) The ground state, where the spins align antiparallel among neighbors. b) Spin-wave scattering spectrum (sum of all scattering channels) for an antiferromagnetic spin chain depicted in (a). The single dispersion branch centered at X is due to two oppositely rotating modes, a clockwise and a counter-clockwise. Model parameters: $J = -1$, $D = 0$, $K = 0.05$, $B = 0$ a.u. For details on the calculation of the inelastic-electron-scattering spectrum, see Chapters 4 and 6.

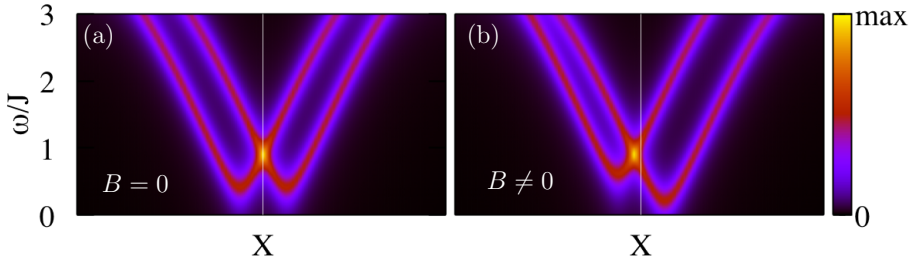

Figure 7.1.2: Spin-wave scattering spectrum of an antiferromagnetic spin chain. (a) The Dzyaloshinskii-Moriya vectors pointing along z shifts to the left and the right the dispersion curves of the $-Q$ and $+Q$ modes, respectively. For zero external magnetic field, the spectrum is symmetric. (b) When a magnetic field is applied, the spectrum becomes nonreciprocal. Despite the DMI, the system has the same collinear ground state shown in Fig. 7.1.1 (a), stabilized by the magnetic anisotropy. Model parameters: $J = -1$, $D = 0.2$, $K = 0.05$, $B = 0.2$ a.u.

7.1.2 Antiferromagnetic spin spiral

If we further increase the magnetic field along z, it becomes very stressful for the system to keep half of the spins oppositely aligned to the external magnetic field. Flipping these antialigned spins would be extremely unfavorable to the exchange energy. Meanwhile, the magnetic anisotropy favors the alignment of the spins along

z. When the external magnetic field is large enough, the system undergoes a spin-flop transition, where a spin spiral is established with the spins mostly lying in the plane perpendicular to the field, but with a small component along the field, see Fig. 7.1.3 (a). Thus, the system gains Zeeman energy due to the small magnetization along the field, and Dzyaloshinskii-Moriya energy from the noncollinearity of the spin spiral. The transition happens when these two contributions overcome the lost anisotropy energy. The pitch of the antiferromagnetic spin spiral is also proportional to the arctangent of the ratio between the D and J, just as for ferromagnetic systems, as we show in Apx. 7.A.

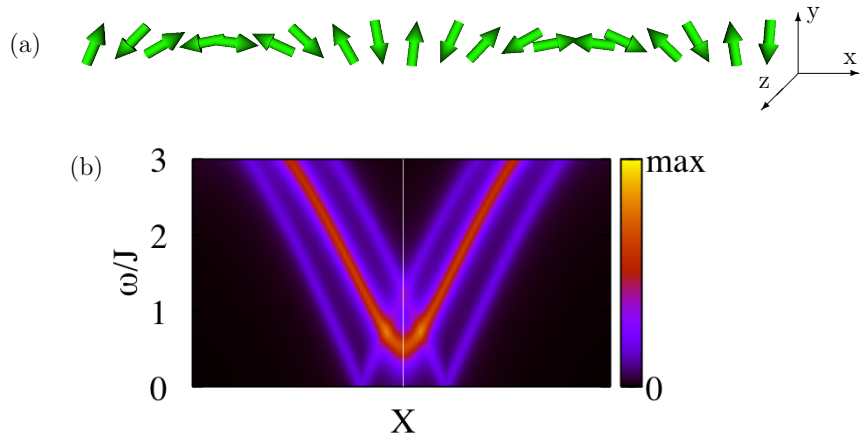

Figure 7.1.3: Antiferromagnetic spin spiral. a) The ground state generated by a spin-flop transition induced by a high external magnetic field along z. The spins lie in the plane perpendicular to the applied field forming an antiferromagnetic spin spiral. A small component of each spin still points along z what makes it a conical spin spiral. b) Spin-wave scattering spectrum of the antiferromagnetic spin spiral as depicted in (a). The spectrum is symmetric and formed by the brightest mode centered at X enclosed by the other two features centered at $\pm q$, where q is the wavevector of the spiral. Model parameters: $J = -1$, $D = 0.2$, $K = 0.05$, $B = 0.8$ a.u.

The reciprocal symmetry is restored to the spectrum, even though there is an even stronger applied field. The signal is formed by a central feature enclosed by two side ones of lower intensity. In Ref. [148], Gitgeatpong *et al.* investigated the bulk antiferromagnet α–$Cu_2V_2O_7$ via inelastic neutron scattering. The spin-wave physics of this compound is analogous to the model just described. They have measured for the first time the nonreciprocity of spin waves in antiferromagnets by applying an external magnetic field as shown in Fig. 7.1.4 (a), which resembles Fig. 7.1.3 (a). Our results presented in this section thoroughly agree with their findings.

A spin spiral hosts three universal spin-wave modes (see Chapter 6), instead of two for antiferromagnets. Two of them have dispersion curves with minima in the wavevector of the spiral $\pm q$ and are oppositely rotational modes. The third mode is symmetric around the zone center (Γ or X), and it has no angular momentum but corresponds to a longitudinal precession of the net magnetization perpendicularly

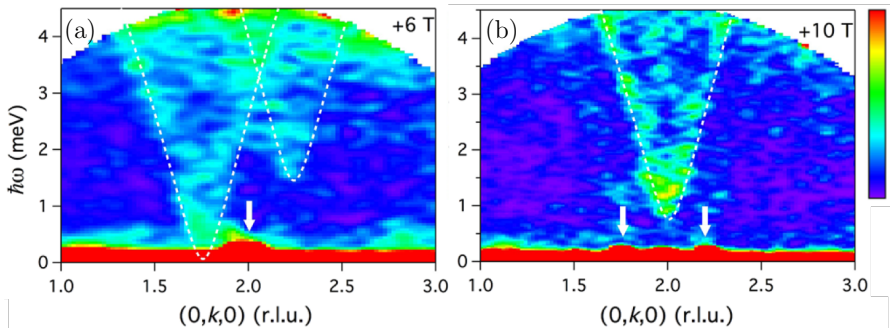

Figure 7.1.4: Inelastic-neutron-scattering measurement on bulk α–$Cu_2V_2O_7$. (a) Nonreciprocal scattering spectrum due to an external magnetic field, +6 T. The system is collinear antiferromagnetic. (b) For a high field, +10 T, the system undergoes a spin-flop transition into a spin spiral. The spectrum becomes symmetric. The arrows denote the magnetic Bragg peaks. Reprinted figure with permission from Gitgeatpong, G. *et al.*, Phys. Rev. Lett. **119**, 047201 (2017) (https://doi.org/10.1103/PhysRevLett.119.047201), Ref. [148]. Copyright (2020) by the American Physical Society.

to the spiral rotation plane, see Chapter 6. Such a mode is responsible for the high-intensity branch in the scattering spectrum, as predicted in Fig. 7.1.3 (b), and observed in Fig. 7.1.4 (b). Furthermore, our theoretical calculation enlightens the existence of two weaker features of the scattering spectrum, see Fig. 7.1.3 (b). These two modes have energy minima at the Bragg peaks, which correspond to the wavevector of the spin spiral $\pm q$. Therefore, the shifts of the minima out of the high-symmetry point are only related to the DMI indirectly through q. Although these two feeble branches appear in the experimental data, the lack of resolution and theoretical support led the authors of Ref. [148] to leave them unremarked.

We will come back to study the nonreciprocity of spin waves in noncollinear systems in Chapter 9, which is entirely dedicated to this subject. There, we present a general theory of when asymmetric spectra are expected and how to detect them.

7.2 Two-dimensional antiferromagnets

In the previous section, we have considered a one-dimensional antiferromagnetic spin chain, which allowed us to study the spin-wave Rashba effect due to the Dzyaloshinskii-Moriya interaction as well as the reciprocal-symmetry breaking in response to an applied magnetic field. Now, we place our focus on the properties of spin waves in two-dimensional antiferromagnetic systems, which have the minimal dimension to host antiferromagnetic skyrmionic structures as discussed, for example, in Refs. [14, 149]. First, we consider the formation of spin spirals, and subsequently the occurrence of antiferromagnetic skyrmions and antiskyrmions.

7.2.1 Antiferromagnetic spin spirals and Rashba spin locking

When the exchange couplings between atoms are predominantly antiferromagnetic, the formation of collinear phases of antiparallel spins takes place. The most common ones are the c(2×2) and p(2×1), where the first contains four atoms in the unit cell and the second only two, if we want to preserve the square Bravais lattice, as shown in Figs. 7.2.1 (a) and (b). In the c(2×2) phase, a spin moment is antialigned to all its nearest neighbors. Meanwhile, in the p(2×1), spins are antiparallel to their nearest neighbors along a given direction but align along the perpendicular direction.

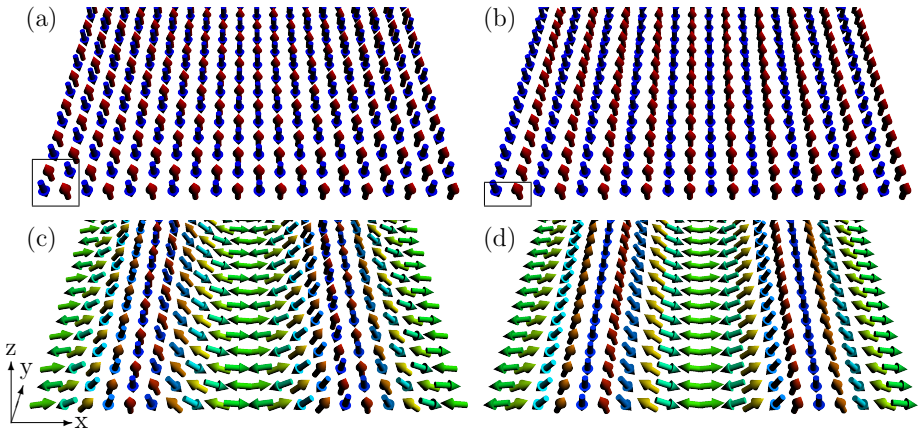

Figure 7.2.1: Predominantly antiferromagnetic two-dimentional structures. (a) The c(2×2) and (b) the p(2×1) collinear antiferromagnetic phases, containing four and two atoms in the unit cell, respectively. The first phase results from Model I, where antiferromagnetic nearest-neighbor-only couplings are considered. The second derives from Model II, which has an anisotropic exchange coupling, being ferromagnetic along the y–direction and antiferromagnetic along x. An easy-axis along z was considered. (c) and (d) show spin spirals formed due to Dzyaloshinskii-Moriya couplings in Models I and II, respectively. The total energy of the configuration in (a) and (b) is $E = -4.050J$, and in (c) and (d) $E = -4.052J$. Model parameters: $|J| = 1$, $D = 0.2$, $K = 0.05$ and $B = 0$ a.u.

Here, we consider two related models with only nearest-neighbor couplings of spins in a square lattice. In Model I, all nearest-neighbor exchange couplings are antiferromagnetic ($J < 0$), which has the c(2×2) phase as the ground state, see Fig. 7.2.1 (a). In an isotropic medium, beyond nearest-neighbor coupling is required to stabilize the p(2×1) phase [150]. Therefore, to stick to our nearest-neighbor-only choice, Model II is based on an anisotropic exchange coupling, such that it is positive along the y and negative along the x directions. Its ground state, the p(2×1) phase, is shown in Fig. 7.2.1 (b). For these ground states, the low-energy spin excitations have wavevectors around the P and X points for the c(2×2) and p(2×1) phases, respectively. The P–point (π, π) corresponds to a precession where a given spin is dephased by π with respect to all its nearest-neighbors. For the c(2×2) phase, this means that nearest-neighbor spins are kept perfectly antiparallel throughout

the whole precession revolution. Such an excitation, therefore, costs no energy and corresponds to the Goldstone mode. Similarly, the X wavevector $(\pi, 0)$ guarantees a precession phase of π between spins along horizontal lines, and no phase shift along the vertical ones, minimizing the excitation energy for the p(2×1) phase.

Since we want to study whether chiral skyrmions are supported by these antiferromagnetic systems, we need to consider the effects of the Dzyaloshinskii-Moriya interactions. Thus, we enhance our two models equally with in-plane isotropic nearest-neighbor Dzyaloshinskii-Moriya vectors, which circulate counterclockwise perpendicularly to the bonds. As Model II is anisotropic, the DMI vectors can be anisotropic as well. However, let us assume that the anisotropy is small and that it does not change the direction of the DMI vector with respect to Model I. Thus, we will be able to assert the effect of the anisotropy solely present in the magnetic exchange interactions. Furthermore, we consider an easy-axis magnetic anisotropy favoring the magnetization orientation along z. The DMI favors a noncollinear alignment among the atoms, while the anisotropy defines a preferred direction for the spin to point along. The competition between all these interactions determines the characteristics of the possible noncollinear states, such as spin spirals and skyrmions.

Figures 7.2.1 (c) and (d) show the ground states from the enhanced Model I and II, respectively, which we shall call c(2×2) and p(2×1)-spirals. They were obtained by considering a 10x1 supercell, which includes 20 atoms for Model I and 10 for Model II. Notice that in the phases c(2×2), p(2×1) and p(2×1)-spiral, there are always certain directions where the spins are aligned ferromagnetically. Only the c(2×2)-spiral does not present such a feature. Instead, we observe along its diagonals a smooth spin rotation forming a helical spin spiral. The wavevector of both spin spirals is $\mathbf{q} = (2\pi/20a)\hat{\mathbf{x}}$.

Next, we focus on the spin-wave spectra of the antiferromagnetic spin spirals. In Fig. 7.2.2 (a), we show the total spectrum, which is the sum of all spin-scattering channels, for Model I with the c(2×2)-spiral. Two different reciprocal-space paths around the P-point were considered, along and perpendicular to the spiral wavevector $\mathbf{q}$. Similarly, Fig. 7.2.2 (b) displays the total spectrum around the X-point for Model II in the p(2×1)-spiral. Overall, the spin-wave dispersion curves of these two systems are similar to each other, featuring three helimagnon modes along $\mathbf{q}$ (left-hand-side of the panels). Two of them are counter-rotating modes that have vanishing energy for $k \to \mathrm{P}(or X) \pm \mathbf{q}$. The other is a longitudinal mode whose energy gap at P (or X) is caused by the magnetic anisotropy. These modes can be separately measured in different SREELS channels by setting the beam polarization along y. The energy scale of the spin waves of the p(2×1)-spiral along $\mathbf{q}$ is roughly half of that for the c(2×2)-spiral.

On the paths perpendicular to $\mathbf{q}$ of Fig. 7.2.2 (a) and (b) (right-hand-side panels), we initially observe two modes, whose energy minima are shifted from the central point. Interestingly, the minima positions are no longer related to the pitch of the spin spiral, but solely to the strength of the Dzyaloshinskii-Moriya interaction in a linear manner. We demonstrate this in Fig. 7.2.3 (a) and (b), where we increased the DMI strength by $\delta D = 0.1/|J|$ without relaxing the spin structure. The minima location changed from P $\pm$ 0.024 to P $\pm$ 0.036. Furthermore, the larger splitting induced by the enhanced DMI reveals a third mode that was indistinguishable before, see also Fig. 7.2.2 (a) and (b) (right-hand-side panels). Once more, these modes

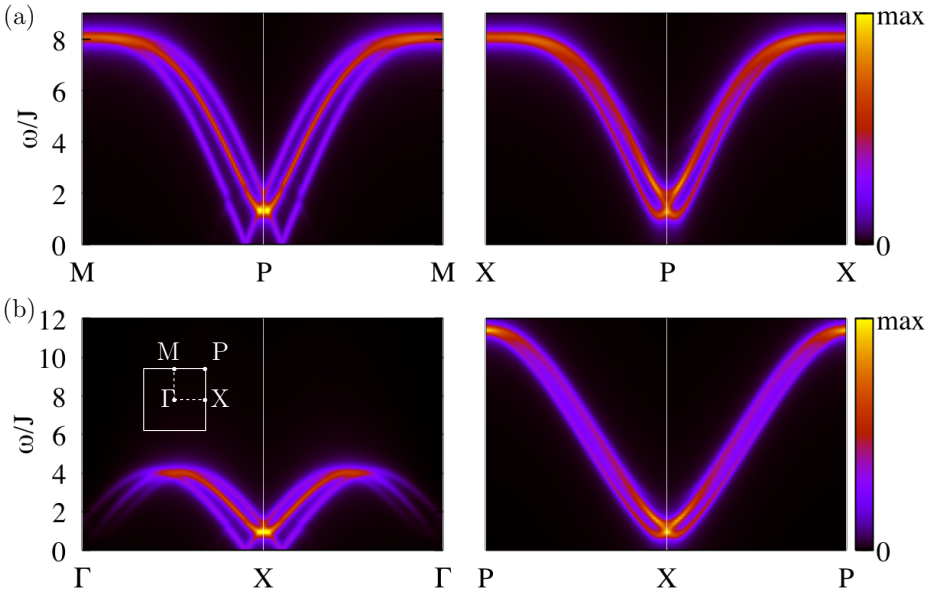

Figure 7.2.2: Spin-wave spectra for 2D antiferromagnetic spin spirals. (a) and (b) show the dispersion curves for the c(2×2) and p(2×1)-spirals, respectively. Paths in the direction of $\mathbf{q}$ are shown in the left-hand side and perpendicular to it on the right-hand side. The inset in (b) depicts the high symmetry points of the crystal Brillouin zone. Both the c(2×2) and p(2×1)-spirals feature the three universal helimagnon bands, seen on the left-hand side. Comparing the two left-hand-side panels, the energy scale for the c(2×2)-spiral is twice as high as for the p(2×1)-spiral.

can be isolated in different scattering channels, however, the polarization should be chosen along x, i.e., parallel to $\mathbf{q}$, instead of along y like in the previous case. All these observations uncover a locking between the linear and angular momenta of the spin waves, which is another characteristic of the Rashba effect discussed in Sec. 7.1.1. Finally, Fig. 7.2.3 (c) demonstrates that the two DMI-shifted modes are susceptible to external magnetic fields. An applied field along the $\mathbf{q}$–direction breaks the reciprocal symmetry around the band center, increasing the energy of one mode while decreasing the energy of the other one.

7.2.2 Antiferromagnetic skyrmions

Skyrmions and antiskyrmions are particle-like excitations of the magnetic structure of some materials. An antiskyrmion is the antiparticle of a skyrmion with opposite topological charge [7, 11, 111]. The great interest in these objects is related to their nontrivial topological character and the unique characteristics which may suit spintronics applications. A skyrmion differs from an antiskyrmion by only a reflection operation, which ends up inverting the sign of the topological charge. In practice, the search for antiskyrmions has focused on finding magnetic materials with highly anisotropic Dzyaloshinskii-Moriya interactions, as will be discussed in

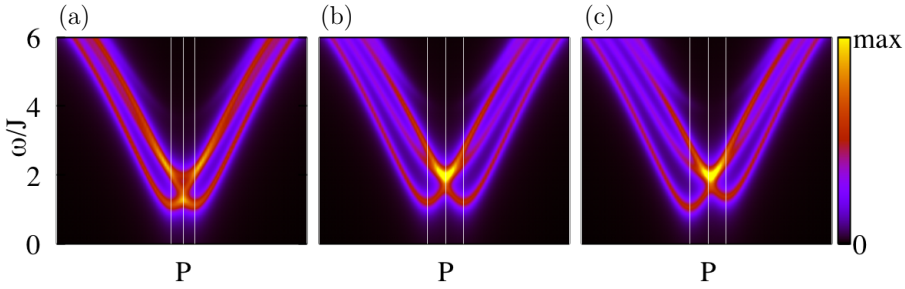

Figure 7.2.3: Spin-wave spectra for the Model I on the c(2×2)-spiral, whose parameters were modified as follows. We increased the DMI from (a) $D = 0.2$ to (b) $D = 0.3$ without relaxing the spin structure. In (a) the energy minima are located at P $\pm$ 0.24, while for (b) they are at P $\pm$ 0.36. The scaling on D is linear. Due to the further splitting, a third mode can be distinguished, which is centered at P. (c) An external magnetic field along $\mathbf{q}$, $B = 0.2$, is applied for the case in (b). The spectra become nonreciprocal because one of the shifted modes gets lifted, while the other is lowered in energy.

Chapter 8: Prediction of the existence of in-plane magnetic skyrmions in Co/W(110). If a material has DMI with different chirality along perpendicular directions, an antiskyrmion might be energetically more favorable than a skyrmion. In this section, we are going to demonstrate that even with an isotropic DMI, i.e., with the same chirality and strength along all directions, an antiskyrmion can be obtained if we consider an antiferromagnetic background.

In the previous section, we considered two model Hamiltonians whose ground state was a c(2×2) and p(2×1) antiferromagnetic spin spirals. These noncollinear ground states are only slightly energetically more favorable than their collinear counterparts, see caption of Fig. 7.2.1. However, the collinear spin configurations are not stable states. Meanwhile, spin-dynamics simulations showed that skyrmionic states can be obtained as metastable configurations of Models I and II, see Fig. 7.2.4. On the one hand, Model I, whose atoms have an antiferromagnetic exchange coupling with all their nearest neighbors, gives rise to an antiferromagnetic skyrmion, as can be seen in Fig. 7.2.4 (a). On the other hand, Model II stabilizes an antiferromagnetic antiskyrmion, see Fig. 7.2.4 (b). Here, it is important to notice that Model I and II share the same set of isotropic DMI. Their only difference lies in the set of exchange interactions, where for Model II the exchange parameter J changes sign for different directions. This shows that an antiskyrmion is more natural to occur in a p(2×1) antiferromagnet.

We carry on by investigating the spin-wave inelastic-electron-scattering spectra related to these skyrmionic phases. Thus, Fig. 7.2.5 (a) shows the spectra for the antiferromagnetic skyrmion, which is related to the c(2×2) antiferromagnetic phase. Meanwhile, Fig. 7.2.5 (b) corresponds to the antiferromagnetic antiskyrmions, whose background is a p(2×1) antiferromagnet. Overall, both spectra are much broader in comparison to the spin spirals in the same antiferromagnetic backgrounds, almost forming an energy continuum. Yet, it is possible to observe some dispersion lines throughout most of the reciprocal path. For the small energy range, we can observe that the dispersion curves are mostly linear, which is in contrast to the quadratic

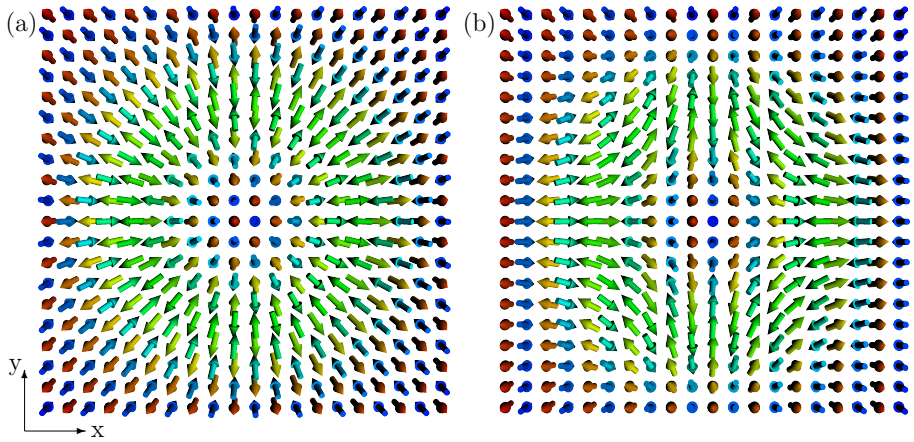

Figure 7.2.4: Skyrmion-like structures in an antiferromagnetic background. (a) Antiferromagnetic skyrmion that is formed when the exchange interaction with all nearest neighbors is negative, Model I. The skyrmion lies in a c(2×2) antiferromagnetic background. (b) Antiferromagnetic antiskyrmion, which results from anisotropy exchange interactions. J is negative along-x and positive along-y, Model II. The antiskyrmion lies in a p(2×1) antiferromagnetic background. Model parameters: $|J| = 1$, $D = 0.2$, $K = 0.05$ and $B = 0$ a.u. The total energy of both spin configuration is $E = -4.041052J$.

behavior of the skyrmions in a ferromagnetic background, as seen in Chapter 6.

7.3 First-principles investigation of Mn/β–W

In this section, we apply the insights gained from studying simple model systems to a realistic anisotropic antiferromagnet, namely a Mn monolayer supported on β–tungsten. Tungsten crystals are found in two forms: the more common α–phase, with a body-centered cubic structure, and the β–phase, which is metastable with an A15 cubic structure. The β–tungsten can be realized in films of thickness below a critical point, after which the system undergoes a transition to the α–phase. The current critical thickness reaches approximately 20 nm [151]. Nonequilibrium synthesis and impurities also play an important role in its stabilization. While most samples of β–tungsten are grown with sputter techniques, leading to polycrystalline phases, M. Costa *et al.* motivated the experimental community to produce single-crystals by further demonstrating the prominence of this material for application in spintronics [151]. Their calculations indicated that a single layer of manganese (Mn) can be grown in a square lattice on the β–W(100), with giant in-plane magnetic anisotropies of about 12 meV. Also, they predicted that the easy-axis could be made out-of-plane by depositing an extra layer of β–tungsten on top of the manganese.

Motivated by these findings, in this section, we explore the magnetic properties of this antiferromagnetic system with a focus on the magnetic exchange and Dzyaloshinskii-Moriya interactions, the ground state, and the spin-wave excitations.

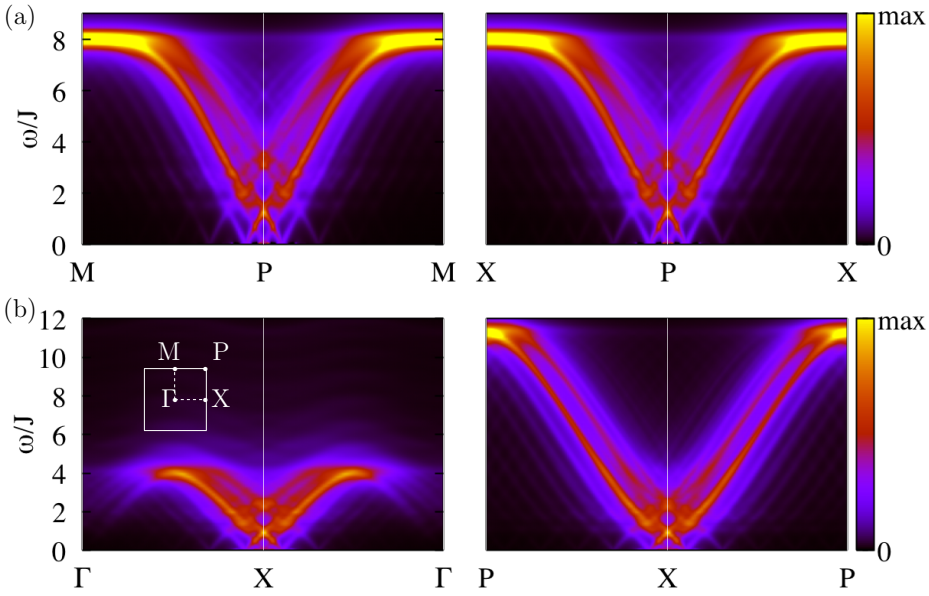

Figure 7.2.5: Total inelastic-electron-scattering spectra of spin waves in antiferromagnetic skyrmionic lattices. (a) shows the inelastic scattering spectra for the antiferromagnetic skyrmion in the c(2×2) background. (a) displays the spectra for the antiferromagnetic antiskyrmion in the p(2×1) background. In contrast to the spin spirals, the spectra for the skyrmion lattices are much more broaden. The inset in (b) depicts the high symmetry points of the crystal Brillouin zone.

7.3.1 The crystal structure

The bulk of β–tungsten can be constructed by an ABCB stacking of three distinct layers. Two of them, layers A and C, have a honeycomb-like structure that divides the space into a square lattice of irregular hexagons, see Fig. 7.3.1. Filling the space left, there are pairs of inverted triangles, which form a diamond shape. Layer C is rotated by 90° with respect to A. The layer B is a square lattice whose atoms are situated in the hexagon hollows of the other layers. This layer is always sandwiched by a pair of A and C layers. These juxtaposed layers form an A15 cubic crystal structure, whose unit cell contains 8 atoms.

It was shown in Ref. [151] that the most stable β–W(001) surface is the honeycomb-like one, upon which a square-lattice of Mn atoms can be grown, see Fig. 7.3.1. We consider, therefore, such a monolayer of Mn deposited on 13 monolayers thin film of β–tungsten, where the relaxed interlayer distances are taken as reported in Ref. [151], which goes up to 33% of the bulk value $d_{bulk} = 1.27$ Å. Fig. 7.3.1 (a) shows the Mn monolayer and the first three layers of β–tungsten. In Fig. 7.3.1 (b), we can see that the Mn atoms lay in the hollow of the W irregular hexagons.

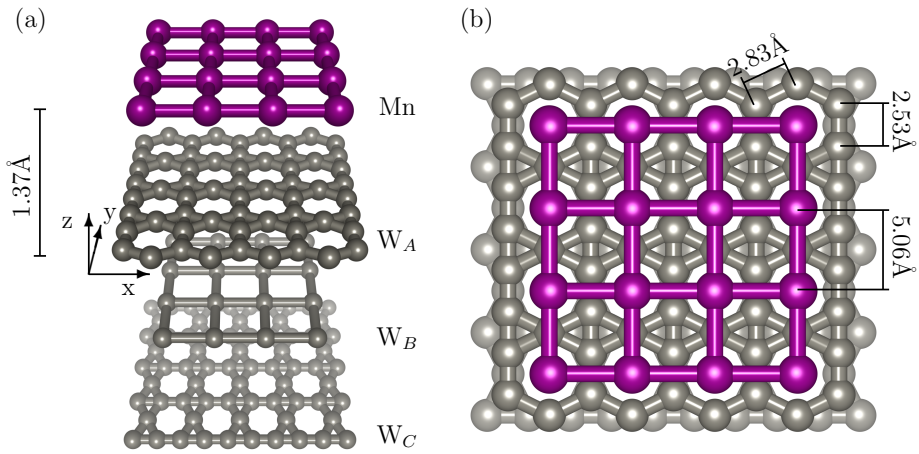

Figure 7.3.1: Manganese monolayer deposited on β–tungsten (001). (a) The β–phase of tungsten is composed by an ABCB stacking of three different layers. The layer A has a honeycomb-like structure, which divides the space into irregular hexagons and pairs of inverted triangles. Meanwhile, layer B is a square lattice whose atoms lay in the hollow position of the irregular hexagons of A and C. Finally, layer C has the same structure of A but rotated by 90°. The overlayer of manganese follows the tungsten B stacking at a distance of 1.37 Å from the β–W surface. (b) A top view of the Mn monolayer deposited on β–W(001). The manganese atoms are situated in the hollows of the tungsten irregular hexagons with a spin magnetic moment of $M = 3.5\mu_{\mathrm{B}}$.

7.3.2 Magnetic exchange and Dzyaloshinskii-Moriya interactions

With the atomic structure described in the previous section, we performed calculations based on density functional theory (DFT) to compute the ground-state magnetic properties using the full-potential relativistic Green-function Korringa-Kohn-Rostoker (KKR) method introduced in Chapter 3. The magnetic exchange and Dzyaloshinskii-Moriya interactions were obtained using the infinitesimal-rotations method also discussed in Chapter 3.

Figure 7.3.2 depicts the Mn/β–W magnetic interactions. In Fig. 7.3.2 (a), we plot the magnetic exchange interaction, where the strength is indicated by the saturation and the color represents the sign, blue and red for ferromagnetic and antiferromagnetic coupling, respectively. The atoms interact most strongly with the nearest-neighbors on the left and right, via a ferromagnetic coupling. Interestingly, the nearest-neighbor interactions along-y and all four second-nearest-neighbor interactions are antiferromagnetic. Thus, this set of interactions favors a horizontal ferromagnetic and a vertical antiferromagnetic alignments. The Dzyaloshinskii-Moriya interactions are very anisotropic for this system, as can be seen in Fig. 7.3.2 (b). The DMI vectors are mostly stronger for the nearest neighbors along the y–direction and they point in-plane perpendicularly to the bonds between the two sites. The nearest-neighbor couplings along x are approximately 20 times smaller than along

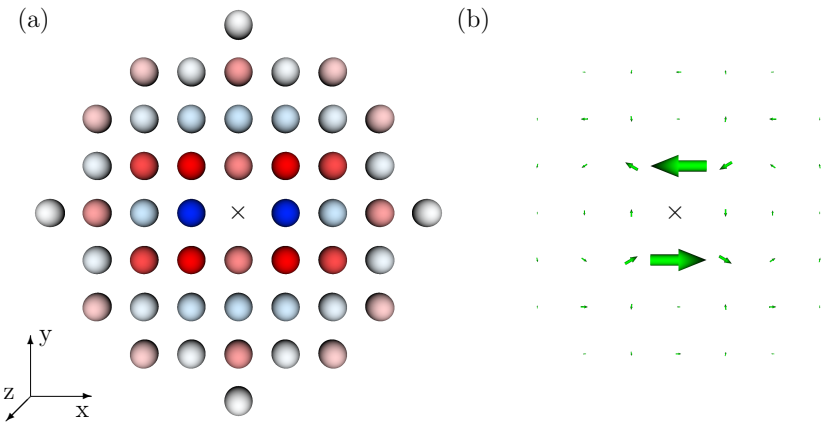

Figure 7.3.2: Mn/β–W magnetic interaction maps. (a) Exchange interactions between the central site, marked by the $\times$ sign, and its neighbors. The blue and red colors represent ferromagnetic and antiferromagnetic coupling, respectively. The saturation indicates the interaction strength. The brightest blue and red correspond to 7.25 meV and -0.90 meV, respectively. (b) Dzyaloshinskii-Moriya vectors, representing the asymmetric exchange interactions between the central atom and its neighbors, which are located where the vectors lay. The intensity of the coupling is represented by the arrow size. The largest arrows correspond to 2.84 meV, which are the couplings to the sites at $(0, \pm 1)a$, and the second largest to 0.74meV, for $(\pm 1, \pm 1)a$.

y and of opposite handedness. Such a set of Dzyaloshinskii-Moriya vectors favors the formation of spin spirals where the spin moment rotates from site-to-site in the $z - y$ plane.

7.3.3 Magnetic ground state and spin-wave dispersion

With the magnetic exchange and Dzyaloshinskii-Moriya interactions discussed in the previous sections, we performed atomistic-spin-dynamics simulations to determine the ground-state magnetic structure of the Mn/β–W. Initially, we considered a 100×100 supercell with periodic boundary conditions and starting from a random spin configuration, see Fig. 7.3.3 (a). From the outcome of this simulation, we could estimate the antiferromagnetic spin-spiral period of 32 atomic distances. Next, we repeated the spin-dynamics simulations considering a supercell of 32×32, whose relaxed magnetic structure is shown in Fig. 7.3.3 (b). Therefore, the Mn/β–W ground state consists of an inhomogeneous spin spiral, where the spins lie mostly in the plane with an antiferromagnetic alignment along y, with fast spin rotation in the $y - z$ plane.

With knowledge of the ground-state spin configuration and the magnetic interactions, we have everything required to study the spin waves of this material. The total spin-wave spectrum is shown in Fig. 7.3.4, which was computed on a reciprocal space path parallel to the spiral wavevector. The spectrum is marked by a fairly large gap of ~ 5 meV, which is due to the very high magnetocrystalline anisotropy. Below the gap, we observe two minima at $\pm q$ with vanishing energy of the rotational modes,

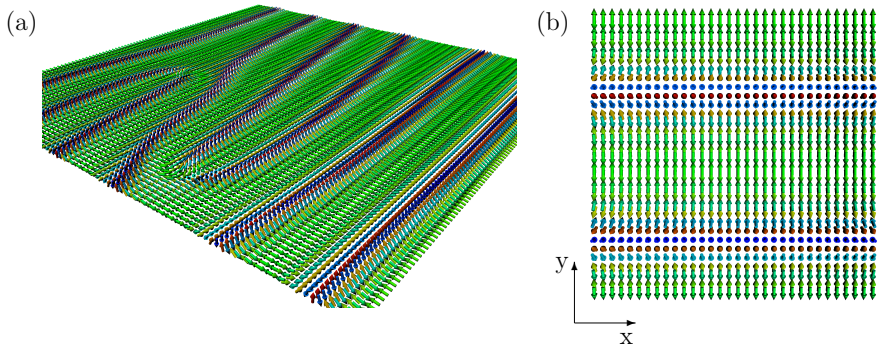

Figure 7.3.3: The ground-state magnetic structure of the Mn monolayer on β–tungsten. (a) A 100×100 super cell with periodic periodic boundary conditions was considered for a spin-relaxation dynamics starting from a random configuration. From this simulation, an antiferromagnetic spin-spiral pitch of 32 atomics distances could be estimated. (b) A 32×32 supercell was considered to obtain the ground-state spin configuration of the Mn/β–W. We used an easy-axis anisotropy along y with $K = 1.5\,\mathrm{meV}$.

where $q = 2\pi/32a$, where the lattice constant is $a = 5.06\,\text{Å}$. Meanwhile, above the gap, the brightest feature is composed of the longitudinal mode centered in M, and the second brightest branch is due to the rotational modes.

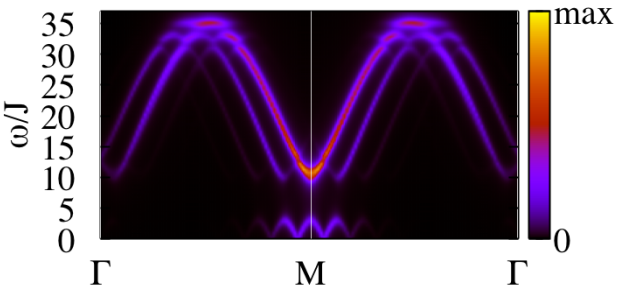

Figure 7.3.4: Total spin-wave scattering spectrum for the Mn/β–W. The figure shows the dispersion curves of the rotational and longitudinal helimagnon modes on a reciprocal path along q. The gap of about 5 meV in the spectrum is due to the magnetocrystalline anisotropy. Below the gap, the minima at $\pm q$ of the rotational modes can be observed. Above, the central and brightest feature is composed of the longitudinal and rotational modes.

We could not find stable antiferromagnetic skyrmions/antiskyrmions in Mn/β–W. However, the occupancy of an antiferromagnetic spin spiral as the ground state allows for a comparison with the simple models upon which we did our initial studies in this chapter.

7.4 First-principles study of Mn_5Si_3

In this section, we study the properties of spin waves in the bulk Mn_5Si_3. It is an antiferromagnetic compound attracting much attention, particularly due to its inverse magnetocaloric effect and large anomalous Hall effect [28, 29]. At high temperature, Mn_5Si_3 crystallizes in the hexagonal space group $P6_3/mcm$ and it features a paramagnetic phase [29, 152]. Lowering the temperature, at $T_{N_1} \approx 100\,\mathrm{K}$, it transits into a collinear antiferromagnetic phase (AFM2), and at $T_{N_2} \approx 66\,\mathrm{K}$, into an noncollinear antiferromagnetic phase (AFM1).

Inelastic neutron scattering suggested that the low temperature noncollinear AFM1 phase is characterized by a well-defined spin-wave spectrum. Also, there were indications that the higher temperature collinear AFM2 phase has a coexistence of spin waves and diffuse spin fluctuations [29]. To test this hypothesis, new measurements focused on the response of the inelastic spectrum as a function of an external field applied perpendicularly to the anisotropy easy-axis in the AFM2 phase [153]. The expectation is that the field would yield to the suppression of the diffuse spin fluctuations. Therefore, to help in understanding the experimental data, we calculated the response of the spin-wave energies as a function of the external magnetic field. We performed *ab initio* calculations to determine the magnetic ground-state properties, and to parametrize a spin Hamiltonian for this material. With the *ab initio* parameters, and with a single free parameter to rescale the magnetic interactions, we obtained a good agreement with the experimental observations.

7.4.1 Ground-state magnetic properties

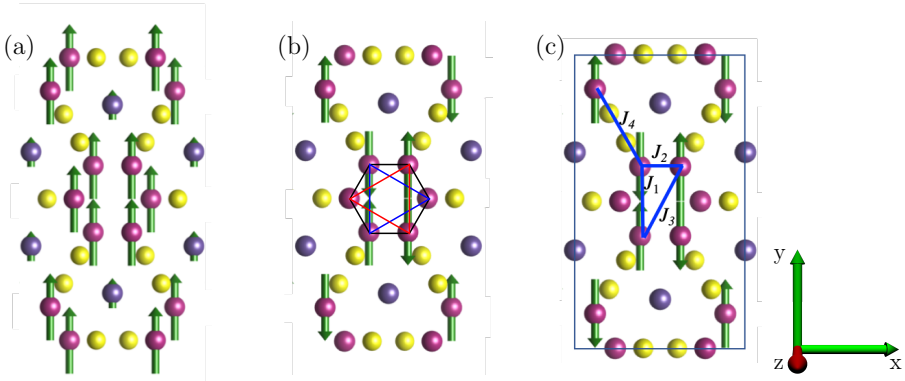

Figure 7.4.1: Different self-consistent magnetic phases. (a) FM: Ferromagnetic phases obtained by spin polarizing the system with a magnetic field during the first self-consist interaction of the Kohn-Sham cycle. The magnetic moments are of 2.6 and 1.1 μ_B. (b) AFM: The antiferromagnetic phase obtained self-consistently after reversing the magnetic moment orientation of some sites of the ferromagnetic phase. The magnetic moments are of 2.4 μ_B. The AFM phase is energetically more favorable than the FM one. (c) Indication of the first few exchange interaction pairs. Atoms connected by the red triangle in (b) are in the same plane, and atoms linked by the blue triangle are in another plane. From this top view, the two triangles together form a hexagon.

Magnetocrystalline anisotropy (meV/per. mag. atom)	
$E_x - E_y$	0.12
$E_z - E_y$	0.09
$E_x - E_z$	0.03
k_y	0.10

Table 7.4.1: Magnetocrystalline anisotropy. We calculated the anisotropy by total energy difference when aligning the magnetic moment in different directions. The lowest energy is that for the moments aligned along y, and there is only a small difference between the alignment along x and z. Therefore, we can model the anisotropy as a uniaxial anisotropy with easy-axis along y.

The magnetic and electronic properties of Mn_5Si_3 was obtained from density functional theory within the relativistic full-potential KKR method, as described in Chapter 3. Initially, we spin-polarized the system by applying an external magnetic field in the first iteration of the self-consistently solving of the Kohn-Sham equation. After convergence, we obtained a stable ferromagnetic phase shown in Fig. 7.4.1(a). From this phase, we started another self-consistent cycle after reversing some of the magnetic moments of the previous ferromagnetic phase. The resulting stable phase is shown in Fig. 7.4.1(b), which is an antiferromagnetic phase consistent with the Mn_5Si_3-AFM2 phase. Our calculations show that the antiferromagnetic phase is energetically more favorable by

$$E_{FM} - E_{AFM} = 292\,\text{meV/unit cell} \quad . \tag{7.2}$$

The magnetic moments in the FM phase are 2.6 and 1.1 μ_B. For the AFM phase, it is of 2.4 μ_B. The experimental values for the magnetic moment range from 3 to 1.7 μ_B when the temperature changes from 12 to 80 K [152].

For the antiferromagnetic phase, we calculated the total energy difference when aligning the magnetic moments along three perpendicular directions. The results are summarized in Tab. 7.4.1. The lowest energy obtained for the magnetic moments along y. The energy difference between the alignment along x and z is small, 0.03 meV, so we could model the anisotropy landscape as a uniaxial anisotropy with easy-axis along y with the parameter $k_y = 0.10$ meV, which corresponds to the average of the first two lines of Tab. 7.4.1.

The magnetic exchange interaction and the magnetocrystalline anisotropy were mapped into the following Hamiltonian:

$$\mathcal{H} = -\sum_{ij} J_{ij}\mathbf{S}_i \cdot \mathbf{S}_j - k^y \sum_i (S_i^y)^2 \quad , \tag{7.3}$$

where $\mathbf{S}$ is a unit vector along the local magnetic moment. The results for the first few interaction pairs indicated in Fig. 7.4.1 (c) are as follows: $J_1 = -9.51$, $J_2 = -1.30$, $J_3 = 5.45$, $J_4 = -2.03$ meV. This shows that the AFM2 phase is favored by all those pair interactions. Within this set of interactions, there is no frustration. Most of the interactions have an antiferromagnetic character. Only J_3 that links magnetic moments of different layers within the same Mn hexagon (shown in Fig. 7.4.1 (b)) is ferromagnetic. The highest value is of J_1 that couples magnetic moments in the same plane within a hexagon.

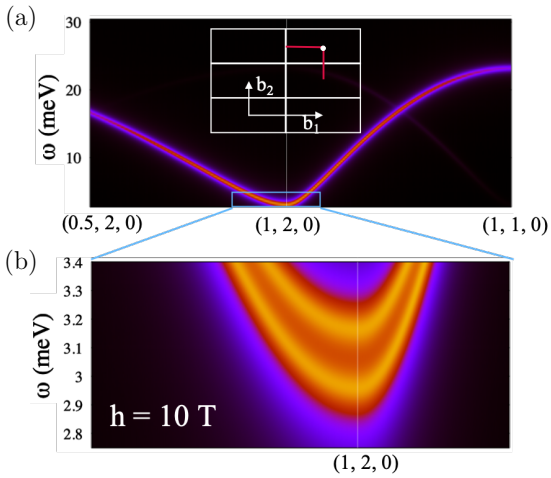

Figure 7.4.2: (a) Spin-wave dispersion around $\mathbf{q} = (1, 2, 0)$ reciprocal-space point (marked by the white dot on the red path) for an external field of 10 T. The complete path is shown in red in the reciprocal-space schematics. (b) Zoom-in into the low energy region. An energy gap of about 3 meV is observed. Direct DFT parameter: $J_1 = -9.51$, $J_2 = -1.30$, $J_3 = 5.45$, $J_4 = -2.03$, $k^y = 0.10$ meV, $m = 2.4\,\mu_B$.

7.4.2 Spin-wave dispersion

When an external magnetic field perpendicular to the easy-axis is applied, the magnetic moments in the AFM2 phase acquire a transversal component leaving the magnetic structure noncollinear. Thus, we used the method described in Chapters 2 and 4 to calculate the spin-wave dispersion in the adiabatic approximation and its inelastic scattering spectra for noncollinear magnets. Using the DFT parameters discussed in the previous section, we obtained the dispersion shown in Fig. 7.4.2(a), which was calculated around the $\mathbf{q} = (1, 2, 0)$ reciprocal-space point for an external magnetic field of 10 T along z. Fig. 7.4.2(b) shows a zoom-in into the low energy region, where we can observe an energy gap of about 3 meV (the lowest energy). We can also resolve a spin-wave mode splitting, which goes to zero in the absence of the external field.

The experimental inelastic neutron scattering data suggest an energy gap of about 0.36 meV [153]. To compare the results between the DFT calculations and the experimental data, we rescaled down the MEI and magnetic-anisotropy parameters by a factor of ten. Now, we traced down the energy of the two spin-wave modes when varying the strength of the external field, as shown in Fig. 7.4.3. The crosses represent the DFT results, and the circles the experimental data [153]. Within the rescaled parameter, the theoretical calculations seem to reproduce well the energy center of the experimental inelastic spectra. The theoretical results also suggest that the lowest-energy mode does not vary with the external field, while the second one has a nonlinear dispersion relation with the field.

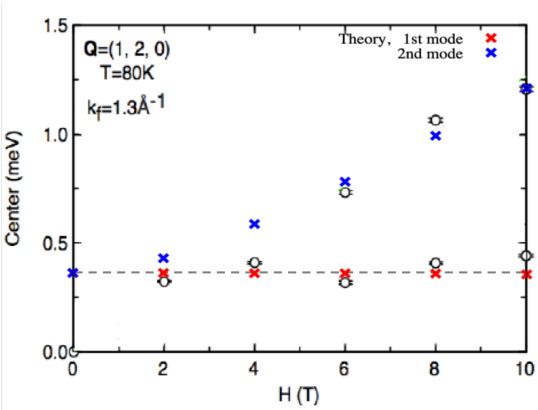

Figure 7.4.3: Spin-wave dispersion at $\mathbf{q} = (1, 2, 0)$ as a function of the external magnetic field (crosses) in comparison to the energy center of the experimental inelastic-neutron-scattering data (open circles) [153]. The magnetic exchange and magnetic anisotropy parameters were rescaled by a factor of 10 to reproduce the experimental energy gap.

7.4.3 Analytical study

To understand the basic physics underlying the experimental and *ab initio* results, we resort to a simple unidimensional model system, namely an antiferromagnetic spin chain. We consider a uniform nearest-neighbors-only interactions and an external magnetic field perpendicular to the uniaxial anisotropy axis. Let us consider that the spin chain is along the x-axis, the uniaxial anisotropy along z and $J < 0$, such to obtain the antiferromagnetic ground state as shown in Fig. 7.4.4 (a), where the spin moments align parallel and antiparallel to $\mathbf{z}$. By applying the magnetic field parallel to $\mathbf{y}$, the magnetic moments tilt by an angle θ from their equilibrium position into the $z - y$ plane, see Fig. 7.4.4 (b). The Hamiltonian is then given by

$$\mathcal{H} = -\frac{1}{2}J\sum_{ij}\mathbf{S}_i \cdot \mathbf{S}_j - h\sum_i S_i^y - k\sum_i (S_i^z)^2 \quad . \tag{7.4}$$

Please note that in this section, we use h for the magnetic field parameter instead of the usual B.

Ground-state spin configuration

We can determine the ground-state spin configuration for a given field of strength h by minimizing the hamiltonian of Eq. (7.4) with respect to θ treating the spin moments as classical vectors. Following Fig. 7.4.4 (b), we have that $S^y = S\sin\theta$ and $S^z_{\uparrow\downarrow} = \pm S\cos\theta$. Therefore, the dot product in Eq. (7.4), considering only n.n. exchange coupling, reads: $S_i^z S_j^z = -S^2\cos\theta$. We are then left with:

$$\mathcal{H} = NS^2 J\cos 2\theta - hNS\sin\theta - kNS^2\cos^2\theta \quad . \tag{7.5}$$

To minimize the total energy in respect to θ, let us derive the above equation:

$$\frac{\mathrm{d}\mathcal{H}}{\mathrm{d}\theta} = NS\big[S(k-2J)\sin 2\theta - h\cos\theta\big] \quad . \tag{7.6}$$

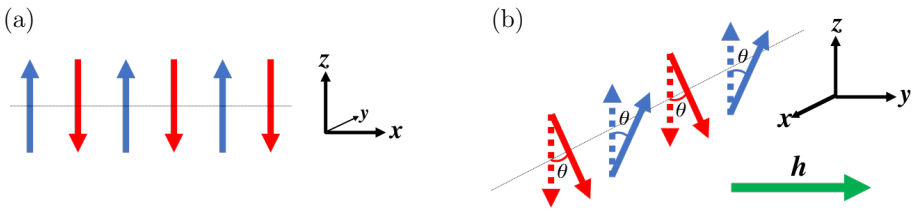

Figure 7.4.4: Unidimensional spin chain. (a) With $J < 0$, we obtain an antiferromagnetic spin alignment. (b) When an external magnetic field is applied $\mathbf{h}$, the spin moments tilt away from the equilibrium by an angle θ.

The energy extrema of the Hamiltonian, given by $\frac{d\mathcal{H}}{d\theta} = 0$, are then given by:

$$\sin\theta = \frac{h}{2S(k-2J)} \quad . \tag{7.7}$$

The above equation provides the tilt caused by the action of the external magnetic field over the magnetic moments. Furthermore, we can derive that the spins should first fully align with the field ($\theta = \pi/2$) when its strength is $h = 2S(k-2J)$.

Spin waves

Following Sec. 2.4, the spin-wave energies is given by the eigenvalues of the dynamical matrix

$$\mathbf{D}(q) = \begin{pmatrix} \begin{pmatrix} -kS\sin^2\theta - h^+ & -kS\sin^2\theta \\ kS\sin^2\theta & kS\sin^2\theta + h^+ \end{pmatrix} & (1+e^{-iqa})JS \begin{pmatrix} -\sin^2\theta & -\cos^2\theta \\ \cos^2\theta & \sin^2\theta \end{pmatrix} \\ (1+e^{iqa})JS \begin{pmatrix} -\sin^2\theta & -\cos^2\theta \\ \cos^2\theta & \sin^2\theta \end{pmatrix} & \begin{pmatrix} -kS\sin^2\theta - h^+ & -kS\sin^2\theta \\ kS\sin^2\theta & kS\sin^2\theta + h^+ \end{pmatrix} \end{pmatrix}, \tag{7.8}$$

where $h^+ = 2S(J-k)$. An analytical diagonalization led us to find the two positive eigenvalues as:

$$\begin{aligned} a_0(h) &= 2S\sqrt{-2Jk\sin^4\theta + (4Jk - k^2)\sin^2\theta - k(2J-k)} \\ a_1(h) &= 2S\sqrt{2Jk\sin^4\theta + (4J^2 - 2Jk - k^2)\sin^2\theta - k(2J-k)} \end{aligned} \quad , \tag{7.9}$$

which are a function of the external field h via $\sin\theta = \frac{h}{2S(k-2J)}$. See detailed derivations in Apx. 7.B.

Using Eq. (7.9), we constructed Fig. 7.4.5 for $J = -10\,\text{meV}$ and $k = 0.3\,\text{meV}$. We can observe that the energy of the lowest mode seems constant only at low fields. In fact, it goes to zero when the spins first fully align with an ever-increasing external field. For even higher fields, the energy of the lowest mode rises again. The second mode, which is degenerate with the first at zero-field, has energy that has a nonlinear variation with low external fields, but for higher fields, it disperses linearly.

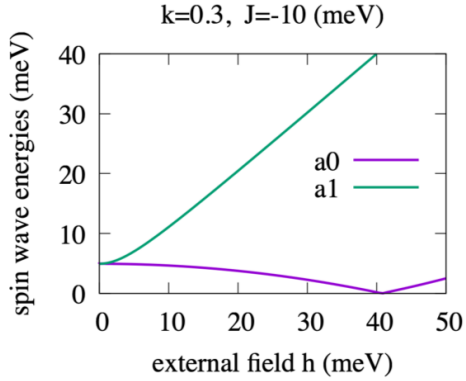

Figure 7.4.5: Spin-gap as a function of the external field h.

The asymptotic behavior of the lowest spin-wave mode when $k \ll J$ is given by:

$$a_0(h) \simeq 2S\sqrt{2\,|J|\,k} \tag{7.10}$$

where $M = 2S$ is the magnetic moment. This result makes it explicit the independence of the lowest mode on the external field. It also corresponds to the energy for zero field, $\Delta = a_0(0) = a_1(0) = M\sqrt{2\,|J|\,k}$, and thus to the energy gap. Therefore, a correct determination of the energy gap from DFT requires a precise determination of the three magnetic properties involved: the magnetic moment, the magnetic exchange and magnetic anisotropy. At 80 K, the magnetic moment of Mn_5Si_3 was experimentally determined to be about $1.7\,\mu_B$ [152], while our DFT results obtained $2.4\,\mu_B$. Obviously, this discrepancy alone cannot account for the difference in Δ between the DFT and experimental results, which should then come from the magnetic exchange or anisotropy, which appear together as a product in Eq. (7.10). In particular, the precise determination of the magnetocrystalline anisotropy from DFT is very problematic, for it relies on very small differences of very large numbers.

7.5 Conclusions

In this chapter, we studied magnetic materials whose magnetic exchange interaction is predominately antiferromagnetic. We saw that the DMI in regular antiferromagnetic lattices can induce a degeneracy breaking of the spin-wave modes similar to the electronic Rashba splitting. The resulting spin-wave spectrum can then be made nonreciprocal by an external magnetic field. We will discuss the spin-wave nonreciprocity phenomenon more in detail in Chapter 9.

When strong enough, the DMI can induce the formation of noncollinear structures, such as antiferromagnetic spin spirals and skyrmion lattices. We computed the inelastic scattering spectra for two model lattices, one with isotropic and another with anisotropic MEI, which share the same set of isotropic DMI. The spin-wave spectra for the antiferromagnetic spin spirals are similar to those for ferromagnetic spin spirals studied in Chapter 6, but they are centered at high-symmetry points

at the edges of the BZ. Confinement effects allowed us to stabilize antiferromagnetic skyrmions in the isotropic model and antiferromagnetic antiskyrmions with the anisotropic model. Remarkably, the antiskyrmions were obtained without the need for anisotropic DMI.

With parameters obtained from first-principles calculations, we studied Mn/β–W and Mn_5Si_3. Due to the tungsten substrate, Mn/β–W features large and anisotropic DMI. Its ground state was found to be an antiferromagnetic spin spiral, whose spin-wave spectrum presents a large gap of about 5 meV due to the magnetic anisotropy. We were unable to stabilize skyrmion lattices in this material.

For Mn_5Si_3, we computed the spin-wave energies as a function of an applied magnetic field in its AFM2 phase, which is collinear and antiferromagnetic. We saw that the magnetic field splits the spin-wave branch in two: one that disperses with the field, and another that does not seem to. Our *ab initio* results agree with the experimental results up to a free scaling factor for the product between the magnetic anisotropy and the magnetic exchange parameters. This means, that the inelastic signals observed in the experimental data can be associated with spin waves only. However, our studies do not rule out the role of diffuse spin fluctuations in this system.

In the next chapter, we investigate ultrathin films of Co/W(110) and how they may host skyrmions in spite of having in-plane magnetizations.

Appendix

7.A Spin spiral in an antiferromagnetic square lattice

Consider a square lattice of localized magnetic moments described by the classical Hamiltonian:

$$\mathcal{H} = -\frac{1}{2}\sum_{ij}\left[J_{ij}\mathbf{S}_i\cdot\mathbf{S}_j + \mathbf{D}_{ij}\cdot(\mathbf{S}_i\times\mathbf{S}_j)\right] \quad . \tag{7.11}$$

We want to determine the spiral pitch that minimizes the free energy. For simplicity, we consider a spin spiral with the spins $\mathbf{S}$ rotating while lying in the xy-plane. We then obtain

$$\begin{aligned}\mathcal{H} &= -\frac{1}{2}\sum_{ij}\left[J_{ij}S_iS_j\cos\theta_{ij} + D^z_{ij}S_iS_j\sin\theta_{ij}\right] \\ &= -\frac{1}{2}S^2\sum_i\left[2J(1+\cos\theta) + 2D^z\sin\theta\right] \\ &= -S^2N\left[J(1+\cos(aQ)) + D^z\sin(aQ)\right]\end{aligned} \tag{7.12}$$

where a is the lattice constant and $Q = |\mathbf{Q}|$ is the wavevector of the spiral, which points along any of the two main axes of the square lattice. We have to make a critical point analysis to determine the minimum energies as a function of Q. The first and second derivative of the Hamiltonian give:

$$\frac{\mathrm{d}\mathcal{H}}{\mathrm{d}Q} = S^2Na\left[J\sin(aQ) - D^z\cos(aQ)\right] \quad \text{and} \tag{7.13}$$

$$\frac{\mathrm{d}^2\mathcal{H}}{\mathrm{d}Q^2} = S^2Na^2\left[J\cos(aQ) + D^z\sin(aQ)\right] \quad , \tag{7.14}$$

which are the same equations as for the hexagonal lattice, discussed in Chapter 2. Therefore, the solution is

$$Q = \frac{\alpha}{a} \quad , \quad \lambda = a\frac{2\pi}{\alpha} \quad , \quad \alpha = \arctan\frac{D^z}{J} \quad . \tag{7.15}$$

For $J = 1$ and $D = 1$, $\lambda = 8a$. For $D = 0.1$, for instance, $\lambda \sim 63a$.

A similar development goes for the antiferromagnetic spin spiral, where $J < 0$ and the n.n. spins are antiparallel, which yields:

$$\begin{aligned}\mathcal{H} &= -\frac{1}{2}S^2\sum_i \left[J\big(2+\cos(\pi+\theta)+\cos(\pi-\theta)\big)+D^z\big(\sin(\pi+\theta)-\sin(\pi-\theta)\big)\right] \\ &= -S^2N\left[J(1-\cos(aQ))-D^z\sin(aQ)\right] \quad ,\end{aligned} \tag{7.16}$$

resulting in

$$\frac{\mathrm{d}\mathcal{H}}{\mathrm{d}Q} = S^2Na\left[|J|\sin(aQ)-D^z\cos(aQ)\right] \quad \text{and} \tag{7.17}$$

$$\frac{\mathrm{d}^2\mathcal{H}}{\mathrm{d}Q^2} = S^2Na^2\left[|J|\cos(aQ)+D^z\sin(aQ)\right] \quad . \tag{7.18}$$

Therefore, we have the same solution, but interchanging J for $|J|$.

7.B Analytical spin-wave dispersion: 1-D antiferromagnetic spin chain under a perpendicular magnetic field

We consider a 1-D spin chain along the x-direction. A uniaxial mag. anisotropy is set along z, and nearest-neighbor-only $J < 0$ makes the moments align antiferromagnetically along z. The hamiltonian is given by Eq. (7.4). An external magnetic field points along $+y$ causing a tilt of the spin moments by an angle θ from the z–axis, which determines the ground-state spin configuration and is given by Eq. (7.7).

7.B.1 Spin-wave energies

Knowing the classical ground-state spin configuration, we can calculate the spin-wave spectrum of the system, as explained in Sec. 2.4. All the spins lie in the $z-y$ plane making an angle of θ from the z–axis. Thus, the rotation matrices that take the spins from the global reference frame into the local one, as in Eq. 2.119, correspond to rotations along the $-x$–axis, R^{-x}, and they are given by:

$$\mathbf{O}_i = \mathbf{R}^{-x}(\theta_i) = \begin{pmatrix} 1 & 0 & 0 \\ 0 & \cos\theta_i & \sin\theta_i \\ 0 & -\sin\theta_i & \cos\theta_i \end{pmatrix} \quad . \tag{7.19}$$

The part of the interaction matrices quadratic in the creation and annihilation operators is given by Eq. 2.127:

$$\begin{aligned}\mathbf{H}_{il,jl'} =& \mathbf{A}^{2\times2}_{il,jl'} - \big(\tilde{B}^z_{il}+\tilde{J}^{zz}_{l\mathbf{0}}\big)\mathbf{I}\delta_{il,jl'} \\ =& \frac{S}{2}\left(\begin{array}{cc|cc} m_{i1,j1} & n_{i1,j1} & m_{i1,j2} & n_{i1,j2} \\ n_{i1,j1} & m_{i1,j1} & n_{i1,j2} & m_{i1,j2} \\ \hline m_{i2,j1} & n_{i2,j1} & m_{i2,j2} & n_{i2,j2} \\ n_{i2,j1} & m_{i2,j1} & n_{i2,j2} & m_{i2,j2} \end{array}\right) \\ &- \left(\begin{array}{c|c} \big(h\sin\theta_{i1}, +\tilde{J}^{zz}_{l=1}(\mathbf{0})\big)\delta_{i1,j1}\mathbf{I} & 0 \\ \hline 0 & \big(h\sin\theta_{i2}+\tilde{J}^{zz}_{l=2}(\mathbf{0})\big)\delta_{i2,j2}\mathbf{I} \end{array}\right) \quad ,\end{aligned} \tag{7.20}$$

where $m_{ij} = J_{ij} + p^+_{ij}$, and $n_{ij} = J_{ij} - p^+_{ij}$, with $p^+_{ij} = J_{ij}\cos\theta_{ij} + 2k\delta_{ij}\sin\theta_i^2$. Indexes 1 and 2 correspond to the two atoms in the unit cell. As we are considering only nearest-neighbour interactions, $J_{<il,jl'>} = J < 0$, and $S_{il} = S$, we have that $\tilde{J}^{zz}_{l\mathbf{0}}$, given by Eq. 2.127, reads

$$\begin{aligned}\tilde{J}^{zz}_{l=1}(\mathbf{0}) =& 2S(-J\cos(2\theta) + k\cos^2\theta) = 2JS + 2S(k-2J)\cos^2\theta \quad ,\\ \tilde{J}^{zz}_{l=2}(\mathbf{0}) =& 4(-J\cos(2\theta) + k\cos^2(\theta)) = 2JS + 2S(k-2J)\cos^2\theta \quad .\end{aligned} \tag{7.21}$$

The dynamical matrix is obtained from Eq. 7.20 as described by Eq. 2.132:

$$\mathbf{D}_{ll'}(\mathbf{q}) = \sum_i e^{i\mathbf{q}\cdot(\mathbf{r}_i - \mathbf{r}_j)} \begin{pmatrix} D^{++}_{il,jl'} & D^{+-}_{il,jl'} \\ D^{-+}_{il,jl'} & D^{--}_{il,jl'} \end{pmatrix} = \begin{pmatrix} D^{++}_{ll'}(\mathbf{q}) & D^{+-}_{ll'}(\mathbf{q}) \\ D^{-+}_{ll'}(\mathbf{q}) & D^{--}_{ll'}(\mathbf{q}) \end{pmatrix} \quad . \tag{7.22}$$

Performing the Fourier transformation by summing over the unit cells, we obtain:

$$\begin{aligned}\mathbf{D}_{11}(\mathbf{q}) = &\begin{pmatrix} -\tilde{A}^{++}_{01,01} & -\tilde{A}^{+-}_{01,01} \\ \tilde{A}^{-+}_{01,01} & \tilde{A}^{--}_{01,01} \end{pmatrix} + e^{iqa}\begin{pmatrix} -\tilde{A}^{++}_{01,11} & -\tilde{A}^{+-}_{01,11} \\ \tilde{A}^{-+}_{01,11} & \tilde{A}^{--}_{01,11} \end{pmatrix} \\ &+ e^{-iqa}\begin{pmatrix} -\tilde{A}^{++}_{01,-11} & -\tilde{A}^{+-}_{01,-11} \\ \tilde{A}^{-+}_{01,-11} & \tilde{A}^{--}_{01,-11} \end{pmatrix} \quad .\end{aligned} \tag{7.23}$$

We need to calculate each of the elements of the matrices:

$$\begin{aligned}A^{++}_{01,01} =& m_{01,01} = A^{--}_{01,01} = J_{01,01} + a^+_{01,01} = J_{01,01} + J_{01,01}c_{01,01} + 2k\delta_{01,01}s^2_{01} = 2k\sin^2(\theta)\\ A^{+-}_{01,01} =& n_{01,01} = A^{-+}_{01,01} = J_{01,01} - a^+_{01,01} = J_{01,01} - J_{01,01}c_{01,01} + 2k\delta_{01,01}s^2_{01} = 2k\sin^2(\theta)\\ \tilde{A}^{++}_{01,01} =& \tilde{A}^{--}_{01,01} = kS\sin^2(\theta) + [-h\sin\theta - (2JS + 2S(k-2J)\cos^2\theta)] = kS\sin^2(\theta) + h^+\\ \tilde{A}^{+-}_{01,01} =& \tilde{A}^{-+}_{01,01} = kS\sin^2(\theta)\\ A^{++}_{01,11} =& m_{01,11} = A^{--}_{01,11} = J_{01,11} + a^+_{01,11} = 0\\ A^{+-}_{01,11} =& n_{01,11} = A^{-+}_{01,11} = J_{01,11} - a^+_{01,11} = 0\\ \tilde{A}^{++}_{01,01} =& \tilde{A}^{--}_{01,01} = \tilde{A}^{+-}_{01,01} = \tilde{A}^{-+}_{01,01} = 0\\ A^{++}_{01,-11} =& m_{01,-11} = A^{--}_{01,-11} = J_{01,-11} + a^+_{01,-11} = 0\\ A^{+-}_{01,-11} =& n_{01,-11} = A^{-+}_{01,-11} = J_{01,-11} - a^+_{01,-11} = 0\\ \tilde{A}^{++}_{01,01} =& \tilde{A}^{--}_{01,01} = \tilde{A}^{+-}_{01,01} = \tilde{A}^{-+}_{01,01} = 0 \quad ,\end{aligned} \tag{7.24}$$

where $h^+ = -h\sin\theta - 2JS - 2S(k-2J)\cos^2\theta$. We then have that

$$\mathbf{D}_{11}(\mathbf{q}) = \begin{pmatrix} -kS\sin^2(\theta) - h^+ & -kS\sin^2(\theta) \\ kS\sin^2(\theta) & kS\sin^2(\theta) + h^+ \end{pmatrix} \quad . \tag{7.25}$$

Similarly for D_{22}:

$$\begin{aligned}A^{++}_{02,02} =& m_{02,02} = A^{--}_{02,02} = 2k\sin^2(\theta)\\ A^{+-}_{02,02} =& n_{02,02} = A^{-+}_{02,02} = 2k\sin^2(\theta)\\ \tilde{A}^{++}_{01,01} =& \tilde{A}^{--}_{01,01} = kS\sin^2(\theta) + [h\sin\theta - (2JS + 2S(k-2J)\cos^2\theta)] = kS\sin^2(\theta) + h^+\\ \tilde{A}^{+-}_{01,01} =& \tilde{A}^{-+}_{01,01} = kS\sin^2(\theta) \quad ,\end{aligned} \tag{7.26}$$

and because we are considering only n.n., the coupling between different cells between the same basis atom is zero, $\tilde{A}^{\alpha\beta}_{il,j\neq il}=0$, then:

$$\mathbf{D}_{22}(\mathbf{q})=\begin{pmatrix}-kS\sin^2(\theta)-h^+ & -kS\sin^2(\theta)\\ kS\sin^2(\theta) & kS\sin^2(\theta)+h^+\end{pmatrix} \quad . \tag{7.27}$$

Now, the off-diagonal matrices. For $\mathbf{D}_{21}(\mathbf{q})$, the matrix elements are:

$$\begin{aligned}
A^{++}_{01,02} =& m_{01,02}=A^{--}_{01,02}=J-J\cos(2\theta)=2J\sin^2(\theta)\\
A^{+-}_{01,02} =& n_{01,02}=A^{-+}_{01,02}=J+J\cos(2\theta)=2J\cos^2(\theta)\\
\tilde{A}^{++}_{01,02} =& \tilde{A}^{--}_{01,02}=JS\sin^2(\theta)\\
\tilde{A}^{+-}_{01,02} =& \tilde{A}^{-+}_{01,02}=JS\cos^2(\theta) \quad ,
\end{aligned} \tag{7.28}$$

$$\begin{aligned}
A^{++}_{01,-12} =& m_{01,-12}=A^{--}_{01,-12}=J_{01,-12}+a^{+}_{01,-12}=2J\sin^2(\theta)\\
A^{+-}_{01,-12} =& n_{01,-12}=A^{-+}_{01,-12}=J_{01,-12}-a^{+}_{01,-12}=2J\cos^2(\theta)\\
\tilde{A}^{++}_{01,-12} =& \tilde{A}^{--}_{01,-12}=JS\sin^2(\theta)\\
\tilde{A}^{+-}_{01,-12} =& \tilde{A}^{-+}_{01,-12}=JS\cos^2(\theta) \quad .
\end{aligned} \tag{7.29}$$

For $\mathbf{D}_{21}(\mathbf{q})$:

$$\begin{aligned}
A^{++}_{02,01} =& m_{02,01}=A^{--}_{02,01}=J_{02,01}+a^{+}_{02,01}=2J\sin^2(\theta)\\
A^{+-}_{02,01} =& n_{02,01}=A^{-+}_{02,01}=J_{02,01}-a^{+}_{02,01}=2J\cos^2(\theta)\\
\tilde{A}^{++}_{02,01} =& \tilde{A}^{--}_{02,01}=JS\sin^2(\theta)\\
\tilde{A}^{+-}_{02,01} =& \tilde{A}^{-+}_{02,01}=JS\cos^2(\theta) \quad ,
\end{aligned} \tag{7.30}$$

$$\begin{aligned}
A^{++}_{02,11} =& m_{02,11}=A^{--}_{02,11}=J_{02,11}+a^{+}_{02,11}=2J\sin^2(\theta)\\
A^{+-}_{02,11} =& n_{02,11}=A^{-+}_{02,11}=J_{02,11}-a^{+}_{02,11}=2J\cos^2(\theta)\\
\tilde{A}^{++}_{02,11} =& \tilde{A}^{--}_{02,11}=JS\sin^2(\theta)\\
\tilde{A}^{+-}_{02,11} =& \tilde{A}^{-+}_{02,11}=JS\cos^2(\theta) \quad .
\end{aligned} \tag{7.31}$$

Putting together all these results, we have the total dynamical matrix shown in Eq. (7.8).

7.B.2 Analytical solution

An analytical diagonalization of Eq. (7.8) at $q=0$ gives:

$$\begin{aligned}
a_0 =& \frac{1}{S(k-2J)^2}\sqrt{-\frac{Jk}{2}h^4+h^2S^2(k-2J)^2(4Jk-k^2)-4kS^4(2J-k)^5} \quad ,\\
a_1 =& \frac{1}{S(k-2J)^2}\sqrt{\frac{Jk}{2}h^4+h^2S^2(k-2J)^2(4J^2-2Jk-k^2)-4kS^4(2J-k)^5} \quad ,
\end{aligned} \tag{7.32}$$

or yet

$$\begin{aligned}
a_0 =& 2|S|\sqrt{-2Jk\sin^4\theta+(4Jk-k^2)\sin^2\theta-k(2J-k)} \quad ,\\
a_1 =& 2|S|\sqrt{2Jk\sin^4\theta+(4J^2-2Jk-k^2)\sin^2\theta-k(2J-k)} \quad .
\end{aligned} \tag{7.33}$$

Let us next understand the asymptotic behaviors of the above expressions.

For $k \ll J$:

$$\begin{aligned} a_0 =& 2|S|\sqrt{-2Jk} \quad , \\ a_1 =& 2|S|\sqrt{\left(\frac{h}{2S}\right)^2 - 2Jk} \quad . \end{aligned} \tag{7.34}$$

In the absence of anisotropy:

$$\begin{aligned} a_0(k=0) =& 0 \\ a_1(k=0) =& |h| \end{aligned} \quad . \tag{7.35}$$

In the absence of field:

$$a_0(h=0) = a_1(h=0) = 2|S|\sqrt{k(k-2J)} \quad , \tag{7.36}$$

whose limits are: $k \gg J$,

$$a_0(h=0) = a_1(h=0) = 2|S||k| \quad , \tag{7.37}$$

and for $k \ll J$,

$$a_0(h=0) = a_1(h=0) = 2|S|\sqrt{2|J|k} \quad . \tag{7.38}$$

The magnetization saturates when $h = 2S(k-2J)$ because then $\sin\theta = 1 \rightarrow \theta = \pi/2$:

$$\begin{aligned} a_0 =& 0 \\ a_1 =& 2|S|\sqrt{2J(2J-k)} \end{aligned} \tag{7.39}$$

that is, when the field is strong enough to fully polarize the magnetization, the spin gap closes: $a_0 = 0$. For even higher fields, it comes to open again.

Chapter 8

Prediction of the existence of in-plane magnetic skyrmions in Co/W(110)

Anisotropic magnetic films are media whose spin-wave properties depend on their direction of propagation. These anisotropies occur in systems with low symmetries. The resulting anisotropic Dzyaloshinskii-Moriya interactions (DMI), for example, can lead to the stabilization of antiskyrmions [111]. Experimentally, such anisotropic DMI was found for Co-films deposited on W(110) and covered with a gold cap [154]. Motivated by these findings, we investigated from first principles the magnetic properties of films containing up to three layers of reconstructed Co on the W(110) surface, which are thinner than those films studied in Chapter 5 and where the DMI might play an important role. Furthermore, we considered a monolayer of pseudomorphic Co/W(110) to simulate the case of below-one-monolayer films, which do not experience the reconstruction. The anisotropy, magnitude, and signs of the interactions are analyzed in detail with a focus on the DMI. We determined the ground state and the stability of different noncollinear spin structures, such as skyrmions and spin spirals, using micromagnetic analytics and atomistic-spin-dynamics simulations. We find that the reconstructed single monolayer film has an in-plane easy axis that can host in-plane skyrmions, i.e., skyrmions that live in the in-plane background magnetization. This is the most important result of the current chapter since such in-plane skyrmions have the advantage of shrinking down in size because of the dipole-dipole interaction in contrast to the usual out-of-plane skyrmions. Furthermore, we demonstrate that these skyrmions are stabilized by the DMI and that their antiparticles, the antiskyrmions, are also stable and energetically degenerate, as guaranteed by the mirror symmetry of the system. Finally, we unveil the spin-wave properties of the in-plane skyrmions in these films.

8.1 Introduction

The first experimental observations of skyrmions in magnetic materials paved the way to an intense effort of the scientific community aiming at the understanding and control of these topologically nontrivial objects [7, 11, 155–158]. Besides being of fundamental interest in the physics of condensed matter, they can lead to

technological development in low-power and ultra-high-density information storage applications, for example. As a quasiparticle, the skyrmion comes accompanied by an antiquasiparticle that is named antiskyrmion: it has the same polarity as the skyrmion, that is, they have the same core orientation, see Fig. 8.1.1 (a) and (b), but they have opposite vorticities and consequently opposite topological charges [159], as shown in Fig. 8.1.1 (c) and (d). Furthermore, together, they are of practical interest as they can respond differently under the influence of various external fields [160–162]. Skyrmions are more likely to occur in systems with isotropic Dzyaloshinskii-Moriya interaction. Meanwhile, symmetry analysis showed that only thin films with the C_{2v} space-group symmetries or lower allow the antiskyrmion to be more stable than its counterpart [111]. Even more restricting can be the conditions under which skyrmions and antiskyrmions coexist.

Furthermore, most research has been focused on magnetic films with an out-of-plane magnetocrystalline anisotropy easy-axis, because an out-of-plane magnetization is the usual background where skyrmions and antiskyrmions live. However, skyrmions living in an in-plane magnetized system described by phenomenological models and stabilized by the frustration of the magnetic exchange interaction (MEI) had also been reported [163, 164]. They were named bimerons for being thought as pairs of coupled merons, which are vortex-like structures whose spins map onto a hemisphere, of equal topological charge $\pm\frac{1}{2}$. We argue in this chapter that they are nothing else than in-plane skyrmions. These in-plane skyrmions might be of particular importance for technological applications because they can be smaller than the usual out-of-plane skyrmions thanks to the dipole-dipole interaction, which shrinks the former and enlarge the latter. Recently and interestingly, using a simple model Hamiltonian, Göbel *et al.* [165] showed that the DMI can also stabilize in-plane skyrmions.

In this chapter, we study ultrathin films, from one to three atomic monolayers (ML), of reconstructed cobalt on tungsten (110), that belong to the C_s space group. This symmetry group, as discussed later on, is essential for the stabilization of the in-plane skyrmions. For comparison, we also consider a single layer of pseudomorphic Co/W(110) of C_{2v} symmetry. We calculated their magnetic properties using density functional theory within the relativistic Korringa-Kohn-Rostoker (KKR) method, and the magnetic exchange tensor was obtained with the infinitesimal-rotation approach, as described in Chapter 3. We calculated the spiralization tensor, which demonstrates a high anisotropy of the DMI interaction as was observed experimentally for Au/Co/W in Ref. [154]. Using the *ab initio* magnetic properties, we determined, using analytical micromagnetic models and atomistic-spin-dynamics simulations, the ground-state spin configurations and the stability of in-plane and out-of-plane skyrmions and antiskyrmions, and other noncollinear spin textures.

We found that only the single monolayer cobalt films, reconstructed and pseudomorphic, can stabilize noncollinear spin structures and that they have in-plane anisotropy easy-axis. We demonstrate that these films can stabilize skyrmions, making Co/W(110) the first material system predicted to host in-plane skyrmions stabilized by DMI. Furthermore, we show that, as this system's mirror symmetry is preserved by the in-plane magnetization, the antiskyrmion also occurs and is degenerate to the skyrmion, for they are mirror images of each other. Finally, we explore the properties of the spin-wave excitations and their spin-resolved inelastic electron

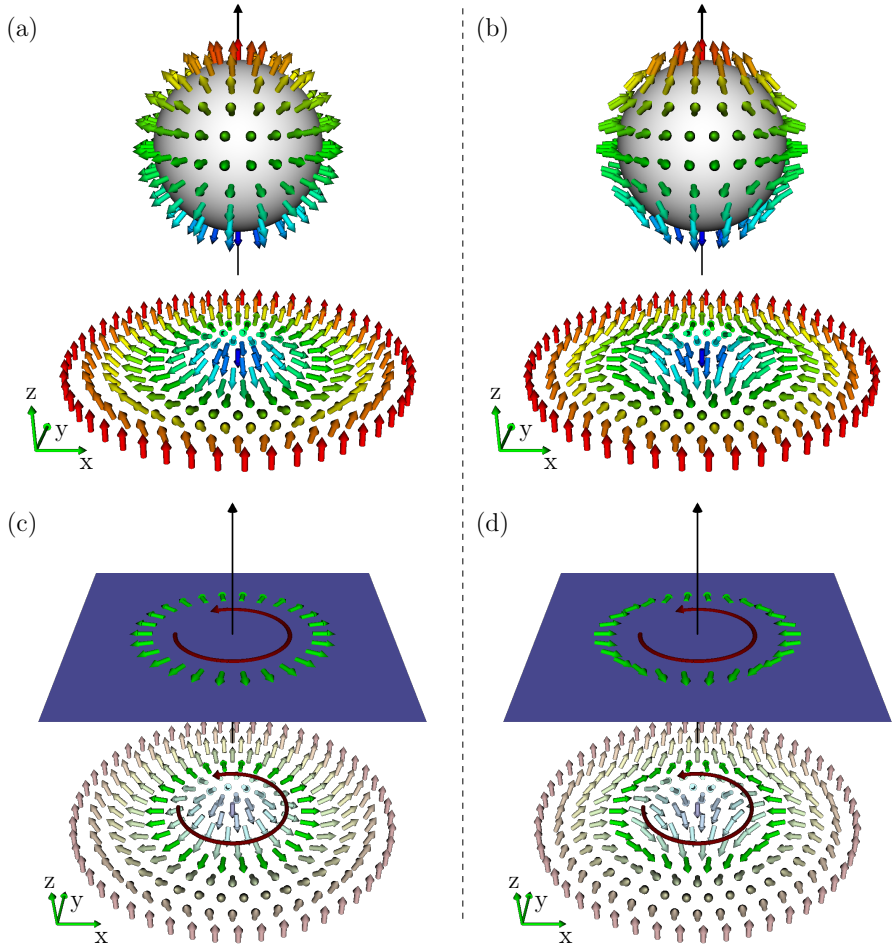

Figure 8.1.1: Skyrmion and antiskyrmion. (a) and (b) depict a skyrmion and an antiskyrmion, respectively, mapped onto spheres. The background magnetization (in red) defines the polarization axis, which is indicated by the long black arrow. The core of both skyrmion and antiskyrmion are antiparallel to the background magnetization and shown in blue. Therefore, they have the same polarization axis. (c) and (d) show the winding of the spins along a circumference around the skyrmion and antiskyrmion cores, respectively. When we move counterclockwise on these paths, the skyrmion spins wind also counterclockwise but the antiskyrmion spins wind clockwise. Therefore, they have opposite vorticity.

scattering spectra.

8.2 Atomic structure and space group

We discussed the atomic structure of Co/W(110) in Chapter 5, which we summarize now. Experimentally, thin films of cobalt can be grown on tungsten via vapor deposition. However, hexagonal close packed Co(0001) and bcc W(110) surfaces have a mismatch of $(a_{\mathrm{W}}-a_{\mathrm{Co}})/a_{\mathrm{Co}} = 26\%$ along the W[001] and $(\sqrt{2}a_{\mathrm{W}}-\sqrt{3}a_{\mathrm{Co}})/\sqrt{3}a_{\mathrm{Co}} = 3\%$ in the $[1\bar{1}0]$ directions, where the lattice constants are $a_{\mathrm{Co}} = 2.51\,\text{Å}$ and $a_{\mathrm{W}} = 3.16\,\text{Å}$. This causes a reconstruction of the pseudomorphically-growing cobalt film already at very low layer coverage, ~ 0.72 MLs, depending on the temperature and annealing conditions, which can be described by a 4×1 tungsten unit cell containing 8 W atoms in each tungsten layer and 10 Co atoms in each cobalt layer [88, 99, 101, 154, 166, 167]. Despite the reconstruction, Co forms a smooth surface and a sharp interface due to its immiscibility to tungsten. For the sake of comparison, and for representing the case of small Co islands on W(110), we also consider a pseudomorphic (unreconstructed) Co on W(110).

The hcp-Co(0001) surface belongs to the C_{3v} space group, and in fact, a free-standing hcp Co monolayer has even higher symmetries belonging to the D_{6h} group. In contrast, the W(110) surface belongs to the C_{2v}, and together, the reconstructed Co/W(110) has the symmetry of the C_s, that is, it is only invariant under reflection by a single mirror plane, which is perpendicular to the W[001] direction. The cobalt reconstruction breaks all rotational symmetries of the film, which will have a profound impact on the magnetic properties of these systems.

We consider cobalt films of 1 to 3 MLs, and we simulate the substrate with a 6 MLs W(110) slab. Further details of the considered crystal structure of the cobalt films on tungsten were discussed in Chapter 5, where we studied the magnetic properties of 3-8 monolayers (ML) films. Here, we focus on even thinner films considering the effects induced by the spin-orbit coupling.

Next, we discuss the magnetic properties of these films, which were obtained from *ab initio* simulations based on density-functional theory, within the relativistic KKR method in the local-spin-density approximation (LSDA), discussed in Chapter 3. Using the infinitesimal-rotations method, we mapped the first-principles calculations onto the following Hamiltonian as introduced in Sec. 2.1.6:

$$\mathcal{H} = -\sum_{ij} J_{ij}\mathbf{S}_i \cdot \mathbf{S}_j - \sum_{ij} \mathbf{D}_{ij} \cdot \mathbf{S}_i \times \mathbf{S}_j - K\sum_i (\hat{\mathbf{K}} \cdot \mathbf{S}_i)^2 \quad . \tag{8.1}$$

The first term corresponds to the exchange energy due to the magnetic exchange interaction J_{ij} between sites i and j. The second is the contribution due to the Dzyaloshinskii-Moriya interaction given by the vector $\mathbf{D}_{ij}$, and the third is due to the uniaxial magnetocrystalline anisotropy with axis along $\hat{\mathbf{K}}$ with strength K. Here, we take $|\mathbf{S}| = 1$, such that J_{ij} and $\mathbf{D}_{ij}$ are multiplied by the magnetic moment of sites i and j, e.g., $J_{ij} \to M_i J_{ij} M_j$. Throughout this chapter, the Cartesian reference frame will have the x and y axes laying in the film plane along W[001] and W$[1\bar{1}0]$, respectively, and the z axis is out-of-plane.

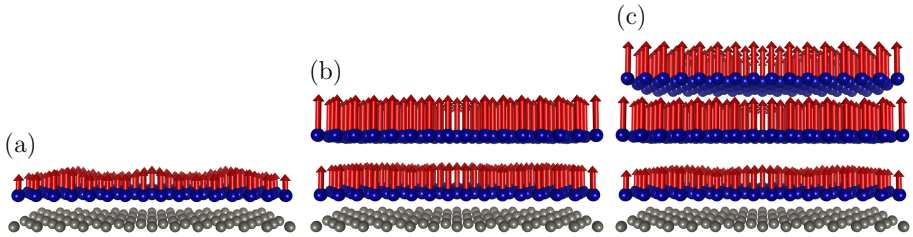

Figure 8.3.1: Magnetic moments of ultrathin films of cobalt on tungsten (110). (a)–(c) Films of 1 to 3 MLs of reconstructed cobalt, respectively. The gray and blue atoms depict tungsten and cobalt, respectively. Meanwhile, the red arrows represent the magnetic moment of individual atoms. The biggest arrow in the figures corresponds to 1.78 μ_B, see Tab. 8.3.1 for the layer-averaged values. Notably, the interface-layer magnetic moments are reduced in comparison to the overlayers because of the hybridization with the tungsten substrate. The depicted displacements between layers are arbitrary.

8.3 Magnetic interactions

8.3.1 Magnetic moments

The atomic magnetic moment of materials is determined by the electronic structure, which is strongly affected by the crystalline structure. For a given element, its magnitude changes from an isolated atom to an atom lying in a crystal. Further variations are observed between the bulk, surface and interface atoms. For 1–3 MLs films of Co/W(110), we observe a layer-dependent variation of the magnetic moment, see Fig. 8.3.1, which also depend on the thickness of the films. The highest magnetic moment is 1.78 μ_B, which corresponds to the experimental bulk-hcp cobalt value [168], and the in-plane-averaged magnetic moments are given in Tab. 8.3.1. In the pseudomorphic cobalt 1 ML (rectangular lattice), the cobalt atoms are farther apart from each other in comparison with the Co atoms in the reconstructed 1 ML film (hexagonal lattice). This causes the magnetic moments of the pseudomorphic 1 ML film to be higher than in the reconstructed film of the same thickness.

	magnetic moments (μ_B)			
layer	pseudomorphic cobalt	reconstructed cobalt		
	1 ML	1 ML	2 MLs	3 MLs
1 (interface)	1.51	1.05 (0.09)	1.33 (0.02)	1.17 (0.04)
2			1.76 (0.01)	1.67 (0.02)
3				1.71 (0.01)

Table 8.3.1: Layer-dependent magnetic moments of ultrathin cobalt films on tungsten (110). We consider films of 1 ML for pseudomorphic and 1–3 MLs for reconstructed cobalt. The values for reconstructed cobalt correspond to the average value within the unit cell, which contains 10 atoms per layer, with the standard deviation shown in parentheses.

Furthermore, a modulation is observed within the Co layers, originated from the spatial heterogeneity at the interface, and therefore mostly noticeable there,

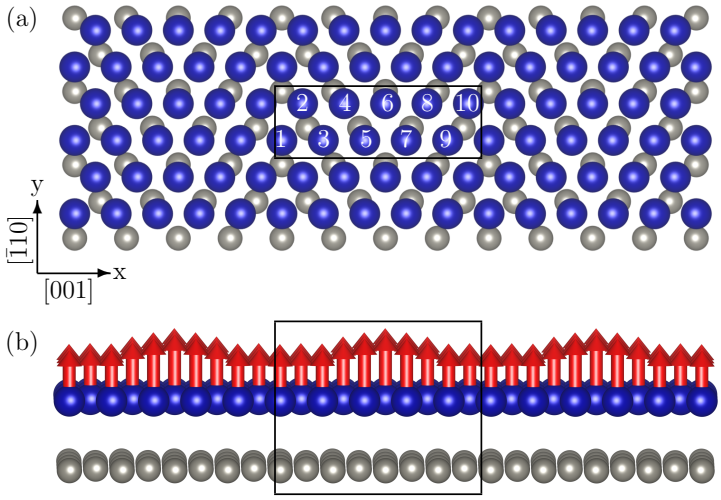

Figure 8.3.2: Cobalt stacking on tungsten (110) and magnetization modulation. (a) The interface layer of reconstructed Co (blue atoms) stacked on the W(110) (gray atoms). The black frame indicates the supercell with its 10 Co atoms numerated, whose magnetic moments, in order, are: 0.96, 0.95, 0.97, 1.07, 1.18, 1.23, 1.18, 1.07, 0.97, 0.95 μ_B. (b) Side view of 1 ML Co film together with its magnetic moments. Relatively strong modulation of the magnetization along the [001] direction is observed. A comparison between (a) and (b) reveals that Co atoms with higher magnet moments mostly atop of W, while smaller magnetic occurs to atoms seated on the hollow to the W lattice.

Fig. 8.3.1 (a). Within the unit cell, different Co atoms have distinct neighborhoods: some lie almost atop of a W atom, and others in a hollow position between three W, see the top view of the interface of reconstructed Co (blue atoms) stacked on W(110) (gray atoms) in Fig. 8.3.2 (a). Those Co atoms seated in the hollows of the tungsten lattice are in close contact with more atoms of the substrate than the Co atop. This yields a higher hybridization of the electronic states of the hollow Co atoms. As a consequence, their magnetic moments reduce, as observed on the edges of the unit cell, see Fig. 8.3.2 (b).

8.3.2 Magnetocrystalline anisotropy

As discussed along this thesis, the relativistic spin-orbit coupling can cause differences in energy for different orientations of the material magnetization with respect to the lattice. Invoking once more the magnetic force theorem, we calculated these anisotropy energies $E^{\alpha\beta} = E^{\alpha} - E^{\beta}$ from the difference of the total band energies per cobalt atoms when the magnetization is set along the α and β–direction, as given by Eq. 3.79. The self-consistent electronic structures of cobalt films were obtained with the magnetization along the z–axis, i.e., out-of-plane. Starting from the obtained converged potential, the total band energy for the other directions were obtained with one-shot calculations after rotating the magnetization to the corresponding direction.

	magnetic anisotropy (meV / per atom)			
	pseudomorphic cobalt	reconstructed cobalt		
	1 ML	1 ML	2 MLs	3 MLs
$K^x = E^z - E^x$	0.14	0.23	-0.29	0.05
$K^y = E^z - E^y$	0.23	0.13	0.06	0.23

Table 8.3.2: Magnetocrystalline anisotropies. E^α is the total band energy per cobalt atom for when the magnetization is set along the α–direction. We consider Co films of 1 pseudomorphic monolayer and 1–3 reconstructed monolayers. K^α is the anisotropy constant along the α–direction, which corresponds to an easy-axis when it is positive, and a hard-axis for negative values. In most cases, it is energetically more favorable for the magnetization to be along one of the in-plane axes than out-of-plane. The only exception is the 2 MLs reconstructed system, where the out-of-plane z–axis is more favorable than the x axis, however, the strongest easy-axis is still in-plane along y.

These DFT energy differences were then mapped onto a biaxial anisotropy model given by,

$$\mathcal{H}_K = -\sum_i \left(K^x (S_i^x)^2 + K^y (S_i^y)^2 \right) \quad . \tag{8.2}$$

This energy is composed of two terms, one for each anisotropy axis. For example, a positive value of K^x corresponds to an easy-axis along the x–axis, i.e., this anisotropy energetically favors an alignment of the magnetic moments along the x–axis. For negative values, a hard-axis along the x–direction is established, and the magnetic moments would lie in the plane perpendicular to this axis. Naturally, the same is true for the other axis, and they might compete or work together. From this model, we obtain that

$$\begin{aligned} K^x &= E^z - E^x \\ K^y &= E^z - E^y \end{aligned} \quad , \tag{8.3}$$

which, therefore, quantify the energy difference between the magnetization alignment along one of the in-plane axes and the out-of-plane direction.

The results are summarized in Tab. 8.3.2. We observe that for all cases, the magnetization has a strong tendency to lie in-plane with z as a hard-axis. This is the case because most K^α in Tab. 8.3.2 are positive. Only for the 2 MLs system, K is negative, indicating that it is more favorable for the magnetization to point along z than along x by -0.29 meV. But when the alignment along z is compared to the alignment along y, we see that the latter is more favorable by 0.06 meV. It also worth to notice that the small values of K^α, as is the case of $K^y = 0.06$ meV for the 2 MLs and $K^x = 0.05$ meV for 3 MLs, indicate that the system is close to a uniaxial behavior. Therefore, the reconstructed 2 and 3 MLs systems can be modeled by a uniaxial anisotropy along x and y with an averaged values of $K^x = -0.32$ meV and $K^y = 0.20$ meV, respectively. Both 1 ML systems, the pseudomorphic and reconstructed cobalt films, are better described by the biaxial anisotropy model. However, the reconstructed film has its strongest easy-axis along x, while the pseudomorphic system has it along y.

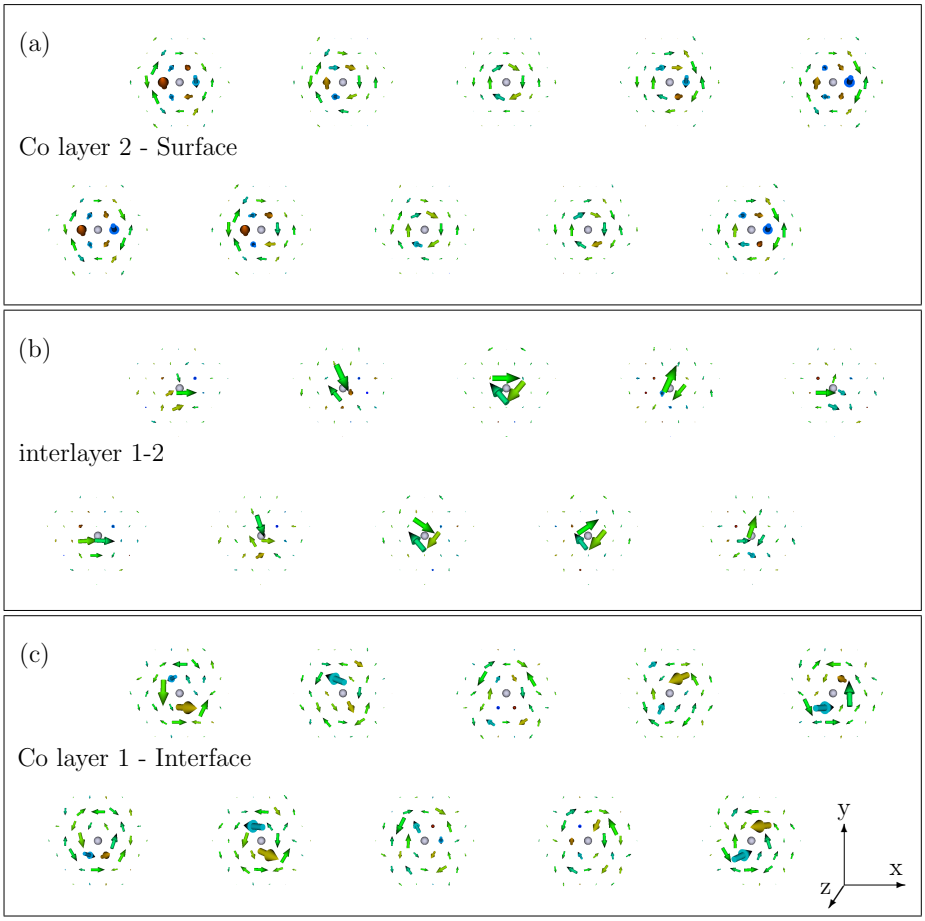

Figure 8.3.3: Dzyaloshinskii-Moriya vectors for the 2 MLs reconstructed cobalt film. (a) and (c) show the intralayer interactions of the film surface and interface, respectively. (b) displays the interlayer DMI interactions between the two cobalt layers. Each cluster of vectors represent the interactions of one atom in the unit cell (the gray sphere) and its neighbors. The centers of the vectors are located on the position of the neighbors. The color code paints in blue and red out-of-plane vectors, and green the in-plane ones. The biggest arrow corresponds to a DMI strength of 0.63 meV. The interface with the substrate makes every cluster different from the others. Out-of-plane components are mostly observed on the nearest-neighbor couplings at the surface.

8.3.3 Dzyaloshinskii-Moriya interaction

Let us start by analyzing the reconstructed 2Co/W(110) film. The DMI vectors are shown in Fig. 8.3.3, where each cluster corresponds to the interactions of a given Co atom of the film. Figures 8.3.3 (a) and 8.3.3 (c) display the intralayer interactions within the surface layer (Co layer 2) and the interface layer (Co layer 1), respectively; and Fig. 8.3.3 (b) corresponds to the coupling between atoms of different layers (interlayer coupling). Each vector represents the interaction between

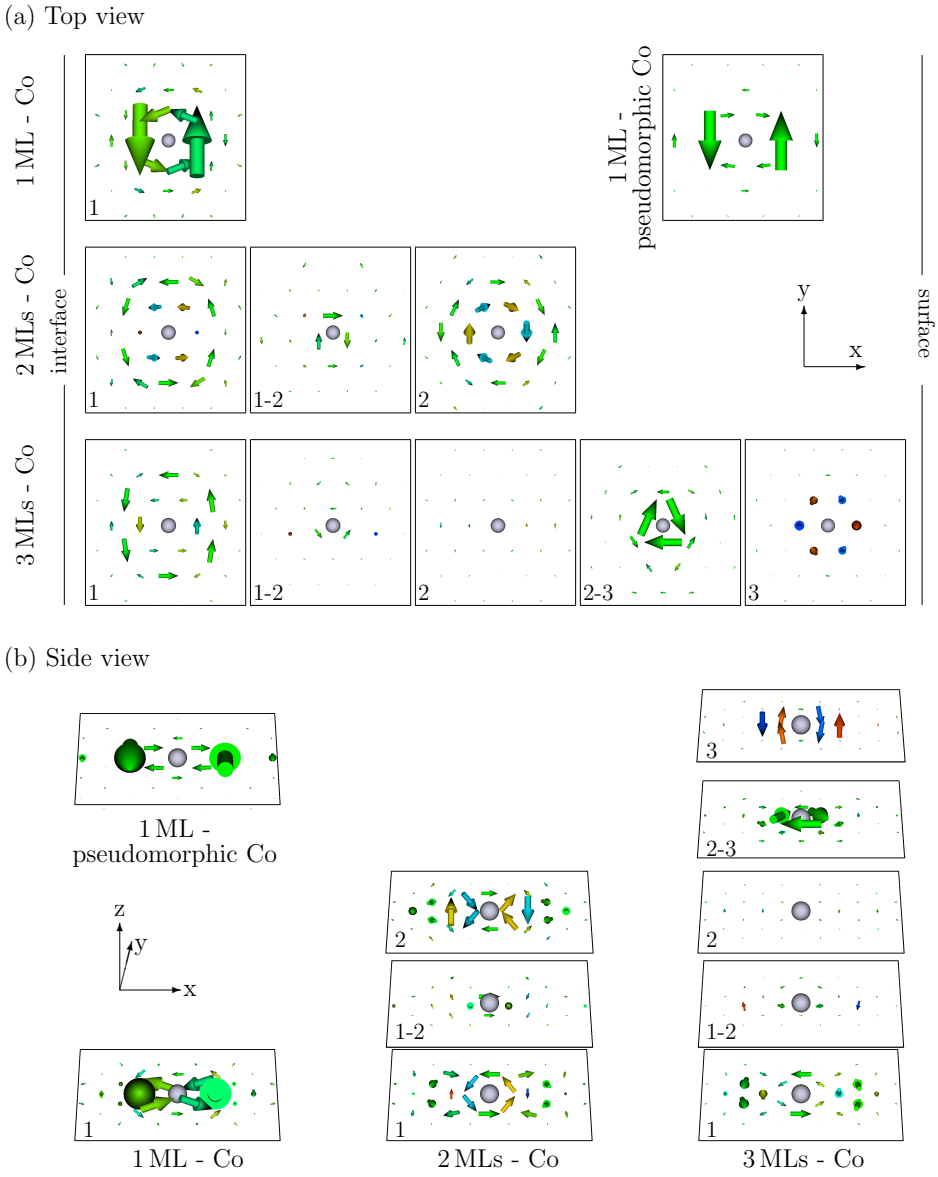

Figure 8.3.4: Averaged Dzyaloshinskii-Moriya vectors for the pseudomorphic and reconstructed films of Co/W(110). We averaged out the 10 atoms per layer in the unit cell. (a) and (b) show a top and side view of the same interactions. Each vector represents the DMI between the central atom (in gray) and the neighbors (not depicted). The size of the arrows depicts the DMI strength and is on the same scale for all charts, except for the pseudomorphic film, which was scaled down by a factor 10. The color code paints in blue and red out-of-plane vectors, and green the in-plane ones. The interactions are highly anisotropic in strength and chirality for all cases. The biggest shown arrow of the reconstructed films has a length corresponding to 0.84 meV, and 3.75 meV for the pseudomorphic film.

the central atom (depicted in gray) and one neighbor — the center of the arrow is located on the position of that neighbor. The size of the arrows scale with the magnitude of the DMI vectors. The color scale marks vectors pointing out-of-plane in opposite directions in blue and red, and in-plane vectors are shown in green. As expected, each interaction cluster that corresponds to a particular atom of the unit cell is distinct from the others. This means that the substrate neighboring is fundamental in determining the DMI for a given Co atom. Furthermore, we notice that the nearest-neighbor DMI vectors of the surface are mostly out-of-plane, while the rest of the interactions have their major components in-plane.

With such a complex set of DMI vectors, it is hard to have an impression of which kind of magnetic structure it will lead to. As a first approach to simplify these data, and also to allow us to systematically compare the DMI of films of various thicknesses, we can average the interaction clusters within each layer of the unit cell. In this way, we are left with one interaction cluster for every layer, instead of ten. Most importantly, this procedure preserves the C_s space group of the original systems. The outcome is shown in Figs. 8.3.4 (a) and 8.3.4 (b), which depict the top and side views of the averaged DMI for the pseudomorphic and reconstructed cobalt films, respectively. The DMI for the pseudomorphic film is scaled down by a factor 10 to be plotted in comparison to the reconstructed cases.

In Fig. 8.3.4 (a), for the reconstructed and pseudomorphic 1 ML, we can observe an anisotropic DMI, which is stronger for the right and left neighbors than for the others. Therefore, these sets of DMI favor the formation of spin spiral or distorted skyrmions. The strongest averaged DMI interaction for each reconstructed Co film has a magnitude of 0.84 meV, 0.33 meV and 0.44 meV, for 1 to 3 MLs, respectively; and it is of 3.75 meV for the 1 ML pseudomorphic film. Without the averaging, these values are: 1.48 meV, 0.63 meV and 0.76 meV, for 1 to 3 MLs, respectively. Focusing on the interface layer of all films, we further notice that most vectors swirl around the origin. Most vectors have the same swirling sense around the central gray atom (or chirality) for the 1 ML and 3 MLs Co films, which can favor the formation of skyrmions; while for 2 MLs Co film, we observe two sets with opposite chirality that could favor antiskyrmions occurrence.

8.3.4 Magnetic exchange interaction

In Fig. 8.3.5, we represent the exchange interaction for our four systems, the 1 ML pseudomorphic and the 1-3 MLs reconstructed cobalt films on tungsten. We follow the same procedure described for the DMI and average the contributions from the 10 Co atoms in each layer. The blue represents a ferromagnetic coupling, while red presents the antiferromagnetic one. The strength of the interaction is given by the saturation, the darker the color, the stronger is the interaction. The strongest blue of Fig. 8.3.5 corresponds to 19.9 meV (occurring for the reconstructed 3 MLs) and the strongest red to -5.9 meV (occurring for the pseudomorphic 1 ML). All the nearest-neighbor couplings are ferromagnetic, which soften at the interface with the tungsten substrate. Shells of antiferromagnetic coupling can be seen for farther-away neighbors. Overall, the magnetic exchange interactions decay with the distance between the sites. Next, we want to study the decay of both the magnetic exchange and the Dzyaloshinskii-Moriya interactions for longer distances.

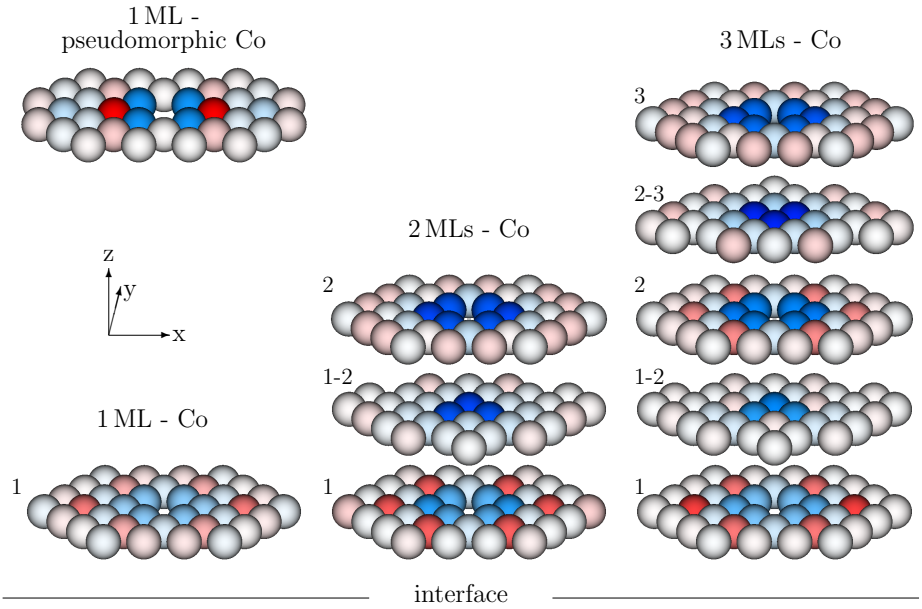

Figure 8.3.5: Averaged magnetic exchange interactions for the pseudomorphic and reconstructed films of Co/W(110). We averaged out the 10 atoms per layer in the unit cell. Each sphere represents a neighbor of the central atom (not shown) whose color corresponds to the exchange coupling between them. The color code paints in blue the ferromagnetic coupling, and in red the antiferromagnetic one. The highest blue saturation corresponds to 19.87 meV, and the highest red to −5.91 meV. The nearest neighbors couple ferromagnetically, whose intensity is weakened on the interface. The MEI decay and oscillate, even changing sign, for farther away neighbors.

8.3.5 MEI and DMI spatial decay

Figure 8.3.6 shows the log-log plot of the absolute value of the magnetic exchange and Dzyaloshinskii-Moriya interactions $|J_{ij}|$ and $|\mathbf{D}_{ij}|$ for all atoms in each system. The red continuous lines are reference decay functions. Once again, the in-plane-averaged interactions were considered. We can see that the MEI decays at least as r^{-3}, and the DMI decays at least as r^{-2}. No significant differences were observed for the decay of the different atoms in the system of multiple layers.

8.4 Micromagnetic analytics

8.4.1 Stiffness and spiralization tensors

In order to study the spin-wave spectra for our four films of cobalt deposited on tungsten, we need first to obtain their ground-state spin configuration. Here we have to perform real-space summations of the interactions ensuring the convergence of the properties of interest. Large wavevector spin-wave energies, which depend mostly on the short-range interactions, converge faster than the spin-wave energies near

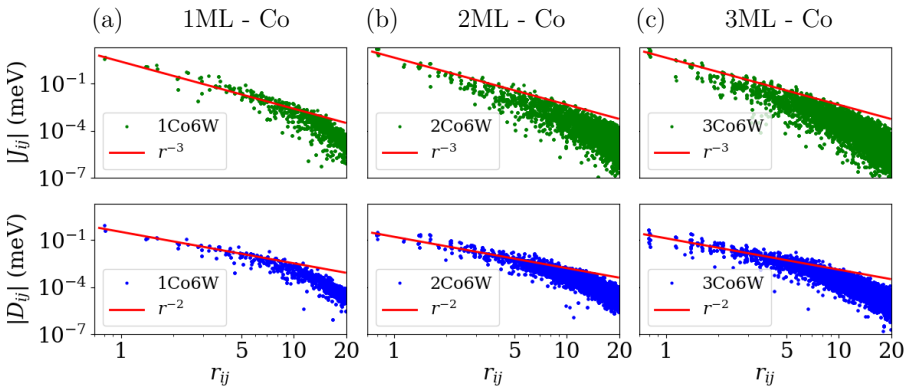

Figure 8.3.6: Spatial decay of the magnetic exchange and the Dzyaloshinskii-Moriya interactions. The result for reconstructed Co films of different thicknesses, from 1 to 3 ML, are shown (a-c). The upper panels correspond to the MEI, while the lower panels to the DMI. The figures are in the log-log scale. The MEI decays faster than the r^{-3} curve, which is shown in red. Meanwhile, the DMI only decays faster than the r^{-2} curve.

the center of the Brillouin zone. Similarly, the ground-state spin configuration can require a sum over large real space distances for a proper and realistic description.

The stiffness tensor is the magnetic property that measures how "hard" is a material's magnetization with respect to the temperature, for example. Meanwhile, the spiralization tensor informs on the magnetization susceptibility to the formation of spin spirals. They can help us to understand the convergence of the real space sums besides being valuable to determine the ground-state spin configurations. We discuss next how to derive these two tensors.

We start by trying to determine whether a spin spiral is the ground state, or at least to check how its energy compares to that of the ferromagnetic state. We are restricting our search among spin spirals of the type

$$\mathbf{S}_i = \cos\phi_i \sin\theta \mathbf{n}^1 + \sin\phi_i \sin\theta \mathbf{n}^2 + \cos\theta \mathbf{n}^3 \quad , \tag{8.4}$$

where $\mathbf{n}^3$ is a unity vector defining the axis around which the spins rotate, and that it forms an orthonormal basis set for the three dimension space together with $\mathbf{n}^1$ and $\mathbf{n}^2$. θ is the cone angle between the spins and $\mathbf{n}^3$, $\phi_i = \mathbf{q} \cdot \mathbf{R}_i$, where $\mathbf{q}$ is the spiral wavevector, and $\mathbf{R}_i$ the position vector of the i-th spin. For simplicity, the modulus of $\mathbf{S}_i$ was chosen to be 1.

In general, the spin-spiral energy, obtained by replacing the spins in the Hamiltonian of Eq. (8.1) by those of the spiral in Eq. (8.4), is a function of all the quantities

that define the spiral: n^α, θ and $\mathbf{q}$:

$$\begin{aligned}\varepsilon = \frac{\mathcal{H}}{N} = &-\frac{1}{2N}\sum_{ij} J_{ij}\left[\cos\left(\mathbf{q}\cdot\mathbf{R}_{ij}\right)\sin^2\theta + \cos^2\theta\right] \\ &-\frac{1}{2N}\sum_{ij}\left\{\sin^2\theta D^3_{ij}\sin(\mathbf{q}\cdot\mathbf{R}_{ij}) + \sin 2\theta\left[\sin(\mathbf{q}\cdot\mathbf{R}_i)D^1_{ij} - \cos(\mathbf{q}\cdot\mathbf{R}_i)D^2_{ij}\right]\right\} \\ &-K\left[\frac{1}{2}\sin^2\theta\big((K^1)^2(\delta_{2\mathbf{q},\{0,\mathbf{Q}\}}+1) + (K^2)^2(1-\delta_{2\mathbf{q},\{0,\mathbf{Q}\}})\big)\right. \\ &\qquad\left. + \sin 2\theta\big(K^1K^3\delta_{\mathbf{q},0}\big) + (K^3)^2\cos^2\theta\right] \quad ,\end{aligned} \tag{8.5}$$

where $D^\alpha_{ij} = \mathbf{D}_{ij}\cdot\mathbf{n}^\alpha$ and $K^\alpha = \hat{\mathbf{K}}\cdot\mathbf{n}^\alpha$, see Apx. 8.A.2. Here, we included a factor of 1/2 in front of the MEI and DMI terms in Eq. (8.1). The term in the first line of the above equation comes from the magnetic exchange interaction; the one in the second line from the Dzyaloshinskii-Moriya interaction; and the last two lines correspond to the contribution of the magnetic anisotropy. The latter is a constant for most spin-spiral wavevectors, but with a singularity for $\mathbf{q} = 0$ and $\mathbf{q} = \mathbf{Q}/2$, which correspond to a ferromagnetic and an antiferromagnetic phase, respectively, and $\mathbf{Q}$ is a reciprocal-lattice primitive vector.

To simplify the expression of the spin-spiral energy, we can perform its Taylor expansion around $\mathbf{q} = 0$ to the second order in the wavevector, see Apx. 8.A.3. The coefficients of the first and second-order terms are given by the gradient and Hessian of the spiral energy, respectively. The first order term is known as the spiralization tensor

$$\mathcal{D}^{\alpha\mu} = -\sum_j D^\alpha_{0j} R^\mu_{0j} \quad , \tag{8.6}$$

where $\alpha = x, y, z$ indicate three orthonormal directions for the spiral axis $\mathbf{n}^3$. And the second order one is the so-called exchange stiffness tensor

$$\mathcal{A}^{\mu\nu} = \sum_j J_{0j} R^\mu_{0j} R^\nu_{0j} \quad , \tag{8.7}$$

where μ and ν label the Cartesian components of the position vector $\mathbf{R}$ [169]. The index 0 labels a reference atom, which can be arbitrary once we are assuming translational invariance. These results we obtained by considering the summation over a Bravais lattice and taking $\theta = \pi/2$, i.e., considering only flat spirals. A full derivation of these expression are shown in the Apx. 8.A. The stiffness and spiralization tensors have a fundamental importance in the dynamical properties of large scale systems, for they parametrize various micromagnetic models.

From the in-plane average magnetic exchange and Dzyaloshinskii-Moriya interactions, we calculated the stiffness and spiralization-tensor elements for different layers as a function of the radius, see Figs. 8.4.1 and 8.4.2. These quantities were obtained by direct real-space summation of Eqs. 8.6 and 8.7. The averaged reconstructed systems have the symmetries of the C_s space group with a mirror plane perpendicular to the x–axis, and thus the only nonvanishing elements of the stiffness

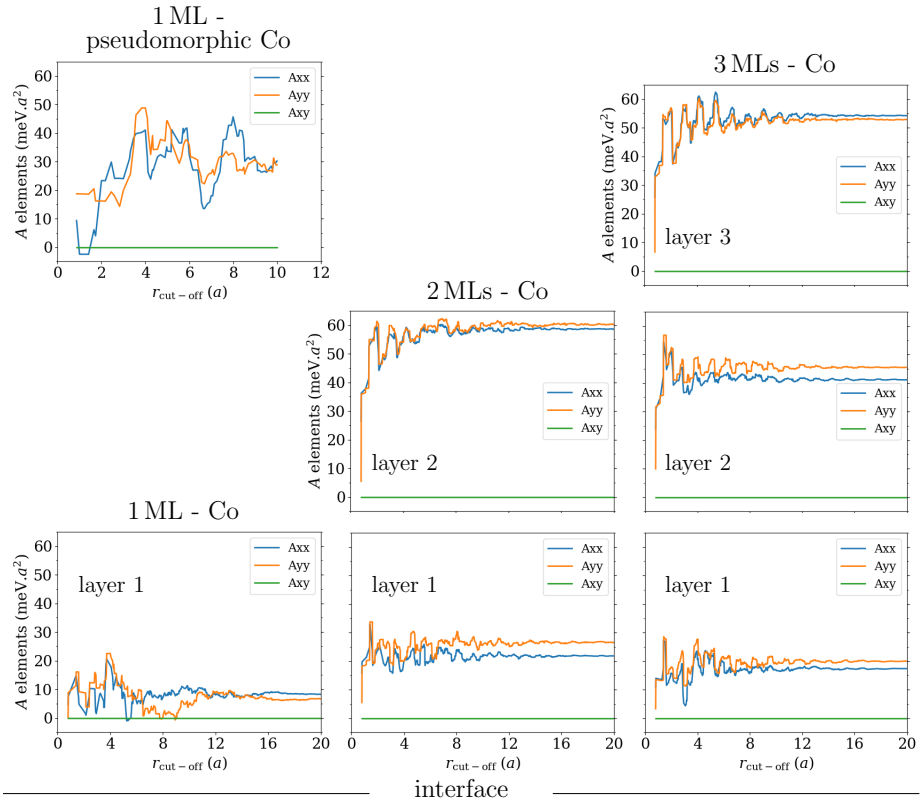

Figure 8.4.1: Stiffness-tensor elements per layer as a function of the cut-off radius calculated via Eq. (8.7). Only A^{xx} and A^{yy} are nonvanishing due to the symmetries of the system. For some systems and layers, we can observe an anisotropy of the stiffness along x and y, as is the clear case of the first layer of 2ML–Co, and layer 2 of 3ML–Co. Overall, a cut-off radius of at least $12a_W$ is required to issue convergence of these quantities.

tensor are $\mathcal{A}^{xx}$ and $\mathcal{A}^{yy}$, and $\mathcal{D}^{xy}$, $\mathcal{D}^{yx}$, and $\mathcal{D}^{zx}$ for the spiralization tensor. Meanwhile, the pseudomorphic-cobalt monolayer has the C_{2v} symmetries, which imposes that $\mathcal{D}^{zx}$ vanishes as well for this system.

In Fig. 8.4.1, we show the stiffness-tensor elements as a function of the cut-off radius, i.e., for every point of the curves, all pair interactions between atoms apart by a distance smaller or equal to the cut-off radius were considered. For a given layer, both intra and interlayer interactions are considered. We can observe that the stiffness-tensor elements are smallest for the reconstructed 1 ML film. This effect is due to the strong hybridization between the electronic states of cobalt and tungsten, which also leads to rather small magnetic moments and hence reduced spin stiffness [170]. In contrast, the stiffness is the largest for the surface layers. We also observe an anisotropy between the x and y–directions for the exchange stiffness. Finally, we can assert that a cut-off radius of at least $r = 12a_W$ is required for the convergence of these quantities. The exception is the pseudomorphic film, which did not converge within the range of interactions available.

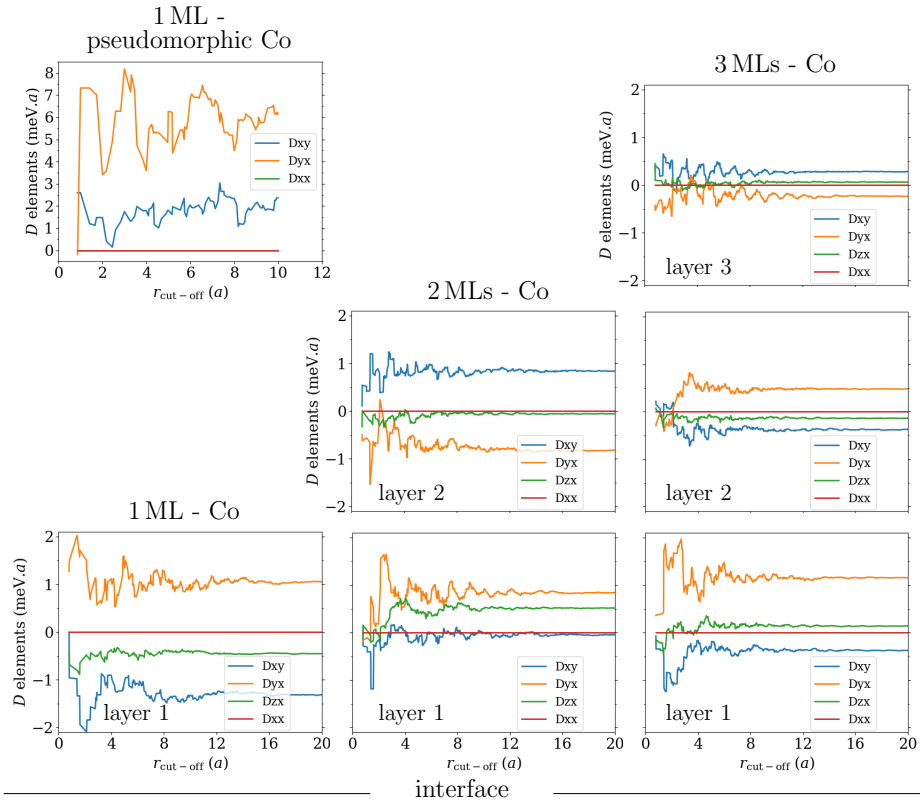

Figure 8.4.2: Spiralization-tensor elements per layer as a function of the cut-off radius calculated via Eq. (8.6). For the reconstructed films, only D^{xy}, D^{yx}, and $D^{x}z$ are non-vanishing due to the system's symmetries. For the pseudomorphic film, D^{xz} does also vanish. The spiralization-tensor is very anisotropic, where D^{xy} is in general different of D^{yx}. Even the sign of the spiralization-tensor elements can change from layer to layer and among different film thicknesses.

In Fig. 8.4.2, we show the spiralization-tensor elements as a function of the cut-off radius of the interaction cluster. Overall, these tensor elements are stronger for the monolayer systems, both pseudomorphic and reconstructed cobalt films, because the small coordination number of the Co atoms in these films reinforces the magnetic interaction between them. We can also observe a sign change of some elements from one layer to the next, for the thicker films, which is the case of D^{yx} in the reconstructed 2 MLs, and for different systems: note that in the reconstructed 1 and 2 MLs films that the sign of D^{zx} at the layer 1 changes.

The results shown in Figs. 8.4.1 and 8.4.2 are summarized in Tabs. 8.4.1 and 8.4.2, respectively, where we collect the values for the tensor elements at last the radius. In Figs. 8.4.1 and 8.4.2, the values for the pseudomorphic film are not converged. Therefore, we used a method that consists in damping the magnetic interactions with an exponentially decaying function, and then extrapolate the result as the damping goes to zero, which we explain in detail in Apx. 8.B. The obtained results

		1MLpseud	1ML	2ML	3ML
layer 3	$\mathcal{A}^{xx}$				54.29
	$\mathcal{A}^{yy}$				52.93
layer 2	$\mathcal{A}^{xx}$			58.67	41.17
	$\mathcal{A}^{yy}$			60.36	45.53
layer 1	$\mathcal{A}^{xx}$	30.22 (28.14)	8.25	21.87	17.36
	$\mathcal{A}^{yy}$	28.86 (29.00)	6.65	26.55	19.94
average	$\mathcal{A}^{xx}$	30.22 (28.14)	8.25	40.27	37.61
	$\mathcal{A}^{yy}$	28.86 (29.00)	6.65	43.45	39.47

Table 8.4.1: Stiffness-tensor elements per layer obtained from the averaged interaction set given in meV.a_W^2. These values were obtained by direct real-space summation of the interactions except for the values in parenthesis, which were obtained with the extrapolation method discussed in Apx. 8.B. We considered the interactions in a cluster of radius $20a_W$ and $10a_W$ for the reconstructed and pseudomorphic films, respectively. These values correspond to the last data point of each chart in Fig. 8.4.1. The values in parenthesis for the pseudomorphic film correspond to the last data point of Fig. 8.B.4 (a). The last row corresponds to the averaging between all the layers.

are shown in Fig. 8.B.4 and given in parenthesis in Tabs. 8.4.1 and 8.4.2. One notices the strong anisotropy between A^{xx} and A^{yy} and between D^{xy} and D^{yx}. As we saw, the nearest-neighbor interactions are ferromagnetic with magnitude increasing with the thickness of the Co films. Therefore, for a system with more than one layer, as a first approximation, we can suppose that the spin moments in different layers rigidly rotate together in the ground state and that these systems can be modeled by an effective monolayer with the interaction tensors averaged between layers. The tensor elements for such an average is shown in the last row of Tabs. 8.4.1 and 8.4.2.

8.4.2 Comparison with the experimental data

In Ref. [154], L. Camosi *et al.* reported on an experimental study of Au/Co/W(110). They used Brillouin light scattering spectroscopy to measure spin-wave energies and thus to determine the DMI anisotropy of this system at room temperature. They found the DMI to be 2-3 times larger along the bcc[$\bar{1}$10] than along the bcc[001]. Their film is composed of a 8 nm thick tungsten substrate, upon which a 6.5 nm-thick cobalt film is deposited that should correspond to about 3 MLs of Co. Finally, a 2 nm thick fcc Au(111) cap layer is grown on top of the stack to favor an out-of-plane anisotropy.

By using a vibrating sample magnetometer, they inferred the spontaneous volumetric magnetization $M_{\text{exp.}} = 1.15 \times 10^6$A/m. We calculated the magnetization for the reconstructed 3 MLs system as the averaged magnetic moment in the unit cell $\mathbf{M} = 1.52\,\mu_{\text{B}}$ (see Tab. 8.3.1) divided by its volume $V = dA_{\text{cell}}$, where $d = 0.644a_{\text{W}}$ is the interlayer distance in our simulations and $A_{\text{cell}} = 4a_{\text{W}} \times \sqrt{2}a_{\text{W}}/10$ is the area of the supercell per atom. Thus, we obtained that $M_{\text{theory}} = 1.22 \times 10^6$A/m, which is in good agreement with the experimental result.

As shown in Sec. 8.3.2, similarly to all the other systems, the reconstructed 3 MLs systems has a preferred axis in-plane along the y–direction. For Au/Co/W(110) of the experimental study of Ref. [154], however, the preferred axis is out-of-plane, due

		1MLpseud	1ML	2ML	3ML
layer 3	$\mathcal{D}^{xy}$				0.28
	$\mathcal{D}^{yx}$				-0.24
	$\mathcal{D}^{zx}$				0.06
layer 2	$\mathcal{D}^{xy}$			0.84	-0.37
	$\mathcal{D}^{yx}$			-0.82	0.48
	$\mathcal{D}^{zx}$			-0.06	-0.14
layer 1	$\mathcal{D}^{xy}$	2.38 (1.38)	-1.31	-0.05	-0.37
	$\mathcal{D}^{yx}$	6.13 (5.78)	1.05	0.84	1.15
	$\mathcal{D}^{zx}$		-0.45	0.52	0.14
average	$\mathcal{D}^{xy}$	2.38 (1.38)	-1.31	0.39	-0.15
	$\mathcal{D}^{yx}$	6.13 (5.78)	1.05	0.01	0.46
	$\mathcal{D}^{zx}$		-0.45	0.23	0.02

Table 8.4.2: Spiralization-tensor elements per layer obtained from the averaged interaction set given in meV.a_W. These values were obtained by direct real-space summation of the interactions except for the values in parenthesis, which were obtained with the extrapolation method discussed in Apx. 8.B. We considered the interactions in a cluster of radius $20a_W$ and $10a_W$ for the reconstructed and pseudomorphic films, respectively. These values correspond to the last data point of each chart in Fig. 8.4.2. The values in parenthesis for the pseudomorphic film correspond to the last data point of Fig. 8.B.4 (b). The last row corresponds to the averaging between all the layers.

to the Au cap layer.

Finally, Ref. [154] reports on the interfacial spiralization tensor, where they found $D^x = 0.12(2)\,\mathrm{pJ/m}$ and $D^y = 0.29(3)\,\mathrm{pJ/m}$, which correspond to the bcc[001] and bcc[$\bar{1}$10] directions, respectively. Our *ab initio* calculations result in $D^x = 0.39\,\mathrm{pJ/m}$ and $D^y = 1.23\,\mathrm{pJ/m}$ for the reconstructed 3 MLs system. Here, $D^x = 3D^{xy}/A_{\mathrm{cell}}$ and $D^y = 3D^{yx}/A_{\mathrm{cell}}$, where 3 is the number of layers. For $D^{\alpha\beta}$, we used the averaged values of Tab. 8.4.2, which is given per layer. The theoretical results overestimate the values of the DMI-tensor elements, nevertheless, the theoretical spiralization-tensor element along the bcc[$\bar{1}$10] is 3 times larger than along the bcc[001], in agreement with the experimentally-observed anisotropy [154]. One of the causes for the quantitative mismatch may be related to the Au capping layer in the experiment and related to the temperature: While the *ab initio* calculations correspond to 0 K, the experiment was performed at room temperature.

8.4.3 Ground-state spin configurations from the micromagnetic model

Within the Taylor expansion of the energy, discussed in Apx. 8.A.3, it is straightforward to calculate the energy minimum as a function of the wavevector by searching for the zeros of its first derivative. For each direction of the spin-spiral axis $\alpha = x, y, z$, the wavevector that minimizes the energy is given by:

$$q^{\alpha\mu} = -\sum_{\nu} D^{\alpha\nu}\overline{\mathcal{A}}^{\nu\mu} \quad , \tag{8.8}$$

where $\overline{\mathcal{A}}$ is the inverse of the stiffness tensor. The corresponding energy is given by

$$\varepsilon^{\alpha}_{\text{total}}(\mathbf{q}^{\alpha}) = \varepsilon^{\alpha}_{\text{Exc}} + \varepsilon^{\alpha}_{K} \quad , \tag{8.9}$$

where the exchange contribution due to MEI and DMI is given by

$$\varepsilon^{\alpha}_{\text{Exc}} = -\frac{1}{2}\sum_{\mu\nu} D^{\alpha\nu}\overline{\mathcal{A}}^{\nu\mu}\mathcal{D}^{\alpha\mu} \quad , \tag{8.10}$$

and the anisotropy contribution, for nonvanishing wavevectors, is given by

$$\varepsilon^{\alpha}_{K} = -\frac{1}{2}\sum_{\beta} K^{\beta} \quad , \tag{8.11}$$

with β running over all anisotropy axes that are perpendicular to the spiral axis α. A detailed derivation of these results is given in Apx. 8.A.5.

Considering that the symmetries of the cobalt films (C_s and C_{2v}) impose that many elements of the stiffness and spiralization tensor vanish, such as A^{xy}, A^{yx}, D^{xx}, D^{yy} and D^{xx}, the cycloidal spin spirals that minimize the energy are given next. For $\alpha = x$ (spiral axis along x):

$$\mathbf{q}^{x} = \left(0 \quad , -\tfrac{\mathcal{D}^{xy}}{\mathcal{A}^{yy}}\right) \quad , \quad \varepsilon^{x}_{\text{Exc}} = -\frac{1}{2}\frac{(D^{xy})^2}{\mathcal{A}^{yy}} \quad , \quad \varepsilon_{K} = -\frac{K^{y}}{2} \quad ; \tag{8.12}$$

For $\alpha = y$ (spiral axis along-y):

$$\mathbf{q}^{y} = \left(-\tfrac{\mathcal{D}^{yx}}{\mathcal{A}^{xx}}, \quad 0\right) \quad , \quad \varepsilon^{y}_{\text{Exc}} = -\frac{1}{2}\frac{(D^{yx})^2}{\mathcal{A}^{xx}} \quad , \quad \varepsilon_{K} = -\frac{K^{x}}{2} \quad ; \tag{8.13}$$

For $\alpha = z$ (spiral axis along-z):

$$\mathbf{q}^{z} = \left(-\tfrac{\mathcal{D}^{zx}}{\mathcal{A}^{xx}}, \quad 0\right) \quad , \quad \varepsilon^{z}_{\text{Exc}} = -\frac{1}{2}\frac{(D^{zx})^2}{\mathcal{A}^{xx}} \quad , \quad \varepsilon^{z}_{K} = -\frac{1}{2}\left[K^{x} + K^{y}\right] \quad . \tag{8.14}$$

We note, however, that the anisotropy energy is discontinuous at $\mathbf{q} = 0$, which corresponds to a ferromagnetic state, and it is given by $\varepsilon_{\text{FM}} = \varepsilon_{K}(\mathbf{q} = 0) = -\max(K^{\alpha})$. When ε_{FM} is smaller than $\varepsilon^{\alpha}_{\text{total}}$, the ferromagnetic state is preferred. Taking the layer-averaged stiffness and spiralization tensors of Tabs. 8.4.1 and 8.4.2 into the above equations, we obtain that for reconstructed 1ML cobalt film, the spin-spiral energies are $\varepsilon_{\text{total}} \sim -0.19\,\text{meV}$ per atom for the spin-spiral axes along the three directions x, y and z, see Tab. 8.4.3. They have an energy difference from the ferromagnetic phase of only $\sim -0.04\,\text{meV}$, and their wavevectors vary in direction and magnitude, $\mathbf{q}^{x} = (0, 0.20, 0)$, $\mathbf{q}^{y} = (-0.13, 0, 0)$ and $\mathbf{q}^{z} = (0.05, 0, 0)$, which correspond to wavelengths of 32, 49, 114 a_W, respectively. For the 2 and 3 ML reconstructed cobalt films, the absolute values of the spiral energies are always smaller than $\varepsilon = 0.01\,\text{meV}$ per atom, which means that they have ferromagnetic ground states and that the occurrence of spin spirals and noncollinear spin textures is improbable.

For all the reconstructed films, the ferromagnetic state has the smallest energy, and therefore it is the micromagnetic ground state. For the pseudomorphic 1ML film, we used the values in parenthesis in Tabs. 8.4.1 and 8.4.2, which were obtained with the extrapolation method discussed in Apx. 8.B. We found that a spiral with axis along y propagating along x with a wavelength of $31a_W$ has lower energy than the ferromagnetic state, see Tab. 8.4.3.

	α-axis	$\mathbf{q}^\alpha$	λ (a_W)	$\varepsilon^\alpha_{\text{Exc}}$	ε^α_K	$\varepsilon^\alpha_{\text{total}}$	ε_{FM}	FM-axis
1ML pseud	x	(0 , -q)	131.90	-0.03	-0.12	-0.15	-0.23	x
	y	(-q , 0)	30.59	-0.59	-0.07	-0.66		
1ML	x	(0 , q)	31.81	-0.13	-0.07	-0.19	-0.23	y
	y	(-q , 0)	49.24	-0.07	-0.12	-0.18		
	z	(q , 0)	114.53	-0.01	-0.18	-0.19		

Table 8.4.3: Cycloidal spin spiral energies. Spin spirals with rotation axes along three orthogonal directions $\alpha = x, y, z$ were considered. The wavevector that minimizes the energy of each spiral is $\mathbf{q}$, and the correspondent wavelength is λ. The MEI and DMI contributions to the total energy are given by ε_{Exc}, while the anisotropy contribution is given by ε_K, adding up to the total energy $\varepsilon_{\text{total}}$. The energy of the ferromagnetic state with magnetization along the strongest easy-axis (FM-axis) is given by ε_{FM}.

8.5 Atomistic-spin-dynamics simulations

While the micromagnetic model can give us a basic and analytical understanding of the magnetic properties of a material, it has also some limitations related to the underlying approximations. To study rapidly-varying spin structures, such as skyrmions with diameters of a few nanometers, an atomistic description is more appropriate. Therefore, we performed atomistic-spin-dynamics simulations, which trace the time evolution of the spins by solving the LLG equation, as implemented in the Spirit-Code [47], to study and determine the stable spin configurations of the investigated films. In agreement with our analytics based on the micromagnetic model, through our simulations for the 2-3MLs systems, we only found ferromagnetic spin configurations to be the ground state, and no noncollinear spin configuration was found stable in these systems. Therefore, in the following, we will discuss the results for the 1 monolayer systems, both, the reconstructed and the pseudomorphic. For the reconstructed case, we will consider two models: one with the set of in-plane-averaged interactions, which effectively reduces the model to a single atom in the unit cell; and another with the supercell set of interactions, which contain 10 inequivalent cobalt atoms in the cell.

8.5.1 Reconstructed 1ML: in-plane-averaged interactions

For the in-plane averaged interactions, we saw that the micromagnetic analysis predicts a ferromagnetic ground-state for all 1-3ML reconstructed systems. However, it was also seen that for the 1ML reconstructed film, two cycloidal spirals, one with axis along $\hat{\mathbf{x}}$ and other along $\hat{\mathbf{y}}$, have energies rather close to the ferromagnetic state with a difference of $\sim 0.04\,\text{meV}$ per atom, and of wavelength of $\sim 32a_{\text{W}}$ and $49a_{\text{W}}$, respectively. We want next to verify these results using atomistic-spin-dynamics simulations.

In the averaged case, we have a simple unit cell with a single atom of a hexagonal lattice. A spin spiral, however, can be best represented in a rectangular unit cell. Therefore, for the following simulations, we used a Bravais lattice given by $\mathbf{a}_1 = a_{\text{Co}}\hat{\mathbf{x}}$ and $\mathbf{a}_2 = \sqrt{3}a_{\text{Co}}\hat{\mathbf{y}}$, where the lattice constant of cobalt is $a_{\text{Co}} = \frac{4}{5}a_{\text{W}}$. The simulation boxes consist of the area expanded by $m\mathbf{a}_1$ and $n\mathbf{a}_2$, which we will represent by $m\times n$.

We first considered an 85×50 simulation box, which is a rectangle of dimension

$21.49 \times 17.88\,\mathrm{nm}^2$, with periodic boundary conditions. The ferromagnetic state with magnetization along x was found to be the ground state. Nevertheless, many metastable states were observed as well. Starting from a random spin configuration, we often obtain states that consist of a spin spiral plus skyrmions mixture (SP+SKs), see an example in Fig. 8.5.1 (a). The colors represent the z component for the spins: blue for spins points along $-z$, red along $+z$, and green for the spins lying in-plane. The SP+SKs state presents skyrmions of different polarities. We can observe skyrmions of predominantly blue cores, therefore with spins pointing along $-z$, when they are closer to the spin-spiral stripes that point along $+z$, and the entire thing reverses for skyrmions with cores predominantly red. A 2×2 expansion of Fig. 8.5.1 (a) is shown in Fig. 8.5.1 (g).

Inspired by Fig. 8.5.1 (a), we initialized a simulation with a spiral of a wavelength of about the simulation box size. After the relaxation, we obtained Fig. 8.5.1 (b), which represents a very stretched spin spiral (SP) [1], indicating that the wavelength is smaller than the dimension of the box. The obtained spiral is not exactly cycloidal or conical like, since the spins in the blue and red regions have components along $-y$ and $+y$, respectively. This is equivalent to superimpose two cycloidal spirals, one with rotational axis along y, and another with axis along z. By starting from the ground state with a circular domain of reversed magnetization, we obtained a skyrmion (SK) shown in Fig. 8.5.1 (c). This skyrmion can also be mapped onto a sphere, covering it completely, and therefore, it has a topological charge of $+1$. We calculated the topological charge using the scheme described in the Apx. 8.C. The occurrence of such a skyrmion is rather peculiar since it lives in an in-plane ferromagnetic background, and for this reason, we will call it an in-plane skyrmion. While most skyrmion research in thin films focuses on systems with out-of-plane magnetic anisotropy, we show that this is not any longer a requirement. We will further study the properties of the in-plane skyrmions in the Sec. 8.6.

Next, we implanted the skyrmion of Fig. 8.5.1 (c) in the left green area of Fig. 8.5.1 (b), which is similar to the skyrmion's original background. After the relaxation, we obtain Fig. 8.5.1 (d), where the skyrmion has slid left to touch with the red stripe of the spin spiral (SP+SK). Interestingly, the skyrmion has no longer a complete in-plane surrounding, yet it preserves its topological charge. We also injected an out-of-plane skyrmion with a red core into the blue spin-spiral stripe. The skyrmion slid left as well and changed its shape resulting in a skyrmion very similar to the previous but with opposite polarity, see Fig. 8.5.1 (e) (SP+SK'). Similarly, we injected two out-of-plane skyrmions in the blue spiral region. This time, the skyrmions not only slid to the left but also got closer together, see (SK+2SK) in Fig. 8.5.1 (f).

In-plane skyrmion stability

Among all different metastable states that we discussed so far, the spin spiral in Fig. 8.5.1 (b) is closest in energy to the ground state with an energy difference of $\Delta_{\mathrm{SP}} = 25.42\,\mathrm{meV}$. For the in-plane skyrmion isolated in the ferromagnetic ground state, we have $\Delta_{\mathrm{SK}} = 127.13\,\mathrm{meV}$. The phase where then combines a single skyrmion

[1] In fact, the spin spiral in Fig. 8.5.1 (b) is so stretched that it could also be seen as domain walls.

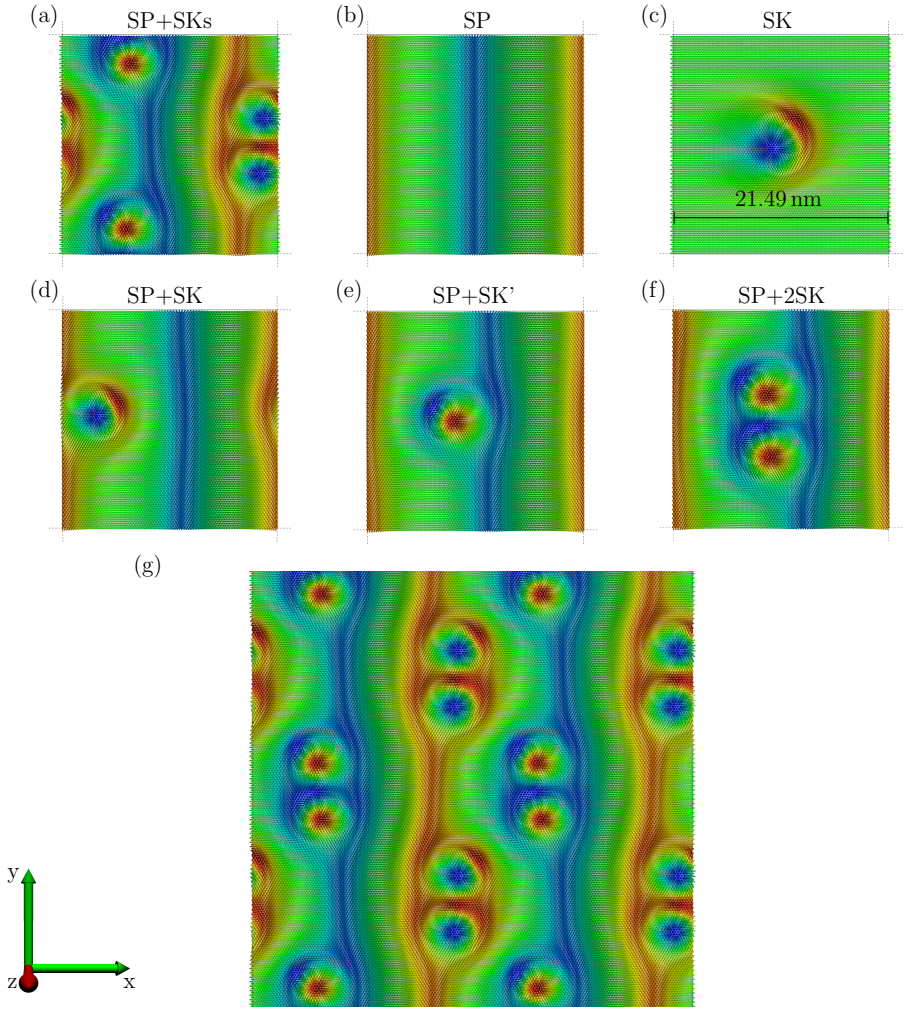

Figure 8.5.1: Spin spiral with axis along y with embedded skyrmions for averaged interactions. Simulation box 85×50 (8500 spins) with periodic boundary conditions. Red and blue represent the spins along $+z$ and $-z$, respectively, and green the in-plane spins. Each metastable configuration can be obtained from different initial spin configuration: (a) Spiral embedding multiple skyrmions (SP+SKs), from a random spin configuration. The skyrmions have different polarities, which match the surrounding regions of the spiral. (b) Spin spiral (SP), from a spiral initial configuration. (c) Single skyrmion (SK), from a circular reversed domain in a ferromagnetic background. (d) Single skyrmion into a spiral (SP+SK), from skyrmion of (c) injected in the middle green region of (b). (e) Single skyrmion into a spiral (SP+SK'), from an out-of-plane skyrmion injected in the middle of the blue region of (b). (f) Double skyrmion into a spiral (SP+2SK), from two out-of-plane skyrmions injected, in the middle of the blue region of (b). (d) SP+SK: Spin spiral embedding skyrmions of different polarities. (g) Shows the SP+SKs state (a) in a 2×2 expansion of the simulation box. With respect to the FM state, the total energy (per supercell) of the spin configurations from (a) to (f) are $\Delta E_{\text{SP+SKs}} = 604.25$, $\Delta E_{\text{SP}} = 25.42$, $\Delta E_{\text{SK}} = 127.13$, $\Delta E_{\text{SP+SK}} = 172.53$, $\Delta E_{\text{SP+SK'}} = 172.53$, $\Delta E_{\text{SP+2SK}} = 305.93\,\text{meV}$.

(a)

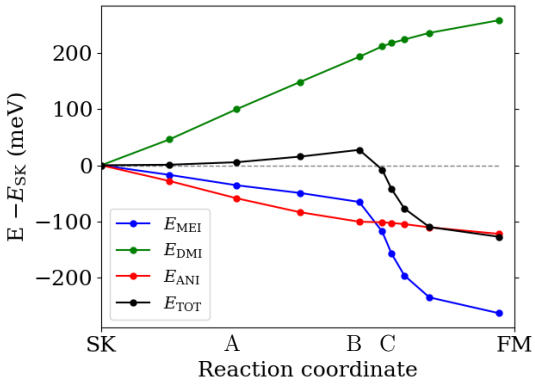

(b)

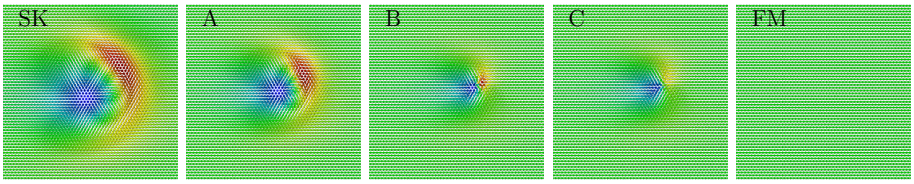

Figure 8.5.2: Minimum energy path calculations using the GNEB method for the transition from an in-plane-skyrmion state, Fig. 8.5.1 (b), to the ferromagnetic ground state along x. Simulation box 85×50 (8500 spins) with periodic boundary conditions. The horizontal axis stands for the reaction coordinate that labels intermediate spin configuration between the skyrmion and the ferromagnetic phases, some of which are represented in (b). The vertical axis in (a) accounts for the energy difference of a given spin configuration and the skyrmion phase. The blue curve shows the magnetic exchange interaction contribution to the total energy, shown in black. The green and red correspond to the Dzyaloshinskii-Moriya interaction and anisotropy contributions, respectively. The total energy difference between the skyrmion state and the ferromagnetic state is of 127.13 meV. The DMI contribution, the only positive one, is responsible for the energy barrier of 27.41 meV, and therefore, it is the mechanism that stabilizes the in-plane skyrmion.

and a spin spiral, however, has higher energy than the sum of these two structures in separation, $\Delta_{\mathrm{SP+SK}} = 172.53\,\mathrm{meV}$.

We can assert about the stability of the in-plane skyrmion of Fig. 8.5.1 (c) by calculating the energy required to transit from the SK phase to the ferromagnetic ground state. We obtained this energy barrier using the geodesic nudged elastic band (GNEB) method [47, 171], where we compute the energies of different stages of a continuous transformation between two stable states. The result is shown in Fig. 8.5.2 (a), where we plot the difference between the energy of each stage, some of which are shown in Fig. 8.5.2 (b), and the skyrmion phase. The total energy is shown in black displaying an energy barrier of 27.41 meV. We can also evaluate the different contributions to the energy: in green, we have the curve for the Dzyaloshinskii-Moriya interaction; in blue for the magnetic exchange interaction;

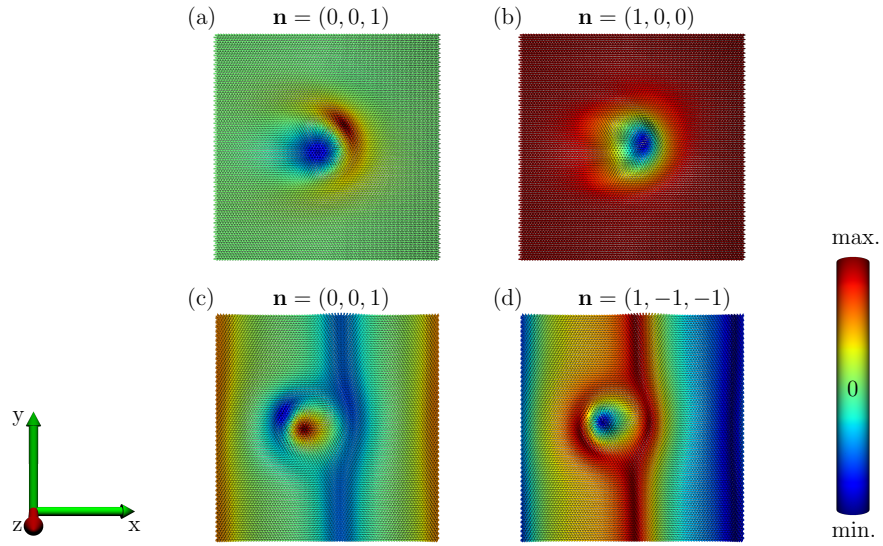

Figure 8.5.3: Skyrmions with different magnetization background. The same in-plane skyrmion is shown in (a) and (b), where the colors represent the spin projection along $\mathbf{n} = (0, 0, 1)$ and $\mathbf{n} = (1, 0, 0)$, respectively. In (b) we can see the skyrmion as a single entity rather than the combination of two. Similarly, (c) and (d) brings two representation of the SP+SK phase, with coloring the spin projection along $\mathbf{n} = (0, 0, 1)$ and $\mathbf{n} = (1, -1, -1)$, respectively.

and in red for the magnetocrystalline anisotropy contribution. Among these three curves, only the DMI contribution is positive, and therefore, it alone is responsible for the raising of the total energy that forms the energy barrier for the transition between the skyrmion phase into the ferromagnetic phase. In contrast to most studies in the literature, where in-plane skyrmions result from the MEI frustration, here, their stability is ensured by the DMI.

Skyrmion outskirts

As the reconstructed 1ML of Co/W(110) has an in-plane anisotropy axis, the out-of-plane skyrmions, in the absence of an external magnetic field, are not stable. We also saw that in-plane skyrmions can also be stable living in an in-plane magnetization. It is most interesting, however, that in the presence of a spin spiral, the skyrmions generates an outermost shell, its outskirt, that is not completely in-plane nor out-of-plane.

In fact, if we change the color-coding of Fig. 8.5.1 (c) by coloring the projection of the spin along x instead of z, see Fig. 8.5.3 (a) and (b), we obtain a more typical skyrmion picture: a circular core (even though distorted) made up of spins mostly point antiparallel to the background magnetization, here depicted in blue, surrounded by shells, each of different color, made of spins that rotate and ultimately align with the background, shown in red. For the SP+SK state, Fig. 8.5.1 (e), a similar picture can be obtained by coloring the spin projections roughly along

$\mathbf{n} = (1, -1, -1)$, see Fig. 8.5.3 (c) and (d). Therefore, these skyrmions attached to the spin spiral has a very peculiar direction for their core and outskirt, which are not in-plane nor out-of-plane. Our interpretation is further corroborated by the fact that the SP+SK state has a net magnetization that points along $(0.97, -0.17, -0.19)$, and therefore, in the same octant as $\mathbf{n}$. The net magnetization has a much higher x–component because this skyrmion enlarges the in-plane region of the spin spiral that points along $+x$. Meanwhile, the pure spin spiral state, Fig. 8.5.1 (b), has zero net magnetization. Thus, we can say that $\mathbf{n}$ defines the skyrmion polarization axis, once in such a spin spiral environment, the magnetization cannot do the job. The polarization axis of the skyrmion in the SP+SK' state, Fig. 8.5.1 (d), is roughly $\mathbf{n} = (1, 1, 1)$, having the x and y–components reversed with respect to the polarization axis of the skyrmion in the SP+SK state. As we will see in the Sec. 8.6, this is a consequence of these two entities being related to each other via the mirror symmetry of the system, which is perpendicular to x–axis.

Spin spirals

The spin spiral of Fig. 8.5.1 (b), as mentioned before, is highly distorted with respect to a uniform rotating spiral. Periodic boundary conditions can impose severe constraints on the spin spiral formation: only wavelength commensurable with the simulation box dimensions can fit in. To avoid this problem, and thus, better determine the natural wavelength of the spin spiral, we considered a new 170×12 simulation box with open boundary condition along x, which has a rectangular shape appropriate to study spirals with an axis along y and propagation direction along x.

Initially, we considered a cycloidal spin spiral of very short wavelength as the initial spin configuration. That spiral relaxes into another of a larger wavelength, see Fig. 8.5.4 (a). The wavelength is of about $\lambda = 62a_{\mathrm{Co}} = 15.67\,\mathrm{nm}$, which matches the wavelength for the most energetically favorable energy for a spiral with the axis along y predicted by the micromagnetic model, $49.24a_{\mathrm{W}} = 61.55a_{\mathrm{Co}}$, see Tab. 8.4.3. A closer look at this picture reveals that, differently from the initial state, in the relaxed structure, some spins acquire a y–component. In fact, the final state can be seen as composed by two spirals of different axes, one with axis along y and a second with axis along z, or yet, a single spiral with rotation axis somewhere in the $y - z$–plane. By calculating the cross product between two adjacent spins displaced along x of the spin spiral, we determined its effective rotation axis to be roughly parallel to $(0, \sqrt{5}/3, -2/3)$, which corresponds to a $42°$ deviation from the y-axis.

Starting the simulations from a random spin configuration, we also obtained a spin spiral of similar wavelength as before, however, many times, the spiral embeds skyrmionic structures, as in Fig. 8.5.4 (b). The size of this skyrmion is that of the transversal dimension of the box, meaning that the skyrmion is in close contact with its periodic image along y. We also considered to start from a ferromagnetic configuration, which is fully spin-polarized with magnetization along x, shown in Fig. 8.5.4 (c). The relaxation of this configuration preserves the ferromagnetic alignment in the bulk of the simulation box, however, the spins slightly twist at both right and left edges, where no periodic boundary conditions are applied, see Fig. 8.5.4 (d). In this manner, the system gains energy from the Dzyaloshinskii-Moriya interactions, which results in a total energy smaller than that of the fully

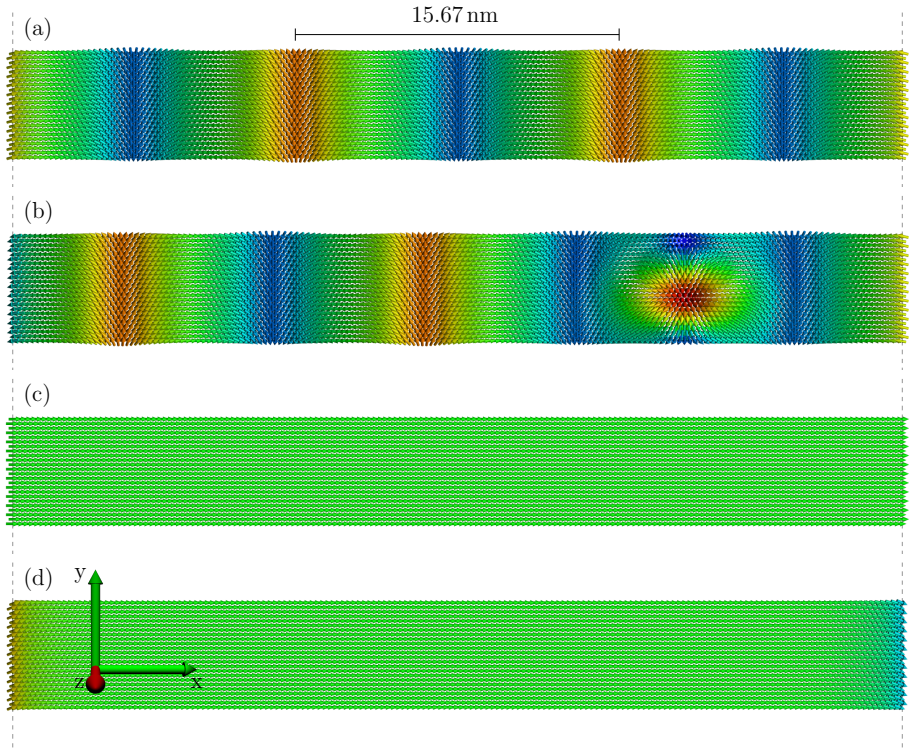

Figure 8.5.4: Spin spiral with axis along y. Simulation box 170×12 (4080 spins) with periodic boundary condition only along y. The different states are obtained from different initial spin configurations. (a) SP: Spin spiral of longer wavelength after initializing the spin configuration with a spiral of much shorter wavelength. (b) SP+SK: Spin spiral embedding a skyrmion: from a random initial spin configuration. The resulting wavelength is incommensurate with the lateral size of the simulation box. (c) FM: Fully spin-polarized state, not relaxed. (d) FM-relax: Fully polarized state after the relaxation, which has the lowest total energy. With respect to the FM-relax state, the total energy of the various spin configurations are: $\Delta E_{\mathrm{SP}} = 31.14$, $\Delta E_{\mathrm{SP+SK}} = 144.05$, $\Delta E_{\mathrm{FM}} = 23.17\,\mathrm{meV}$.

spin-polarized state.

To compare the energy of the spin spiral shown in Fig. 8.5.4 (a) with the micromagnetic analytics, we considered a simulation box commensurate with the spiral wavelength, 62×12, this time with complete in-plane periodic boundary conditions. The energy of a perfect cycloidal spiral with axis along y and wavelength $\lambda = 62 a_{\mathrm{Co}}$ was calculated to be 0.05 meV per atom above the ferromagnetic ground state, which is in close agreement with the results obtained from the micromagnetic model, 0.04 meV per atom, which also considers a perfect spin spiral. The relaxed spin spiral, which is equivalent to that of Fig. 8.5.4 (a), has an energy of only 0.01 meV per atom above the ground state.

In Sec. 8.4.3, using the micromagnetic model, we predicted that cycloidal spin spirals with axes along y, as studied above, but also along x and z can have energies close to the ferromagnetic ground state, see Tab. 8.4.3. Thus, to investigate spirals

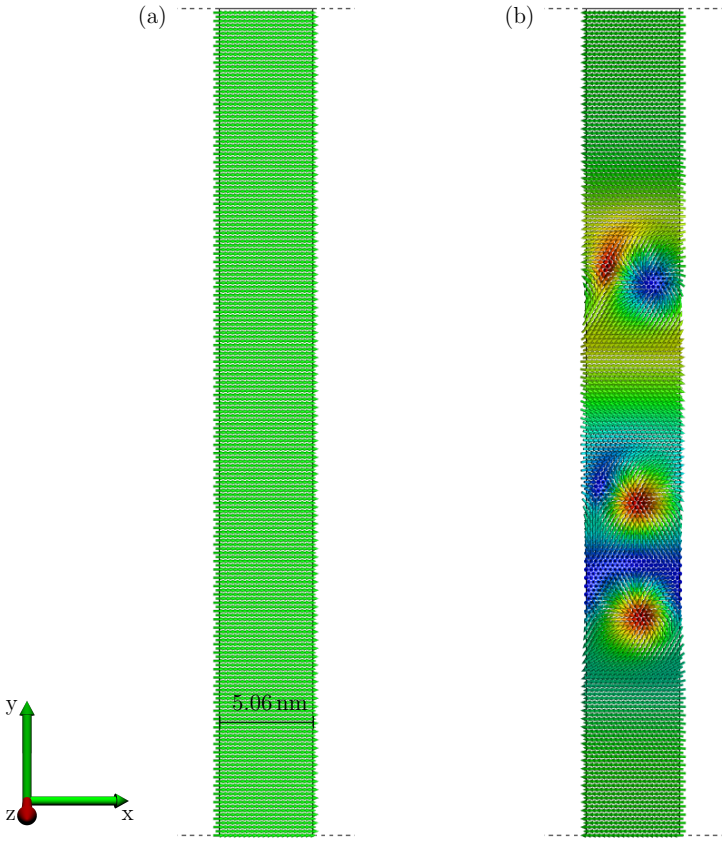

Figure 8.5.5: Spin spiral with axis along y. Simulation box 20×100 (4000 spins) with periodic boundary condition only along x. The different states are obtained from different initial spin configurations. (a) FM: Fully spin-polarized state obtained from a spin spiral with axis along x of very short wavelength. (b) SKs: Skyrmions embedded on a ferromagnetic surrounding, whose energy with respect to the FM state is $\Delta E_{\mathrm{SKs}} = 434.10\,\mathrm{meV}$. This state was obtained from a random initial spin configuration.

with rotational axes along x and propagation direction y, we considered a 20×100 simulation box with open boundary conditions along the y–axis. Again, we started by considering a spin spiral of very short wavelength as the initial spin configuration, which resulted in a ferromagnetic state after the convergence, as shown in Fig. 8.5.5 (a). We obtained no stable spin spiral with an axis along x. Next, we considered a random spin configuration as the initial state, and again skyrmions could be stabilized, this time, however, in a ferromagnetic background, see Fig. 8.5.5 (b). Finally, we also did not manage to stabilize any spin spiral with axis along z propagating along the x–axis.

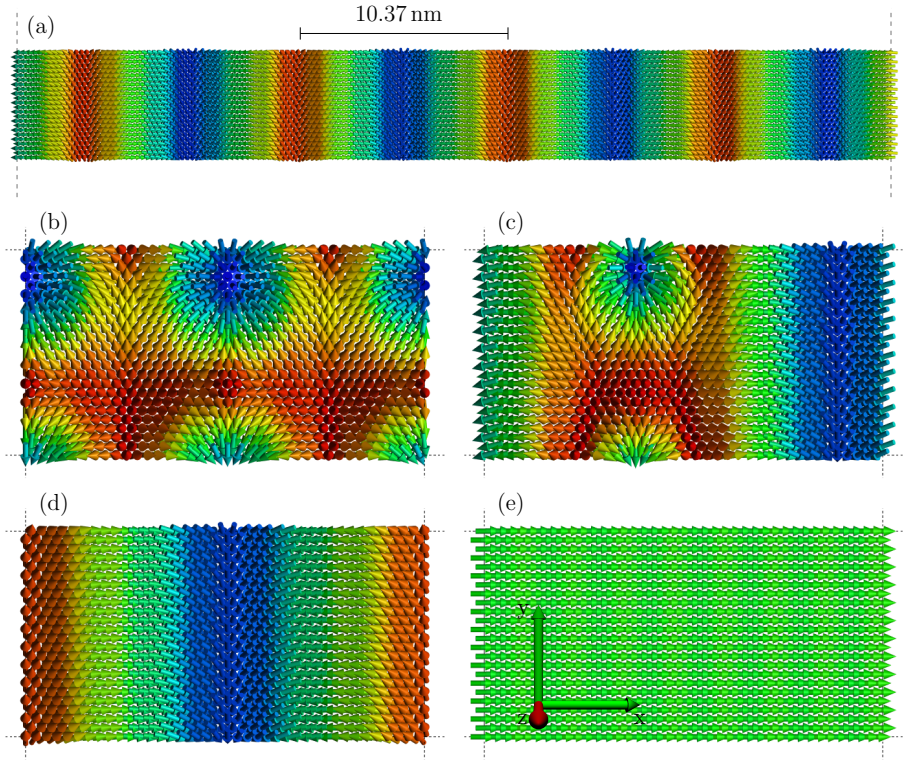

Figure 8.5.6: Metastable states for the supercell interaction set. (a) Spin spiral with axis along y propagating along x obtained from a similar spin-spiral initial configuration of much short wavelength. 34×12 (4080 spins) simulation box with open periodic boundary condition along x. (b) SK-lat: Skyrmion lattice and (c) SP+SK: skyrmion embedded into a spin spiral. 8×12 (960 spins) simulation box with complete periodic boundary conditions, whose dimension along x is equivalent to the wavelength of the spin spiral in (a). (d) SP: Spin spiral equivalent to that of (a). (e) FM: Ferromagnetic state with magnetization along x. With respect to the FM state, the total energy of the various spin configurations are: $\Delta E_{\text{SK-lat}} = 160.25$, $\Delta E_{\text{SP+SK}} = 108.73$, $\Delta E_{\text{SP}} = -33.09\,\text{meV}$.

8.5.2 Reconstructed 1ML: supercell interactions

The Bravais lattice for the supercell reconstructed-cobalt films is given by $\mathbf{a}_1 = 4a_{\text{W}}\hat{\mathbf{x}} = 5a_{\text{Co}}\hat{\mathbf{x}}$ and $\mathbf{a}_2 = \sqrt{2}a_{\text{W}}\hat{\mathbf{y}} \simeq \sqrt{3}a_{\text{Co}}\hat{\mathbf{y}}$, where $a_{\text{Co}} = \frac{4}{5}a_{\text{W}}$. First, we considered a 34×12 simulation box with open periodic boundary condition along x, which is suitable to study spin spirals propagating along x. We started one spin dynamics simulation from a cycloidal spin spiral of very short wavelength with axis along y. After convergence, we obtain a spin spiral of wavelength $41a_{\text{Co}} = 10.37\,\text{nm}$, much longer than the initial wavelength, see Fig. 8.5.6 (a). Yet, this predicted wavelength is shorter than that obtained from the averaged set of interactions, $62a_{\text{Co}}$.

Having determined the optimal wavelength, we considered an 8×12 box, which is commensurate along x with that wavelength, see Fig. 8.5.6 (b-e). The states in Fig. 8.5.6 (b) and (c) correspond to a skyrmion lattice and a spin spiral embedding

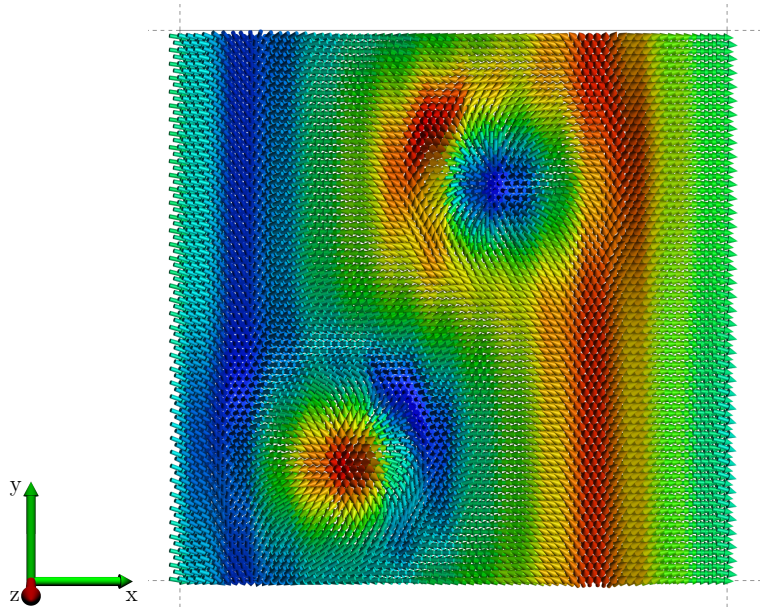

Figure 8.5.7: Skyrmions embedded into spin spiral at zero external magnetic field. 14×40 (5600 spins) simulation box with complete periodic boundary conditions in-plane. State obtained from a random initial spin configuration, which is similar to states obtained for the averaged set of interactions.

a skyrmion, respectively, and they were obtained from random initial spin configurations. Meanwhile, the states in Fig. 8.5.6 (d) and (e) were induced, and the geometry of this simulation box allows us to compare their energies. We find that the energy of the pure spin-spiral state is now lower than that of the ferromagnetic state by 33.09 meV. Thus, within the phase space that we covered, the spin spiral in Fig. 8.5.6 (d) corresponds to the ground state. Its averaged rotation axis is deflected off the y axis by 28° in the direction of z, pointing roughly along $(0, \sqrt{3}/2, -1/2)$.

We also considered a 4×100 simulation box with open periodic boundary condition along y. Similarly to the results for the averaged set of interactions, no spin spiral was found stable. We mostly obtained the ferromagnetic state with magnetization long x, with the occasional occurrence of domain walls or skyrmions stabilized by the geometry confinement effects. For larger simulation boxes, the spin-dynamics simulations mostly lead to states that consist of spin spirals embedding skyrmions, such as the one shown in Fig. 8.5.7, which resemble those states obtained for the averaged set of interactions, see Fig. 8.5.1.

As the ground state is a spin spiral, skyrmions living in a ferromagnetic background is not a stable configuration. Thus, we applied an external magnetic field along the strongest anisotropy easy-axis, that is, parallel to x. At around 1 T, the spin spiral stops being the ground state, and the ferromagnetic state becomes the most energetically favorable. We obtained stable skyrmions in that ferromagnetic background for fields between 1 and 3 T. Figure 8.5.8 (a) and (b) correspond to 1 and 2 T, respectively, in a 12×35 simulation box. The skyrmion size reduces with

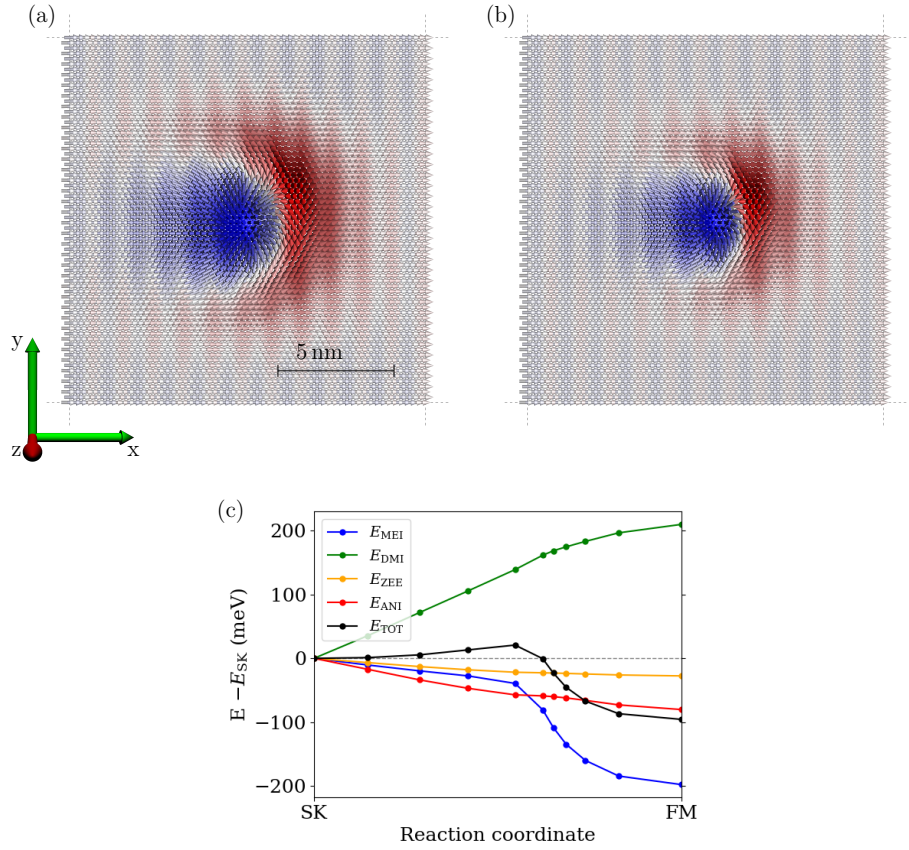

Figure 8.5.8: In-plane skyrmions stabilized by an in-plane external magnetic field. Simulation box 12×35 (4200 spins) with periodic boundary conditions in-plane. Magnetic field of (a) 1 T and (b) 2 T along x was considered. The skyrmion size is reduced for higher fields, and they are stable up to 3 T. (c) Minimum energy path calculations using the GNEB method for the transition between an in-plane-skyrmion state in (a) and the ferromagnetic state along x. The horizontal axis stands for the reaction coordinate that labels intermediate spin configuration between the skyrmion and the ferromagnetic phases. The vertical axis accounts for the energy difference of a given spin configuration and the skyrmion phase. The blue, green, orange and red correspond respectively to the MEI, DMI, Zeeman and anisotropy contributions for the total energy, which is shown in black. The total energy difference between the skyrmion state and the ferromagnetic state is of 95.65 meV, and the energy barrier for a continuous transformation between these states if of 20.78 meV that comes from the DMI.

an increasing magnetic field. In these figures, we have switched the green color used for in-plane spins to the white color because the neutrality of this color allows for a better contrast with red and blue. Thus, we can better visualize the local variation of the spin configuration throughout the supercell, which occurs in the ferromagnetic background. We changed the color map painting the spins with respect to

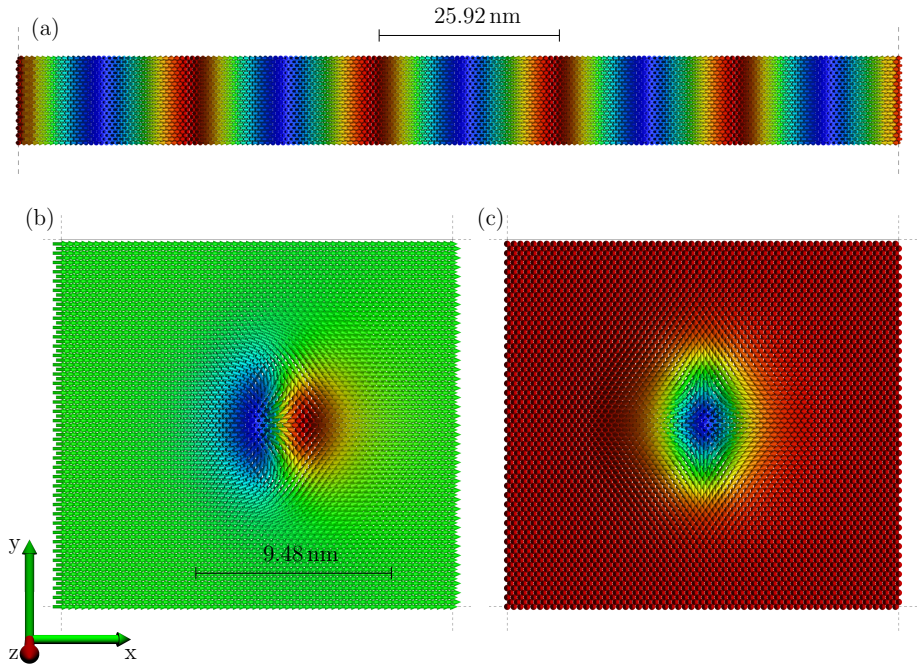

Figure 8.5.9: Noncollinear spin textures of the pseudomorphic 1ML Co/W(110). (a) Spin spiral with axis along y with propagating along x. It corresponds to the ground state. Simulation box 170×12 (4080 spins) with open periodic boundary conditions along x. With an external magnetic field of (a) 9 T along x and (b) 12 T along z, we could stabilize an in-plane and an out-of-plane skyrmionic structures. In particular, the texture in (c) can be trivially identified as an antiskyrmion. Simulation box 60×40 (4800 spins) with complete periodic boundary conditions in-plane. In comparison with the ferromagnetic states, with the magnetization along the external field, the energies of the in-plane skyrmion and the out-of-plane antiskyrmion are 355.43 and 255.3 meV, respectively.

their out-of-plane components with red and blue passing by white for the in-plane components.

The skyrmions states in Fig. 8.5.8 (a) and (b), for 1 and 2 T, were higher in energy than the ferromagnetic state with magnetization along the corresponding field. For the skyrmion subjected to a field of 1 T, we calculated the energy barrier needed to be overcome for a continuous transformation between the skyrmion and the ferromagnetic states, see Fig. 8.5.8 (c), which was found to be 20.78 meV, while their energy difference is 95.65 meV.

8.5.3 Pseudomorphic 1ML

The Bravais lattice of the pseudomorphic film matches the one of the W(110) substrate, therefore, it is expanded by $\mathbf{a}_1 = a_\mathrm{W}\hat{\mathbf{x}}$ and $\mathbf{a}_2 = \sqrt{2}a_\mathrm{W}\hat{\mathbf{y}}$. Once again, we started by checking the possible stabilization of spin spirals by considering long rectangular simulation boxes with open periodic boundary condition along the box longer axis. In a 170×12 simulation box, we obtained a cycloidal spin spiral with axis

along y propagating along x with wavelength of $36a_{\mathrm{W}} = 11.38\,\mathrm{nm}$, see Fig. 8.5.9 (a), which compares well with the outcomes of the micromagnetic model, $31a_{\mathrm{W}}$. Taking a 20×100 box, we obtained a cycloidal spin spiral with axis along x propagating along y with wavelength of $82a_{\mathrm{W}} = 25.92\,\mathrm{nm}$, which is roughly two thirds of that determined by the micromagnetic model in Sec. 8.4.3, $132a_{\mathrm{W}}$.

Next, we considered a simulation box commensurate with the wavelength of the y-axis spin spiral, 70×40, with complete periodic boundary conditions. We performed various simulations starting from random spin configurations, which always resulted in a spin spiral corresponding to that of Fig. 8.5.9 (a). Compared with the ferromagnetic state with magnetization along y, that is, along the strongest anisotropy easy-axis, this spin spiral has an energy of $\Delta E = -0.44\,\mathrm{meV}$ per atom, which is in very good agreement with the micromagnetic model, $\Delta E = -0.43\,\mathrm{meV}$ per atom (Tab.8.4.3). Thus, we conclude that the obtained spin spiral is the ground state of the 1ML Co film pseudomorphically grown on W(110).

Now, we applied an external magnetic field, both in-plane along x and out-of-plane along z. For a field of 12 T out-of-plane, we managed to stabilize an out-of-plane antiskyrmion, Fig. 8.5.9 (b), and for a field of 9 T in-plane, we obtained an in-plane skyrmion, Fig. 8.5.9 (c). The field range of stability of these skyrmions is rather small. The stability of an antiskyrmion could have been anticipated from the micromagnetic model, for the signs of the spiralization-tensor elements, D^{xy} and D^{yx}, were the same [111] for the pseudomorphic film, see Sec. 8.4.1 and Tab. 8.4.2. In the pseudomorphic film, the magnetic interactions are not as soft as for the reconstructed case, and it is characterized by higher symmetries than the latter, which reduces the complexity of the DMI interactions, for example. This leads to a less rich collection of noncollinear structures in comparison with the reconstructed Co monolayer.

8.6 In-plane skyrmion model

If we rotate each spin of the out-of-plane skyrmion in Fig. 8.1.1 (a) by 90° around an in-plane axis, e.g., around the y–axis, we obtain the in-plane skyrmion of Fig. 8.6.1 (a). It also maps onto a sphere and its polarization axis lies in-plane parallel to the background magnetization. A similar procedure can be performed to the out-of-plane antiskyrmion of Fig. 8.1.1 (b), which can be transformed into the in-plane antiskyrmion of Fig. 8.6.1 (b). A crucial difference between an out-of-plane skyrmion and an in-plane skyrmion concerns the determination of the vorticity. Consider the spins of a circular path around the in-plane skyrmion core, such as the ones highlighted in Fig. 8.6.1 (c). When we walk through this path, the spins wind a full 2π revolution in the plane normal to the polarization axis. Note that this plane is also perpendicular to the $x - y$ plane where the in-plane skyrmion lives. The winding sense is opposite between the in-plane skyrmion and in-plane antiskyrmion, see Fig. 8.6.1 (c) and (d). However, the winding number sign, being positive or negative, depends on the convention one chooses to circulate along the path around the core since there is no out-of-plane net magnetization to fix it.

Currently, we can find only a handful of works studying in-plane skyrmions [164, 172]. Furthermore, these studies focus on the stabilization of these entities through magnetic exchange frustration. In a phenomenological model-based study, Göbel

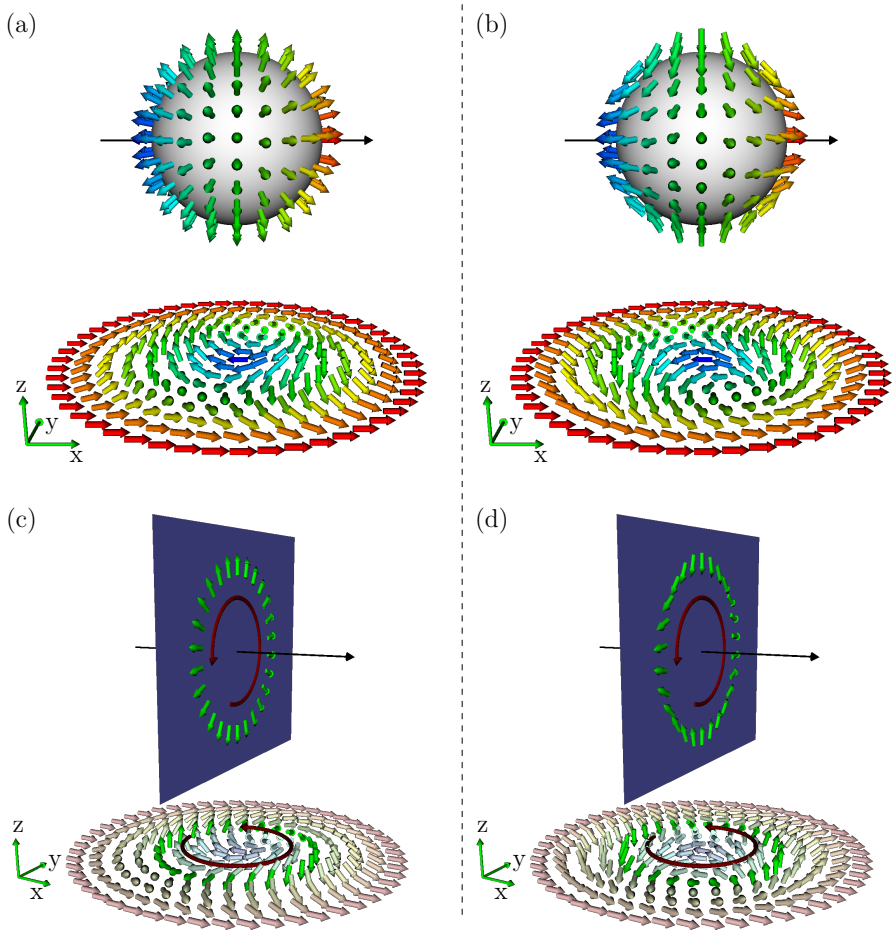

Figure 8.6.1: In-plane skyrmion and antiskyrmion. (a) and (b) depict an in-plane skyrmion and an in-plane antiskyrmion, respectively, mapped onto spheres. The background magnetization (in red) defines the polarization axis, which is indicated by the long black arrow. The core of both skyrmion and antiskyrmion are antiparallel to the background magnetization and shown in blue. (c) and (d) show the winding of the spins along a circumference around the skyrmion and antiskyrmion cores as mapped into the plane normal to the polarization axis.

et al. in Ref. [165] discussed for the first time the possibility of Dzyaloshinskii-Moriya interaction stabilizing in-plane skyrmions via an out-of-plane DMI component. As demonstrated in the previous section, we predicted the existence of in-plane skyrmions as metastable states of a reconstructed Co/W(110) monolayer, which are stabilized by the Dzyaloshinskii-Moriya interaction. In their work, Göbel *et al.* call an in-plane skyrmion a bimeron, because it can be seen as a pair of coupled merons. However, in their model, a meron cannot exist by itself. From most properties point-of-view, we cannot distinguish an in-plane skyrmion from a regular

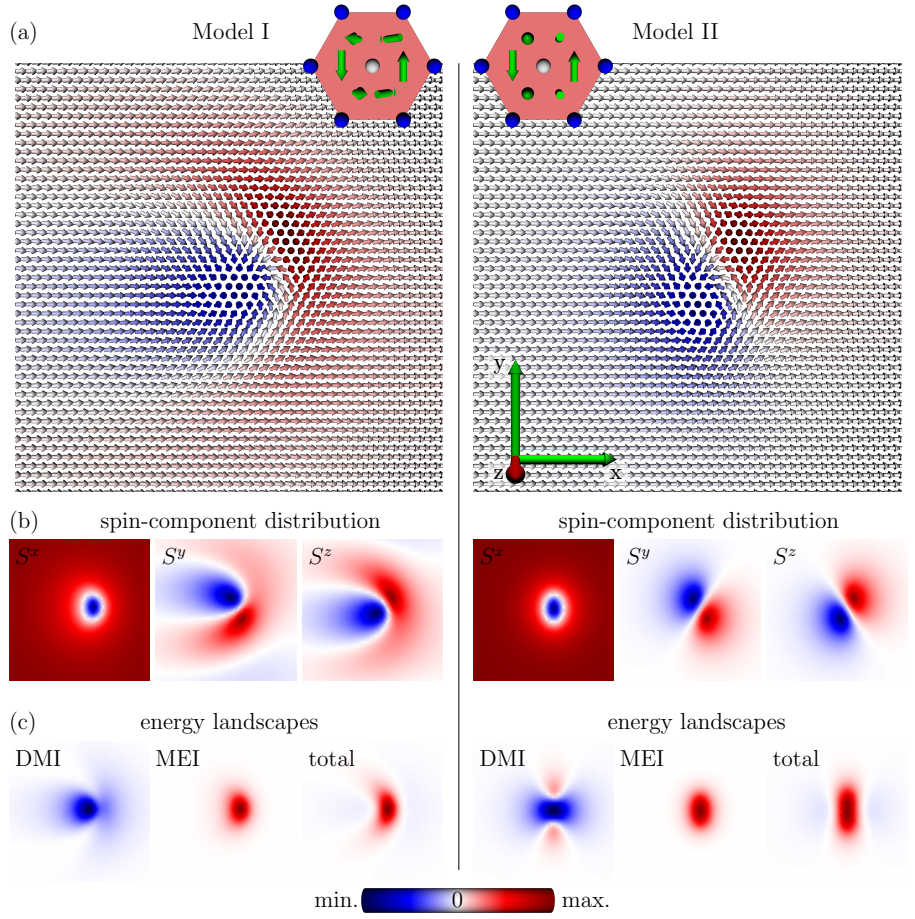

Figure 8.6.2: (a) In-plane skyrmion of Models I and II. Both models have nearest-neighbor ferromagnetic MEI, but Model I have DMI vectors with components along x, y and z. Model II has DMI only along y and z. The shown skyrmion was obtained with $B = 1.7\,\mathrm{T}$ and $B = 1.5\,\mathrm{T}$ along $\hat{\mathbf{x}}$ for Models I and II, respectively. (b) The color maps represent the different components of the spins. (c) The energy landscape of the in-plane skyrmion. The contributions of DMI and MEI are shown separately, and the total map includes DMI, MEI, and Zeeman contributions. Parameters: $J_{ij} = 1\,\mathrm{meV}$, $|D_{ij}| = 0.2\,\mathrm{meV}$.

out-of-plane skyrmion, and therefore, we will keep naming it skyrmion.

Aiming to better understand the process of stabilization, in this section, we focus on two models including only the nearest-neighbor interactions, both with the same isotropic ferromagnetic MEI but with different DMI. In Model I, the DMI vectors mimic those of the Co/W(110) containing components along all three orthonormal directions x, y, and z. Model II differs from Model I by not featuring the DMI components along x, see the insert in Fig. 8.6.2 (a). For the two models, all the DMI vectors have the same length, and their moduli are 20% of the MEI strength.

In the absence of external magnetic fields, both models have spin spirals as their ground state. Applying a strong enough magnetic field along x, we can spin polarize the system (all spins align with the field). For fields not too strong, however, in-plane skyrmions can be observed as metastable states, see Fig. 8.6.2 (a), where we used atomistic-spin-dynamics simulations to perform spin relaxation. The red and blue colors represent the projection of the spins along the z–direction. The in-plane skyrmion core can be identified as the region where the spins are anti-aligned to the background magnetization, in the case of Fig. 8.6.2 (a), where the spins point along $-x$. Surrounding the core, there are two vortex-like structures, whose local spins go out-of-plane. When we move from the outside towards this skyrmion core, the spins rotate with rotational axis in-plane or out-of-plane, depending on the direction you choose to walk on. This allows the in-plane skyrmion to efficiently gain energy from the out-of-plane components of the DMI too. This is in contrast to the usual Néel or Bloch-type skyrmions, whose cross-sections correspond to spirals with in-plane rotational axes only.

The structural aspects of the skyrmion depend, naturally, on the DMI structure. In the absence of D^x, the two vortices are equivalent and have similar size, as seen for Model II in Fig. 8.6.2 (b), where the spin projections along the different orthonormal directions are depicted by color maps. Blue and red represent negative and positive values, respectively. Adding the D^x contained in Model I, one of the vortices is favored and therefore expands, while the other shrinks. Besides that, the shape of the vortices are also altered, see Model I in Fig. 8.6.2 (b). The D^x component of all pairs in Model I have the same chirality, meaning that they swirl with the same sense, which shows that each vortex is individually chiral.

Figure 8.6.2 (c) presents the energy landscape of the correspondent skyrmion in Model I and II, having as reference the energy landscape of their spin-polarized states. It shows the DMI and MEI energy contributions separately, but also their sum that together with the Zeeman contribution compose the total energy. In the blue regions, the energy contribution is negative, which means they are energetically favorable with respect to the ferromagnetic state. Regions in red correspond to an increase of energy, and therefore, they are energetically unfavorable. Overall, the total energy landscape is more red-like, which indicates that the spin-polarized state is lower in energy. Nevertheless, the DMI manages to create an energy barrier high enough to stabilize these in-plane skyrmions. Furthermore, we can notice that the energy landscape is asymmetric with respect to the x–direction for Model I, even though a mirror plane perpendicular to the x–axis is a symmetry operator of both models.

Please notice that the mirror operation preserves the orientation of the background magnetization. In fact, the mirror images of these skyrmions, obtained by making $x \to -x$ and $(S^y, S^z) \to (-S^y, -S^z)$, are stable as well, and they are degenerate in energy to their original partners. Furthermore, the skyrmion and its mirror image have opposite topological charge, and they tend to annihilate each other. Also, when moving along a circular contour around the skyrmion core, with a fixed rotational sense, the spins along the path have projections onto the plane transversal to the background magnetization that rotate with one sense for the skyrmion and the opposite sense for its image, indicating that they have opposite vorticity. Because of that, we name one skyrmion and the second antiskyrmion, having in mind

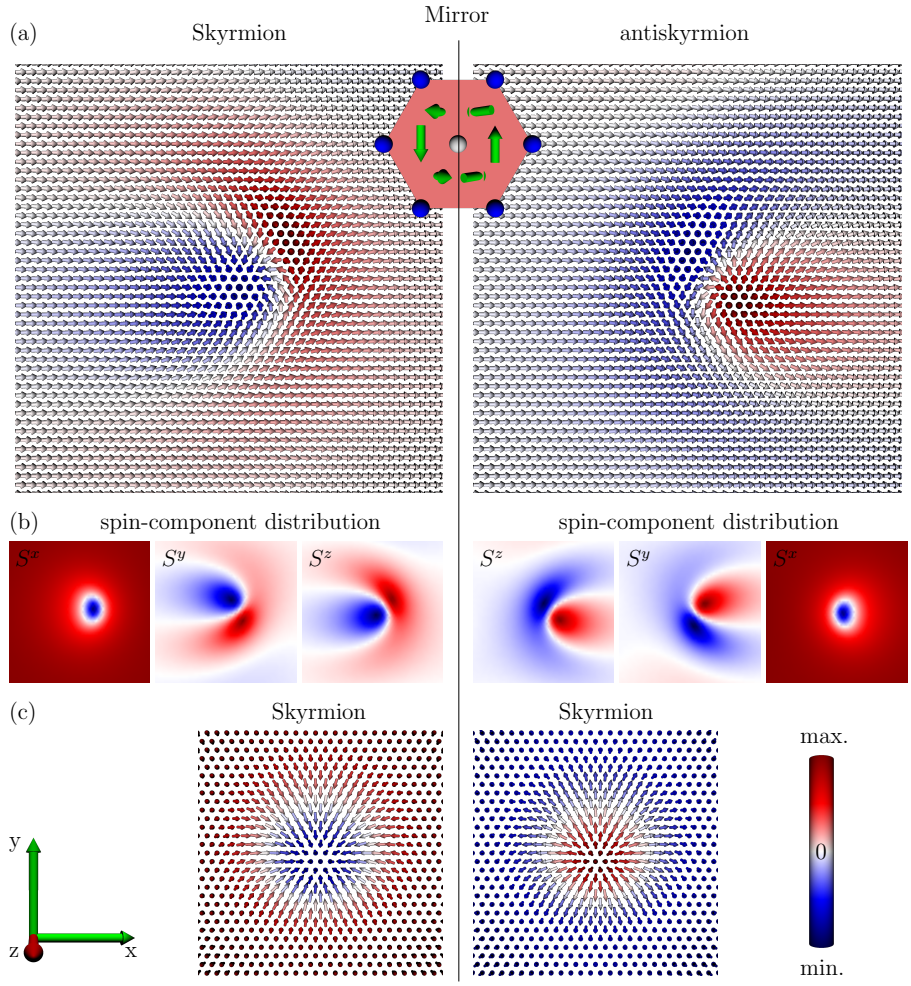

Figure 8.6.3: (a) In-plane skyrmion and antiskyrmion, two degenerated metastable states of Model I with external magnetic field along x, whose topological charge are ± 1. The system has a mirror plane perpendicular to the x–axis, such that each of these quasi-particles is the mirror image of each other. (b) The color maps represent the different components of the spins. (c) Applying the field out-of-plane instead, the mirror image of the skyrmion is another skyrmion with reserved core living in a reversed background magnetization, nevertheless with opposite topological charge. Parameters: $J_{ij} = 1\,\text{meV}$, $|D_{ij}| = 0.2\,\text{meV}$, $B = 1.7\,\text{T}$.

that the choice on where to start labeling is a matter of convention. Figure 8.6.3 (a) shows an in-plane skyrmion and in-plane antiskyrmion for Model I, both featuring an asymmetric energy landscape (shown later), but with the same total energy. We can understand this phenomenon in analogy to the hydrogen atom, where a spherically symmetric potential can give rise to the p–orbitals, which individually do not have the same symmetries of the potential. In Fig. 8.6.3 (b), we can see the spin-component distributions for the skyrmions, and how they look like in the

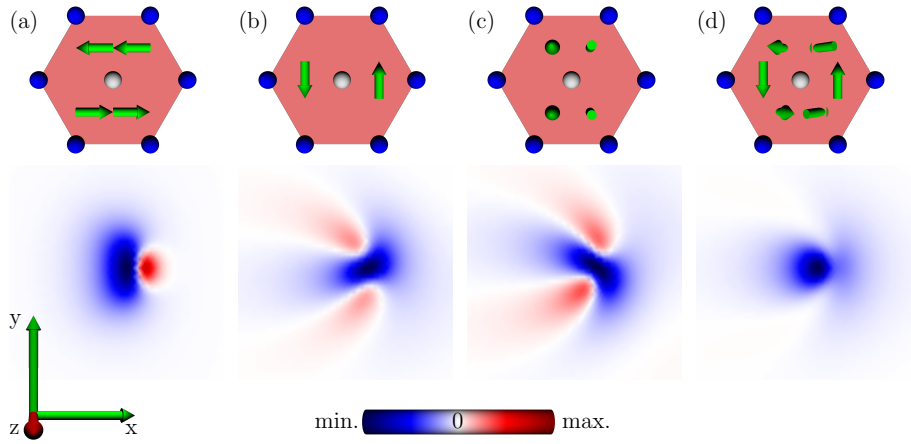

Figure 8.6.4: Energy landscape of each DMI component in the in-plane skyrmion of Fig. 8.6.2 (a). (a-c) energy contribution due to the x, y, and z DMI components, respectively. (d) the sum of the contributions of all the DMI components. The blue color indicates regions of the in-plane where the local spin texture is favored by the DMI, and the red color marks regions which are unfavorable.

mirror.

Next, we applied the external magnetic field out-of-plane instead. In consequence, we could obtain a regular out-of-plane skyrmion. Its mirror image, which has opposite topological charge, is no more than a skyrmion with a reversed core in a reversed background magnetization, see Fig. 8.6.3 (c). Despite having opposite topological charge, the out-of-plane skyrmion and its image have the same vorticity. An antiskyrmion, which has opposite topological charge, opposite vorticity, and that lives in the same background magnetization as the skyrmion, is not stable for this model. The same will occur if the field is put along y, for the magnetization would lie in the mirror plane. This reveals the peculiarity of having a system with an easy axis perpendicular to the system's mirror plane: there, a skyrmion and an antiskyrmion living in the same background magnetization can co-exist and are degenerate in energy.

By relaxing a random spin configuration with the atomistic-spin-dynamics simulation for Model I in a large simulation box with respect to the skyrmion size, we found that many skyrmions and antiskyrmions can be nucleated. They often attract each other until they come close enough and their mutual annihilation happens. As the random seeding of skyrmion and antiskyrmion is often and by chance uneven, we end up with a finite but small population of one type of quasiparticles, either skyrmions or antiskyrmions. Nevertheless, the probability of ending up with a given amount of skyrmions or antiskyrmions is the same. However, we can favor the seeding of one or the other by applying and controlling the direction of an external magnetic field perpendicular to the film.

The last question we set ourselves to answer here is, which components of the DMI are stabilizing the in-plane skyrmion and how? To answer this question, we plotted the energy landscape induced by the in-plane skyrmion of Model I,

Fig. 8.6.2 (a), under the action of each component of the DMI individually. Figure 8.6.4 (a) shows the energy landscape due to D^x, which is responsible to favor one of the in-plane-skyrmion vortices, which breaks the symmetry along x. We can see that the in-plane skyrmion lowers the energy via D^x over a large area on the left-hand side, which is shown in blue. Meanwhile, it has a smaller pocket in red, which is energetically unfavorable. Had the D^x changed its chirality, the right-hand-side pocket would be enlarged becoming now energetically favorable, and therefore blue.

Figure 8.6.4 (b) and (c) depict the energy landscape for D^y and D^z, respectively, which are very similar in shape indicating that these two components are equivalent. Interestingly, these two energy landscapes are not symmetric under a mirror operation perpendicular to y. The contribution of D^y and D^z combined, however, is invariant under such a symmetry operation, which explains the preservation of that symmetry in the total energy landscape, see Fig. 8.6.4 (d). The absence of red regions for the total energy landscape shows that the spin structure manages to gain energy from all three components of the DMI, guaranteeing the stabilization of the in-plane skyrmion.

8.6.1 Spin waves in an in-plane skyrmion lattice

Now, we want to construct a lattice of in-plane skyrmions. Let us consider again the interactions of Model I, with $J = 1\,\text{meV}$ and $|D| = 0.5\,\text{meV}$. This high ration helps us to keep the size of the in-plane skyrmion small, which yields a small unit cell. By applying an in-plane external field of 8 T along x, we obtain the metastable in-plane skyrmion lattice shown in Fig. 8.6.5 (a), which has a total magnetization parallel to $(0.64, 0.14, 0.18)$. The DMI vectors are depicted in Fig. 8.6.5 (b) together with the path in the reciprocal space where we calculated the spin-resolved electron-energy-loss spectroscopy (SREELS) of the in-plane-skyrmion lattice. We chose to align the polarization axis of the probing electrons along the magnetic field. Figures 8.6.5 (c-e) display the various SREELS scattering channels.

The non-spin-flip channels are shown in Fig. 8.6.5 (c), and the spin-flip channels are shown in Fig. 8.6.5 (e). The strongest inelastic signal appears in the left-right scattering channel because the incoming probing electrons have spins almost antiparallel to the total magnetization, which increases the chances of angular momentum exchange with the magnetic material to create spin waves. In all scattering channels, we observe an asymmetry of the spectra around the center of the Brillouin zone (Γ–point). For instance, note that the spectrum energy minima on the M–Γ–M path of Figs. 8.6.5 (e) and (d) are not centered in the Γ–point. This phenomenon is called nonreciprocity of spin waves, that is, spin waves of the same wavelength propagating in opposite directions acquire different properties, such as group velocity and energy. It occurs because the DMI vectors have components parallel to the total magnetization. We will discuss this subject in great detail in Chapter 9: Nonreciprocity of spin waves due to the Dzyaloshinskii-Moriya interaction.

8.7 Conclusions

In this chapter, we investigated from first-principles the magnetic properties of ultrathin films of cobalt deposited on tungsten (110) surface. We studied films with

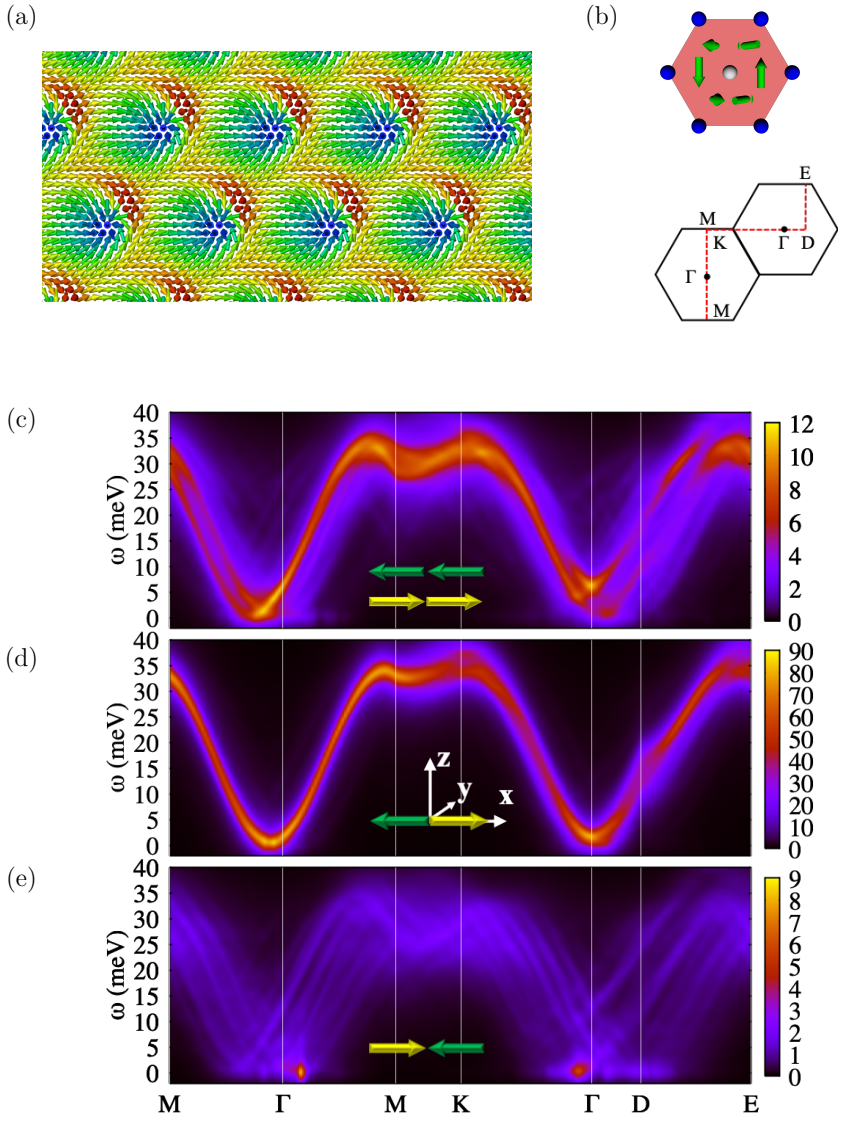

Figure 8.6.5: Spin-wave spectra for a lattice of in-plane skyrmions. (a) the in-plane-skyrmion lattice for Model I with $J = 1\,\text{meV}$, $|D| = 0.5\,\text{meV}$, magnetic moment of $1\,\mu_\text{B}$, and an in-plane magnetic field of 8 T along the x–axis. (b) DMI vectors of the model and Brillouin zone path where the inelastic electron scattering spectra were calculated. (c-e) different SREELS scattering channels. The polarization of the probing electrons is set along the magnetic field, as indicated by the inserted arrows. (c) represents the two degenerate non-spin-flip scattering channels. (d) the spin-flip left-right scattering channel, which has the strongest inelastic signal. (e) the spin-flip right-left scattering channel, which has the weakest signal.

1 up to 3 MLs of reconstructed cobalt films, as well as 1 ML of pseudomorphic film. In particular, for the reconstructed 1 ML film, we observed a significant modulation of the magnetic properties within the supercell: the magnetic moment, as well as the MEI and DMI, would vary from site to site. The 1 ML Co films, both reconstructed and pseudomorphic, have a biaxial in-plane magnetocrystalline anisotropy. In contrast, the anisotropies of reconstructed 2 and 3 MLs films can be modeled as uniaxial. The only out-of-plane easy-axis found was for the reconstructed 2 MLs film.

We showed that these systems have anisotropic magnetic exchange and Dzyaloshinskii-Moriya interactions. For example, we found that the spiralization-tensor element along bcc[$\bar{1}$10] is 3 times larger than that along bcc[001], which stresses the anisotropy of the DMI. This result is in agreement with measurements reported in Ref. [154] on Au-capped Co films.

We investigated the ground state and possible metastable spin textures of the reconstructed cobalt films using two approaches: first averaging the interactions and magnetic moments within each cobalt plane, which results in a simple single atom per layer in the unit cell; and second, using the full supercell interactions obtained directly from the DFT calculations. With the first approach, we could determine parameters for a micromagnetic model, with which we could derive an analytical study of the stability of spin spirals. The results of this study were shown to be in good agreement with the results obtained with the atomistic-spin-dynamics simulations.

With further atomistic-spin-dynamics calculations, we determined that 2 and 3 MLs have a ferromagnetic ground state, and we could not observe any stable noncollinear magnetic structures in these systems. For the reconstructed 1 ML, within the in-plane averaging approach, we predicted for the first time using *ab initio* methods the existence of in-plane skyrmions stabilized by the DMI. Furthermore, for this system, we observed and studied the occurrence of skyrmions in a spin-spiral background, where we demonstrated that their polarization axis (direction of the skyrmion core and outskirts) can point along nontrivial directions.

Using the supercell interactions, we confirmed the stability and features of skyrmions living in a spin spiral. This time, however, stable skyrmions embedded in a ferromagnetic background could only be achieved under the action of an external magnetic field. That is because contrary to the in-plane averaged scheme, the ground state was found to be a spin spiral with a wavelength of 10 nm propagating along the bcc[001] direction.

The averaging approach, which provides a simple model for micromagnetic analysis, allowed us to predict the existence of in-plane skyrmions since it preserves the symmetry of the reconstructed structure. With such models, not all detailed properties can be correctly described. For instance, the wavelength of the metastable spin spirals is slightly offset, which influences the prediction of the skyrmion size, as well as the external-magnetic-field range for the in-plane skyrmion stability.

In contrast to the assessments in Ref. [154], reconstructed Co/W(110) cannot be regarded as belonging to the C_{2v} space group. For example, the in-plane skyrmions predicted to occur in 1 MLCo/W(110) could only be stabilized because of the out-of-plane component of the DMI, which only survived due to very few symmetries of the reconstructed cobalt films.

While the strong hybridization of reconstructed cobalt leads to a strong softening of the magnetic interactions at the interface, the same is not true for pseudomorphic cobalt. As a result, the pseudomorphic 1 ML film features much larger stiffness and spiralization-tensor elements than those associated with the reconstructed 1 ML film. With a rather high ratio the elements of the spiralization and the stiffness tensor, this system has a spin spiral ground state with a wavelength of 26 nm propagating along bcc[001]. With an applied field of 10 T, we obtained an in-plane skyrmion and an out-of-plane antiskyrmion.

Finally, we studied a nearest-neighbor model inspired by the in-plane-averaged interaction scheme. Within this model, we investigated how the stabilization due to the DMI of an in-plane skyrmion is possible. We demonstrated that for systems with the magnetization in-plane and perpendicular to the mirror plane of the system, in-plane skyrmion and antiskyrmion can coexist and are degenerate because one is the mirror image of the other. Within this model, we also stabilized an in-plane-skyrmion lattice for which we computed the SREELS spectra. We observed that the spin-wave spectra of this spin texture feature a strong asymmetry around the center of the Brillouin zone.

Thus, in this chapter, we demonstrated that skyrmions can also occur in in-plane anisotropy films, which will expand the range of systems where skyrmions can be studied, possibly facilitating their application for technological devices. This new class of skyrmionic systems also has the advantage of hosting skyrmions and antiskyrmions simultaneously, which is another important feature for possible applications. Finally, we expect that in-plane skyrmions can be made very smaller than the regular out-of-plane skyrmions. That is because the dipole-dipole interaction acts effectively as an in-plane magnetocrystalline anisotropy, which helps to reduce the in-plane-skyrmion size but enlarges the out-of-plane skyrmions.

Appendix

8.A Stiffness-constant and spiralization-tensor definitions

8.A.1 Spin spiral

Let us suppose that we have the magnetic properties of a given system. That is, we have the spin moment of each site and the magnetic interactions, both the exchange and the Dzyaloshinskii-Moriya, from each pair of atoms. We want to determine whether a spin spiral can be an energetically more favorable state than a ferromagnetic phase. However, there can be many types of spin spirals, with different orientations, wavevectors, etc. Thus, we restrict our search among spirals given by the following equation:

$$\mathbf{S}_i = \cos\phi_i \sin\theta \mathbf{n}^1 + \sin\phi_i \sin\theta \mathbf{n}^2 + \cos\theta \mathbf{n}^3 \quad , \tag{8.15}$$

where $\mathbf{n}^3$ is a unity vector defining the axis around which the spins rotate, and that forms an orthonormal basis set for the three dimension space together with $\mathbf{n}^1$ and $\mathbf{n}^2$. θ is the conical angle between the spins and $\mathbf{n}^3$, and $\phi_i = \mathbf{q} \cdot \mathbf{R}_i$, where $\mathbf{q}$ is the spiral wavevector, and $\mathbf{R}_i$ the position vector of the i-th spin.

8.A.2 Spin-spiral energy

Regarding the hamiltonian of Eq. (8.1) (with a factor of 1/2 in front of the MEI and DMI terms), the classical energy (per atom) of such spin spiral can be decomposed in three terms. The exchange one:

$$\begin{aligned}
\varepsilon_J(\mathbf{q}) &= -\frac{1}{2N}\sum_{ij} J_{ij}\mathbf{S}_i \cdot \mathbf{S}_j \\
&= -\frac{1}{2N}\sum_{ij} J_{ij}\left[(\cos\phi_i\cos\phi_j + \sin\phi_i\sin\phi_j)\sin^2\theta + \cos^2\theta\right] \\
&= -\frac{1}{2N}\sum_{ij} J_{ij}\left[\cos\phi_{ij}\sin^2\theta + \cos^2\theta\right] \\
&= -\frac{1}{2N}\sum_{ij} J_{ij}\left[\cos\left(\mathbf{q}\cdot\mathbf{R}_{ij}\right)\sin^2\theta + \cos^2\theta\right] \quad .
\end{aligned} \tag{8.16}$$

The Dzyaloshinskii-Moriya term:

$$\begin{aligned}
\varepsilon_D(\mathbf{q}) =& -\frac{1}{2N}\sum_{ij}\mathbf{D}_{ij}\cdot\mathbf{S}_i\times\mathbf{S}_j \\
=& -\frac{1}{2N}\sum_{ij}\Big\{\sin^2\theta D^3_{ij}\sin(\phi_{ij}) \\
&\quad +\cos\theta\sin\theta\left[D^1_{ij}(\sin\phi_i-\sin\phi_j)+D^2_{ij}(\cos\phi_j-\cos\phi_i)\right]\Big\} \\
=& -\frac{1}{2N}\sum_{ij}\Big\{\sin^2\theta D^3_{ij}\sin(\phi_{ij}) \\
&\quad +\cos\theta\sin\theta\left[(\sin\phi_i D^1_{ij}-\sin\phi_i D^1_{ji})+(\cos\phi_i D^2_{ji}-\cos\phi_i D^2_{ij})\right]\Big\} \\
=& -\frac{1}{2N}\sum_{ij}\Big\{\sin^2\theta D^3_{ij}\sin(\phi_{ij}) \\
&\quad +\cos\theta\sin\theta\left[(\sin\phi_i D^1_{ij}+\sin\phi_i D^1_{ij})-(\cos\phi_i D^2_{ij}+\cos\phi_i D^2_{ij})\right]\Big\} \\
=& -\frac{1}{2N}\sum_{ij}\Big\{\sin^2\theta D^3_{ij}\sin(\mathbf{q}\cdot\mathbf{R}_{ij}) \\
&\quad +\sin 2\theta\left[\sin(\mathbf{q}\cdot\mathbf{R}_i)D^1_{ij}-\cos(\mathbf{q}\cdot\mathbf{R}_i)D^2_{ij}\right]\Big\} \quad ,
\end{aligned} \tag{8.17}$$

where we swap some of the indices in the third line. In the fourth line, we used the symmetry properties of the Dzyaloshinskii-Moriya interaction that imposes $\mathbf{D}_{ij} = -\mathbf{D}_{ji}$.

And the magneto-crystalline anisotropy contribution:

$$\begin{aligned}
\varepsilon_K(\mathbf{q}) =& -\frac{K}{N}\sum_i(\hat{\mathbf{K}}\cdot\mathbf{S}_i)^2 \\
=& -\frac{K}{N}\sum_i(K^1\cos\phi_i\sin\theta+K^2\sin\phi_i\sin\theta+K^3\cos\theta)^2 \\
=& -\frac{K}{N}\sum_i\Big[\sin^2\theta\big((K^1)^2\cos^2\phi_i+K^1K^2\sin 2\phi_i+(K^2)^2\sin^2\phi_i\big) \\
&\quad +\sin 2\theta\big(K^1K^3\cos\phi_i+K^2K^3\sin\phi_i\big)+(K^3)^2\cos^2\theta\Big] \\
=& -\frac{K}{N}\sum_i\Bigg[\sin^2\theta\big((K^1)^2\frac{\cos(2\phi_i)+1}{2}+K^1K^2\sin 2\phi_i+(K^2)^2\frac{1-\cos(2\phi_i)}{2}\big) \\
&\quad +\sin 2\theta\big(K^1K^3\cos\phi_i+K^2K^3\sin\phi_i\big)+(K^3)^2\cos^2\theta\Bigg] \\
=& -K\left[\frac{1}{2}\sin^2\theta\big((K^1)^2(\delta_{2\mathbf{q},\{0,\mathbf{Q}\}}+1)+(K^2)^2(1-\delta_{2\mathbf{q},\{0,\mathbf{Q}\}})\big)\right. \\
&\quad \left.+\sin 2\theta\big(K^1K^3\delta_{\mathbf{q},0}\big)+(K^3)^2\cos^2\theta\right] \quad ,
\end{aligned} \tag{8.18}$$

where we used the summation properties discussed in the Apx. 4.A and considered that $\mathbf{q}$ is restricted to the first Brillouin zone. The unit vector that represent the magnetic anisotropy axis decomposes as $\hat{\mathbf{K}} = K^1\mathbf{n}^1+K^2\mathbf{n}^2+K^3\mathbf{n}^3$ with $\sum^\alpha(K^\alpha)^2 = 1$. Thus, we can see that the anisotropy energy is a constant for every wavevector

different of zero:

$$\varepsilon_K(\mathbf{q}\neq 0) = -\,K\left\{\frac{1}{2}\sin^2\theta\left[(K^1)^2+(K^2)^2\right]+(K^3)^2\cos^2\theta\right\} \quad , \tag{8.19}$$

and it contains a singularity for the ferromagnetic state:

$$\varepsilon_K(\mathbf{q}=0) = -\,K\left[\sin^2\theta(K^1)^2+\sin 2\theta K^1K^3+(K^3)^2\cos^2\theta\right] \quad . \tag{8.20}$$

The component K^2 does not appear in this last result because for $\mathbf{q}=0$ in the definition of the spin spiral, Eq. (8.15), the circular components of the spins point along $\mathbf{n}^1$ only.

8.A.3 Taylor expansion of the spin-spiral energy

For a system with slowly varying magnetization, the regime of long-wavelength is the most important. Let us then consider a Taylor expansion of the spin-spiral energy $\varepsilon=\varepsilon_J+\varepsilon_D$ around $\mathbf{q}=0$, without including the magnetocrystalline term because its behavior at $\mathbf{q}=0$ is singular (it is discontinuous there):

$$\varepsilon(\mathbf{q}) = \varepsilon_0+\mathcal{D}^T\cdot\mathbf{q}+\frac{1}{2!}\mathbf{q}^T\mathcal{A}\mathbf{q}+\mathcal{O}(\mathbf{q}^3) \quad . \tag{8.21}$$

$\varepsilon_0=\varepsilon(\mathbf{q}=0)$ corresponds to the energy of a ferromagnetic state. $\mathcal{D}$ is given by the gradient of the energy function:

$$\mathcal{D} = \nabla\varepsilon\big|_{\mathbf{q}=0} = \left.\begin{pmatrix}\frac{\partial\varepsilon}{\partial q_x}\\ \frac{\partial\varepsilon}{\partial q_y}\\ \frac{\partial\varepsilon}{\partial q_z}\end{pmatrix}\right|_{\mathbf{q}=0} \quad , \tag{8.22}$$

and $\mathcal{A}$ is the energy Hessian :

$$\mathcal{A} = \mathbf{H}\big(\varepsilon\big)\big|_{\mathbf{q}=0} = \left.\begin{pmatrix}\frac{\partial^2\varepsilon}{\partial q_x^2} & \frac{\partial^2\varepsilon}{\partial q_x\partial y}\\ \frac{\partial^2\varepsilon}{\partial q_y\partial q_x} & \frac{\partial^2\varepsilon}{\partial q_y^2}\end{pmatrix}\right|_{\mathbf{q}=0} \quad . \tag{8.23}$$

Let us evaluate the gradient and Hessian of the spiral energy. For the exchange term, we obtain:

$$\nabla\varepsilon_J = \frac{1}{2N}\sin^2\theta\sum_{ij}J_{ij}\mathbf{R}_{ij}\sin\left(\mathbf{q}\cdot\mathbf{R}_{ij}\right) \quad , \tag{8.24}$$

and

$$H^{\mu\nu}(\varepsilon_J) = \frac{1}{2N}\sin^2\theta\sum_{ij}J_{ij}R_{ij}^{\mu}R_{ij}^{\nu}\cos\left(\mathbf{q}\cdot\mathbf{R}_{ij}\right) \quad , \tag{8.25}$$

where $\mu,\nu=x,y,z$ index the Cartesian components of the position vectors. For the Dzyaloshinskii-Moriya contribution:

$$\begin{aligned}\nabla\varepsilon_D = -\,\frac{1}{2N}\sum_{ij}\big\{&\sin^2\theta D_{ij}^3\mathbf{R}_{ij}\cos(\mathbf{q}\cdot\mathbf{R}_{ij})\\ &+\sin 2\theta\mathbf{R}_i\left[\cos(\mathbf{q}\cdot\mathbf{R}_i)D_{ij}^1+\sin(\mathbf{q}\cdot\mathbf{R}_i)D_{ij}^2\right]\big\} \quad ,\end{aligned} \tag{8.26}$$

and

$$H^{\mu\nu}(\varepsilon_D) = \frac{1}{2N}\sum_{ij}\Big\{\sin^2\theta D^3_{ij}R^\mu_{ij}R^\nu_{ij}\sin(\mathbf{q}\cdot\mathbf{R}_{ij}) + \sin 2\theta R^\mu_i R^\nu_i\left[\sin(\mathbf{q}\cdot\mathbf{R}_i)D^1_{ij} - \cos(\mathbf{q}\cdot\mathbf{R}_i)D^2_{ij}\right]\Big\} \quad . \tag{8.27}$$

8.A.4 Stiffness and spiralization tensors

Evaluating the gradient and Hessian of ε at $\mathbf{q} = 0$, we obtain the constant of the Taylor expansion:

$$\nabla\varepsilon\big|_0 = -\frac{1}{2N}\sum_{ij}\left\{\sin^2\theta D^3_{ij}\mathbf{R}_{ij} + \sin 2\theta \mathbf{R}_i D^1_{ij}\right\} \quad , \tag{8.28}$$

and

$$\mathcal{H}^{\mu\nu}(\varepsilon)\big|_0 = \frac{1}{2N}\sum_{ij}\left\{\sin^2\theta J_{ij}R^\mu_{ij}R^\nu_{ij} - \sin 2\theta R^\mu_i R^\nu_i D^2_{ij}\right\} \quad . \tag{8.29}$$

If the summation is over a Bravais lattice, the translational symmetry ensures that for each bond interaction $\mathbf{D}_{ij}$ between spins resting in $\mathbf{R}_i$ and $\mathbf{R}_j$, there is another interaction $\mathbf{D}_{i,-j}$ between sites in $\mathbf{R}_i$ and $-\mathbf{R}_j$, such that $\mathbf{D}_{ij} = -\mathbf{D}_{i,-j}$. This result guarantees that $\sum_j D^\mu_{ij} = 0$, so we are left with

$$\mathcal{D}^\mu = -\frac{1}{2N}\sin^2\theta\sum_{ij} D^3_{ij}R^\mu_{ij} \quad . \tag{8.30}$$

Note that $\mathcal{D}$ is a function of the spiral orientation via $D^3_{ij} = \mathbf{D}_{ij}\cdot\mathbf{n}^3$. Therefore, a straightforward generalization is obtained by computing $\mathcal{D}$ for three orthogonal directions of $\mathbf{n}^3$, $\alpha = x, y, z$, which leads to the known definition of the so-called spiralization tensor [169]:

$$\mathcal{D}^{\alpha\mu} = -\sum_j D^\alpha_{0j}R^\mu_{0j} \quad , \tag{8.31}$$

which describes the susceptibility for the magnetic structure to become a spin spiral. Each line of this tensor stores a vector that defines the spin-spiral rotational axis. We also made $\theta = \pi/2$, which yields a flat spiral in Eq. (8.15). In the same manner, we obtain $\mathcal{A}$, known as the stiffness tensor:

$$\mathcal{A}^{\mu\nu} = \sum_j J_{0j}R^\mu_{0j}R^\nu_{0j} \quad , \tag{8.32}$$

which is related to the "hardness" of the ferromagnetism of the material. It is worth noticing that the stiffness tensor is a symmetric matrix. The stiffness and spiralization tensors are quantities used in the micromagnetic simulations of magnetic material, which are very useful for large scale simulation where the atomistic ones become impractical.

8.A.5 The ground state

Once Taylor-expansion coefficients of the spin-spiral energy in Eq. (8.21) are known, we can easily determine whether a spin spiral is energetically more favorable than the ferromagnetic state, and if so, for which wavevector. For that, we need to analyze the spin-spiral energy in contrast with the ferromagnetic phase, where there is the singular contribution of the magnetocrystalline anisotropy.

Let us rewrite the Taylor expansion of the energy, Eq. (8.21), in the element notation:

$$\varepsilon^{\alpha}(\mathbf{q}) = \varepsilon_0 + \sum_{\mu} \mathcal{D}^{\alpha\mu} q^{\mu} + \frac{1}{2} \sum_{\mu\nu} q^{\mu} \mathcal{A}^{\mu\nu} q^{\nu} \quad , \tag{8.33}$$

where we have three energies for $\alpha = x, y, z$, one for each Cartesian alignment of the spin-spiral rotational axis. At the energy minimum, we have that its derivative in respect to the wavevector is zero:

$$\begin{aligned}
\frac{\partial \varepsilon^{\alpha}}{\partial q^{\xi}} =& \sum_{\mu} \mathcal{D}^{\alpha\mu} \delta_{\xi\mu} + \frac{1}{2} \sum_{\mu\nu} \delta_{\xi\mu} \mathcal{A}^{\mu\nu} q^{\nu} + \frac{1}{2} \sum_{\mu\nu} q^{\mu} \mathcal{A}^{\mu\nu} \delta_{\xi\nu} = 0 \\
\frac{\partial \varepsilon^{\alpha}}{\partial q^{\xi}} =& \mathcal{D}^{\alpha\xi} + \frac{1}{2} \sum_{\nu} \mathcal{A}^{\xi\nu} q^{\nu} + \frac{1}{2} \sum_{\mu} q^{\mu} \mathcal{A}^{\mu\xi} = 0 \\
\frac{\partial \varepsilon^{\alpha}}{\partial q^{\xi}} =& \mathcal{D}^{\alpha\xi} + \sum_{\mu} q^{\mu} \mathcal{A}^{\mu\xi} = 0 \\
\mathcal{D}^{\alpha\xi} =& - \sum_{\mu} q^{\mu} \mathcal{A}^{\mu\xi} \quad ,
\end{aligned} \tag{8.34}$$

where ξ is also an index for the Cartesian components of $\mathbf{q}$, and we used the fact that $\mathcal{A}$ is a symmetric matrix. Therefore, the wavevector $\mathbf{q}^{\alpha}$ that minimizes the energy for a spiral with axis along α, is given by:

$$q^{\alpha\mu} = - \sum_{\nu} D^{\alpha\nu} \overline{\mathcal{A}}^{\nu\mu} \quad , \tag{8.35}$$

where the matrix $\overline{\mathcal{A}}$ is the inverse of $\mathcal{A}$.

Now we can calculate the energy for this spin spiral by replacing the wavevector of Eq. (8.35) into the energy Taylor expansion:

$$\begin{aligned}
\varepsilon^{\alpha} =& \varepsilon_0 - \sum_{\mu\nu} \mathcal{D}^{\alpha\mu} \overline{\mathcal{A}}^{\nu\mu} D^{\alpha\nu} + \frac{1}{2} \sum_{\nu\xi\kappa} D^{\alpha\xi} \left(\sum_{\mu} \overline{\mathcal{A}}^{\xi\mu} \mathcal{A}^{\mu\nu} \right) \overline{\mathcal{A}}^{\kappa\nu} D^{\alpha\kappa} \\
\varepsilon^{\alpha} =& \varepsilon_0 - \sum_{\mu\nu} \mathcal{D}^{\alpha\mu} \overline{\mathcal{A}}^{\nu\mu} D^{\alpha\nu} + \frac{1}{2} \sum_{\nu\xi\kappa} D^{\alpha\xi} \delta_{\xi\nu} \overline{\mathcal{A}}^{\kappa\nu} D^{\alpha\kappa} \\
\varepsilon^{\alpha} =& \varepsilon_0 - \sum_{\mu\nu} \mathcal{D}^{\alpha\mu} \overline{\mathcal{A}}^{\nu\mu} D^{\alpha\nu} + \frac{1}{2} \sum_{\mu\nu} D^{\alpha\mu} \overline{\mathcal{A}}^{\nu\mu} D^{\alpha\nu} \\
\varepsilon^{\alpha} =& \varepsilon_0 - \frac{1}{2} \sum_{\mu\nu} D^{\alpha\nu} \overline{\mathcal{A}}^{\nu\mu} \mathcal{D}^{\alpha\mu}
\end{aligned} \tag{8.36}$$

The spin-spiral ground state is given by $\mathbf{q}^{\alpha}$ of smaller energy.

8.B The exponential enveloping and extrapolation method for the exchange tensor

8.B.1 Exchange interaction model

We want to perform a controlled study on how to calculate the exchange stiffness, given by Eq. (8.32), through the method based on an extrapolation method when applying an exponential envelop to the exchange interaction, which was introduced in Ref. [173]. To do so, let us consider an exchange interaction model given by the formula:

$$J_{ij} = \cos\left(2\pi \frac{r_{ij} - a}{\lambda}\right) r_{ij}^{-\alpha}. \tag{8.37}$$

It consists of a periodic function multiplied by a power-law decaying function of damping coefficient α. The period of the cosine function is given by wavelength λ, and its phase was chosen such that it gives 1 for $r_{ij} = a$, that is, at the nearest neighbor distance given by the lattice constant a.

8.B.2 Exchange stiffness convergence

Let us consider a one-dimensional system and calculate the exchange stiffness A, which involves a summation over an infinite lattice, as a function of the cut-off radius for several values for α and $\lambda = 4a$, see green-square points in Fig. 8.B.1. The blue dashed lines represent the decay of the exchange interaction model represented by the black dots. For $\alpha = 2.0$, Fig. 8.B.1 (a), the stiffness does not converge at all, for each term of the summation in Eq. (8.32) does not decay but solely oscillates changing sign. For $\alpha = 2.5$ and $\alpha = 3.0$, we observe signs of a slow convergence of A, see Fig. 8.B.1 (b) and (c). And finally, for $\alpha = 4.0$, the exchange-interaction decay is fast enough to ensure a rapid convergence of the stiffness constant.

8.B.3 Exponential enveloping and extrapolation

We could see in Fig. 8.B.1 that, only for very fast decaying exchange a converged stiffness can be calculated for a small cut-off radius for the exchange interaction cluster. However, for transition metals, this is not the case. Instead of computing the stiffness constant by summing over a very large cluster, one can envelop the exchange interaction with an exponentially decaying function of different exponential factors, which ensures convergence of A even for small cut-off radius, then extrapolate to small damping.

In practice, we update our definition of exchange interaction by multiplying it with an exponential function:

$$J_{ij} = \cos\left(2\pi \frac{r_{ij} - a}{\lambda}\right) r_{ij}^{-\alpha}\ e^{-\beta(r_{ij}-a)}. \tag{8.38}$$

We then need to calculate the stiffness constant for several values of β that are large enough for the summation to be converged at the end of the available cluster.

Let us pick the case $\alpha = 3$, for the exponential coefficient β of about 0.36, the overall decay is already so fast that A converges within a radius of $20a$, see

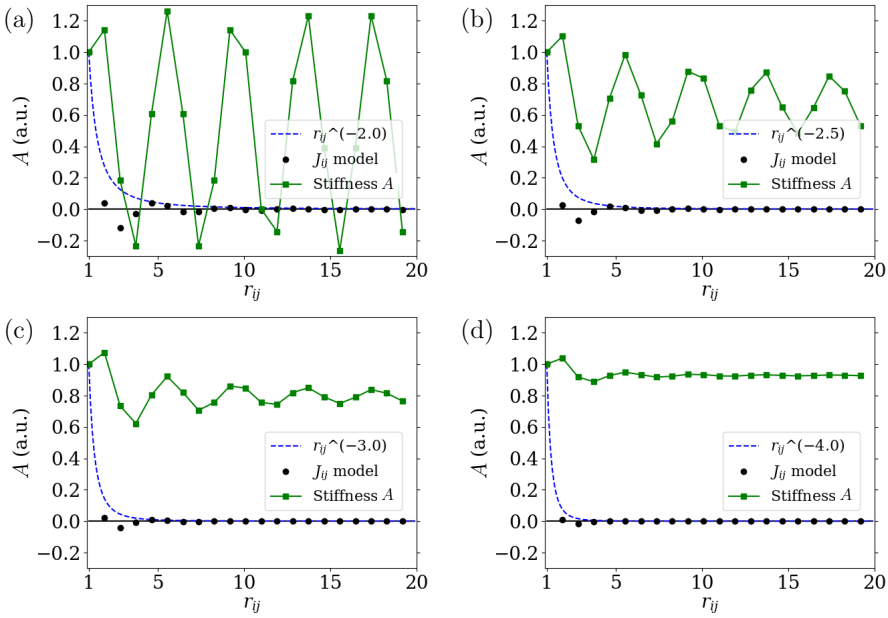

Figure 8.B.1: Convergence of the exchange-stiffness constant as a function of the cut-off radius. Panels (a)–(d) corresponds to different power-law decay of the exchange interaction: $\alpha = 2.0, 2.5, 3.0, 4.0$. The green square points connected by the green lines are the exchange stiffness summed up until the given radius r_{ij}. The blue dashed lines correspond to the power-law decaying function of the exchange interaction, which is given by the black dots. Only for $\alpha = 4.0$, panel (d), we observe a convergence of A within a cluster of radius $20a$. Parameters: $a = 1$, $\lambda = 4a$.

Fig. 8.B.2 (a). Naturally, the same is true for higher values of β. We plot in Fig. 8.B.2 (b) the converged stiffness constants obtained for several values of β. Using a quadratic least-square extrapolation method, we made a quadratic fit to this curve and extrapolated for $\beta = 0$, which gives us $A = 0.80$ that is the value we would obtain by summing up A over a cluster of cut-off radius of $200a$, within this precision.

8.B.4 Choosing the exponential factor range

Naturally, there is a lot of freedom in applying the above-discussed method. For example, it is not obvious which range of β one should take to generate the extrapolation. Hereby, we propose an approach based on the cut-off radius. It consists of choosing a minimum exponential factor β_{min} such that the exponential function at the cut-off radius is a small fraction ϵ of its values at the nearest-neighbor distance, $\exp(-\beta_{min}(r_{cut} - a)) = \epsilon$, thus we obtain:

$$\beta_{min} = \frac{\ln \epsilon}{a - r_{cut}} \quad . \tag{8.39}$$

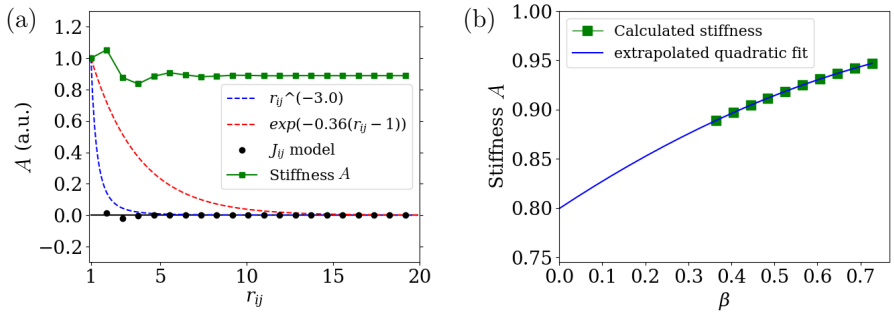

Figure 8.B.2: Rapidly stiffness-constant convergence and extrapolation. (a) Stiffness constant summed up until the given radius r_{ij}, the green square points. The dashed blue and red correspond to the power-law and exponential decay, respectively, of the exchange interaction given by the black dots. (b) Converged stiffness constant for several exponential factors β represented by the green squares. The blue straight line corresponds to the quadratic fit extrapolated until $\beta = 0$. To obtain the converged stiffness constant for smaller β, it would require larger exchange-interaction clusters. Nevertheless, we can extrapolate the calculated constant to estimate the $\beta = 0$. Parameters: $a = 1$, $\lambda = 4a$.

Analogously, the maximum β can be estimated by imposing the same decay at half of the cut-off radius:

$$\beta_{max} = \frac{\ln \epsilon}{a - r_{cut}/2} \quad . \tag{8.40}$$

These conditions ensure that the extrapolation procedure is carried out into the range where the actual exchange data available can meaningfully contribute. For example, for β too high, the exponential decay is so fast, that most of the exchange interaction data do not contribute to the calculated stiffness constant. Make it too small, and the stiffness does not converge for the cluster of available data. For Fig. 8.B.2, we took $\epsilon = 0.001$ and once the maximum cut-off was $r_{cut} = 20a$, we obtain $\beta_{min} = 0.36$ and $\beta_{max} = 0.77$, with $a = 1$.

8.B.5 Minimum cut-off radius

The next question that arises is, how small can be the cut-off radius still allowing us to make a decent estimate of the stiffness constant? It would be natural for one to suppose that the answer to this question must be related to how fast the exchange interactions decay, therefore, it is related to α. To test this hypothesis, we used the extrapolation method to estimate the stiffness constant as a function of the cut-off radius for different power-law coefficients α, see Fig. 8.B.3. The last points of all curves correspond to a radius cut-off long enough to ensure the exact numerical solutions. Estimating A with a cut-off too small can lead to large discrepancies, which are larger for smaller α. We can see that within our model, a cut-off of 15 can be good for the case with $\alpha = 4.0$, but not so much for $\alpha = 2.5$. Nevertheless, it seems that one gets a reasonable estimate of A with a cut-off of 20, and beyond, for any α considered.

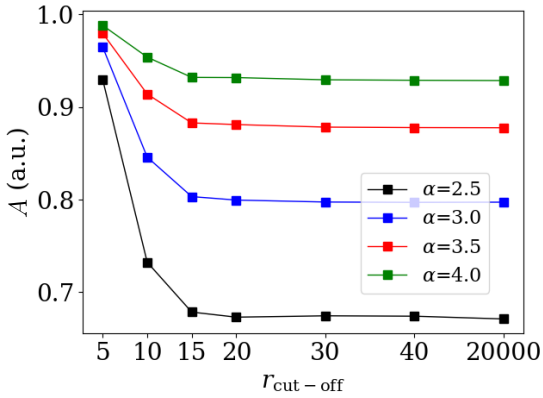

Figure 8.B.3: Stiffness constant estimate as a function of the cut-off radius for different power-law coefficients α. The estimates were obtained via the extrapolation methods discussed in the text. The last point of all curves corresponds to the exact numerical solution. A cut-off radius equal or bigger to 20 seems to yield a good estimate of A. For a smaller radius, we can observe discrepancies from the exact solution, which are bigger the smaller α is. Parameters: $a = 1$, $\lambda = 4a$.

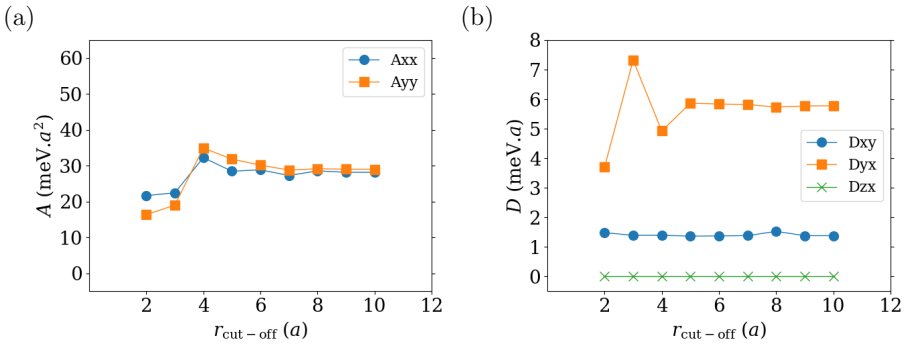

Figure 8.B.4: Estimate of the stiffness and spiralization-tensor elements as a function of the cut-off radius, using the extrapolation method, for the pseudomorphic 1ML Co/W(110). (a) shows the convergence of the stiffness-tensor elements and (b) represents the spiralization-tensor elements. These values converge much quicker than those obtained through direct summation shown in Figs. 8.4.1 and 8.4.2.

8.B.6 Pseudomorphic 1ML Co/W(110)

As seen in Sec. 8.4.1, the available interactions cluster of radius $10a_W$ for the pseudomorphic 1ML Co/W(110) was not enough to ensure convergence of the stiffness and spiralization-tensor elements, see Figs. 8.4.1 and 8.4.2. Therefore, we applied the extrapolation method discussed in the previous sections to obtain the results shown in Fig. 8.B.4. The values quickly converge as function of the cut-off radius and represent a better estimate than those in Figs. 8.4.1 and 8.4.2.

8.C Skyrmion topological charge

We determine the skyrmion topological charge by computing its winding number. The winding number in a discrete lattice can be defined as [7, 174, 175]

$$\nu = \sum_{\langle i,j,k \rangle} \Omega\left(\mathbf{S}_i, \mathbf{S}_j, \mathbf{S}_k\right) \quad , \tag{8.41}$$

which is the summation of the solid angles delimited by every set of three neighbouring spins. For small Ω, this solid angle can be approximated by

$$\tan\left[\frac{\Omega\left(\mathbf{a},\mathbf{b},\mathbf{c}\right)}{2}\right] = \frac{\mathbf{a}\cdot\left(\mathbf{b}\times\mathbf{c}\right)}{|\mathbf{a}|\,|\mathbf{b}|\,|\mathbf{c}| + \left(\mathbf{a}\cdot\mathbf{b}\right)|\mathbf{c}| + \left(\mathbf{a}\cdot\mathbf{c}\right)|\mathbf{b}| + \left(\mathbf{b}\cdot\mathbf{c}\right)|\mathbf{a}|} \quad . \tag{8.42}$$

The vectors $\mathbf{a}$, $\mathbf{b}$ and $\mathbf{c}$ should always be ordered with the same clockwise sense.

Chapter 9

Nonreciprocity of spin waves due to the Dzyaloshinskii-Moriya interaction

Can spin-wave measurements help to distinguish the occurrence of skyrmions from antiskyrmions in magnetic systems? The stabilization of one or the other is related to the details and symmetries of the Dzyaloshinskii-Moriya interaction (DMI) [111], which in turn can be determined by measuring its effect on the spin-wave properties [33, 176]. For example, in ferromagnets, the Dzyaloshinskii-Moriya interaction induces a chiral asymmetry on the spin-wave energies of opposite wavevector [31, 32], effectively shifting the minimum of the spin-wave dispersion curve out of the Brillouin zone center. We then say that the spin-wave spectrum is nonreciprocal [145, 148, 177–183]. In other words, this makes spin waves propagating in opposite directions to acquire different group velocity, energy, lifetime, etc. This phenomenon allows us to determine the DMI strength and its sign! However, it is not clear how these DMI-induced asymmetries manifest in systems more complex than ferromagnets, such as noncollinear magnetic structures and antiferromagnets.

In this chapter, we provide a complete picture of when and how the Dzyaloshinskii-Moriya interaction induces nonreciprocal spin waves in complex spin structures, and how they shall manifest in spin-resolved inelastic-electron-scattering experiments. We demonstrate an important connection between angular momentum and chiral handedness of a spin-wave mode, which allows us to predict the occurrence of a nonreciprocal spin-wave scattering spectrum. We show that only when a magnetic system has finite net magnetization, that is, when the sum of all magnetic moments is nonzero can it present a total nonreciprocal spin-wave spectrum. However, even zero-net-magnetization systems, such as collinear antiferromagnets and cycloidal spin spirals, can have modes that are individually nonreciprocal, while the total spectrum remains reciprocal. Furthermore, we demonstrate that excitation spectra obtained with inelastic electron scattering, such as spin-resolved/polarized electron-energy-loss spectroscopy (SREELS or SPEELS), can present asymmetric scattering rates due to the DMI when measured at opposite wavevector, which allows us to determine the DMI chirality that helps us then to answer our initial question.

9.1 Introduction

In the publication "More is different" from 1972, P. W. Anderson discusses the importance of symmetry breaking in nature [184]. Since then, we observe an ever-growing interest in the symmetries and symmetry-breaking of condensed-matter systems. An example is the Dzyaloshinskii-Moriya interaction itself, which has origin in the spin-orbit coupling combined with a breaking of inversion symmetry.

Some static and dynamical physical properties of magnetic materials can acquire the chirality of the Dzyaloshinskii-Moriya interaction, which is given by its vectorial direction. In a single atomic layer of manganese deposited on tungsten, for example, spin spirals of a unique rotational sense were observed using spin-polarized scanning tunneling microscopy, which was explained in terms of the DMI [185, 186]. It is also the chirality and symmetries of the DMI that determine whether a skyrmion or an antiskyrmion can be stabilized [111]. In conclusion, knowing the DMI is essential to understand many of the properties of some magnetic systems. However, one can not directly measure it, instead, we measure some DMI-dependent properties, which in turn allow us to obtain the DMI structure of a particular system. Therefore, it is crucial to discover better ways to experimentally access these interactions.

Udvardi and Szunyogh [31] and Costa *et al.* [32] showed that the spin-wave dispersion of ferromagnets acquires a chiral asymmetry under certain conditions due to the presence of Dzyaloshinskii-Moriya interaction. They realized that when the DMI vectors have a component along the sample's magnetization, the spin-wave dispersion becomes nonreciprocal with its energy minimum shifted out of the Γ–point, see Fig. 9.1.1. This means that the energies of counterpropagating spin waves with the same wavelength are no longer degenerate. In particular, if the magnetization lies in a mirror plane of the system, this nonreciprocity does not manifest on the spin-wave dispersion along the magnetization direction, because, following Moriya's rule, the DMI has to vanish in that case. These seminal papers have demonstrated a route to probe the DMI: From the measured asymmetry on the dispersion one can deduce the strength and chirality of the DMI by fitting the result to a Heisenberg model Hamiltonian. The chirality can be measured because it is related to the direction of the spin-wave dispersion shift. That has been successfully realized experimentally by Zakeri *et al.* in Ref. [33] when studying thin films of Fe/W(110). Similarly, nonreciprocity was observed in antiferromagnets, but only when subjected to an external magnetic field [148].

Spin waves in ferromagnets are characterized by having a well-defined angular momentum, which is antiparallel to the magnetization, effectively decreasing the total magnetization of the system, as discussed in Chapter 2. As we will demonstrate, the angular momentum of a spin wave in ferromagnets is associated with its handedness, a spatial chirality that defines the sign of the phase difference of precessing adjacent spin moments due to that spin wave. The handedness, for example, defines the direction where the dispersion shifts in response to a given set of Dzyaloshinskii-Moriya interactions. However, systems with strong DMI often generate noncollinear ground states [185, 186]. As we showed in Chapter 6, noncollinear magnetic structures in general host spin waves of different angular momenta, such as counter-rotating spin-wave modes of a spin spiral, and other modes can even have no angular momentum at all, which is the case of the longitudinal spin-wave modes

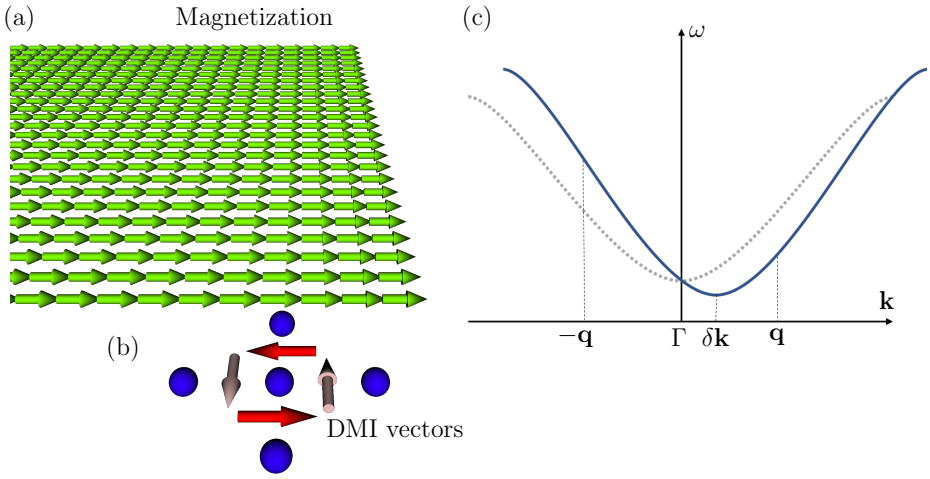

Figure 9.1.1: The shift of the spin-wave dispersion due to the DMI in ferromagnets. (a) In our convention, the magnetization direction of a ferromagnetic is given by the direction of the spins. (b) The Dzyaloshinskii-Moriya-interaction vectors lying in the plane. (c) The DMI components along the magnetization direction, shown in red in (c), induce an asymmetry of the spin-wave dispersion curve, which shifts sideways. Spin waves with opposite wavevectors, $\mathbf{q}$ and $-\mathbf{q}$, are no longer degenerate, such as in the absence of the DMI (indicated by the gray dotted line). Measuring the localization of the new energy minimum $\delta\mathbf{k}$ provides the chirality (spatial orientation) and magnitude of the DMI.

of a spin spiral. The same is true also for collinear magnets of zero total magnetization, such as antiferromagnets, which host two counter-rotational spin-wave modes whose degeneracy is broken by the DMI, see Chapter 7.

In the following, we show that even for these complex spin structures, the angular momentum can still be associated with the spin-wave handedness, which allows us to predict the effect of the DMI on the properties of a given spin-wave mode. Furthermore, we demonstrate that only systems of finite total magnetization can feature a nonreciprocal total spin-wave spectrum, e.g., when considering the spin-wave energies of all modes. Moreover, this nonreciprocity is observed on the reciprocal-space directions where the Fourier-transformed-DMI vector has a finite projection on the magnetization.

We demonstrate that in zero-net-magnetization systems, individual modes can be nonreciprocal, and these nonreciprocal modes usually come in pairs, each with opposite angular momentum. In such a pair, each mode has an opposite handedness leading to their dispersion shifting in opposite directions, all while keeping the total spin-wave spectrum reciprocal.

We also demonstrate that spin-resolved/polarized inelastic-electron/neutron-scattering experiments, such as spin-resolved/polarized energy-loss-spectroscopy (SREELS or SPEELS), can be used to reveal the DMI-induced nonreciprocity of individual spin-wave modes. The nonreciprocity in practice leads to an asymmetric scattering rate for opposite wavevectors, which only appears when the probing beam polariza-

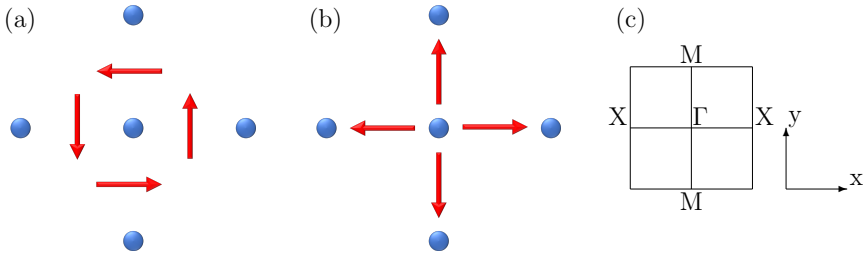

Figure 9.2.1: Model systems. The models consist of a square-lattice monolayer with nearest-neighbor interactions only. The exchange interaction is the same for both models, but (a) Model I has DMI vectors perpendicular to the bonds and swirling counterclockwise, while (b) Model II has DMI vectors diverging from the sites being parallel to the bonds. Model I has a cycloidal spin spiral as its ground state, while Model II realizes a helical spiral. c) Brillouin zone with its high-symmetry points and our choice of the frame of reference: The M–Γ–M path is along the $\hat{\mathbf{y}}$ and the X–Γ–X along the $\hat{\mathbf{x}}$.

tion, angular momentum, and Fourier-transformed-DMI vector align. Furthermore, we show that the angular momenta of the spin-wave modes are strongly related to the DMI, that is, they are given not only by the spin configuration, but they are also directly influenced by the DMI itself. Thus, SREELS and SPEELS measurements allow us to determine the chirality of the Dzyaloshinskii-Moriya interaction, which in turn helps to distinguish skyrmions from antiskyrmions in a lattice, for example.

9.2 Theoretical framework and model systems

The discussions throughout this chapter combine analytical and numerical results. We employ the generalized Heisenberg model introduced in Chapter 2, whose Hamiltonian reads

$$\mathcal{H} = -\frac{1}{2}\sum_{ij}\left(J_{ij}\mathbf{S}_i\cdot\mathbf{S}_j + \mathbf{D}_{ij}\cdot\mathbf{S}_i\times\mathbf{S}_j\right) - \sum_i \mathbf{B}\cdot\mathbf{S}_i \quad , \tag{9.1}$$

where J_{ij} is the magnetic exchange interaction parameter, and $\mathbf{D}_{ij}$ is the Dzyaloshiskii-Moriya interaction vector between sites i and j. A uniform external magnetic field is given by $\mathbf{B}$.

Also, we often calculate the SREELS spectra following the procedure discussed in Chapter 4 and 6, which are based on time-dependent perturbation theory in the adiabatic description for spin waves in noncollinear magnets.

We resort to two simple model systems, in order to demonstrate and exemplify our results and conclusions. Both models consist of a monolayer of a square-lattice crystal with only nearest-neighbor interactions and a lattice constant a. They share the same set of magnetic exchange interactions, but each features a different set of DMI vectors: Model I has the DMI vectors perpendicular to the bond connecting the corresponding sites, lying in the plane of the film and circulating counterclockwise, see Fig. 9.2.1 (a); Model II has the DMI vectors parallel to the bonds, also lying in-plane and having a given site i acting as a source of the $\mathbf{D}_{ij}$ vectors, see Fig. 9.2.1

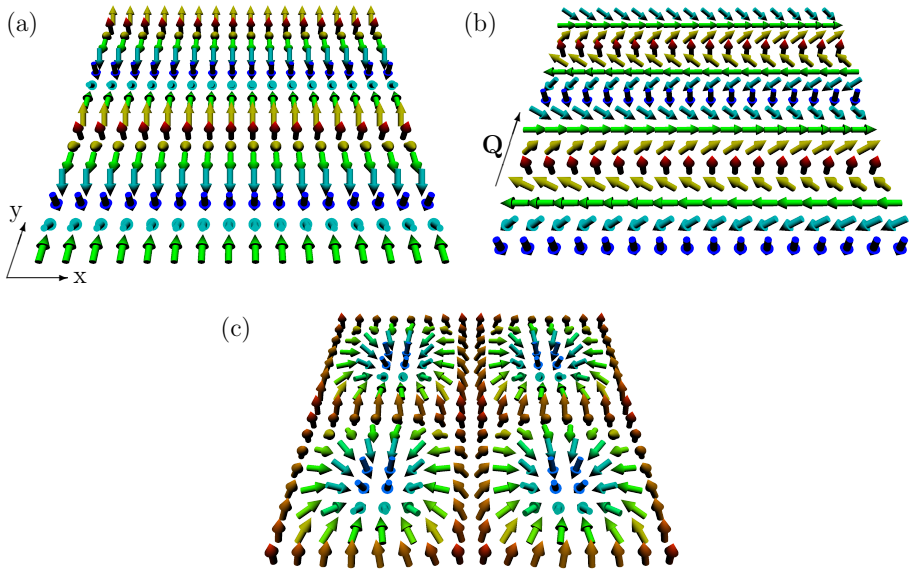

Figure 9.2.2: Spin configuration stabilized by the two models, which assume the MEI and DMI to be limited to the nearest neighbors and $J = D = 1$. (a) A cycloidal spin spiral being the ground state of Model I. (b) The helical spin spiral stabilized by Model II. Both spin spiral have the same wavevector $\mathbf{Q} = (2\pi/8)\hat{\mathbf{y}}$. (c) Skyrmion lattice obtained by adding an out-of-plane magnetic field to Model I.

(b). Figure 9.2.1 (c) shows the square-lattice Brillouin zone marking some of its high-symmetry points. For the simulation presented throughout the chapter, we took the parameters to be: $J = 1$, $D = 1$.

We extract the ground-state spin configuration for Model I and II using numerical spin-dynamics simulations by solving the Landau–Lifshitz–Gilbert equation with the *Spirit* code [47], see Sec. 2.2.3. Using a unit cell of 8×8 atoms, one obtains for Model I a cycloidal spin spiral, see Fig. 9.2.2 (a), and a helical spin spiral for Model II, Fig. 9.2.2 (b). In these figures, the wavevector $\mathbf{Q} = (2\pi/8)\hat{\mathbf{y}}$ of the spin spirals is along $\hat{\mathbf{y}}$, however, the spin spirals with wavevector along $\hat{\mathbf{x}}$ are also possible, which are degenerate to the ones we are showing. By adding an external magnetic field normal to the film in Model I, we can as well stabilize a skyrmion lattice as shown in Fig. 9.2.2 (c). In this case, the square arrangement of skyrmions is imposed by the choice of the unit cell. The direction of the net magnetization of any spin texture will be denoted by $\mathbf{n}^0$.

9.3 Results

Our understanding of how the Dzyaloshinskii-Moriya interaction affects the spin-wave dynamics and energetics in collinear and noncollinear magnetic systems can be summarized in five items:

(i) Nonreciprocal spin-wave spectrum only occurs, in the absence of an external magnetic field, for systems of finite magnetization and when $\mathbf{n}^0 \cdot \mathbf{D}(\mathbf{k}) \neq 0$, i.e., if the projection of the Fourier-transformed DMI on the magnetization direction is finite.

(ii) The angular momentum of a spin-wave mode can be regarded as the handedness attribute, which defines the direction towards which the dispersion of the given mode shifts out of the Γ–point due to the DMI.

(iii) Systems of zero net magnetization can host spin-wave modes individually nonreciprocal induced by the DMI, while the total spin-wave spectrum remains reciprocal. An external magnetic field can induce nonreciprocity.

(iv) Polarized inelastic-scattering experiments can be used to unveil the DMI-induced nonreciprocity, and thus allowing to measure the DMI orientation. A nonreciprocal spectrum only occurs for spin-flip scattering processes due to spin-wave modes whose angular momentum aligns with the polarization of the probing particles and $\mathbf{D}(\mathbf{k})$.

(v) All spin textures that are favored by the DMI have nonreciprocal spin-wave modes with angular momentum aligned to the component of $\mathbf{D}(\mathbf{k})$ that contributes to the DMI energy gain.

We the following, we discuss and demonstrate these five items.

9.3.(i) Nonreciprocal spin-wave spectrum

Nonreciprocal (energetically asymmetric) spin-wave spectrum only occurs, in the absence of an external magnetic field, for systems of finite magnetization. Such a spectrum manifests in the reciprocal-space directions along which a component of $\mathbf{D}(\mathbf{k})$ aligns with the net magnetization.

The first statement is related to the breaking of time-reversal symmetry. If a system is invariant under time reversal operator Θ, then $\Theta H(\mathbf{k})\Theta^{-1} = H(-\mathbf{k})$, and the reciprocity of the system is guaranteed. In fact, if the net magnetization is zero, but via some other means the time-reversal is broken, the spin-wave dispersion could be nonreciprocal too. Systems of zero net magnetization, such as antiferromagnets and cycloidal spin spirals, are not invariant under time reversal, nor under partial translation $T_{\lambda/2}$ (λ is the wavelength of the spin spiral), individually. However, they are invariant under a combined operation of time reversal plus partial translation $\mathcal{S} = \Theta T_{\lambda/2}$, which leads to $\mathcal{S}_{\mathbf{k}} H(\mathbf{k}) \mathcal{S}_{\mathbf{k}}^{-1} = H(-\mathbf{k})$ [187]. If the system has a finite net magnetization, it is not possible to find such a combined operation that leaves the Hamiltonian invariant.

We can prove the second statement, following Ref. [31], considering a static snapshot of a spin wave in a ferromagnet, given by

$$\mathbf{S}_i = \cos\phi_i \sin\theta \mathbf{n}^1 + c \sin\phi_i \sin\theta \mathbf{n}^2 + \cos\theta \mathbf{n}^0 \quad , \tag{9.2}$$

where $\mathbf{n}_0$ is a unitarian vector along the magnetization, which forms an orthonormal basis together with $\mathbf{n}^1$ and $\mathbf{n}^2$, see Fig. 9.3.1. θ corresponds to a small deviation

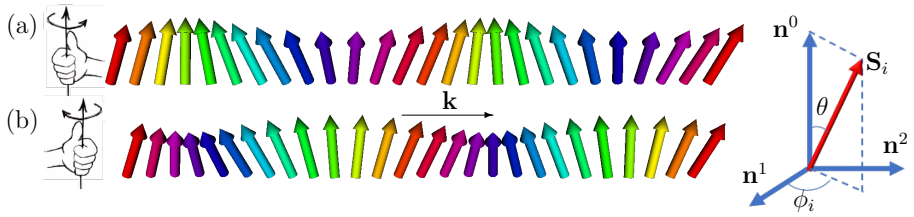

Figure 9.3.1: Time snapshot of the spin wave of a ferromagnet for a given wavevector $\mathbf{k}$ as given by Eq. (9.2). (a) For $c = +1$, the spin wave has a right-handed chirality. (b) For $c = -1$, it has a left-handed chirality. The magnetization direction is given by $\mathbf{n}^0$. During the precession due to the spin wave, all spins deviate from $\mathbf{n}^0$ by a fixed angle θ. The phase of precession of the i–th spin is given by $\phi_i = \mathbf{k} \cdot \mathbf{R}_i$, where $\mathbf{R}_i$ is the spin position, and it is used to color code the spins.

from the magnetization direction $\mathbf{n}^0$, while $\phi_i = \mathbf{k} \cdot \mathbf{R}_i$ corresponds to a transversal rotation of the spin moments with rotational sense (chirality) given by $c = \pm 1$. Placing this expression into Eq.(9.1), we obtain that the only chirality-dependent term is given by

$$E(\mathbf{k}, c) \propto c\ \mathbf{n}^0 \cdot \mathbf{D}(\mathbf{k}) \quad , \tag{9.3}$$

where $\mathbf{D}(\mathbf{k})$ is the lattice Fourier transform of the Dzyaloshinskii-Moriya vectors. For details on how to obtain the above equation, see Appendix 9.A.1.

For Model I, where the ferromagnetic state can be stabilized by an external magnetic field, the chiral asymmetry will only manifest when the magnetization is in-plane. The Fourier transformation of the DMI interaction gives $\mathbf{D}(\mathbf{k}) = 2D \begin{pmatrix} -\sin(ak^y) \\ \sin(ak^x) \end{pmatrix}$, and therefore, the asymmetry occurs most strongly for spin waves propagating perpendicularly to the magnetization, and mostly vanishes when parallel to it, see Fig. 9.3.2 (a). For Model II, however, $\mathbf{D}(\mathbf{k}) = 2D \begin{pmatrix} \sin(ak^x) \\ \sin(ak^y) \end{pmatrix}$ and the asymmetry is stronger mostly for wavevectors parallel to the magnetization, see Fig. 9.3.2 (b).

9.3.(ii) Spin-wave angular momentum and spin-wave handedness

Now we need to establish an important relation between spin-wave chirality, handedness and angular momentum. In the previous section, our *ansatz* of spin waves considers two possible spin-wave chiralities. In the following, we demonstrate that only one of them is a solution to the coupled equation of motions that govern the dynamics. Besides that, we define a spin-wave handedness, which is a chiral invariant for the spin waves whose sign is related to the direction of the spin-wave dispersion shift in the reciprocal space. And finally, we show that there is a one-to-one relation between the spin-wave handedness and the angular momentum. That relation is fundamental in providing an easy and comprehensive way to predict chiral asymmetry in spin-wave dynamics induced by DMI.

Thus far, we know that the spin-wave dispersion curve of a ferromagnet can

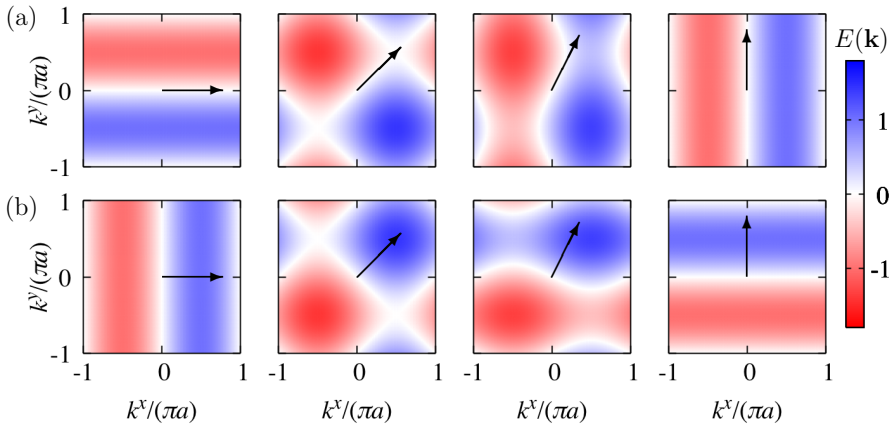

Figure 9.3.2: Chirality dependent spin-wave energy landscape throughout the Brillouin zone, obtained from Eq. (9.3). The (a) row corresponds to the energy landscape for Model I and row (b) for Model II. Each column corresponds to a different in-plane magnetization direction, which is represented by the black arrows.

be shifted out of the Γ–point due to the influence of the Dzyaloshinskii-Moriya interactions. This shift was measured in the electron scattering experiments of Zakeri *et al.* [33], and it occurs towards a very well-defined direction for a fixed direction of the magnetization (given that the DMI is a constant of the material). From this fact, we can infer that spin waves in a ferromagnet have a given handedness that defines how the spin-wave energies respond to the DMI, for example, setting the direction of the dispersion shift. Can a ferromagnet of fixed magnetization host spin waves of opposite handedness, such that their dispersion curves would shift to the opposite directions? A hint comes from the fact that spin waves in a ferromagnetic system always possess angular momenta along the same direction (antiparallel to the magnetization).

With the previous question in mind, we will review the motion of the spin moments of a ferromagnet when hosting a spin wave. We consider classical spin moments represented by vectors and the phenomenological Landau-Lifshitz equation, Eq. (2.80), which describes the time evolution of every spin moment:

$$\frac{\mathrm{d}\mathbf{S}_i(t)}{\mathrm{d}t} = -\gamma \mathbf{S}_i(t) \times \mathbf{B}_i^{\mathrm{eff}}(t) \quad . \tag{9.4}$$

The effective field is given by

$$\mathbf{B}_i^{\mathrm{eff}}(t) = -\frac{\partial H}{\partial \mathbf{S}_i} = \sum_j \left(J_{ij}\mathbf{S}_j + \mathbf{S}_j \times \mathbf{D}_{ij} \right) \quad , \tag{9.5}$$

where we considered the Hamiltonian of Eq. (9.1). We have one equation of motion for each magnetic atom of our material, and these equations are coupled because the effective field in each site depends on the dynamics of the neighboring site to which they couple to via the magnetic interactions.

To solve this problem, one can start by assuming that the precession is of small amplitude around its equilibrium direction that corresponds to the magnetization for ferromagnets. We have solved this problem in great detail in Apx. 9.A.1 in linear approximation. Taking the magnetization direction along $\hat{\mathbf{z}}$, the time evolution of the spin at site i reads

$$\mathbf{S}_i(\mathbf{k},t) = \frac{1}{\sqrt{N}}\big(\cos(-\mathbf{k}\cdot\mathbf{R}_i+\omega_{\mathbf{k}}t)\hat{\mathbf{x}}+\sin(-\mathbf{k}\cdot\mathbf{R}_i+\omega_{\mathbf{k}}t)\hat{\mathbf{y}}\big)+S\hat{\mathbf{z}} \quad , \tag{9.6}$$

which corresponds to a spin wave of wavevector $\mathbf{k}$ and frequency $\omega_{\mathbf{k}}$. Considering that our system has $D^z(\mathbf{k}) = 0$, we have that $\omega_{\mathbf{k}} \geq 0$ and thus every spin has a counterclockwise precession around the magnetization. In the ferromagnetic ground state, all the spins are aligned, and so the total angular momentum of the system is maximal along $\hat{\mathbf{z}}$ (the magnetization direction). With a spin wave, as the spins are precessing, the total angular momentum is reduced, which means that the spin-wave angular momentum is antiparallel to $\hat{\mathbf{z}}$.

The DMI favors certain cantings between spin moments. Let us then define a spin-wave chirality based on the canting between adjacent spins as the sign of the cross product between their projections onto the magnetization direction, and integrated over a full revolution of the precessional motion:

$$c_{12}(\mathbf{k}) = \operatorname{sgn}\left(\int_0^\tau \hat{\mathbf{z}}\cdot\big[\mathbf{S}_1(\mathbf{k},t)\times\mathbf{S}_2(\mathbf{k},t)\big]\mathrm{d}t\right) = -\operatorname{sgn}\left(\sin(a\mathbf{k}\cdot\hat{\mathbf{r}}_{12})\right) \quad , \tag{9.7}$$

where a is the lattice constant and $\hat{\mathbf{r}}_{12}$ is a unitarian vector along the vector that connects site 1 and 2 [1], and $\tau = 2\pi/\omega_{\mathbf{k}}$ is the precession period. This equation tells us that the chirality changes periodically as a function of $\mathbf{k}$, and it is zero for $\mathbf{k}\cdot\hat{\mathbf{r}}_{12} = n\pi/a$ or $\mathbf{k}\perp\mathbf{r}_{12}$. Let us take two wavevectors close to the Γ–point, one parallel and another antiparallel to $\hat{\mathbf{r}}_{12}$, snapshots of the correspondent spin waves are shown in Figs. 9.3.3 (a) and (b), respectively. As the DMI favors one of the two chiralities, one of the spin-wave energies is lowered while the other is raised, effectively shifting the energy minimum of the spin-wave dispersion curve out of the Γ–point in the direction of $\mathbf{k}$ that provides the favorable chirality.

Next, let us define a more general chirality invariant that does not vary with the wavevector, which we will call the spin-wave handedness:

$$\mathcal{C}_{12} = \frac{c_{12}(\mathbf{k})}{\operatorname{sgn}(\mathbf{k}\cdot\hat{\mathbf{r}}_{12})} \quad . \tag{9.8}$$

For the spin-wave solution given by Eq. (9.6), we get $\mathcal{C}_{12} = -1$. The direction towards which the spin-wave dispersion shifts couples to the spin-wave handedness. If the handedness were to be $+1$, instead, the shift would have been in the opposite direction. That is the case if the spin wave were to be given by

$$\mathbf{S}_i(\mathbf{k},t) = \frac{1}{\sqrt{N}}\big(\cos(\mathbf{k}\cdot\mathbf{R}_i-\omega_{\mathbf{k}}t)\hat{\mathbf{x}}+\sin(\mathbf{k}\cdot\mathbf{R}_i-\omega_{\mathbf{k}}t)\hat{\mathbf{y}}\big)-S\hat{\mathbf{z}} \quad , \tag{9.9}$$

which corresponds to a clockwise rotation and an angular momentum parallel to $\hat{\mathbf{z}}$. Then, we would have $\mathcal{C}_{12} = +1$. That is, a change of handedness comes together

[1] Naturally, this definition depends on the choice of the spin pair. It is important to choose a pair such that $D^z(\mathbf{k})$ does not vanish for $\mathbf{k}\parallel\hat{\mathbf{r}}_{12}$.

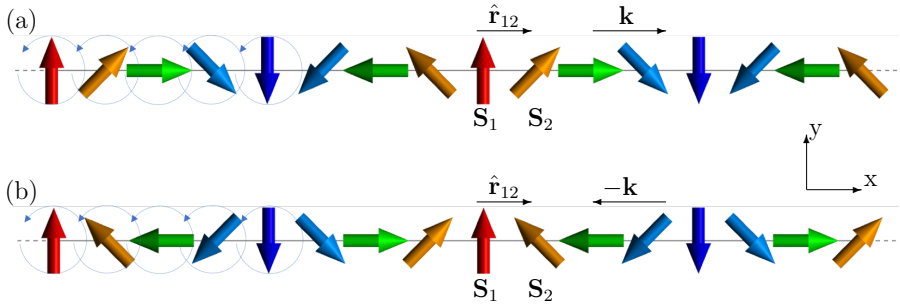

Figure 9.3.3: Spin wave chirality. In our *ansatz*, S^z is a constant of motion, therefore we represent here only the transversal components, S^x and S^y, which change over time. The open circles indicate the precession sense which is fixed by the equation of motion. The precession phase is given by $\mathbf{k}\cdot\mathbf{R}_i$. With a spin wave, the system has two inequivalent configurations: (a) one if the wavevector is parallel to $\hat{\mathbf{r}}_{12}$ yielding a left-handed spin wave $c_{12} = -1$ (the tilt direction is given by left-hand thumb rule); (b) another if the wavevector is antiparallel to $\hat{\mathbf{r}}_{12}$, which results in a right-handed spin wave $c_{12} = +1$ (the tilt direction is given by right-hand thumb rule).

with an inversion of the angular momentum, and the dispersion shift due to DMI will occur in the opposite direction of that for spin waves with handedness $\mathcal{C}_{12} = -1$. By the way, this second solution corresponds in fact to the spin waves for a ferromagnet with the magnetization along $-\hat{\mathbf{z}}$. This momentum-handedness coupling is imposed by the equation of motion that accepts only wave-like solutions.

As we will demonstrate in the following, this linking between angular momentum and handedness also holds for noncollinear magnetic systems, where the spatial chirality can be rather difficult to track. Nevertheless, often these systems have excitations of very well-defined angular momentum, which will then allow us to infer their handedness and thus their response to the DMI. This result is very powerful in allowing us to predict the effect of the DMI on the spin-wave energy and vice-versa, as we demonstrate next.

9.3.(iii) External magnetic field and zero-net-magnetization systems

Previously, we saw that only systems with finite net magnetization can produce a nonreciprocal spin-wave spectrum due to DMI. Something analogous to that also happens for systems of zero net magnetization: The Dzyaloshinskii-Moriya interaction can induce chiral asymmetries in those systems too. However, it can now only break chirality degeneracy between rotational spin-wave modes, i.e., with angular momenta, but leaving the total spectrum reciprocally symmetric in the absence of an external magnetic field.

Let us then consider an antiferromagnet, and that the $\mathbf{D}(\mathbf{k})$ aligns with the axis of the magnetic moments of the systems. We can regard the antiferromagnet as a superposition of two ferromagnetic sublattices of opposite magnetization. In ferromagnets, flipping the entire magnetization makes the DMI-induced asymmetry to reverse in the reciprocal space [33]. Thus, the spin wave hosted by each of

the antiferromagnet sublattices is shifted in opposite directions, which effectively leaves the total spectrum of the system reciprocally symmetric. The system becomes nonreciprocal once again under the **action of an external magnetic field** parallel to the alignment axis of the magnetic moments, see Chapter 7 [Antiferromagnets] and Ref. [148, 180]. And here we have the first means through which one can reveal the asymmetry induced by DMI in systems of zero net magnetization.

9.3.(iv) Role of spin-polarized/resolved inelastic scattering

Now we know that DMI can induce hidden chiral asymmetry in the spin-wave spectrum in a system of zero net magnetization and that an external magnetic field can be used to reveal that. We proceed by demonstrating that in the absence of an external magnetic field, we still can identify these asymmetries utilizing spin-polarized/resolved scattering experiments.

Often, zero-magnetization systems, such as spin spirals and antiferromagnets, host spin waves that come in pairs, where the counter-partner has opposite angular momentum, and therefore, opposite handedness, e.g., two rotational modes of opposite angular momentum. In the absence of DMI, these modes are degenerated and reciprocally symmetric, which would be the case of the two modes in an antiferromagnet. But, as we have seen in the previous subsection, this degeneracy can be lifted by the DMI, leaving each mode nonreciprocal while the total spectrum remains reciprocal. As we have also seen, an external magnetic field couples differently to each mode, energetically favoring one and disfavoring the other, which generates an overall nonreciprocal spectrum.

An alternative way to couple with the angular momentum of the spin waves is by means of a spin-resolved scattering experiment, as demonstrated in Chapter 6 (SREELS). In the example of an antiferromagnet, this would allow us to measure each mode separately by aligning the polarization of the probing particles to the precession axis of one of the spin-wave modes, and measuring only the spin-flip channel. Similarly, the same perfect mode selection can be achieved for spin-spiral systems, see Chapter 6. This makes of spin-polarized/resolved inelastic scattering a second means through which one can reveal the DMI-induced nonreciprocity on the spin-wave spectrum.

Next, we conjecture the conditions that rule the occurrence or not of nonreciprocal spin-wave spectrum in inelastic-scattering experiments:

a) **Nonreciprocal spectrum only occurs for spin-wave modes of finite angular momentum:**

This is a generalization of the requirement that a system needs a finite magnetization to feature a total nonreciprocal spin-wave spectrum induced by DMI in item (i). However, this general rule allows us to apply it also for zero-net-magnetization systems. As we have seen, angular momentum translates into the chiral handedness of the spin wave. Without angular momentum, a spin wave is nonchiral and cannot manifest nonreciprocity due to DMI.

b) **Only spin-flip channels may present a nonreciprocal spectrum:**

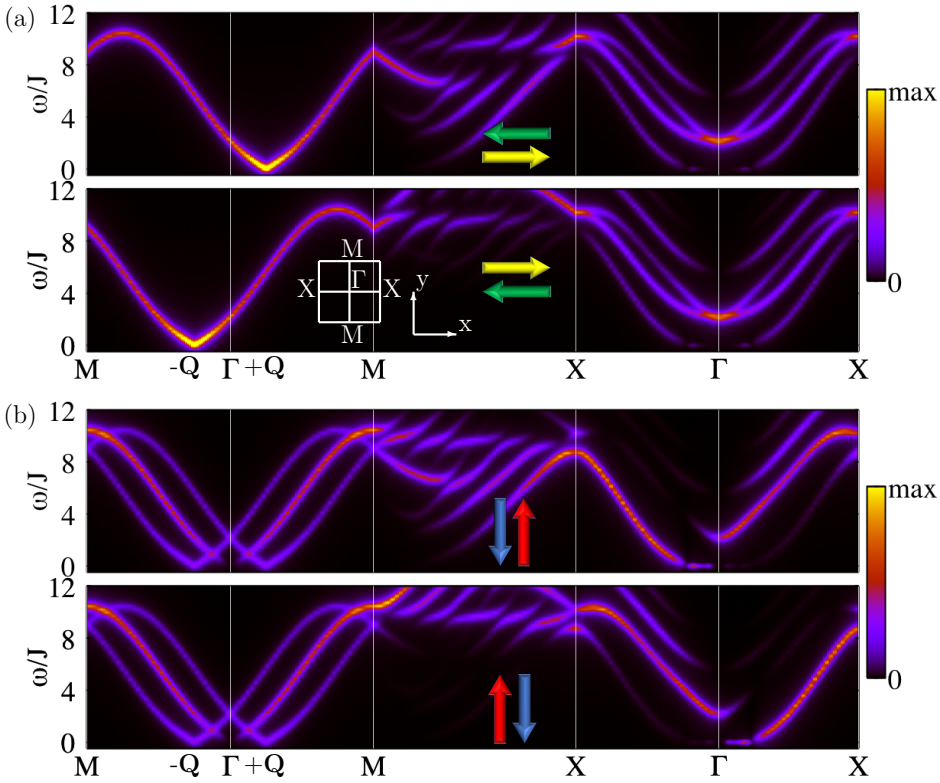

Figure 9.3.4: Spin-resolved inelastic-scattering spectra for the spin spiral generated by Model I. (a) Shows the two spin-flip channels for polarization along $\hat{\mathbf{x}}$, as indicated by the horizontal arrows. Nonreciprocity occurs in the reciprocal space where a component of $\mathbf{D}(\mathbf{k})$, polarization and angular momentum align with each other. For Model I on path M–Γ–M, $\mathbf{D}(\mathbf{k})$ and the angular momentum of the spin-wave modes with minima at $\mathbf{k} = \pm\mathbf{Q}$ are parallel to $\hat{\mathbf{x}}$. (b) Shows the case for the polarization along $\hat{\mathbf{y}}$, indicated by the vertical arrows. Thus, nonreciprocity is only seen in the X–Γ–X, when $\mathbf{D}(\mathbf{k}) \parallel \hat{\mathbf{y}}$ that couples to the angular momentum of those spin waves.

This is a direct consequence of item (iv - a). If only modes of finite angular momenta can be nonreciprocal, and usually these modes are paired to modes of opposite angular momenta, only a spin-flip channel has the capability of measuring one disregarding the other.

c) **Only the component D(k) parallel to the spin-wave angular momentum can influence its nonreciprocal spectrum.**

d) **Only a scattering experiment with the polarization of the probing particles aligned along the spin-wave angular momentum can reveal the nonreciprocity of this mode.**

Next, we demonstrate and exemplify items c) and d). Let us demonstrate that by calculating the spin-resolved spectrum for the spin spirals that results from Models I

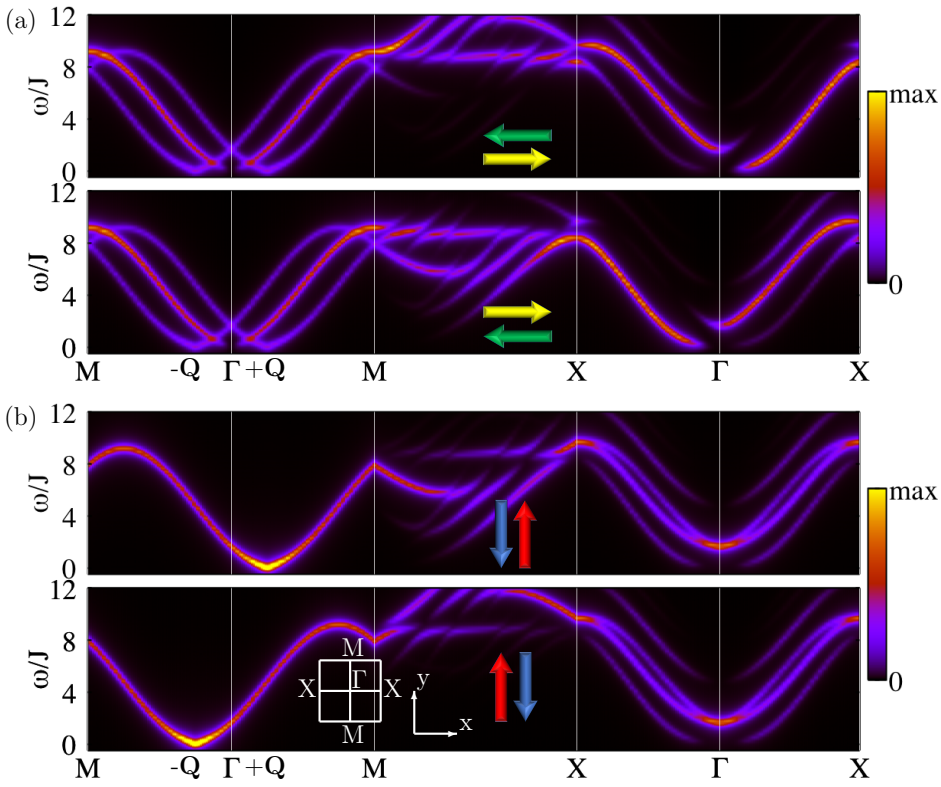

Figure 9.3.5: Spin-resolved inelastic-scattering spectra for the spin spiral generated by Model II. (a) Shows the two spin-flip channels for polarization along $\hat{\mathbf{x}}$, as indicated by the horizontal arrows. Nonreciprocity occurs in the reciprocal space where a component of $\mathbf{D}(\mathbf{k})$, polarization and angular momentum align with each other. For Model II on path X–Γ–X, $\mathbf{D}(\mathbf{k})$ and the angular momentum of some spin-wave modes are parallel to $\hat{\mathbf{x}}$. (b) Shows the case for the polarization along $\hat{\mathbf{y}}$, indicated by the vertical arrows. Thus, nonreciprocity is only seen in the M–Γ–M, when $\mathbf{D}(\mathbf{k}) \parallel \hat{\mathbf{y}}$ that couples to the angular momentum of the spin-wave modes whose energy minima are at $\mathbf{k} = \pm\mathbf{Q}$

and II, see Sec. 9.2, with $\mathbf{Q} \parallel \hat{\mathbf{y}}$, shown respectively in Figs. 9.3.4 and 9.3.5. Model I stabilizes a cycloidal spiral whose spins lay in the y–z plane, see Fig. 9.2.2 (a), while Model II leads to a helical spiral with spins lying in the x–z plane, see Fig. 9.2.2 (b).

Figure 9.3.4 (a) shows the spin-flip channels for polarization along $\hat{\mathbf{x}}$ (represented by horizontal arrows), which present a nonreciprocal spectrum in the M–Γ–M path, i.e., in a reciprocal-space direction perpendicular to the polarization. For Model I, $\mathbf{D}(\mathbf{k}) = -2D\sin(ak^y)\hat{\mathbf{x}}$ on this path, and therefore, it is parallel to the polarization and to the angular momentum of the spin-wave modes whose energy minima are at $\mathbf{k} = \pm\mathbf{Q}$. For Fig. 9.3.4 (b), the polarization is set along $\hat{\mathbf{y}}$ (represented by vertical arrows), and nonreciprocity is only seen for the X–Γ–X path, again because on this path $\mathbf{D}(\mathbf{k}) = 2D\sin(ak^x)\hat{\mathbf{y}}$ is parallel to the polarization and the angular momentum of some spin-wave modes. Naturally, a polarization along z will not

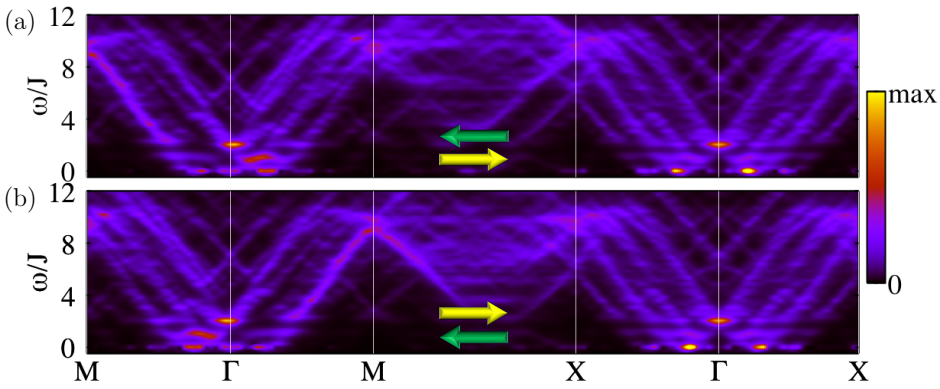

Figure 9.3.6: Spin-resolved inelastic-scattering spectra for a skyrmion lattice generated by Model I added with an out-of-plane external magnetic field. Panel (a) represents the left-right spin-flip channel, and (b) shows the right-left one, as indicated by the horizontal arrows. The polarization is along $\hat{\mathbf{x}}$. The spectra resemble a continuum of excitations rather than well-defined dispersing lines. Nevertheless, the nonreciprocities are visible, and their occurrence conditions match those for the spin spiral established for the same DMI model in the absence of the external field, see also Fig. 9.3.4 (a).

feature any nonreciprocity, because the DMI model has no component along that direction.

For Model II, the Fourier transformed DMI vector on path M–Γ–M is $\mathbf{D}(\mathbf{k}) = 2D\sin(ak^y)\hat{\mathbf{y}}$, and along X–Γ–X it is $\mathbf{D}(\mathbf{k}) = 2D\sin(ak^x)\hat{\mathbf{x}}$. Thus, in contrast to Model I, we will observe the nonreciprocity on the reciprocal-space direction parallel to the polarization, see Fig. 9.3.5 (a) and (b), where the polarization is along $\hat{\mathbf{x}}$ and $\hat{\mathbf{y}}$, respectively. In both Models, the spin-spiral wavevector points along the same direction, but the direction where the nonreciprocity occurs changes from one model to the other, which shows that the direction of the spiral wavevector has no role on the nonreciprocity.

For more complex systems with lower symmetries, such as skyrmion lattices, the spectrum of each spin wave mode is not well-defined throughout the reciprocal space in inelastic-scattering experiments. The spectra are closer to a continuum of excitations instead of the well-separated branches seen for the spin-spiral configurations, see Fig. 9.3.6, whereupon adding an out-of-plane external magnetic field to Model I could stabilize a skyrmion lattice in an 8×8 atoms unit cell, see also Fig. 9.2.2 (c). Naturally, it is also hard to identify the direction of the angular momentum of the underlying spin wave corresponding to each high-intensity region of the spectrum. Nevertheless, the nonreciprocity is still present and measurable. In Fig. 9.3.6, we observe a nonreciprocity on the same path, M–Γ–M, as seen for the spin spiral established in the absence of the external magnetic field, see Fig. 9.3.4 (a), for the same polarization along $\hat{\mathbf{x}}$. Even though the two systems look rather different from each other, the reciprocity on their spectra occurs under the same condition because they share the same DMI structure.

As we have demonstrated, only spin-flip channels can present a nonreciprocal spectrum. However, not always a spin-resolved inelastic-scattering experiment is available, as is currently the case of electron scattering setup to study spin waves.

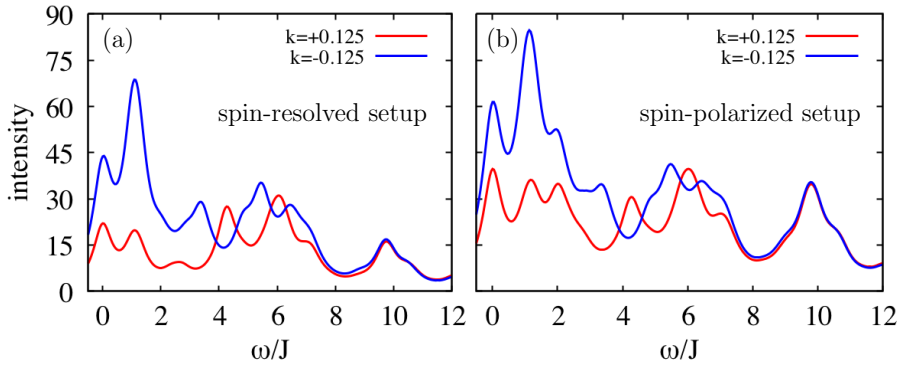

Figure 9.3.7: Constant-wavevector inelastic-scattering spectra for a skyrmion lattice generated by Model I added with an out-of-plane external magnetic field. The spectra were calculated for two opposite wavevector $\mathbf{k} = \pm 2\pi k\hat{\mathbf{y}}$. The polarization is along $\hat{\mathbf{x}}$. (a) shows the spin-resolved setup, where only one spin-flip channel is taken (left-right scattering channel). (b) presents the spin-polarized setup, which results from adding a spin-flip and a non-spin-flip (left-right + left-left scattering channels). In both cases, we can observe that the inelastic signal at $-\mathbf{k}$ is higher than at $\mathbf{k}$, therefore, it is nonreciprocal. The multiple peaks correspond to the various spin-wave modes of the skyrmion lattice, in contrast to the expected single peak for a ferromagnetic phase and the three modes of a spin spiral.

A more easily accessible experiment is the spin-polarized setups, where a source of spin-polarized projectiles is used to scatter from the magnetic material and the spin of the scattered projectile is disregarded. The resulting spectrum is equivalent to the addition of a spin-flip and a non-spin-slip channel, e.g., down-up plus down-down. While the latter cannot be nonreciprocal, the first can and so is their sum.

Figure 9.3.7 represents constant wave-vector spectra, which are the typical measurements done in inelastic electron and neutron scattering experiments. The wavevector of the spin excitations are fixed by controlling the ratio between the incident and scattering angles, and the intensity corresponds to the number of probing particles that have transferred a given amount of energy to the excitations in an interval of time. We calculated the spectra for wavevectors opposite to each other in the reciprocal space, $\mathbf{k} = \pm 2\pi k\hat{\mathbf{y}}$, and the polarization was set along the $\hat{\mathbf{x}}$ direction, which aligns with $\mathbf{D}(\mathbf{k})$. Figure 9.3.7 (a) shows the results for a spin-resolved setup (which corresponds to a vertical line of the spectrum shown in Fig. 9.3.6 (a)), while Fig. 9.3.7 (b) presents the spin-polarized spectrum. In the low-energy region, we clearly observe for both setups, spin-resolved or spin-polarized, a difference in the scattering intensity. For higher energies, some peaks vanish and others appear when comparing the spectra for the two opposite wavevectors.

It is the DMI directional sense that determines which scattering intensity will be bigger, at $+\mathbf{k}$ or $-\mathbf{k}$. Upon reversing the DMI, the spectra would be swapped in Fig. 9.3.7. This implies that such an experiment measures the DMI sense.

Let us take Model I with an out-of-plane magnetic field which stabilized a skyrmion lattice, and now reverse the chirality of the DMI along one direction only, making $D^x \to -D^x$. This modified model then stabilizes an antiskyrmion lattice.

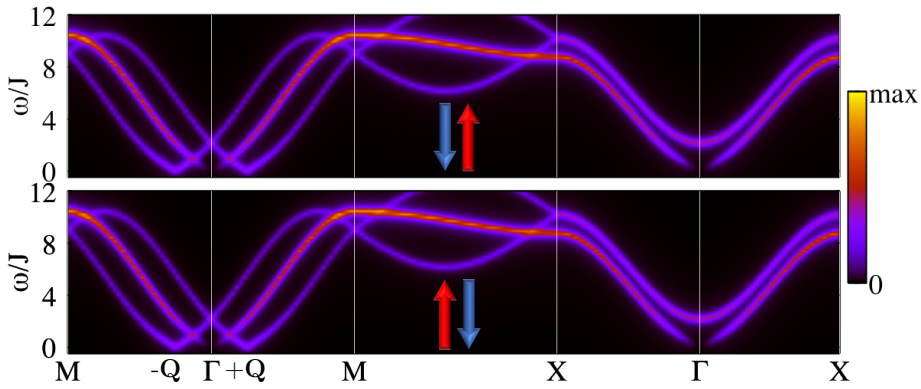

Figure 9.3.8: Spin-resolved inelastic-scattering spectra for the spin spiral generated by Model I with $D^y = 0$. Note that the spiral itself is stabilized by D_x. The polarization is set along $\hat{\mathbf{y}}$, as indicated by the vertical arrows. The two spin-flip channels are degenerate and reciprocal because $\mathbf{D}(\mathbf{k})$ has no component along the polarization to induce angular momentum of the spin-wave modes along that direction. Restoring the D^y of the original Model I, a nonreciprocity occurs on the X–Γ–X while the ground-state spin configuration is not affected, proving that the DMI can directly induce the nonreciprocity of spin waves.

Because the skyrmion and antiskyrmion systems translate into the other only by a mirror reflection operation, their total spin-wave spectra, which are reciprocal, do not differ. However, as we have shown, the scattering rate can depend directly on the DMI orientation, and we should be able in this case to identify it.

9.3.(v) Dzyaloshinskii-Moriya interaction and spin-wave angular momentum

We saw that the nonreciprocity is seen when the probing-beam polarization, the $\mathbf{D}(\mathbf{k})$, and the spin wave's angular momentum align. It is easy to see that the polarization couples to the angular momentum, however, how does the angular momentum couple to the DMI? Is the angular momentum, which is the property that allows the nonreciprocal inelastic measurement, given by the spin structure or by the Dzyaloshinskii-Moriya interactions? The answer is that both, spin configuration and the DMI set the angular momentum of the spin waves.

Let us consider Model I with D^y set to zero. The same cycloidal spin spiral with $\mathbf{Q} \parallel \hat{\mathbf{y}}$ is still the ground state. Previously, we have seen on Fig. 9.3.4 (b) that spin-resolved inelastic-scattering spectra for polarization along $\hat{\mathbf{y}}$ featured nonreciprocity in the X–Γ–X path because there $\mathbf{D}(\mathbf{k})$ was parallel to $\hat{\mathbf{y}}$. Now, once $\mathbf{D}(\mathbf{k}) = 0$ on that same path, the spectrum becomes reciprocal, see Fig. 9.3.8. This proves that the nonreciprocity is not only induced by the spin structure but also directly by the DMI. Similarly, one observes that a spin spiral stabilized by exchange interaction frustration, without involving DMI, can also feature nonreciprocity as if the DMI that could favor that structure were there.

We have seen that the DMI only influences the dispersion and the inelastic spectra of spin-wave modes whose angular momenta have a finite projection on $\mathbf{D}(\mathbf{k})$. An antiferromagnet hosts two counter-rotating spin-wave modes that precess in the

plane perpendicular to the axis of the magnetic moments. That is why we discussed in item (iii) an example where $\mathbf{D}(\mathbf{k})$ is parallel to this axis, which guarantees that the DMI would maximally influence the spin-wave modes. However, for a general noncollinear magnetic structure, the angular momenta of the spin waves are not obvious, and thus, only knowing the DMI structure will not be enough to predict the occurrence of the asymmetries. Our observations have shown, however, that spin structures that are energetically favored by a given component of $\mathbf{D}(\mathbf{k})$ will host spin waves whose angular momenta are along this same DMI component, i.e., they will also induce nonreciprocity to the system. We can exemplify this by taking the Models I and II again, and the spin spirals that each one favors as the ground state. For Model I, the cycloidal spiral with spins lying in the $y-z$ plane is stabilized by D^x, and so the angular momenta of the $+\mathbf{Q}$ and $-\mathbf{Q}$ modes are along $\hat{\mathbf{x}}$. Meanwhile, the helical spiral of Model II is stabilized by D^y, and its $\pm\mathbf{Q}$ modes have angular momenta along $\hat{\mathbf{y}}$.

9.4 Conclusions

In this chapter, we contributed to the problem of mapping the Dzyaloshinskii-Moriya interaction in systems of complex magnetic structures. We did that by studying the effect of the DMI on the dynamics of spin waves. We made an important connection between the angular momentum and the chiral handedness of a spin-wave mode. Effectively, this allows us to predict when a given spin-wave mode energy and scattering rate is affected by the DMI.

We saw that the DMI can induce nonreciprocity in the spin waves. We concluded that only systems of finite magnetization can have a total spin-wave spectrum that is nonreciprocal. Nevertheless, nonreciprocity can also occur for individual spin-wave modes in systems with zero-net-magnetization and noncollinear spin textures, while the total spectrum remains reciprocal.

We showed that an external magnetic field and spin-resolved energy loss spectroscopy (SREELS) proposed in Chapter 6, can help to reveal the nonreciprocity of individual modes. We saw that only spin-flip scattering spectrum can present nonreciprocity, and that a nonreciprocal spectrum is expected when a component of $\mathbf{D}(\mathbf{k})$ is parallel to the angular momentum and the polarization of the probing electrons. As we can control the polarization of the probe beam, and the spin-resolved measurements can also determine the angular momentum of the spin waves, ultimately we can determine the DMI chirality even for zero-net-magnetization systems. This achievement is in contrast to previous expectations found on the literature [188], where other authors resorted to controlling the phase and amplitude of the probing beam to be able to determine the DMI chirality.

For the case of a skyrmion lattice, despite having a finite net magnetization out-of-plane, no component of the DMI projects along that net magnetization (which is in-plane), guaranteeing that the total spin-wave spectrum is reciprocal. Nevertheless, the scattering rate still can have nonreciprocity induced by the DMI. This allowed us to detect a change in the chirality of the DMI along different directions, which permits us, for instance, to infer the existence of antiskyrmions instead of skyrmions [111].

Finally, we learned that the Dzyaloshinskii-Moriya interaction can influence the

angular momentum of the spin waves directly and indirectly. In general, the DMI favors the formation of spin structures that naturally hosts spin waves whose precession axis aligns with the DMI. That is, the spin-wave angular momenta tend to be along $\mathbf{D}(\mathbf{k})$ that favored the spin configuration in the first place. However, even those components of $\mathbf{D}(\mathbf{k})$ that do not contribute to the energy of the ground state can directly influence the dynamics of spin waves, in particular of their angular momentum and thus their scattering rate.

Appendix

9.A On the chiral asymmetry of spin waves

9.A.1 Spin-wave chirality in ferromagnets

The only contribution in the Hamiltonian that can be sensitive to the chirality of a spin wave (see Sec. 9.3.(i)) is that of the Dzyaloshinskii-Moriya interaction. It goes with the cross product of two spin moments at different sites. If we consider the *ansatz* for a spin-wave snapshot given by Eq. (9.2), we get:

$$\begin{aligned}
\mathbf{S}_i \times \mathbf{S}_j &= \big[(S_i^2 S_j^0 - S_i^0 S_j^2)\mathbf{n}^1 + (S_i^0 S_j^1 - S_i^1 S_j^0)\mathbf{n}^2 + (S_i^1 S_j^2 - S_i^2 S_j^1)\mathbf{n}^0\big] \\
&= \big[(c\sin\phi_i \sin\theta\cos\theta - \cos\theta c\sin\phi_j \sin\theta)\mathbf{n}^1 \\
&\quad + (\cos\theta\cos\phi_j \sin\theta - \cos\phi_i \sin\theta\cos\theta)\mathbf{n}^2 \\
&\quad + (\cos\phi_i \sin\theta c\sin\phi_j \sin\theta - c\sin\phi_i \sin\theta\cos\phi_j \sin\theta)\mathbf{n}^0\big] \\
&= \big[c\sin\theta\cos\theta(\sin\phi_i - \sin\phi_j)\mathbf{n}^1 \\
&\quad + \cos\theta\sin\theta(\cos\phi_j - \cos\phi_i)\mathbf{n}^2 \\
&\quad + c\sin^2\theta(\sin\phi_j\cos\phi_i - \cos\phi_j\sin\phi_i)\mathbf{n}^0\big] \qquad (9.10) \\
&= \big[c\sin\theta\cos\theta(\sin\phi_i - \sin\phi_j)\mathbf{n}^1 \\
&\quad + \cos\theta\sin\theta(\cos\phi_j - \cos\phi_i)\mathbf{n}^2 \\
&\quad + c\sin^2\theta\sin(\phi_j - \phi_i)\mathbf{n}^0\big] \\
&= \big[c\sin\theta\cos\theta(\sin\phi_i - \sin\phi_j)\mathbf{n}^1 \\
&\quad + \cos\theta\sin\theta(\cos\phi_j - \cos\phi_i)\mathbf{n}^2 \\
&\quad + c\sin^2\theta\sin(\mathbf{k}\cdot(\mathbf{R}_j - \mathbf{R}_i))\mathbf{n}^0\big] \quad ,
\end{aligned}$$

and therefore, two terms depend on the chirality constance c. However, evaluating the sum over all lattice points required by the hamiltonian Eq. (9.1), the first term venishes:

$$\begin{aligned}
\sum_{ij} D_{ij}^1(\sin\phi_i - \sin\phi_j) &= 0 \\
\sum_{ij}(\sin\phi_i D_{ij}^1 - \sin\phi_i D_{ji}^1) &= 0 \\
\sum_{ij}(\sin\phi_i D_{ij}^1 + \sin\phi_i D_{ij}^1) &= 0 \\
\sum_{ij} 2D_{ij}^1 \sin\phi_i &= 0 \quad ,
\end{aligned} \qquad (9.11)$$

because $D^1_{ij} = -D^1_{ji}$.

Thus, the only term that depends on the spin-wave chirality in the energy, obtained by substituting the spin-wave equation of Eq. (9.2) into the Hamiltonian in Eq. (9.1), has the form

$$\begin{aligned} E(\mathbf{k}, c) &= -\frac{1}{2} c \sin^2\theta \sum_{ij} \sin(\mathbf{k}\cdot(\mathbf{R}_j - \mathbf{R}_i)\mathbf{D}_{ij}\cdot\mathbf{n}^0 \\ &= -\frac{1}{2} c \sin^2\theta N \mathbf{n}^0 \cdot \mathbf{D}(\mathbf{k}) \quad , \end{aligned} \tag{9.12}$$

where

$$\mathbf{D}(\mathbf{k}) = \sum_j \sin(\mathbf{k}\cdot\mathbf{R}_{ij})\mathbf{D}_{ij} \quad . \tag{9.13}$$

We can notice that only the $\mathbf{D}(\mathbf{k})$ component along the magnetization contributes to the chirality. This result matches the conclusion of L. Udvardi and L. Szunyogh [31].

9.A.2 Spin waves in a classical approach

In this section, we solve the equation of motion for every spin in a ferromagnet to understand the dynamics of its spin waves and the corresponding local spin precession.

Effective field

Considering the magnetic moments of a ferromagnet as classical vectors, their dynamics are governed by the phenomenological equation of motion given by Eq. (9.4). Solving this equation simultaneously for all sites provides spin-wave solutions. First, we need to determine the effective field, given by Eq. (9.5), which for the Hamiltonian of Eq. (9.1) that includes the exchange interaction and Dzyaloshinskii-Moriya, we get

$$\begin{aligned} B_i^{\text{eff}} =& -\frac{\partial H}{\partial \mathbf{S}_i} \\ =& \frac{1}{2}\frac{\partial}{\partial \mathbf{S}_i}\sum_{kj}\left(J_{kj}\mathbf{S}_k\cdot\mathbf{S}_j + \mathbf{D}_{kj}\cdot(\mathbf{S}_k\times\mathbf{S}_j)\right) \\ =& \frac{1}{2}\frac{\partial}{\partial \mathbf{S}_i}\left[\sum_j\left(J_{ij}\mathbf{S}_i\cdot\mathbf{S}_j + \mathbf{S}_i\cdot(\mathbf{S}_j\times\mathbf{D}_{ij})\right) + \sum_k\left(J_{ki}\mathbf{S}_k\cdot\mathbf{S}_i + \mathbf{S}_i\cdot(\mathbf{D}_{ki}\times\mathbf{S}_k)\right)\right. \\ & \left. + \sum_{k\neq i, j\neq i}\left(J_{kj}\mathbf{S}_k\cdot\mathbf{S}_j + \mathbf{D}_{kj}\cdot\mathbf{S}_k\times\mathbf{S}_j\right)\right] \\ =& \frac{1}{2}\sum_j\left(J_{ij}\mathbf{S}_j + \mathbf{S}_j\times\mathbf{D}_{ij}\right) + \frac{1}{2}\sum_j\left(J_{ji}\mathbf{S}_j + \mathbf{D}_{ji}\times\mathbf{S}_j\right) \\ =& \sum_j\left(J_{ij}\mathbf{S}_j + \mathbf{S}_j\times\mathbf{D}_{ij}\right) \quad . \end{aligned} \tag{9.14}$$

In calculating the derivative of the Hamiltonian, we did not have to take care of terms with $k = j = i$ because J_{ij} and $\mathbf{D}_{ij}$ are zero. Also, we made use of the cyclic permutation of the scalar triple product: $\mathbf{a} \cdot (\mathbf{b} \times \mathbf{c}) = \mathbf{c} \cdot (\mathbf{a} \times \mathbf{b}) = \mathbf{b} \cdot (\mathbf{c} \times \mathbf{a})$; and we swapped the interaction parameters index respecting their symmetries: $J_{ij} = J_{ji}$ and $\mathbf{D}_{ij} = -\mathbf{D}_{ji}$.

Equation of motion

Thus, the equation of motion in Eq. (9.4) reads

$$\begin{aligned}
\frac{\mathrm{d}\mathbf{S}_i}{\mathrm{d}t} &= -\sum_j \left(J_{ij}\mathbf{S}_i \times \mathbf{S}_j + \mathbf{S}_i \times (\mathbf{S}_j \times \mathbf{D}_{ij})\right) \\
&= -\sum_j \left(J_{ij}\mathbf{S}_i \times \mathbf{S}_j + \mathbf{S}_j(\mathbf{S}_i \cdot \mathbf{D}_{ij}) - \mathbf{D}_{ij}(\mathbf{S}_i \cdot \mathbf{S}_j)\right) \\
&= -\sum_j \left[J_{ij}\left(S_i^y S_j^z - S_i^z S_j^y\right) + S_j^x(\mathbf{S}_i \cdot \mathbf{D}_{ij}) - D_{ij}^x(\mathbf{S}_i \cdot \mathbf{S}_j)\right]\hat{\mathbf{x}} \\
&\quad -\sum_j \left[J_{ij}\left(S_i^z S_j^x - S_i^x S_j^z\right) + S_j^y(\mathbf{S}_i \cdot \mathbf{D}_{ij}) - D_{ij}^y(\mathbf{S}_i \cdot \mathbf{S}_j)\right]\hat{\mathbf{y}} \\
&\quad -\sum_j \left[J_{ij}\left(S_i^y S_j^x - S_i^x S_j^y\right) + S_j^z(\mathbf{S}_i \cdot \mathbf{D}_{ij}) - D_{ij}^z(\mathbf{S}_i \cdot \mathbf{S}_j)\right]\hat{\mathbf{z}} \quad .
\end{aligned} \tag{9.15}$$

Let us take the magnetization to be along the z direction and that the motion of each spin is of a small amplitude around the equilibrium direction. This implies that we consider that $S_i^x, S_i^y \ll 1$, and in first order approximation we disregard all products between them and take $S_i^z \sim S$. Thus, the above equation becomes

$$\begin{aligned}
\frac{\mathrm{d}\mathbf{S}_i}{\mathrm{d}t} &= -S\sum_j \left[J_{ij}\left(S_i^y - S_j^y\right) + D_{ij}^z S_j^x - S D_{ij}^x\right]\hat{\mathbf{x}} \\
&\quad -S\sum_j \left[J_{ij}\left(S_j^x - S_i^x\right) + D_{ij}^z S_j^y - S D_{ij}^y\right]\hat{\mathbf{y}} \\
&\quad -S\sum_j \left[D_{ij}^x S_i^x + D_{ij}^y S_i^y\right]\hat{\mathbf{z}} \\
&= -S\sum_j \left[J_{ij}\left(S_i^y - S_j^y\right) + D_{ij}^z S_j^x\right]\hat{\mathbf{x}} \\
&\quad -S\sum_j \left[J_{ij}\left(S_j^x - S_i^x\right) + D_{ij}^z S_j^y\right]\hat{\mathbf{y}} \quad ,
\end{aligned} \tag{9.16}$$

because $\sum_j D_{ij}^{x,y} = 0$ when the summation is over a Bravais lattice due the anti-symmetry of the DMI. We can see that, within the linear approximation, only the component of DMI along the magnetization matters.

This is a vectorial equation, which represents two equations: one for the x and one for the y components of the spin moment. Here note that the dynamics of one of the components depends on that of the other, therefore, we have a set of two coupled equations. Then, let us consider the following transformation:

$$\begin{aligned}
S_i^+ = S_i^x + \mathrm{i}S_i^y \quad \text{and} \quad S_i^- = S_i^x - \mathrm{i}S_i^y \\
S_i^x = \frac{1}{2}\left(S_i^+ + S_i^-\right) \quad \text{and} \quad S_i^y = \frac{1}{2\mathrm{i}}\left(S_i^+ - S_i^-\right) \quad ,
\end{aligned} \tag{9.17}$$

which define the circular components of the spin moments. Applying that to Eq. (9.16), we find

$$\begin{aligned} \mathrm{i}\frac{\mathrm{d}S_i^+ + S_i^-}{\mathrm{d}t} =& S\sum_j \left[J_{ij}\left(-S_i^+ + S_i^- + S_j^+ - S_j^-\right) - \mathrm{i}D_{ij}^z(S_j^+ + S_j^-)\right] \\ \mathrm{i}\frac{\mathrm{d}S_i^+ - S_i^-}{\mathrm{d}t} =& S\sum_j \left[J_{ij}\left(-S_i^+ - S_i^- + S_j^+ + S_j^-\right) - \mathrm{i}D_{ij}^z(S_j^+ - S_j^-)\right] \quad . \end{aligned} \tag{9.18}$$

Combining these two equations, we get

$$\begin{aligned} -\mathrm{i}\frac{\mathrm{d}S_i^+}{\mathrm{d}t} =& S\sum_j \left[J_{ij}\left(S_i^+ - S_j^+\right) + \mathrm{i}D_{ij}^z S_j^+\right] \\ \mathrm{i}\frac{\mathrm{d}S_i^-}{\mathrm{d}t} =& S\sum_j \left[J_{ij}\left(S_i^- - S_j^-\right) - \mathrm{i}D_{ij}^z S_j^-\right] \quad , \end{aligned} \tag{9.19}$$

which can be simplified by introducing the following definition

$$J_{ij}^{\pm} = J_{ij} \pm \mathrm{i}D_{ij}^z \quad , \tag{9.20}$$

that allow us to write

$$\begin{aligned} -\mathrm{i}\frac{\mathrm{d}S_i^+}{\mathrm{d}t} =& S\sum_j \left[J_{ij}S_i^+ - J_{ij}^- S_j^+\right] \\ \mathrm{i}\frac{\mathrm{d}S_i^-}{\mathrm{d}t} =& S\sum_j \left[J_{ij}S_i^- - J_{ij}^+ S_j^-\right] \quad , \end{aligned} \tag{9.21}$$

defining two *decoupled* equations of motion.

Fourier transformation

The dynamics of a given site depends on what is happening to all sites connected to it via the exchange interaction. However, if the system has translational symmetry, we can Fourier transform these equations defining

$$S_{\mathbf{k}}^{\pm} = \frac{1}{\sqrt{N}}\sum_i e^{-\mathrm{i}\mathbf{k}\cdot\mathbf{R}_i} S_i^{\pm} \quad , \quad S_i^{\pm} = \frac{1}{\sqrt{N}}\sum_{\mathbf{k}} e^{\mathrm{i}\mathbf{k}\cdot\mathbf{R}_i} S_{\mathbf{k}}^{\pm} \quad . \tag{9.22}$$

Then, by left multiplying Eq. (9.21) with $\frac{1}{\sqrt{N}}\sum_i e^{-\mathrm{i}\mathbf{k}\cdot\mathbf{R}_i}$, one gets

$$\begin{aligned} -\mathrm{i}\frac{\mathrm{d}S_{\mathbf{k}}^+(t)}{\mathrm{d}t} =& \frac{S}{\sqrt{N}}\left(\sum_i e^{-\mathrm{i}\mathbf{k}\cdot\mathbf{R}_i} S_i^+(t)\sum_j J_{ij} - \sum_j e^{-\mathrm{i}\mathbf{k}\cdot\mathbf{R}_j} S_j^+(t)\sum_i e^{+\mathrm{i}\mathbf{k}\cdot(\mathbf{R}_j-\mathbf{R}_i)} J_{ij}^-\right) \\ \mathrm{i}\frac{\mathrm{d}S_{\mathbf{k}}^-(t)}{\mathrm{d}t} =& \frac{S}{\sqrt{N}}\left(\sum_i e^{-\mathrm{i}\mathbf{k}\cdot\mathbf{R}_i} S_i^-(t)\sum_j J_{ij} - \sum_j e^{-\mathrm{i}\mathbf{k}\cdot\mathbf{R}_j} S_j^-(t)\sum_i e^{+\mathrm{i}\mathbf{k}\cdot(\mathbf{R}_j-\mathbf{R}_i)} J_{ij}^+\right) \quad , \end{aligned} \tag{9.23}$$

where we multiplied the second term of the r.h.s by 1 in the form of $e^{-\mathrm{i}\mathbf{k}\cdot\mathbf{R}_j}e^{\mathrm{i}\mathbf{k}\cdot\mathbf{R}_j}$. We then obtain

$$\begin{aligned} -\mathrm{i}\frac{\mathrm{d}S^+_{\mathbf{k}}(t)}{\mathrm{d}t} &= S\left(J_{\mathbf{0}} - J^-_{\mathbf{k}}\right) S^+_{\mathbf{k}}(t) \\ \mathrm{i}\frac{\mathrm{d}S^-_{\mathbf{k}}(t)}{\mathrm{d}t} &= S\left(J_{\mathbf{0}} - J^+_{\mathbf{k}}\right) S^-_{\mathbf{k}}(t) \quad , \end{aligned} \tag{9.24}$$

where the Fourier transformed interactions is defined as

$$J^{\pm}_{\mathbf{k}} = \sum_i e^{\mathrm{i}\mathbf{k}\cdot\mathbf{R}_{ij}} J^{\pm}_{ij} \quad , \tag{9.25}$$

which assumes a translational symmetry, such that $J^{\pm}_{ij}$ only depends on the difference $\mathbf{R}_{ij} = \mathbf{R}_j - \mathbf{R}_i$. Note as well, that $J^{\pm}_{\mathbf{0}} = \sum_i (J_{ij} \pm \mathrm{i}D^z_{ij}) = \sum_i J_{ij} = J_{\mathbf{0}}$, again because of the DMI antisymmetry. Next follows some useful properties of the interactions in the reciprocal space:

$$J^{\pm}_{-\mathbf{k}} = \sum_i e^{-\mathrm{i}\mathbf{k}\cdot\mathbf{R}_{ij}} J^{\pm}_{ij} = \sum_i e^{\mathrm{i}\mathbf{k}\cdot\mathbf{R}_{ji}} J^{\mp}_{ji} = J^{\mp}_{\mathbf{k}} \quad , \tag{9.26}$$

and

$$\begin{aligned} J^{\pm}_{\mathbf{k}} &= \sum_i \big(\cos(\mathbf{k}\cdot\mathbf{R}_{ij}) + \mathrm{i}\sin(\mathbf{k}\cdot\mathbf{R}_{ij})\big)(J_{ij} \pm \mathrm{i}D^z_{ij}) \\ &= \sum_i \big(\cos(\mathbf{k}\cdot\mathbf{R}_{ij})J_{ij} \mp \sin(\mathbf{k}\cdot\mathbf{R}_{ij})D^z_{ij}\big) \\ &= \sum_i A_{ij}\big(\cos(\mathbf{k}\cdot\mathbf{R}_{ij})\cos\theta_{ij} \mp \sin(\mathbf{k}\cdot\mathbf{R}_{ij})\sin\theta_{ij}\big) \\ &= \sum_i A_{ij}\cos\left(\mathbf{k}\cdot\mathbf{R}_{ij} \pm \theta_{ij}\right) \quad , \end{aligned} \tag{9.27}$$

where $\theta_{ij} = \arctan(D^z_{ij}/J_{ij})$ and $A_{ij} = \sqrt{(D^z_{ij})^2 + (J_{ij})^2}$. The last equation shows that $J^{\pm}_{\mathbf{k}}$ is purely real and, that it can be expanded in terms of cosine functions whose phase is given by the magnetic exchange and DMI ratio. This derives from the fact that the sum of a Bravais lattice of an antisymmetric function vanishes, $\sum_i \sin(\mathbf{k}\cdot\mathbf{R}_{ij})J_{ij} = \sum_i \cos(\mathbf{k}\cdot\mathbf{R}_{ij})D^z_{ij} = 0$.

Eigenvalues: the frequencies

The differential equations in (9.24) have solutions of the type

$$S^{\pm}_{\mathbf{k}}(t) = S^{\pm}_{\mathbf{k}} e^{-\mathrm{i}\omega^{\pm}_{\mathbf{k}} t} \quad , \tag{9.28}$$

which plugging into Eqs. (9.24) results in

$$\begin{aligned} -\omega^+_{\mathbf{k}} S^+_{\mathbf{k}} &= S\left(J_{\mathbf{0}} - J^-_{\mathbf{k}}\right) S^+_{\mathbf{k}} \\ \omega^-_{\mathbf{k}} S^-_{\mathbf{k}} &= S\left(J_{\mathbf{0}} - J^+_{\mathbf{k}}\right) S^-_{\mathbf{k}} \quad , \end{aligned} \tag{9.29}$$

and therefore, the eigenvalues of these equations that correspond to the solution frequencies are given by

$$\omega^{\pm}_{\mathbf{k}} = \mp S\left(J_{\mathbf{0}} - J^{\mp}_{\mathbf{k}}\right) \quad . \tag{9.30}$$

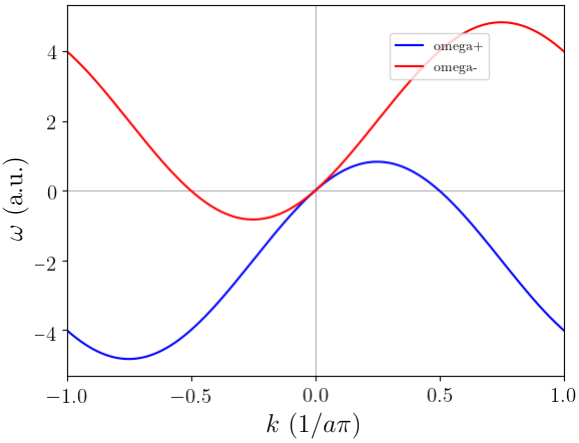

Figure 9.A.1: Spin-wave dispersion for a ferromagnet with DMI. The red and blue curves correspond to the values ω^- and ω^+, respectively. The negative part of ω^- indicates an instability of the ferromagnetic spin configuration: with the DMI, the ground state passes to be a spin spiral. The blue curve is obtained from the red one by reversing the space and time, which take $k \to -k$ and $\omega^+ \to -\omega^-$.

For a one-dimensional ferromagnet with nearest-neighbour-only MEI and DMI, $J = D^z = 1$, we plotted the above equation in Fig. 9.A.1.

Using Eq. (9.26), we can notice that

$$\omega^{\pm}_{-\mathbf{k}} = -(\pm S\left(J_{\mathbf{0}} - J^{\pm}_{\mathbf{k}}\right)) = -\omega^{\mp}_{\mathbf{k}} \quad , \tag{9.31}$$

that is, the frequency of each solution is related to the other by an inversion of space and a sign change of the frequency, which can be translated into an inversion of time in Eq. (9.28), see Fig. 9.A.1. Due to $J^{\pm}_{\mathbf{0}} = J_{\mathbf{0}}$, we have that $\omega^{\pm}_{\mathbf{k}} \to 0$ when $\mathbf{k} \to 0$.

In the absence of DMI, and if $J_{ij} > 0$, we have that $\omega^{\pm}_{\mathbf{k}} = \omega^{\pm}_{-\mathbf{k}} = \pm\omega_{\mathbf{k}}$, which imply that the frequencies are reciprocally symmetric and additive inverse of each other. Furthermore, $\omega_{\mathbf{k}}$ is always real and positive, as we expect for a ferromagnetic system:

$$\omega_{\mathbf{k}} = S\sum_i \left[1 - \cos(\mathbf{k}\cdot\mathbf{R}_{ij})\right] J_{ij} > 0 \quad . \tag{9.32}$$

For nonzero D^z_{ij}, the phases of the cosines change, which can results in the frequency switching sign for $\mathbf{k}$ at some parts of the reciprocal space. This indicates an instability that arises from the DMI favoring a spin-spiral ground state rather than a collinear ferromagnetic alignment.

Local spin dynamics

Now, it is time to transform back, from the circular components to the Cartesian ones in order to understand the precession of individual spins. For a given wavevector

$\mathbf{k}$, we have that

$$\begin{aligned} S_i^+(\mathbf{k},t) =& \frac{1}{\sqrt{N}} e^{\mathrm{i}\mathbf{k}\cdot\mathbf{R}_i} S_{\mathbf{k}}^+(t) = \frac{S_{\mathbf{k}}^+}{\sqrt{N}} \left(\cos(\mathbf{k}\cdot\mathbf{R}_i - \omega_{\mathbf{k}}^+ t) + \mathrm{i}\sin(\mathbf{k}\cdot\mathbf{R}_i - \omega_{\mathbf{k}}^+ t)\right) \\ S_i^-(\mathbf{k},t) =& \frac{1}{\sqrt{N}} e^{\mathrm{i}\mathbf{k}\cdot\mathbf{R}_i} S_{\mathbf{k}}^-(t) = \frac{S_{\mathbf{k}}^-}{\sqrt{N}} \left(\cos(\mathbf{k}\cdot\mathbf{R}_i - \omega_{\mathbf{k}}^- t) + \mathrm{i}\sin(\mathbf{k}\cdot\mathbf{R}_i - \omega_{\mathbf{k}}^- t)\right) \quad . \end{aligned} \tag{9.33}$$

Comparing these equations with their definitions at Eq. (9.17) in terms of the Cartesian components, $S_i^+ = S_i^x + \mathrm{i}S_i^y$ and $S_i^- = S_i^x - \mathrm{i}S_i^y$, we get a solution for each equation:

$$\begin{aligned} \left(S_i^x, S_i^y\right)(\mathbf{k}) =& \frac{S_{\mathbf{k}}^+}{\sqrt{N}} \left(\cos(\mathbf{k}\cdot\mathbf{R}_i - \omega_{\mathbf{k}}^+ t)\ ,\ \sin(\mathbf{k}\cdot\mathbf{R}_i - \omega_{\mathbf{k}}^+ t)\right) \\ \left(S_i^x, S_i^y\right)(\mathbf{k}) =& \frac{S_{\mathbf{k}}^-}{\sqrt{N}} \left(\cos(-\mathbf{k}\cdot\mathbf{R}_i + \omega_{\mathbf{k}}^- t)\ ,\ \sin(-\mathbf{k}\cdot\mathbf{R}_i + \omega_{\mathbf{k}}^- t)\right) \end{aligned} \tag{9.34}$$

We can show that these two equations are equivalent by substituting one of the amplitude by its dual: $\left(S_{\mathbf{k}}^{\pm}\right)^* = S_{-\mathbf{k}}^{\mp}$, see Eq. (9.37), and using the relation derived in Eq. (9.31). Doing so in the second solution of Eq. (9.34), we get

$$\left(S_i^x, S_i^y\right)(-\mathbf{k}) = \frac{(S_{\mathbf{k}}^+)^*}{\sqrt{N}} \left(\cos(\mathbf{k}\cdot\mathbf{R}_i - \omega_{\mathbf{k}}^+ t)\ ,\ \sin(\mathbf{k}\cdot\mathbf{R}_i - \omega_{\mathbf{k}}^+ t)\right) \quad , \tag{9.35}$$

which is, considering $S_{\mathbf{k}}^+$ real, equivalent to the first solution in Eq. (9.34) but with opposite wavevector. These solutions represent counterclockwise circular precessions, and they are related to each other by an inversion of time and space!

9.A.3 Circular components duality

The following reviews the duality between the circular components of the spin moments and how they evolve through the transformation considered previously, such as the Fourier transformation.

From the definition of the circular components in Eq. (9.17), we have that

$$\left(S_i^{\pm}\right)^* = S_i^{\mp} \quad , \tag{9.36}$$

that is, one is the complex conjugate of the other. Given the Fourier transformation definitions by Eq. (9.22), the complex conjugate duality of the Fourier counterparts is given by

$$\left(S_{\mathbf{k}}^{\pm}\right)^* = S_{-\mathbf{k}}^{\mp} \quad . \tag{9.37}$$

Given the definition of the time evolution, Eq. (9.28), we have that

$$\left(S_{\mathbf{k}}^{\pm}(t)\right)^* = S_{-\mathbf{k}}^{\mp}(-t) \quad . \tag{9.38}$$

Chapter 10

Conclusions and perspectives

Throughout this thesis, we studied the fundamental properties of the collective spin excitations of noncollinear magnets. We described these spin waves in the adiabatic approximation for systems of localized magnetic moments whose dynamics are governed by a generalized quantum Heisenberg Hamiltonian, which we discussed in Chapter 2. We took into account relativistic effects due to the spin-orbit coupling, such as the magnetocrystalline anisotropy and the Dzyaloshinskii-Moriya interaction, the latter being responsible for the magnetic noncollinearity of the investigated systems.

To provide a material-specific description, we performed first-principles calculations based on the density functional theory within the Green-function Korringa-Kohn-Rostoker method, which we introduced in Chapter 3. These simulations were performed using a full-potential relativistic method within the local spin density approximation (LSDA). Besides providing the electronic and magnetic properties of the ground state, the calculations also allowed us to parametrize the generalized Heisenberg Hamiltonian by means of the infinitesimal-rotation method.

We demonstrated how spin waves of noncollinear magnets can be probed using the inelastic scattering of neutrons or electrons. While neutrons are employed to study bulk systems, electrons are more suitable for surface and thin films, due to their high cross-section and low penetration length. Thus, we developed an inelastic-scattering theory in Chapter 4, where we derived the spin-spin correlation tensor for spin waves in noncollinear magnets. Together with the first-principles calculations, this allowed us to make predictions directly compatible with the experimental measurements of spin waves.

Our first case study was cobalt deposited on the tungsten (110) surface, which we investigated in Chapter 5. We studied Co films with 3 up to 8 monolayers (MLs), which feature a ferromagnetic order. Recent electron-energy-loss spectroscopy with the highest energy resolution in the literature observed for the first time up to three spin-wave modes in these films. Therefore, we chose these Co films as test systems for our methodology. Because of the large mismatch between Co and W lattice constants, a reconstruction of the cobalt films occurs already for films as thin as 1 monolayer thick. The resulting supercell yields a reduction of the Brillouin zones of these materials. Thus, to compare our theoretical results with the experimental data, we employed an unfolding scheme, which comes naturally from the inelastic scattering theory of Chapter 6. We obtained overall good agreement with the ex-

perimental data for the spin-wave dispersions for films of various thicknesses. To achieve that, we rescaled the exchange splitting self-consistently to correct for its overestimation by the DFT in the LSDA approximation.

Upon the inelastic scattering theory developed in Chapter 4, we proposed in Chapter 6 a new experimental protocol to probe spin waves in noncollinear magnetic thin films. It consists of spin-polarized electron-energy-loss spectroscopy (SPEELS) augmented with a spin filter, resulting in spin-resolved electron-energy-loss spectroscopy (SREELS). Then, we computed the SREELS spectra for a spin spiral and a skyrmion lattice. From that, we could draw our first understanding of the nature of spin waves in noncollinear spin textures. For instance, these systems can host spin waves with different angular momenta, which is in contrast to the physics of ferromagnets. A spin spiral has two rotational modes with opposite angular momenta that point parallel to the spiralization axis of the spin texture, and another with no angular moment associated with a longitudinal precession of the net magnetization. Furthermore, we learned that during the scattering of electrons, even non-spin-flip processes can create spin waves in noncollinear magnets and that we can select a mode to be measured by controlling the polarization of the electron beam and properly choosing the scattering spin channel. While for ferromagnets SPEELS is sufficient to fully characterize the properties of spin waves, spin-resolved spectroscopy through SREELS becomes mandatory to achieve the same result.

Next, we explored noncollinear spin textures of antiferromagnetic materials in Chapter 7. We saw that the DMI induces a splitting of the two otherwise degenerate bands of a collinear antiferromagnet. This splitting occurs such that the energy minimum of each band is shifted in opposite directions of the reciprocal space. This phenomenon is known as the spin-wave Rashba effect. When the Rashba spin-wave modes are subject to an external field, the dispersion of one is raised in energy and the other is lowered, causing an asymmetry in the spin-wave spectrum. We also studied the formation of spin spirals and skyrmion lattices in two-dimension systems. In particular, we saw that in antiferromagnets, an anisotropic magnetic exchange interaction can also produce antiskyrmions, without the need of an anisotropic DMI. Beyond model systems, we chose two antiferromagnetic materials, Mn/β-W and Mn_5Si_3 to investigate. The first has a remarkably high magnetocrystalline anisotropy and a strongly anisotropic DMI. The ground state is an antiferromagnetic spin spiral whose spin-wave spectrum presents an energy gap. The second is a system of experimental interest where inelastic-neutron-scattering data suggested that in its collinear antiferromagnetic phase, Mn_5Si_3 has a regime of coexistence of spin waves and diffusive spin fluctuations. Even though we could not rule out the role of the spin fluctuations, we showed that the spin-wave dispersion as a function of the applied field matches the behavior of the experimental inelastic-neutron-scattering data.

In Chapter 8, our investigation of ultrathin films of Co/W(110) led us to the prediction of the first material to host in-plane skyrmions. We studied films with 1 to 3 reconstructed Co monolayers and 1 pseudomorphic Co monolayer using a combination of analytical micromagnetic models and spin-dynamics simulations. We concluded that all three reconstructed Co films have ferromagnetic ground states. However, we showed that the 1ML Co film can host meta-stable in-plane skyrmions. The in-plane magnetization of this system preserves the crystal mirror symmetry

because it is perpendicular to the mirror plane. This guarantees the coexistence of the in-plane antiskyrmions, because such a mirror-symmetry operation maps a skyrmion into antiskyrmion, and in this case without switching the magnetization background. The ability to simultaneously host skyrmions and antiskyrmions is very important for spintronics, once these quasiparticles respond differently to the applied fields. Furthermore, in-plane skyrmions are expected to be in general smaller than the out-of-plane skyrmions because the dipole-dipole interaction acts to reduce the size of the earlier and to enlarge the latter. The ground state for the pseudomorphic Co ML film was found to be a spin spiral. Under the action of external magnetic fields, we could stabilize both an in-plane skyrmion and an out-of-plane antiskyrmion.

Finally, in Chapter 9, we investigated the breaking of reciprocal symmetry (nonreciprocity) of the spin-wave properties due to the Dzyaloshinskii-Moriya interaction. Here we have to differentiate between the intrinsic spin-wave spectrum, which is composed of the energies of all spin-wave modes for all wavevectors, and the inelastic-scattering spectrum, which results in the interaction of the probing electrons with the spin waves of the system often not exciting all possible modes. We showed that only a system with finite magnetization can have a nonreciprocal intrinsic spin-wave spectrum and that this happens when the DMI has a finite component along the magnetization. In ferromagnets, the magnetization direction imposed the chirality and handedness of the spin waves, which are the attributes that determine how the energies of the spin waves will respond to the DMI. We generalized this concept for noncollinear magnets, where we demonstrated that the angular momentum of the spin-wave modes can be regarded as their handedness attributes. In a system with zero magnetization, such as antiferromagnets and cycloidal spin spirals, individual modes can be nonreciprocal, while the total intrinsic spectrum remains symmetric in the reciprocal space (in the absence of an external magnetic field). However, even for these zero-magnetization systems, the inelastic-scattering spectrum can be nonreciprocal. This happens in the spin-flip channel of the inelastic-scattering measurements when the polarization of the probing particle aligns with the spin-wave angular momentum and the DMI. This mechanism gives us the possibility to determine the DMI chirality from inelastic-scattering experiments in noncollinear spin textures.

Future perspectives

Despite the extensive work we carried on, there is much left to be done. Within the adiabatic approximation, there are many different interactions to be considered, and thus, expanding the range of possible materials to be described. For instance, to describe the spin waves of very long wavelengths, such as the ones probed by Brillouin light scattering, it is needed to consider the dipole-dipole interaction [189]. Another example is the topological three-spin chiral interactions driven by emergent orbital magnetism [190].

Inevitably, accounting for these new magnetic interactions will lead to the discovery of novel spin textures. Even with the old set of interactions that we considered in this thesis, there are other spin textures that we left unexplored. Examples are: Reduced-dimensionality spin textures, such as the one-dimensional periodic

arrangement of skyrmions; Interfaces between phases of different topological characters, such as between a skyrmion lattice and a ferromagnetic phase, where edge states topologically protected against backscattering are expected to occur [13, 14]; 3D localized spin textures, such as hopfions and magnetic bobbers[8, 10, 191].

The adiabatic approximation for spin waves used in this work is a very powerful tool to understand the fundamental properties of spin waves, and it is computationally very efficient. However, to describe the lifetime of the spin waves and other properties, one has to go beyond. This requires considering the coupling of the spin-wave bath with the other particles and quasiparticles, such as phonons, electrons, and even magnons themselves [192–194]. Some of these can be treated utilizing linear response theory, for example, by calculating the magnetic susceptibility including the appropriate self-energies [195]. Other theoretical frameworks such as time-dependent density functional theory in combination with many-body perturbation theory are suitable as well [196, 197].

Our discovery of in-plane skyrmions in Co/W(110) opens new paths for the search of host materials that can be used in spintronics and other research fields. High-throughput methods should now be used to prospect material systems with in-plane magnetic anisotropy. Another important aspect is to better understand in this context the importance of the ultra-low symmetry systems.

We demonstrated the power of controlling and detecting the spin polarization of the probing particles in the studies of spin waves. A natural extension of our inelastic scattering theory is to consider the effect of more complex polarizations. By manipulating and combining the beam phase and polarization, it is possible to build a probing beam with circular polarization that carries spin angular momentum, but also more involving polarization that carries orbital angular momentum [198]. These different polarizations are expected to couple to different spin-wave modes making possible to explore other parts of the intrinsic spin-wave spectrum which were not observed before.

Our studies were conducted for zero temperature. However, many interesting problems are intrinsically temperature dependent, such as the softening of the magnetic interactions which directly affects the spin-wave spectra [109]. Accounting for the temperature effects can be done, for example, by considering longitudinal spin-fluctuations to be added to the Heisenberg Hamiltonian [199, 200]. The finite-temperature statistics should also be considered in our theory of inelastic electron/neutron scattering.

Bibliography

[1] F. Bloch. "Zur Theorie des Ferromagnetismus". de. In: *Zeitschrift für Physik* 61.3 (Mar. 1930), pp. 206–219. ISSN: 0044-3328. DOI: 10.1007/BF01339661.

[2] B. N. Brockhouse. "Scattering of Neutrons by Spin Waves in Magnetite". In: *Physical Review* 106.5 (June 1957), pp. 859–864. DOI: 10.1103/PhysRev.106.859.

[3] "The next wave". en. In: *Nature Physics* 11.6 (June 2015), p. 437. ISSN: 1745-2481. DOI: 10.1038/nphys3367.

[4] V. V. Kruglyak, S. O. Demokritov, and D. Grundler. "Magnonics". en. In: *Journal of Physics D: Applied Physics* 43.26 (June 2010), p. 260301. ISSN: 0022-3727. DOI: 10.1088/0022-3727/43/26/260301.

[5] A. V. Chumak et al. "Magnon spintronics". en. In: *Nature Physics* 11.6 (June 2015), pp. 453–461. ISSN: 1745-2473. DOI: 10.1038/nphys3347.

[6] A. V. Chumak and H. Schultheiss. "Magnonics: spin waves connecting charges, spins and photons". en. In: *Journal of Physics D: Applied Physics* 50.30 (July 2017), p. 300201. ISSN: 0022-3727. DOI: 10.1088/1361-6463/aa7715.

[7] Naoto Nagaosa and Yoshinori Tokura. "Topological properties and dynamics of magnetic skyrmions". en. In: *Nature Nanotechnology* 8.12 (Dec. 2013), pp. 899–911. ISSN: 1748-3387. DOI: 10.1038/nnano.2013.243.

[8] Filipp N. Rybakov et al. "New spiral state and skyrmion lattice in 3D model of chiral magnets". In: *New J. Phys.* 18.4 (2016), p. 045002. ISSN: 1367-2630. DOI: 10.1088/1367-2630/18/4/045002.

[9] Markus Garst, Johannes Waizner, and Dirk Grundler. "Collective spin excitations of helices and magnetic skyrmions: review and perspectives of magnonics in non-centrosymmetric magnets". en. In: *Journal of Physics D: Applied Physics* 50.29 (June 2017), p. 293002. ISSN: 0022-3727. DOI: 10.1088/1361-6463/aa7573.

[10] Fengshan Zheng et al. "Experimental observation of chiral magnetic bobbers in B20-type FeGe". en. In: *Nature Nanotechnology* 13.6 (June 2018), pp. 451–455. ISSN: 1748-3395. DOI: 10.1038/s41565-018-0093-3.

[11] AN Bogdanov and DA Yablonskii. "Thermodynamically stable "vortices" in magnetically ordered crystals. The mixed state of magnets". In: 95.1 (1989), p. 178.

[12] A. N. Bogdanov and U. K. Rößler. "Chiral Symmetry Breaking in Magnetic Thin Films and Multilayers". In: *Physical Review Letters* 87.3 (June 2001), p. 037203. DOI: 10.1103/PhysRevLett.87.037203.

[13] A. Roldán-Molina, A. S. Nunez, and J. Fernández-Rossier. "Topological spin waves in the atomic-scale magnetic skyrmion crystal". en. In: *New Journal of Physics* 18.4 (2016), p. 045015. ISSN: 1367-2630. DOI: 10.1088/1367-2630/18/4/045015.

[14] Sebastián A. Díaz, Jelena Klinovaja, and Daniel Loss. "Topological Magnons and Edge States in Antiferromagnetic Skyrmion Crystals". In: *Physical Review Letters* 122.18 (May 2019), p. 187203. DOI: 10.1103/PhysRevLett.122.187203.

[15] Bertrand Dupé et al. "Tailoring magnetic skyrmions in ultra-thin transition metal films". En. In: *Nature Communications* 5 (June 2014), p. 4030. ISSN: 2041-1723. DOI: 10.1038/ncomms5030.

[16] Imara Lima Fernandes et al. "Universality of defect-skyrmion interaction profiles". En. In: *Nature Communications* 9.1 (Oct. 2018), p. 4395. ISSN: 2041-1723. DOI: 10.1038/s41467-018-06827-5.

[17] M. Plihal, D. L. Mills, and J. Kirschner. "Spin Wave Signature in the Spin Polarized Electron Energy Loss Spectrum of Ultrathin Fe Films: Theory and Experiment". In: *Physical Review Letters* 82.12 (Mar. 1999), pp. 2579–2582. DOI: 10.1103/PhysRevLett.82.2579.

[18] R. Vollmer et al. "Spin-Polarized Electron Energy Loss Spectroscopy of High Energy, Large Wave Vector Spin Waves in Ultrathin fcc Co Films on Cu(001)". In: *Physical Review Letters* 91.14 (Sept. 2003), p. 147201. DOI: 10.1103/PhysRevLett.91.147201.

[19] Thomas Sebastian et al. "Micro-focused Brillouin light scattering: imaging spin waves at the nanoscale". English. In: *Frontiers in Physics* 3 (2015). ISSN: 2296-424X. DOI: 10.3389/fphy.2015.00035.

[20] R. Zeller. "Multiple-scattering solution of Schrodinger's equation for potentials of general shape". en. In: *Journal of Physics C: Solid State Physics* 20.16 (June 1987), p. 2347. ISSN: 0022-3719. DOI: 10.1088/0022-3719/20/16/010.

[21] A. I. Liechtenstein et al. "Local spin density functional approach to the theory of exchange interactions in ferromagnetic metals and alloys". In: *Journal of Magnetism and Magnetic Materials* 67.1 (May 1987), pp. 65–74. ISSN: 0304-8853. DOI: 10.1016/0304-8853(87)90721-9.

[22] L. Udvardi et al. "First-principles relativistic study of spin waves in thin magnetic films". In: *Physical Review B* 68.10 (Sept. 2003), p. 104436. DOI: 10.1103/PhysRevB.68.104436.

[23] Harald Ibach. "High resolution electron energy loss spectroscopy of spin waves in ultra-thin film — The return of the adiabatic approximation?" In: *Surface Science* 630 (Dec. 2014), pp. 301–310. ISSN: 0039-6028. DOI: 10.1016/j.susc.2014.07.015.

[24] E. Michel, H. Ibach, and C. M. Schneider. "Spin waves in ultrathin hexagonal cobalt films on W(110), Cu(111), and Au(111) surfaces". In: *Physical Review B* 92.2 (July 2015), p. 024407. DOI: 10.1103/PhysRevB.92.024407.

[25] E. Michel et al. “Lifetime and mean free path of spin waves in ultrathin cobalt films”. In: *Physical Review B* 94.1 (July 2016), p. 014420. DOI: 10.1103/PhysRevB.94.014420.

[26] Flaviano José dos Santos et al. “Spin-resolved inelastic electron scattering by spin waves in noncollinear magnets”. In: *Physical Review B* 97.2 (Jan. 2018), p. 024431. DOI: 10.1103/PhysRevB.97.024431.

[27] P. J. Brown and J. B. Forsyth. “Antiferromagnetism in Mn5Si3: the magnetic structure of the AF2 phase at 70 K”. en. In: *Journal of Physics: Condensed Matter* 7.39 (Sept. 1995), pp. 7619–7628. ISSN: 0953-8984. DOI: 10.1088/0953-8984/7/39/004.

[28] Christoph Sürgers et al. “Switching of a large anomalous Hall effect between metamagnetic phases of a non-collinear antiferromagnet”. en. In: *Scientific Reports* 7 (Feb. 2017), p. 42982. ISSN: 2045-2322. DOI: 10.1038/srep42982.

[29] N. Biniskos et al. “Spin Fluctuations Drive the Inverse Magnetocaloric Effect in Mn_5Si_3”. In: *Physical Review Letters* 120.25 (June 2018), p. 257205. DOI: 10.1103/PhysRevLett.120.257205.

[30] William Legrand et al. “Room-temperature stabilization of antiferromagnetic skyrmions in synthetic antiferromagnets”. en. In: *Nature Materials* (Sept. 2019), pp. 1–9. ISSN: 1476-4660. DOI: 10.1038/s41563-019-0468-3.

[31] L. Udvardi and L. Szunyogh. “Chiral Asymmetry of the Spin-Wave Spectra in Ultrathin Magnetic Films”. In: *Physical Review Letters* 102.20 (May 2009), p. 207204. DOI: 10.1103/PhysRevLett.102.207204.

[32] A. T. Costa et al. “Spin-orbit coupling and spin waves in ultrathin ferromagnets: The spin-wave Rashba effect”. In: *Physical Review B* 82.1 (July 2010), p. 014428. DOI: 10.1103/PhysRevB.82.014428.

[33] Kh. Zakeri et al. “Asymmetric Spin-Wave Dispersion on Fe(110): Direct Evidence of the Dzyaloshinskii-Moriya Interaction”. In: *Physical Review Letters* 104.13 (Mar. 2010), p. 137203. DOI: 10.1103/PhysRevLett.104.137203.

[34] Charles Kittel. *Introduction to Solid State Physics*. Englisch. 8th edition. Hoboken, NJ: Wiley John + Sons, Oct. 2004. ISBN: 978-0-471-41526-8.

[35] Neil W. Ashcroft and N. Mermin. *Solid State Physics*. Englisch. New ed edition. New York: Cengage Learning, Jan. 1976. ISBN: 978-0-03-083993-1.

[36] Norberto Majlis. *Quantum Theory of Magnetism, 2nd Ed.* English. 2nd edition. New Jersey: World Scientific Pub Co Inc, Nov. 2007. ISBN: 978-981-256-792-5.

[37] Wolfgang Nolting and Anupuru Ramakanth. *Quantum Theory of Magnetism*. Englisch. 2010 edition. Heidelberg ; New York: Springer, Oct. 2009. ISBN: 978-3-540-85415-9.

[38] Daniel D. Stancil and Anil Prabhakar. *Spin Waves: Theory and Applications*. English. 2009 edition. New York: Springer, Apr. 2009. ISBN: 978-0-387-77864-8.

[39] Randy S. Fishman, Jaime A. Fernandez-Baca, and Toomas Rõõm. *Spin-Wave Theory and its Applications to Neutron Scattering and THz Spectroscopy*. en. Google-Books-ID: irt2DwAAQBAJ. Morgan & Claypool Publishers, Nov. 2018. ISBN: 978-1-64327-114-9.

[40] Hubbard J. and Flowers Brian Hilton. "Electron correlations in narrow energy bands". In: *Proceedings of the Royal Society of London. Series A. Mathematical and Physical Sciences* 276.1365 (Nov. 1963), pp. 238–257. DOI: 10.1098/rspa.1963.0204.

[41] I. Dzyaloshinsky. "A thermodynamic theory of "weak" ferromagnetism of antiferromagnetics". In: *Journal of Physics and Chemistry of Solids* 4.4 (Jan. 1958), pp. 241–255. ISSN: 0022-3697. DOI: 10.1016/0022-3697(58)90076-3.

[42] Tôru Moriya. "Anisotropic Superexchange Interaction and Weak Ferromagnetism". In: *Physical Review* 120.1 (Oct. 1960), pp. 91–98. DOI: 10.1103/PhysRev.120.91.

[43] N. D. Mermin and H. Wagner. "Absence of Ferromagnetism or Antiferromagnetism in One- or Two-Dimensional Isotropic Heisenberg Models". In: *Physical Review Letters* 17.22 (Nov. 1966), pp. 1133–1136. DOI: 10.1103/PhysRevLett.17.1133.

[44] L. Landau and E. Lifshitz. "On the theory of the dispersion of magnetic permeability in ferromagnetic bodies". In: *Phys. Zeitsch. der Sow. Ukr. J. Phys* 8.53 (1935), pp. 14–22.

[45] T. L. Gilbert. "A Lagrangian formulation of the gyromagnetic equation of the magnetization field". In: *Phys. Rev.* 100 (1955), p. 1243.

[46] R. F. L. Evans et al. "Atomistic spin model simulations of magnetic nanomaterials". en. In: *Journal of Physics: Condensed Matter* 26.10 (Feb. 2014), p. 103202. ISSN: 0953-8984. DOI: 10.1088/0953-8984/26/10/103202.

[47] Gideon P. Müller et al. "Spirit: Multifunctional framework for atomistic spin simulations". In: *Physical Review B* 99.22 (June 2019), p. 224414. DOI: 10.1103/PhysRevB.99.224414.

[48] T. Holstein and H. Primakoff. "Field Dependence of the Intrinsic Domain Magnetization of a Ferromagnet". In: *Physical Review* 58.12 (Dec. 1940), pp. 1098–1113. DOI: 10.1103/PhysRev.58.1098.

[49] J. T. Haraldsen and R. S. Fishman. "Spin rotation technique for non-collinear magnetic systems: application to the generalized Villain model". en. In: *Journal of Physics: Condensed Matter* 21.21 (2009), p. 216001. ISSN: 0953-8984. DOI: 10.1088/0953-8984/21/21/216001.

[50] A. Roldán-Molina et al. "Quantum theory of spin waves in finite chiral spin chains". In: *Physical Review B* 89.5 (Feb. 2014), p. 054403. DOI: 10.1103/PhysRevB.89.054403.

[51] R. P. Erickson and D. L. Mills. "Thermodynamics of thin ferromagnetic films in the presence of anisotropy and dipolar coupling". In: *Physical Review B* 44.21 (Dec. 1991), pp. 11825–11835. DOI: 10.1103/PhysRevB.44.11825.

[52] Ming-wen Xiao. “Theory of transformation for the diagonalization of quadratic Hamiltonians”. In: *arXiv:0908.0787 [math-ph]* (Aug. 2009). arXiv: 0908.0787.

[53] S. Toth and B. Lake. “Linear spin wave theory for single-Q incommensurate magnetic structures”. en. In: *Journal of Physics: Condensed Matter* 27.16 (2015), p. 166002. ISSN: 0953-8984. DOI: 10.1088/0953-8984/27/16/166002.

[54] D. L. Mills and Pascal Lederer. “Dynamical Properties of Magnetic Impurities in Transition Metals”. In: *Physical Review* 160.3 (Aug. 1967), pp. 590–599. DOI: 10.1103/PhysRev.160.590.

[55] R. B. Muniz and D. L. Mills. “Local spin dynamics of magnetic moments on metal surfaces”. In: *Physical Review B* 68.22 (Dec. 2003), p. 224414. DOI: 10.1103/PhysRevB.68.224414.

[56] S. Lounis et al. “Dynamical Magnetic Excitations of Nanostructures from First Principles”. In: *Physical Review Letters* 105.18 (Oct. 2010), p. 187205. DOI: 10.1103/PhysRevLett.105.187205.

[57] P. Hohenberg and W. Kohn. “Inhomogeneous Electron Gas”. In: *Physical Review* 136.3B (Nov. 1964), B864–B871. DOI: 10.1103/PhysRev.136.B864.

[58] W. Kohn and L. J. Sham. “Self-Consistent Equations Including Exchange and Correlation Effects”. In: *Physical Review* 140.4A (Nov. 1965), A1133–A1138. DOI: 10.1103/PhysRev.140.A1133.

[59] J Korringa. “On the calculation of the energy of a Bloch wave in a metal”. In: *Physica* 13.6 (Aug. 1947), pp. 392–400. ISSN: 0031-8914. DOI: 10.1016/0031-8914(47)90013-X.

[60] W. Kohn and N. Rostoker. “Solution of the Schrödinger Equation in Periodic Lattices with an Application to Metallic Lithium”. In: *Physical Review* 94.5 (June 1954), pp. 1111–1120. DOI: 10.1103/PhysRev.94.1111.

[61] N. Papanikolaou, R. Zeller, and P. H. Dederichs. “Conceptual improvements of the KKR method”. en. In: *Journal of Physics: Condensed Matter* 14.11 (Mar. 2002), pp. 2799–2823. ISSN: 0953-8984. DOI: 10.1088/0953-8984/14/11/304.

[62] H. Ebert, D. Ködderitzsch, and J. Minár. “Calculating condensed matter properties using the KKR-Green’s function method—recent developments and applications”. en. In: *Reports on Progress in Physics* 74.9 (Aug. 2011), p. 096501. ISSN: 0034-4885. DOI: 10.1088/0034-4885/74/9/096501.

[63] H. Ebert and S. Mankovsky. “Anisotropic exchange coupling in diluted magnetic semiconductors: Ab initio spin-density functional theory”. In: *Physical Review B* 79.4 (Jan. 2009), p. 045209. DOI: 10.1103/PhysRevB.79.045209.

[64] Benedikt Johannes Schweflinghaus. “First-principles investigation of inelastic magnetic excitations in nanostructures deposited on surfaces”. PhD thesis. RWTH Aachen University, 2015.

[65] John Carl Villanueva. *How Many Atoms Are There in the Universe?* en-US. July 2009.

[66] M. Born and R. Oppenheimer. "Zur Quantentheorie der Molekeln". en. In: *Annalen der Physik* 389.20 (1927), pp. 457–484. ISSN: 1521-3889. DOI: 10.1002/andp.19273892002.

[67] S. H. Vosko, L. Wilk, and M. Nusair. "Accurate spin-dependent electron liquid correlation energies for local spin density calculations: a critical analysis". In: *Canadian Journal of Physics* 58.8 (Aug. 1980), pp. 1200–1211. ISSN: 0008-4204. DOI: 10.1139/p80-159.

[68] Thomas H Dupree. "Electron scattering in a crystal lattice". In: *Annals of Physics* 15.1 (July 1961), pp. 63–78. ISSN: 0003-4916. DOI: 10.1016/0003-4916(61)90166-X.

[69] Alexander R. Thieß. "Development and application of a massively parallel KKR Green function method for large scale systems". PhD thesis. RWTH Aachen University, 2011.

[70] David Siegfried Georg Bauer. "Development of a relativistic full-potential first-principles multiple scattering Green function method applied to complex magnetic textures of nano structures at surfaces". en. OCLC: 931516104. PhD thesis. Jülich: Forschungszentrum Jülich, 2014.

[71] Flaviano José dos Santos. *Transporte de carga e spin em nanofitas de grafeno com adsorção de impurezas e desordem*. Master Thesis. Universidade Federal Fluminense, 2014.

[72] K. Wildberger et al. "Fermi-Dirac distribution in ab initio Green's-function calculations". In: *Physical Review B* 52.15 (Oct. 1995), pp. 11502–11508. DOI: 10.1103/PhysRevB.52.11502.

[73] K. Wildberger, R. Zeller, and P. H. Dederichs. "Screened KKR-Green's-function method for layered systems". In: *Physical Review B* 55.15 (Apr. 1997), pp. 10074–10080. DOI: 10.1103/PhysRevB.55.10074.

[74] A. Thiess et al. "Massively parallel density functional calculations for thousands of atoms: KKRnano". In: *Physical Review B* 85.23 (June 2012), p. 235103. DOI: 10.1103/PhysRevB.85.235103.

[75] Swantje Heers and Stefan Blügel. "Effect of spin-orbit scattering on transport properties of low-dimensional dilute alloys". English. PhD thesis. Aachen: Publikationsserver der RWTH Aachen University, 2011.

[76] T. Oguchi, K. Terakura, and A. R. Williams. "Band theory of the magnetic interaction in MnO, MnS, and NiO". In: *Physical Review B* 28.11 (Dec. 1983), pp. 6443–6452. DOI: 10.1103/PhysRevB.28.6443.

[77] A. R. Mackintosh and O. K. Andersen. *Electrons at the Fermi surface*. Ed. by Michael Springford and D. Shoenberg. Cambridge [Eng.] ; New York: Cambridge University Press, 1980. ISBN: 978-0-521-22337-9.

[78] V. Heine. *Solid state physics: advances in research and applications. Volume 35 Volume 35*. English. Ed. by Henry Ehrenreich, Frederick Seitz, and David Turnbull. OCLC: 646775678. New York: Academic Press, 1980. ISBN: 978-0-08-086499-0 978-0-12-607735-3.

[79] P. Lloyd. “Wave propagation through an assembly of spheres: III. The density of states in a liquid”. en. In: *Proceedings of the Physical Society* 90.1 (Jan. 1967), pp. 217–231. ISSN: 0370-1328. DOI: 10.1088/0370-1328/90/1/324.

[80] EDWARD PRINCE. “Neutron Scattering Instrumentation: A Tutorial Review”. In: *Applied Spectroscopy Reviews* 34.3 (Sept. 2004), pp. 159–172. ISSN: 0570-4928. DOI: 10.1081/ASR-100100843.

[81] “Inelastic Electron Scattering and Spectroscopy”. en. In: *Transmission Electron Microscopy and Diffractometry of Materials*. Ed. by Brent Fultz and James M. Howe. Berlin, Heidelberg: Springer Berlin Heidelberg, 2008, pp. 163–221. ISBN: 978-3-540-73886-2. DOI: 10.1007/978-3-540-73886-2_4.

[82] Haifeng Yang et al. “Visualizing electronic structures of quantum materials by angle-resolved photoemission spectroscopy”. En. In: *Nature Reviews Materials* 3.9 (Sept. 2018), p. 341. ISSN: 2058-8437. DOI: 10.1038/s41578-018-0047-2.

[83] Robin Woracek et al. “Diffraction in neutron imaging—A review”. In: *Nuclear Instruments and Methods in Physics Research Section A: Accelerators, Spectrometers, Detectors and Associated Equipment*. Radiation Imaging Techniques and Applications 878 (Jan. 2018), pp. 141–158. ISSN: 0168-9002. DOI: 10.1016/j.nima.2017.07.040.

[84] J. R. Sandercock and W. Wettling. “Light scattering from thermal acoustic magnons in yttrium iron garnet”. In: *Solid State Communications* 13.10 (Nov. 1973), pp. 1729–1732. ISSN: 0038-1098. DOI: 10.1016/0038-1098(73)90276-7.

[85] D. L. Mills. “On the magnetic scattering of low energy electrons from the surface of a ferromagnetic crystal”. In: *Journal of Physics and Chemistry of Solids* 28.11 (Nov. 1967), pp. 2245–2255. ISSN: 0022-3697. DOI: 10.1016/0022-3697(67)90250-8.

[86] Schober Helmut. “An introduction to the theory of nuclear neutron scattering in condensed matter”. In: *Journal of Neutron Research* 3-4 (2014), pp. 109–357. ISSN: 1023-8166. DOI: 10.3233/JNR-140016.

[87] Michael P. Marder. *Condensed Matter Physics*. Second Edition. John Wiley & Sons, Nov. 2010. ISBN: 978-0-470-61798-4.

[88] Flaviano José dos Santos, Manuel dos Santos Dias, and Samir Lounis. “First-principles investigation of spin-wave dispersions in surface-reconstructed Co thin films on W(110)”. In: *Physical Review B* 95.13 (Apr. 2017), p. 134408. DOI: 10.1103/PhysRevB.95.134408.

[89] A. T. Costa, R. B. Muniz, and D. L. Mills. “Theory of spin waves in ultrathin ferromagnetic films: The case of Co on Cu(100)”. In: *Phys. Rev. B* 69.6 (Feb. 2004), p. 064413. DOI: 10.1103/PhysRevB.69.064413.

[90] Eugen Michel, Harald Ibach, and Claus M. Schneider. “High resolution electron energy loss spectroscopy of spin waves in ultra-thin cobalt films”. In: *Surface and Interface Analysis* 48.11 (2016), pp. 1104–1107. ISSN: 1096-9918. DOI: 10.1002/sia.6127.

[91] J. F. Cooke, J. W. Lynn, and H. L. Davis. "Calculations of the dynamic susceptibility of nickel and iron". In: *Phys. Rev. B* 21.9 (May 1980), pp. 4118–4131. DOI: 10.1103/PhysRevB.21.4118.

[92] R. B. Muniz and D. L. Mills. "Theory of spin excitations in Fe(110) monolayers". In: *Phys. Rev. B* 66.17 (Nov. 2002), p. 174417. DOI: 10.1103/PhysRevB.66.174417.

[93] A. T. Costa, R. B. Muniz, and D. L. Mills. "Theory of large-wave-vector spin waves in ultrathin ferromagnetic films: Sensitivity to electronic structure". In: *Phys. Rev. B* 70.5 (Aug. 2004), p. 054406. DOI: 10.1103/PhysRevB.70.054406.

[94] P. Buczek et al. "The energies and life times of magnons in bulk iron and one-monolayer Fe film". In: *Journal of Magnetism and Magnetic Materials* 322 (May 2010), pp. 1396–1398. DOI: 10.1016/j.jmmm.2009.03.010.

[95] Andrea Taroni et al. "Suppression of Standing Spin Waves in Low-Dimensional Ferromagnets". In: *Phys. Rev. Lett.* 107.3 (July 2011), p. 037202. DOI: 10.1103/PhysRevLett.107.037202.

[96] J. Rajeswari et al. "Surface spin waves of fcc cobalt films on Cu(100): High-resolution spectra and comparison to theory". In: *Phys. Rev. B* 86.16 (Oct. 2012), p. 165436. DOI: 10.1103/PhysRevB.86.165436.

[97] Paolo Giannozzi et al. "QUANTUM ESPRESSO: a modular and open-source software project for quantum simulations of materials". In: *J. Phys.: Condens. Matter* 21.39 (2009), p. 395502.

[98] H. Knoppe and E. Bauer. "Electronic structure of ultrathin cobalt films on W(110)". In: *Phys. Rev. B* 48.3 (July 1993), pp. 1794–1805. DOI: 10.1103/PhysRevB.48.1794.

[99] J. G. Ociepa et al. "Re-emitted positron energy spectroscopy from thin Co films on W(110)". In: *Surface Science* 225.3 (Jan. 1990), pp. 281–291. ISSN: 0039-6028. DOI: 10.1016/0039-6028(90)90449-I.

[100] D. Spišák and J. Hafner. "Theoretical study of FeCo/W(1 1 0) surface alloys". In: *Journal of Magnetism and Magnetic Materials*. Proceedings of the 5th International Symposium on Metallic Multilayers 286 (Feb. 2005), pp. 386–389. ISSN: 0304-8853. DOI: 10.1016/j.jmmm.2004.09.096.

[101] H. Fritzsche, J. Kohlhepp, and U. Gradmann. "Epitaxial strain and magnetic anisotropy in ultrathin Co films on W(110)". In: *Phys. Rev. B* 51.22 (June 1995), pp. 15933–15941. DOI: 10.1103/PhysRevB.51.15933.

[102] M. Pratzer, H. J. Elmers, and M. Getzlaff. "Heteroepitaxial growth of Co on W(110) investigated by scanning tunneling microscopy". In: *Phys. Rev. B* 67.15 (Apr. 2003), p. 153405. DOI: 10.1103/PhysRevB.67.153405.

[103] Henning Prüser et al. "Interplay between the Kondo effect and the Ruderman–Kittel–Kasuya–Yosida interaction". In: *Nature Communications* 5 (Nov. 2014), p. 5417. ISSN: 2041-1723. DOI: 10.1038/ncomms6417.

[104] Mohammed Bouhassoune et al. "Quantum well states and amplified spin-dependent Friedel oscillations in thin films". en. In: *Nat Commun* 5 (Nov. 2014). DOI: 10.1038/ncomms6558.

[105] Alexander Weismann et al. “Seeing the Fermi Surface in Real Space by Nanoscale Electron Focusing”. In: *Science* 323.5918 (Feb. 2009), pp. 1190–1193. ISSN: 0036-8075, 1095-9203. DOI: 10.1126/science.1168738.

[106] Samir Lounis et al. “Theory of real space imaging of Fermi surface parts”. In: *Phys. Rev. B* 83.3 (Jan. 2011), p. 035427. DOI: 10.1103/PhysRevB.83.035427.

[107] Mathias C. T. D. Müller, Christoph Friedrich, and Stefan Blügel. “Acoustic magnons in the long-wavelength limit: Investigating the Goldstone violation in many-body perturbation theory”. In: *Physical Review B* 94.6 (Aug. 2016), p. 064433. DOI: 10.1103/PhysRevB.94.064433.

[108] J. Rajeswari, H. Ibach, and C. M. Schneider. “Standing Spin Waves in Ultrathin Magnetic Films: A Method to Test for Layer-Dependent Exchange Coupling”. In: *Phys. Rev. Lett.* 112.12 (Mar. 2014), p. 127202. DOI: 10.1103/PhysRevLett.112.127202.

[109] D. C. M. Rodrigues et al. “Finite-temperature interatomic exchange and magnon softening in Fe overlayers on Ir(001)”. In: *Phys. Rev. B* 94.1 (July 2016), p. 014413.

[110] A. Szilva et al. “Interatomic Exchange Interactions for Finite-Temperature Magnetism and Nonequilibrium Spin Dynamics”. In: *Phys. Rev. Lett.* 111.12 (Sept. 2013), p. 127204. DOI: 10.1103/PhysRevLett.111.127204.

[111] Markus Hoffmann et al. “Antiskyrmions stabilized at interfaces by anisotropic Dzyaloshinskii-Moriya interactions”. En. In: *Nature Communications* 8.1 (Aug. 2017), p. 308. ISSN: 2041-1723. DOI: 10.1038/s41467-017-00313-0.

[112] N. S. Kiselev et al. “Chiral skyrmions in thin magnetic films: new objects for magnetic storage technologies?” In: *J. Phys. D: Appl. Phys.* 44.39 (2011), p. 392001. ISSN: 0022-3727. DOI: 10.1088/0022-3727/44/39/392001.

[113] Albert Fert, Vincent Cros, and João Sampaio. “Skyrmions on the track”. en. In: *Nature Nanotechnology* 8.3 (Mar. 2013), pp. 152–156. ISSN: 1748-3387. DOI: 10.1038/nnano.2013.29.

[114] Niklas Romming et al. “Writing and Deleting Single Magnetic Skyrmions”. In: *Science* 341.6146 (Aug. 2013), pp. 636–639. ISSN: 0036-8075, 1095-9203. DOI: 10.1126/science.1240573.

[115] Stefan Heinze et al. “Spontaneous atomic-scale magnetic skyrmion lattice in two dimensions”. In: *Nat Phys* 7.9 (Sept. 2011), pp. 713–718. ISSN: 1745-2473. DOI: 10.1038/nphys2045.

[116] B. Lenk et al. “The building blocks of magnonics”. In: *Physics Reports* 507.4 (Oct. 2011), pp. 107–136. ISSN: 0370-1573. DOI: 10.1016/j.physrep.2011.06.003.

[117] Manuel Pereiro et al. “Topological excitations in a kagome magnet”. In: *Nature Communications* 5 (Sept. 2014), ncomms5815. ISSN: 2041-1723. DOI: 10.1038/ncomms5815.

[118] R. Chisnell et al. “Topological Magnon Bands in a Kagome Lattice Ferromagnet”. In: *Phys. Rev. Lett.* 115.14 (Sept. 2015), p. 147201. DOI: 10.1103/PhysRevLett.115.147201.

[119] D. Belitz, T. R. Kirkpatrick, and A. Rosch. "Theory of helimagnons in itinerant quantum systems". In: *Phys. Rev. B* 73.5 (Feb. 2006), p. 054431. DOI: 10.1103/PhysRevB.73.054431.

[120] M. Janoschek et al. "Helimagnon bands as universal excitations of chiral magnets". In: *Phys. Rev. B* 81.21 (June 2010), p. 214436. DOI: 10.1103/PhysRevB.81.214436.

[121] Masahito Mochizuki. "Spin-Wave Modes and Their Intense Excitation Effects in Skyrmion Crystals". In: *Phys. Rev. Lett.* 108.1 (Jan. 2012), p. 017601. DOI: 10.1103/PhysRevLett.108.017601.

[122] Junichi Iwasaki, Aron J. Beekman, and Naoto Nagaosa. "Theory of magnon-skyrmion scattering in chiral magnets". In: *Phys. Rev. B* 89.6 (Feb. 2014), p. 064412. DOI: 10.1103/PhysRevB.89.064412.

[123] T. Schwarze et al. "Universal helimagnon and skyrmion excitations in metallic, semiconducting and insulating chiral magnets". In: *Nat Mater* 14.5 (May 2015), pp. 478–483. ISSN: 1476-1122. DOI: 10.1038/nmat4223.

[124] Fusheng Ma et al. "Skyrmion-Based Dynamic Magnonic Crystal". In: *Nano Lett.* 15.6 (June 2015), pp. 4029–4036. ISSN: 1530-6984. DOI: 10.1021/acs.nanolett.5b00996.

[125] A. L. Chernyshev and P. A. Maksimov. "Damped Topological Magnons in the Kagome-Lattice Ferromagnets". In: *Phys. Rev. Lett.* 117.18 (Oct. 2016), p. 187203. DOI: 10.1103/PhysRevLett.117.187203.

[126] Mathias Weiler et al. "Helimagnon Resonances in an Intrinsic Chiral Magnonic Crystal". In: *Physical Review Letters* 119.23 (Dec. 2017), p. 237204. DOI: 10.1103/PhysRevLett.119.237204.

[127] Sahbi El Hog, H. T. Diep, and Henryk Puszkarski. "Theory of magnons in spin systems with Dzyaloshinskii–Moriya interaction". In: *J. Phys.: Condens. Matter* 29.30 (2017), p. 305001. ISSN: 0953-8984. DOI: 10.1088/1361-648X/aa75a4.

[128] W. X. Tang et al. "Large Wave Vector Spin Waves and Dispersion in Two Monolayer Fe on $W(110)$". In: *Phys. Rev. Lett.* 99.8 (Aug. 2007), p. 087202. DOI: 10.1103/PhysRevLett.99.087202.

[129] J. Prokop et al. "Magnons in a Ferromagnetic Monolayer". In: *Phys. Rev. Lett.* 102.17 (Apr. 2009), p. 177206. DOI: 10.1103/PhysRevLett.102.177206.

[130] Y. Zhang et al. "Elementary Excitations at Magnetic Surfaces and Their Spin Dependence". In: *Phys. Rev. Lett.* 106.12 (Mar. 2011), p. 127201. DOI: 10.1103/PhysRevLett.106.127201.

[131] Kh Zakeri et al. "Direct probing of the exchange interaction at buried interfaces". In: *Nat Nano* 8.11 (Nov. 2013), pp. 853–858. ISSN: 1748-3387. DOI: 10.1038/nnano.2013.188.

[132] H. J. Qin et al. "Temperature Dependence of Magnetic Excitations: Terahertz Magnons above the Curie Temperature". In: *Phys. Rev. Lett.* 118.12 (Mar. 2017), p. 127203. DOI: 10.1103/PhysRevLett.118.127203.

[133] M. P. Gokhale, A. Ormeci, and D. L. Mills. "Inelastic scattering of low-energy electrons by spin excitations on ferromagnets". In: *Physical Review B* 46.14 (Oct. 1992), pp. 8978–8993. DOI: 10.1103/PhysRevB.46.8978.

[134] S. V. Maleyev. "Cubic magnets with Dzyaloshinskii-Moriya interaction at low temperature". In: *Phys. Rev. B* 73.17 (May 2006), p. 174402. DOI: 10.1103/PhysRevB.73.174402.

[135] I. Fischer and A. Rosch. "Weak spin-orbit interactions induce exponentially flat mini-bands in magnetic metals without inversion symmetry". In: *EPL* 68.1 (Oct. 2004), p. 93. ISSN: 0295-5075. DOI: 10.1209/epl/i2004-10174-9.

[136] Pengcheng Dai et al. "Magnon damping by magnon-phonon coupling in manganese perovskites". In: *Physical Review B* 61.14 (Apr. 2000), pp. 9553–9557. DOI: 10.1103/PhysRevB.61.9553.

[137] R. B. Muniz, A. T. Costa, and D. L. Mills. "Microscopic theory of spin waves in ultrathin ferromagnetic films: Fe on W(110)". In: *J. Phys.: Condens. Matter* 15.5 (Jan. 2003), S495. ISSN: 0953-8984. DOI: 10.1088/0953-8984/15/5/305.

[138] Erik D. Schaefer et al. "Vectorial spin polarization detection in multichannel spin-resolved photoemission spectroscopy using an Ir(001) imaging spin filter". In: *Phys. Rev. B* 95.10 (Mar. 2017), p. 104423. DOI: 10.1103/PhysRevB.95.104423.

[139] H. Batelaan, T. J. Gay, and J. J. Schwendiman. "Stern-Gerlach Effect for Electron Beams". In: *Phys. Rev. Lett.* 79.23 (Dec. 1997), pp. 4517–4521. DOI: 10.1103/PhysRevLett.79.4517.

[140] George H. Rutherford and Rainer Grobe. "Comment on "Stern-Gerlach Effect for Electron Beams"". In: *Phys. Rev. Lett.* 81.21 (Nov. 1998), pp. 4772–4772. DOI: 10.1103/PhysRevLett.81.4772.

[141] B. M. Garraway and S. Stenholm. "Observing the spin of a free electron". In: *Phys. Rev. A* 60.1 (July 1999), pp. 63–79. DOI: 10.1103/PhysRevA.60.63.

[142] B. M. Garraway and S. Stenholm. "Does a flying electron spin?" In: *Contemporary Physics* 43.3 (May 2002), pp. 147–160. ISSN: 0010-7514. DOI: 10.1080/00107510110102119.

[143] J. Larson, B. M. Garraway, and S. Stenholm. "Transient effects on electron spin observation". In: *Phys. Rev. A* 69.3 (Mar. 2004), p. 032103. DOI: 10.1103/PhysRevA.69.032103.

[144] Ebrahim Karimi et al. "Spin-to-Orbital Angular Momentum Conversion and Spin-Polarization Filtering in Electron Beams". In: *Phys. Rev. Lett.* 108.4 (Jan. 2012), p. 044801. DOI: 10.1103/PhysRevLett.108.044801.

[145] T. Jungwirth et al. "Antiferromagnetic spintronics". En. In: *Nature Nanotechnology* 11.3 (Mar. 2016), p. 231. ISSN: 1748-3395. DOI: 10.1038/nnano.2016.18.

[146] O. Gomonay, T. Jungwirth, and J. Sinova. "Concepts of antiferromagnetic spintronics". en. In: *physica status solidi (RRL) – Rapid Research Letters* 11.4 (Apr. 2017), n/a–n/a. ISSN: 1862-6270. DOI: 10.1002/pssr.201700022.

[147] X. Marti et al. “Room-temperature antiferromagnetic memory resistor”. En. In: *Nature Materials* 13.4 (Apr. 2014), p. 367. ISSN: 1476-4660. DOI: 10.1038/nmat3861.

[148] G. Gitgeatpong et al. “Nonreciprocal Magnons and Symmetry-Breaking in the Noncentrosymmetric Antiferromagnet”. In: *Physical Review Letters* 119.4 (July 2017), p. 047201. DOI: 10.1103/PhysRevLett.119.047201.

[149] Joseph Barker and Oleg A. Tretiakov. “Static and Dynamical Properties of Antiferromagnetic Skyrmions in the Presence of Applied Current and Temperature”. In: *Physical Review Letters* 116.14 (Apr. 2016), p. 147203. DOI: 10.1103/PhysRevLett.116.147203.

[150] P. Ferriani et al. “Magnetic Phase Control in Monolayer Films by Substrate Tuning”. In: *Physical Review Letters* 99.18 (Nov. 2007), p. 187203. DOI: 10.1103/PhysRevLett.99.187203.

[151] M. Costa et al. “β-tungsten: a promising metal for spintronics”. en. In: *Journal of Physics: Condensed Matter* 30.30 (July 2018), p. 305802. ISSN: 0953-8984. DOI: 10.1088/1361-648X/aacc08.

[152] Michael Gottschilch et al. “Study of the antiferromagnetism of Mn5Si3: an inverse magnetocaloric effect material”. en. In: *Journal of Materials Chemistry* 22.30 (July 2012), pp. 15275–15284. ISSN: 1364-5501. DOI: 10.1039/C2JM00154C.

[153] Nikolaos Biniskos, Karin Schmalzl, and Stephane Raymond. “Experimental data of inelastic neutron scattering spectroscopy on Mn5Si3”. In: *Private communication* (2018).

[154] Lorenzo Camosi et al. “Anisotropic Dzyaloshinskii-Moriya interaction in ultrathin epitaxial Au/Co/W(110)”. In: *Physical Review B* 95.21 (June 2017), p. 214422. DOI: 10.1103/PhysRevB.95.214422.

[155] U. K. Rößler, A. N. Bogdanov, and C. Pfleiderer. “Spontaneous skyrmion ground states in magnetic metals”. En. In: *Nature* 442.7104 (Aug. 2006), p. 797. ISSN: 1476-4687. DOI: 10.1038/nature05056.

[156] S. Mühlbauer et al. “Skyrmion Lattice in a Chiral Magnet”. en. In: *Science* 323.5916 (Feb. 2009), pp. 915–919. ISSN: 0036-8075, 1095-9203. DOI: 10.1126/science.1166767.

[157] X. Z. Yu et al. “Real-space observation of a two-dimensional skyrmion crystal”. en. In: *Nature* 465.7300 (June 2010), pp. 901–904. ISSN: 1476-4687. DOI: 10.1038/nature09124.

[158] T. Adams et al. “Long-Wavelength Helimagnetic Order and Skyrmion Lattice Phase in Cu_2OSeO_3”. In: *Physical Review Letters* 108.23 (June 2012), p. 237204. DOI: 10.1103/PhysRevLett.108.237204.

[159] Wataru Koshibae and Naoto Nagaosa. “Theory of antiskyrmions in magnets”. En. In: *Nature Communications* 7 (Jan. 2016), p. 10542. ISSN: 2041-1723. DOI: 10.1038/ncomms10542.

[160] Ulrike Ritzmann et al. “Trochoidal motion and pair generation in skyrmion and antiskyrmion dynamics under spin–orbit torques”. En. In: *Nature Electronics* 1.8 (Aug. 2018), p. 451. ISSN: 2520-1131. DOI: 10.1038/s41928-018-0114-0.

[161] Alexey A. Kovalev and Shane Sandhoefner. “Skyrmions and Antiskyrmions in Quasi-Two-Dimensional Magnets”. English. In: *Frontiers in Physics* 6 (2018). ISSN: 2296-424X. DOI: 10.3389/fphy.2018.00098.

[162] J. J. Liang et al. “Magnetic field gradient driven dynamics of isolated skyrmions and antiskyrmions in frustrated magnets”. en. In: *New Journal of Physics* 20.5 (May 2018), p. 053037. ISSN: 1367-2630. DOI: 10.1088/1367-2630/aac24c.

[163] Changhoon Heo et al. “Switching of chiral magnetic skyrmions by picosecond magnetic field pulses via transient topological states”. en. In: *Scientific Reports* 6 (June 2016), p. 27146. ISSN: 2045-2322. DOI: 10.1038/srep27146.

[164] Y. A. Kharkov, O. P. Sushkov, and M. Mostovoy. “Bound States of Skyrmions and Merons near the Lifshitz Point”. In: *Physical Review Letters* 119.20 (Nov. 2017), p. 207201. DOI: 10.1103/PhysRevLett.119.207201.

[165] Börge Göbel et al. “Magnetic bimerons as skyrmion analogues in in-plane magnets”. In: *Physical Review B* 99.6 (Feb. 2019), p. 060407. DOI: 10.1103/PhysRevB.99.060407.

[166] Byron G. Johnson et al. “The structural and chemisorptive properties of ultrathin cobalt overlayers on W(110) and W(100)”. In: *Surface Science* 217.1 (July 1989), pp. 13–37. ISSN: 0039-6028. DOI: 10.1016/0039-6028(89)90532-3.

[167] A. Bettac et al. “Structure and magnetism of hcp(0001) and fcc(001) thin cobalt films on a clean and carbon-reconstructed W(110) surface”. In: *Surface Science* 454-456 (May 2000), pp. 936–941. ISSN: 0039-6028. DOI: 10.1016/S0039-6028(00)00184-9.

[168] Isabelle M. L. Billas, A. Châtelain, and Walt A. de Heer. “Magnetism from the Atom to the Bulk in Iron, Cobalt, and Nickel Clusters”. en. In: *Science* 265.5179 (Sept. 1994), pp. 1682–1684. ISSN: 0036-8075, 1095-9203. DOI: 10.1126/science.265.5179.1682.

[169] B. Schweflinghaus et al. “Role of Dzyaloshinskii-Moriya interaction for magnetism in transition-metal chains at Pt step edges”. In: *Physical Review B* 94.2 (July 2016), p. 024403. DOI: 10.1103/PhysRevB.94.024403.

[170] Miriam Hinzen. *Magnetisierungsfelder in ferromagnetischen Kristallen mit Dzyaloshinskii-Moriya-Wechselwirkung*. Master Thesis. RWTH Aachen University, 2015.

[171] Pavel F. Bessarab, Valery M. Uzdin, and Hannes Jónsson. “Method for finding mechanism and activation energy of magnetic transitions, applied to skyrmion and antivortex annihilation”. In: *Computer Physics Communications* 196 (Nov. 2015), pp. 335–347. ISSN: 0010-4655. DOI: 10.1016/j.cpc.2015.07.001.

[172] Se Kwon Kim. "Dynamics of bimeron skyrmions in easy-plane magnets induced by a spin supercurrent". In: *Physical Review B* 99.22 (June 2019), p. 224406. DOI: 10.1103/PhysRevB.99.224406.

[173] M. Pajda et al. "Ab initio calculations of exchange interactions, spin-wave stiffness constants, and Curie temperatures of Fe, Co, and Ni". In: *Physical Review B* 64.17 (Oct. 2001), p. 174402. DOI: 10.1103/PhysRevB.64.174402.

[174] A. Van Oosterom and J. Strackee. "The Solid Angle of a Plane Triangle". In: *IEEE Transactions on Biomedical Engineering* BME-30.2 (Feb. 1983), pp. 125–126. ISSN: 0018-9294. DOI: 10.1109/TBME.1983.325207.

[175] E Alba, J K Pachos, and J J García-Ripoll. "Winding number order in the Haldane model with interactions". en. In: *New Journal of Physics* 18.3 (Mar. 2016), p. 033022. ISSN: 1367-2630. DOI: 10.1088/1367-2630/18/3/033022.

[176] Kai Di et al. "Direct Observation of the Dzyaloshinskii-Moriya Interaction in a Pt/Co/Ni Film". In: *Physical Review Letters* 114.4 (Jan. 2015), p. 047201. DOI: 10.1103/PhysRevLett.114.047201.

[177] Y. Iguchi et al. "Nonreciprocal magnon propagation in a noncentrosymmetric ferromagnet $LiFe_5O_8$". In: *Physical Review B* 92.18 (Nov. 2015), p. 184419. DOI: 10.1103/PhysRevB.92.184419.

[178] Taku J. Sato et al. "Magnon dispersion shift in the induced ferromagnetic phase of noncentrosymmetric MnSi". In: *Physical Review B* 94.14 (Oct. 2016), p. 144420. DOI: 10.1103/PhysRevB.94.144420.

[179] T. Weber et al. "Field dependence of nonreciprocal magnons in chiral MnSi". In: *Physical Review B* 97.22 (June 2018), p. 224403. DOI: 10.1103/PhysRevB.97.224403.

[180] T. Weber et al. "Non-reciprocal magnons in non-centrosymmetric MnSi". In: *AIP Advances* 8.10 (Oct. 2018), p. 101328. DOI: 10.1063/1.5041036.

[181] Sang-Wook Cheong et al. "Broken symmetries, non-reciprocity, and multiferroicity". en. In: *npj Quantum Materials* 3.1 (Apr. 2018), p. 19. ISSN: 2397-4648. DOI: 10.1038/s41535-018-0092-5.

[182] Suik Cheon, Hyun-Woo Lee, and Sang-Wook Cheong. "Nonreciprocal spin waves in a chiral antiferromagnet without the Dzyaloshinskii-Moriya interaction". In: *Physical Review B* 98.18 (Nov. 2018), p. 184405. DOI: 10.1103/PhysRevB.98.184405.

[183] R. A. Gallardo et al. "Flat Bands, Indirect Gaps, and Unconventional Spin-Wave Behavior Induced by a Periodic Dzyaloshinskii-Moriya Interaction". In: *Physical Review Letters* 122.6 (Feb. 2019), p. 067204. DOI: 10.1103/PhysRevLett.122.067204.

[184] P. W. Anderson. "More Is Different". en. In: *Science* 177.4047 (Aug. 1972), pp. 393–396. ISSN: 0036-8075, 1095-9203. DOI: 10.1126/science.177.4047.393.

[185] M. Bode et al. "Chiral magnetic order at surfaces driven by inversion asymmetry". en. In: *Nature* 447.7141 (May 2007), pp. 190–193. ISSN: 0028-0836. DOI: 10.1038/nature05802.

[186] P. Ferriani et al. “Atomic-Scale Spin Spiral with a Unique Rotational Sense: Mn Monolayer on W(001)”. In: *Physical Review Letters* 101.2 (July 2008), p. 027201. DOI: 10.1103/PhysRevLett.101.027201.

[187] Roger S. K. Mong, Andrew M. Essin, and Joel E. Moore. “Antiferromagnetic topological insulators”. In: *Physical Review B* 81.24 (June 2010), p. 245209. DOI: 10.1103/PhysRevB.81.245209.

[188] V. E. Dmitrienko et al. “Measuring the Dzyaloshinskii–Moriya interaction in a weak ferromagnet”. en. In: *Nature Physics* 10.3 (Mar. 2014), pp. 202–206. ISSN: 1745-2481. DOI: 10.1038/nphys2859.

[189] Chuanpu Liu et al. “Long-distance propagation of short-wavelength spin waves”. en. In: *Nature Communications* 9.1 (Feb. 2018), pp. 1–8. ISSN: 2041-1723. DOI: 10.1038/s41467-018-03199-8.

[190] S. Grytsiuk et al. “Topological-chiral magnetic interactions driven by emergent orbital magnetism”. In: *arXiv:1904.02369 [cond-mat]* (Apr. 2019). arXiv: 1904.02369.

[191] F. N. Rybakov et al. “Magnetic hopfions in solids”. In: *arXiv:1904.00250 [cond-mat, physics:nlin]* (Mar. 2019). arXiv: 1904.00250.

[192] Simon Streib et al. “Magnon-phonon interactions in magnetic insulators”. In: *Physical Review B* 99.18 (May 2019), p. 184442. DOI: 10.1103/PhysRevB.99.184442.

[193] Subrata Chakraborty and Tero T. Heikkilä. “Thermalization of hot electrons via interfacial electron-magnon interaction”. In: *Physical Review B* 100.3 (July 2019), p. 035423. DOI: 10.1103/PhysRevB.100.035423.

[194] M. Merdan and Yang Xian. “The Effects of Three Magnons Interactions in the Magnon-Density Waves of Triangular Spin Lattices”. en. In: *Journal of Low Temperature Physics* 197.1 (Oct. 2019), pp. 81–94. ISSN: 1573-7357. DOI: 10.1007/s10909-019-02217-3.

[195] Filipe S. M. Guimarães et al. “Engineering elliptical spin-excitations by complex anisotropy fields in Fe adatoms and dimers on Cu(111)”. In: *Physical Review B* 96.14 (Oct. 2017), p. 144401. DOI: 10.1103/PhysRevB.96.144401.

[196] Benedikt Schweflinghaus et al. “Renormalization of electron self-energies via their interaction with spin excitations: A first-principles investigation”. In: *Physical Review B* 89.23 (June 2014), p. 235439. DOI: 10.1103/PhysRevB.89.235439.

[197] Benedikt Schweflinghaus, Manuel dos Santos Dias, and Samir Lounis. “Observing spin excitations in 3*d* transition-metal adatoms on Pt(111) with inelastic scanning tunneling spectroscopy: A first-principles perspective”. In: *Physical Review B* 93.3 (Jan. 2016), p. 035451. DOI: 10.1103/PhysRevB.93.035451.

[198] A. A. Sirenko et al. “Terahertz Vortex Beam as a Spectroscopic Probe of Magnetic Excitations”. In: *Physical Review Letters* 122.23 (June 2019), p. 237401. DOI: 10.1103/PhysRevLett.122.237401.

[199] A. V. Ruban et al. “Temperature-induced longitudinal spin fluctuations in Fe and Ni”. In: *Physical Review B* 75.5 (Feb. 2007), p. 054402. DOI: 10.1103/PhysRevB.75.054402.

[200] A. M. Belemuk and S. M. Stishov. “Influence of longitudinal spin fluctuations on the phase transition features in chiral magnets”. In: *Physical Review B* 97.14 (Apr. 2018), p. 144419. DOI: 10.1103/PhysRevB.97.144419.

List of Figures

List of Tables

Curriculum vitae

Flaviano José dos Santos

Peter Grünberg Institut & Institute for Advanced Simulation
Forschungszentrum Jülich, D-52425 Jülich – Germany
+49 1511 9665115
f.dos.santos@fz-juelich.de
www.researchgate.net/profile
Date of Birth: 09.11.1989, Brazil

Education

2014–2019	**Ph.D. in Physics**, *Forschungszentrum Jülich & RWTH Aachen* Jülich – Germany
Thesis title	*First-principles study of collective spin excitations in noncollinear magnets*
Supervisor	Prof. Dr. Samir Lounis
2012–2014	**Master in Physics (M.Sc.)**, *Fluminense Federal University* Niterói, Rio de Janeiro – Brazil
Thesis title	*Charge and spin transport in graphene nanoribbons with absorbed impurities and disorder*
Supervisor	Prof. Dr. Roberto Bechara Muniz
2008–2012	**Bachelor in Physics (B.Sc.)**, *Federal University of Alagoas* Maceió, Alagoas – Brazil
Thesis title	*Interacting neural networks*
Supervisor	Prof. Dr. Crisógono R. da Silva

Awards

- 2018 – Best Poster Award - 21st International Conference on Magnetism (ICM-2018), San Francisco, USA.

- 2014 – 4-years abroad Ph.D. scholarship from CAPES - Coordination for the Improvement of Higher Education Personnel, Brazil.
- 2013 – Prize for the second-highest grade at the UFPE Summer School 2013 - Federal University of Pernambuco.
- 2012 – 2-years Master scholarship from CNPq - National Council for Scientific and Technological Development.
- 2009 – 3-years Scientific Initiation scholarship from CNPq - National Council for Scientific and Technological Development.
- 2005 – Honorable mention at the OBMEP - Brazilian Mathematics Olympics of the public schools.

Main scientific topics

- Static and dynamical properties of noncollinear spin textures in bulk and low-dimensional systems
- First-principles electronic and magnetic properties of real magnetic materials
- Collective spin excitations (spin waves) in topologically nontrivial magnetic structures
- Antiferromagnetic noncollinear magnets
- Theory of electron-energy-loss spectroscopy
- Theory of inelastic neutron scattering
- Spin-orbit coupling effects on the static and dynamical magnetic properties
- Nonreciprocity of spin waves in noncollinear magnets
- Charge and spin quantum transport in graphene nanoribbon
- Spin-orbit coupling effects induced by adatoms in graphene
- Quantum-spin-Hall phases in graphene

Collaborations

I currently benefit from and maintain collaborations with these theoretical and experimental groups:

- Experiment: Inelastic neutron scattering, with Nikolaos Biniskos[1,2], Karin Schmalzl[1] and Stéphane Raymond[2]
  1 Jülich Centre for Neutron Science, Forschungszentrum Jülich, Germany
  2 Université Grenoble Alpes, CEA, INAC, MEM, 38000 Grenoble, France
- Experiment: Electron-energy-loss Spectroscopy (EELS), with Harold Ibach
  Electronic Properties, Peter Grünberg Institut (PGI-6), Forschungszentrum Jülich, Germany

- Theory: Spin transport and spin-orbitronics, with Aires Ferreira
  Department of Physics University of York, United Kingdom

List of Publications

Published:

[1] **F. J. dos Santos**, M. dos Santos Dias, and S. Lounis, "First-principles investigation of spin-wave dispersions in surface-reconstructed Co thin films on W(110)," *Physical Review B* 95, 134408 (2017).

[2] **F. J. dos Santos**, M. dos Santos Dias, F. S. M. Guimarães, J. Bouaziz, and S. Lounis, "Spin-resolved inelastic electron scattering by spin waves in noncollinear magnets," *Physical Review B* 97, 024431 (2018).

[3] **F. J. dos Santos**, D. A. Bahamon, R. B. Muniz, K. McKenna, E. V. Castro, J. Lischner, and A. Ferreira, "Impact of complex adatom-induced interactions on quantum spin Hall phases," *Physical Review B (Rapid Communication)* 98, 081407(R) (2018).

In preparation:

[4] **F. J. dos Santos**, M. Hoffmann, M. dos Santos Dias, B. Zimmermann, S. Blügel, and S. Lounis, "First-principles prediction of in-plane skyrmions"

[5] **F. J. dos Santos**, N. Biniskos, M. dos Santos Dias, K. Schmalzl, S. Blügel, S. Raymond, and S. Lounis, "Spin waves and spin fluctuations in the Mn_5Si_3 compound"

[6] **F. J. dos Santos**, M. dos Santos Dias, and S. Lounis, "Nonreciprocity of spin waves in noncollinear magnets due to the Dzyaloshinskii-Moriya interaction"

Computational skills

- Programming and developing: Fortran 90/95, Python, Git, bash script, C/C++, OpenMP, MPI, LAPACK
- Productivity and scientific visualization: GR framework (in python), matplotlib, gnuplot, xmgrace, LaTeX, Mathematica, Microsoft Office
- OS: macOS, Linux, Windows
- Experience with the usage and high-performance development for supercomputers. Among others, I have worked with the JURECA supercomputer in Germany and the ARCHER supercomputer in the United Kingdom, two of the largest supercomputers in Europe.

Selected scientific communications

- DPG Spring Meeting, *Electronic properties and spin waves of Mn_5Si_3 from first principles*, Regensburg, Germany (2019)
- DPG Spring Meeting, *Nonreciprocity of spin waves due to the Dzyaloshinskii-Moriya interaction*, Regensburg, Germany (2019)
- Invited lecture, *Topological phases in adatom-decorated graphene*, 2nd Advanced School on Materials modeling and simulations from first principles and beyond, Mohammed V University in Rabat, Morocco (2018)
- Sol-SkyMag Spring Meeting, *Spin-resolved inelastic electron scattering by spin waves in noncollinear magnets*, San Sebastian, Spain (2018)
- Invited talk, *Large-scale quantum transport studies of topological phases in adatom-decorated graphene*, First-Principles Modelling and Quantum Transport Simulations of 2D Materials workshop, University of York, United Kingdom (2018)
- DPG Spring Meeting, *Prospecting antiskyrmions in ultrathin Co films deposited on W(110)*, Berlin, Germany (2018)
- DPG Spring Meeting, *Theory of inelastic electron scattering by spin waves in non-collinear magnets*, Germany (2017)
- Invited talk, *Spin waves in thin films and non-collinear magnetic structures from first-principles*, UFAL - Brazil (2016)
- DPG Spring Meeting, *Investigation of spin-wave dispersions in Co thin films on W(110) from first-principles*, Germany (2016)
- Invited talk, DAAD Ph.D. Seminar, *Spin waves! A first principle investigation.*, Germany (2015)
- DPG Spring Meeting, *Charge and spin transport in graphene nanoribbons with adatoms and defects*, Germany (2015)
- Invited talk, *Charge and spin transport in graphene ribbons with absorbed impurities and disorder*, UFAL - Brazil (2014)
- XXXV ENFMC Brazilian Physical Society Meeting, *Mutually Assisted Recognition in Hopfield type Coupled Neural Networks*, Brazil (2012)

Teaching Experience

- 2018 – Guest Lecturer for the Moroccan-German partnership on "Advanced School on Materials modelling and simulations from first principles and beyond", at the Mohammed V University, Rabat - Morocco.

- 2017 – Guest Lecturer and co-organizer for the Moroccan-German partnership on "Modelling and simulations of physical properties of nanomaterials II", at the Mohammed V University, Rabat - Morocco.
- 2012 - 2014 – Tutor in Basic Math, Calculus 1, Linear Algebra and Analytical Geometry for physics undergraduate students at Fluminense Federal University, Rio de Janeiro - Brazil.

Extracurricular education

- 50th IFF Spring School on *Scattering! Soft, Functional and Quantum Materials*, Forschungszentrum Jülich, Germany (2019)
- ViCoM Winter School on *Magnetism*, Vienna University of Technology, Austria (2017)
- CAMD Summer School on *Electronic Structure Theory and Materials Design*, Denmark (2016)
- 47th IFF Spring School on *Memristive Phenomena*, Germany (2016)
- UPFE Summer School on *Quantum Mechanics, Thermodynamics and advanced seminars*, Federal University of Pernambuco, Brazil (2013)
- UPFE Summer School on *Electromagnetism, Statistical mechanics and advanced seminars*, Federal University of Pernambuco, Brazil (2012)
- UFMG Winter School, colloquia, minicourses and lab visits, Federal University of Minas Gerais, Brazil (2011)

Language proficiencies

- Portuguese: native speaker
- English: fluent
- German: intermediate

Acknowledgments

It was a long journey that brought me here to the conclusion of this thesis. On the way, I could count on the help and support of many people. Here, I would like to thank them, but with an immediate realization that words will not live up to my feelings.

Initially, I would like to thank Prof. Dr. Samir Lounis for receiving me into his research group and guarding me under his supervision. Without him having first entrusted the job to me, this thesis would not come to be. Also, I am extremely grateful to Dr. Manuel dos Santos Dias who closely accompanied my work during my PhD studies.

Next, I would like to thank Prof. Dr. Riccardo Mazzarello for accepting to read and report on this dissertation. Many thanks go to Prof. Dr. Stefan Blügel for welcoming me to the PGI-1/IAS-1 institute and for guaranteeing the resources and enjoyable environment of our institute. I am also grateful to Prof. Dr. Roberto Bechara Muniz, who always supported me even from so far away, and the Brazilian people who funded most of my PhD studies. I hope you too have learned a thing or two in the past few years.

I thank every friend and colleague I encountered throughout my stay in Jülich and Düren in the past years. They made this period pleasant and memorable. Special thanks go to Philippe Czaja and Marta Gibertini, Dr. Alexei Richter and Dr. Maria Quade and little Nikita, Elisa Polesa, Aude Berbezier, Aryak Singh, Philipp and Resi Böhnke, Guido Kruschwitz, and Lucas da Costa Campos. Also, thanks to all my sports friends (they are too many to be individually mentioned here). Many thanks for all the volleyball, football, skiing and much more.

From PGI-1, my gratitude goes to Dr. Benedikt Schweflinghaus, Dr. Juba Bouaziz, Elias Rabel, Dr. Marcel Bornemann, Dr. Bernd Zimmermann, Dr. Philipp Rüssmann, Markus Hoffmann, Sasha Brinker, Sufyan Shehada, Donya Mazhjoo... Especially, I thank Dr. Julen Ibañez Azpiroz and Nerea Ibarra for all the cycling, hiking and friendship. Also to dear Dr. Imara Lima Fernandes for her friendship and all the marvelous cakes she has spoiled us with. What about Dr. Filipe Souza Mendes Guimarães? I cannot thank him enough for his friendship, brotherhood, and love that I have the privilege to share with him and his family. I also would like to thank Marina Capistrano, Arthur and Oliver Guimarães, for filling my heart with love in this distant land. Also, many thanks to Samir, Manuel, Filipe, Imara, Juba, Bernd and Sasha for reading and commenting on the manuscripts of this thesis. A big thanks to Christian Philipps for translating my abstract into German.

Finally, I would like to thank my family and friends from Brazil. Even though far away, their love has always supported me. Immeasurable thanks go to my mom, Sra. Amara Josefa dos Santos. You are such a warrior! Your perseverance has taught

me to endure the hardest times. Thank you for your sweet love. Many thanks also to my father, José Antônio dos Santos (Zezo for short), to my brothers Fabiano and Juninho, and my dear sister Valdineide (Preta). To Francisco José Lins Peixoto and Clara Maria Dick Peixoto, you guys have taught me so much and for that, I will be always grateful. Finally, I would like to thank my fiancée Dr. Estefani Marchiori Pereira. My dearest, you have always been there for me, even on my worst days — thank you! You are my number one adventure partner because you are always ready for the next call. I love you very much.

Band / Volume 198
Shortcut to the carbon-efficient microbial production of chemical building blocks from lignocellulose-derived D-xylose
C. Brüsseler (2019), X, 62 pp
ISBN: 978-3-95806-409-6

Band / Volume 199
Regulation and assembly of the cytochrome *bc*$_1$-*aa*$_3$ supercomplex in *Corynebacterium glutamicum*
C.-F. Davoudi (2019), 135 pp
ISBN: 978-3-95806-416-4

Band / Volume 200
Variability and compensation in Alzheimer's disease across different neuronal network scales
C. Bachmann (2019), xvi, 165 pp
ISBN: 978-3-95806-420-1

Band / Volume 201
Crystal structures and vibrational properties of chalcogenides: the role of temperature and pressure
M. G. Herrmann (2019), xi, 156 pp
ISBN: 978-3-95806-421-8

Band / Volume 202
Current-induced magnetization switching in a model epitaxial Fe/Au bilayer
P. Gospodarič (2019), vi, 120, XXXVIII pp
ISBN: 978-3-95806-423-2

Band / Volume 203
Network architecture and heme-responsive gene regulation of the two-component systems HrrSA and ChrSA
M. Keppel (2019), IV, 169 pp
ISBN: 978-3-95806-427-0

Band / Volume 204
Spin-orbitronics at the nanoscale: From analytical models to real materials
J. Bouaziz (2019), 228 pp
ISBN: 978-3-95806-429-4

Band / Volume 205
Advanced methods for atomic scale spin simulations and application to localized magnetic states
G. P. Müller (2019), xx, 194 pp
ISBN: 978-3-95806-432-4

Band / Volume 206
Different growth modes of molecular adsorbate systems and 2D materials investigated by low-energy electron microscopy
J. E. Felter (2019), vi, 114, XXXIV pp
ISBN: 978-3-95806-434-8

Band / Volume 207
NADPH-related studies performed with a SoxR-based biosensor in *Escherichia coli*
A. Spielmann (2019), IV, 73 pp
ISBN: 978-3-95806-438-6

Band / Volume 208
Chemisorption aromatischer Moleküle auf Übergangsmetalloberflächen: Bildung molekularer Hybridmagnete
S. Schleicher (2019), 109 pp
ISBN: 978-3-95806-442-3

Band / Volume 209
Regulatory interactions between *Corynebacterium glutamicum* and its prophages
M. Hünnefeld (2019), IV, 209 pp
ISBN: 978-3-95806-445-4

Band / Volume 210
Quantum Technology
Lecture Notes of the 51st IFF Spring School 2020
23 March – 03 April 2020, Jülich, Germany
ed. by H. Bluhm, T. Calarco, D. DiVincenzo (2020), ca. 700 pp
ISBN: 978-3-95806-449-2

Band / Volume 211
Interaction of physical fields with nanostructured materials
(2020), 255 pp
ISBN: 978-3-95806-450-8

Band / Volume 212
First-principles study of collective spin excitations in noncollinear magnets
F.J. dos Santos (2020), 270 pp
ISBN: 978-3-95806-459-1

Schlüsseltechnologien / Key Technologies
Band / Volume 212
ISBN 978-3-95806-459-1

Mitglied der Helmholtz-Gemeinschaft

JÜLICH
Forschungszentrum